Ion irradiation effects on high purity bcc Fe and model FeCr alloys

Arunodaya Bhattacharya

Arunodaya Bhattacharya. Ion irradiation effects on high purity bcc Fe and model FeCr alloys. Other [cond-mat.other]. Université Paris Sud - Paris XI, 2014. English. NNT : 2014PA112398 . tel-01252243

HAL Id: tel-01252243
https://theses.hal.science/tel-01252243

UNIVERSITÉ PARIS-SUD

ÉCOLE DOCTORALE 534 :
MODÉLISATION ET INSTRUMENTATION EN PHYSIQUE, ÉNERGIES, GÉOSCIENCES
ET ENVIRONNEMENT

Laboratoire : DEN/DMN/SRMP, CEA-Saclay et CSNSM, Orsay

THÈSE DE DOCTORAT

PHYSIQUE

par

Arunodaya BHATTACHARYA

Ion irradiation effects on high purity bcc Fe and model FeCr alloys.

Date de soutenance : 09/12/2014

Composition du jury :

Directrice de thèse :	Brigitte DÉCAMPS	Directrice de Recherches (CSNSM, Orsay)
Rapporteurs :	Isabelle MONNET	Ingénieur de Recherche (CIMAP, Caen)
	Philippe VERMAUT	Maître de Conférences (ENSCP, Paris)
Examinateurs :	Frédérico GARRIDO	Professeur (Université Paris-SUD, Orsay)
	Jean-Luc BECHADE	Professeur (INSTN, CEA, Saclay)
	Kazuto ARAKAWA	Associate Professor (Shimane University, Japan)
	Brigitte DÉCAMPS	Directrice de Recherches (CSNSM, Orsay)
Membres invités :	Estelle Meslin	Ingénieur de Recherche (CEA, Saclay)
	ou Jean HENRY	Ingénieur de Recherche (CEA, Saclay)

Contents

Nomenclature

aDLD	Advanced Delay Line Detector
appm	Atomic parts per million
APT	Atom Probe Tomography
ASTRID	Advanced Sodium Technological Reactor for Industrial Demonstration
bcc	body centered cubic
BF	Bright Field
CALPHAD	Calculation of Phase Diagrams
CEA	Commissariat à l'énergie atomique et aux énergies alternatives
Cr	Chromium
CSNSM	Centre de Sciences Nucléaires et de Sciences de la Matière
DBTT	Ductile-to-Brittle Transition Temperature
DFT	Density Functional Theory
dpa	Displacements per atom
EBR	Experimental Breeder Reactor
EDF	Électricité de France
EDS	Energy Dispersive X-ray Spectroscopy
EFDA	European Fusion Development Agreement
EMIR	Études des Matériaux sous Irradiation
F-M steels	Ferritic-Martensitic steels
FFTF-MOTA	Fast Flux Test Facility-Materials Open Test Assembly
FIB	Focused Ion Beam

GFR	Gas Cooled Fast Reactor
He	Helium
HVEM	High Voltage Electron Microscope
IFMIF	International Fusion Materials Irradiation Facility
IR	Infra red
ITER	International Thermonuclear Experimental Reactor
JANNuS	Joint Accelerators for Nano-science and Nuclear Simulation
KBF	Kinematic Bright Field
LaWATAP	Laser Assisted Wide Angle Tomographic Atom Probe
LFR	Lead Cooled Fast Reactor
MD	Molecular Dynamics
MSR	Molten Salt Reactor
NRT	Norgett Robinson Torrens
ODS	Oxide Dispersion Strengthened
PAS	Positron Annihilation Spectroscopy
PD	Point Defects
PDE	Partial differential equations
PFBR	Prototype Fast Breeder Reactor
PKA	Primary Knock-on Atom
RID	Radiation Induced Depletion
RIS	Radiation Induced Segregation
RT	Room Temperature
RTNS	Rotating Target Neutron Source
SCWR	Super Critical Water Reactor
SFR	Sodium Cooled Fast Reactor
SIA	Self Interstitial Atom

SRIM	Stopping and Range of Ions in Matter
SRMA	Service de Recherches Métallurgiques Appliquées
SRMP	Service de Recherches de Métallurgie Physique
SRO	Short Range Ordering
STEM	Scanning Transmission Electron Microscopy
TEM	Transmission Electron Microscopy
TOF	Time of Flight
VHTR	Very High Temperature Reactor

Chapter 1

Introduction

Reduced activation high chromium content based ferritic/martensitic (F-M) steels are envisaged as promising candidates for structural materials of next generation sodium cooled fast reactors (SFR) and fusion reactors, due to their good thermo-mechanical properties and moderate void swelling under irradiation [1, 2, 3, 4]. The fine dispersion of nano-dispersoids in the oxide dispersion strengthened (ODS) variant of the F-M steels further enhances their high temperature creep strengths. This makes ODS alloys a candidate for the cladding tubes for the SFRs [4]. Apart from enhancing the creep properties, the other expected role of the nano-dispersoids is to improve the radiation resistance. The interface of these particles with the matrix is supposed to act as a trap for the point defects, thereby enhancing recombination rates.

In these steels, the chromium (Cr) content must be optimised to obtain the desired material response. However, the role of Cr on microstructural evolution in high temperature radiative environments in these materials is not well known.

Another crucial problem of using F-M steels in neutron irradiation environments is the generation of transmutation products. Transmutants induces a progressive evolution of the chemical composition of the material. In particular to fusion environments with 14 MeV neutrons, large amount of helium (He) generation is expected (~10 appm He/dpa). The presence of He and its synergistic effect with ballistic damage can induce strong material property degradation. For instance, He is known to induce embrittlement of steels at high temperatures. Presence of helium on grain boundaries can induce grain boundary de-cohesion and inter-granular ruptures [5, 6, 7]. Furthermore, He can also play a crucial role on void swelling under irradiations [8].

However, a clear picture of the radiation effects on industrial steels is difficult to obtain due to the presence of other minor alloying elements and impurities. Thus, to simplify the problem, binary FeCr alloys are studied, which are the representatives of the industrial F-M steels

In our case, the objective of the thesis was to understand the basics of radiation behaviour in high purity FeCr alloys and a reference bcc Fe. In particular, the interest of the study was focused to know the influence of Cr and He on the microstructural evolution under irradiation in these materials. The work is a collaborative effort between SRMP/SRMA at CEA-Saclay and CSNSM, Orsay, under the direction of B. Décamps and co-supervision of E. Meslin, J. Henry and A. Barbu. The materials were provided by EFDA. Energetic ions, instead of neutrons, were used as a source of ballistic damage. The behaviour of He was simulated by performing co-implantation of He (dual beam irradiations). The ion irradiation experiments were performed at the JANNuS multi-beam irradiation facility of the French EMIR network of accelerators. For our study, JANNuS dual beam in-situ irradiation facility at CSNSM, Orsay, was utilised to analyse the real time evolution of defects, courtesy to the coupling of two accelerators with a transmission electron microscope (TEM). JANNuS triple beam facility at CEA-Saclay was utilised to perform ex-situ irradiations to relatively high doses. The advantage of using ion irradiations is that a wide range of doses, He implantation rates and damage rates can be achieved with good a command over the irradiation temperature. Three different doses were reached, with and without simultaneous implantation of He: high dose (157 dpa, 17 appm He/dpa for the dual beam case), intermediate dose (45 dpa, 58 appm He/dpa for the dual beam case) and low dose (0.33 dpa, 3030 appm He/dpa for the dual beam case). The former two cases were ex-situ type irradiations, while the later was in-situ type. The irradiations were performed on electro-polished TEM thin foils and on bulk discs of 100 μm thickness.

The irradiation temperature was fixed at 500 ºC. It was selected for two reasons: peak swelling temperature in ion irradiated bcc Fe and FeCr alloys is claimed to be around this value [9, 10, 11, 12]. Secondly, a part of the study was aimed at comparing results in FeCr alloys with those obtained on bcc Fe in a related thesis work of D. Brimbal [13], where the irradiations were performed at 500 ºC.

The microstructure was characterized after the irradiation, principally by conventional TEM. The study was performed on the as-irradiated specimens and on focused ion beam (FIB) specimens extracted from the irradiated samples to have access to the complete depth distribution of the radiation damage. Energy dispersive X-ray spectroscopy (EDS) in scanning TEM (STEM) mode and atom probe tomography (APT) have also been used in the study. These analytical tools were employed to analyse the distribution of Cr adjacent to radiation induced defects. Furthermore, a part of the results on the experimental study focused on void swelling are discussed by simulations utilising the cluster dynamics code CRESCENDO developed at SRMP, CEA-Saclay and EDF R&D.

The plan of the manuscript is as follows: a detailed bibliography is given in the next chapter, which summarises the material needs for the next generation of reactors, a brief overview of radiation damage process, the differences between neutron, ion and electron irradiations and the current status of knowledge on radiation effects in bcc Fe and FeCr alloys. Then, the materials used and the techniques utilised are presented. This is followed by two chapters on experimental results. The first chapter presents the results obtained after irradiation to high dose. The main focus is the cavity microstructure and swelling. Then, the next chapter presents the results on the dislocation loop microstructure observed after low and intermediate dose. Then, a discussion of the results is given. Finally, the general conclusions are presented in the last chapter.

This work was performed within the framework of the joint program "CPR ODISSEE" funded by AREVA, CEA, CNRS, EDF and Mécachrome under contract n°070551. It was supported by EFDA, EMIR and the JANNuS platform.

Chapter 2

Bibliography

Structural materials will be exposed to unprecedented radiation environments in the next generation fission and fusion reactors [4]. Thus, the need for optimum material performance is stringent. As we shall see in this chapter that currently F-M steels and their nano-structured variant ODS steels are considered as promising candidates [1, 2]. However, the key to success for ensuring safe and satisfactory operation in high temperature radiative environment lies in basic understanding of the effects of radiation on these materials. For this purpose, it is essential to limit the number of variables in terms of impurities and minor alloying elements. Thus, a large amount of research work has been focussed on the binary FeCr model alloys, which are representative of these steels. In the first section of this chapter, a literature survey on the key issues concerning the material needs and available choices for the future generation of reactors is given. The second section briefly describes the main microstructural modifications that can occur in particular to metallic materials whey they are exposed to radiation. It also details the essential fundamental differences between different type of radiations that can produce material damage. Then, the current status of research on radiation damage in bcc Fe and the effect of Cr on radiation damage in FeCr alloys is given. For both the cases, the bibliography is broken up into sections describing separately the interstitial type defects and the vacancy type defects. Then, the influence of helium on the microstructure is presented. Finally, a brief summary of the essential points concerning the radiation damage in bcc Fe and FeCr alloys is given.

2.1 Materials for next generation fission and fusion reactors

2.1.1 In-service conditions and material requirements

In Generation IV fast fission reactors and fusion reactors, the structural materials will be exposed to high neutron fluence at elevated temperatures in a corrosive environment such as liquid metals, water or gas. The operating conditions are, hence, severe and will test the functionality of materials to their extreme limits. In terms of radiation damage, the major difference between the fission and the fusion environment is the neutron spectrum. Fission neutrons are between 1 - 2 MeV, while fusion neutrons are 14.1 MeV [14, 15]. Furthermore, for iron atoms, the cross-section for (n, α) transmutation reaction is high for fusion relevant conditions, between 10 - 15 MeV [16, 17, 18]. Thus, the helium generation rate is much larger in a fusion environment (10 appm He/dpa[1]) as compared to the fast fission reactors (less than 1 appm He/dpa) [7, 4]. A comparison of the irradiation conditions and He generation of these two systems, along with other type of reactors and neutron irradiation facilities, can been seen in figure 2.1.

Given the operating limits, the materials should have the following characteristics:

- High temperature thermal and irradiation creep strength which will determine the maximum operating temperature.
- Resistance to void swelling.
- The mechanical properties (like ductility, tensile strength, fracture toughness etc.) should be within acceptable limits after prolonged exposure during in-service conditions.
- Coolant compatibility and resistance to corrosion.
- Additionally for fusion, the materials should not cause field perturbations to the plasma.

If all these parameters are met, the engineering (weldability, workability etc.) and economic concerns would take over.

2.1.2 Candidate choices

In the previous and current generation sodium cooled fast reactors (SFR), austenitic steels are used for the fuel cladding tubes [1, 2, 19]. However, they exhibit high void swelling rates, high thermal stresses due to low thermal conductivity and high thermal expansion coefficients [1]. At present, for the next generation SFRs, advanced Ti modified swelling resistant variants of austenitic steels would still be used for fuel cladding tubes [2]. For example AIM1 (15%Cr, 15%Ni, and 0.4%Ti)[2] for future French fast reactor ASTRID (Advanced Sodium Technological Reactor for Industrial Demonstration) [2] or modified D9

---

[1] The concept of dpa is described in section 2.3.

[2] The compositions of all the materials in this manuscript is given in weight percent. However, at some places atomic percent is utilised for the sake of convenience, for example, for some results available on simulations and for analysis by EDS or APT.

steel, named as InD9 austenitic steel (15%Cr, 15%Ni, and 0.2%Ti), for the under-construction Prototype Fast Breeder Reactor (PFBR) in India [19] . However, they still exhibit higher swelling rate as compared to F-M steels (see figure 2.2 and reference [2]). Thus, a strong interest is building towards F-M steels or nano-structured variant of F-M steels for the Gen. IV systems.

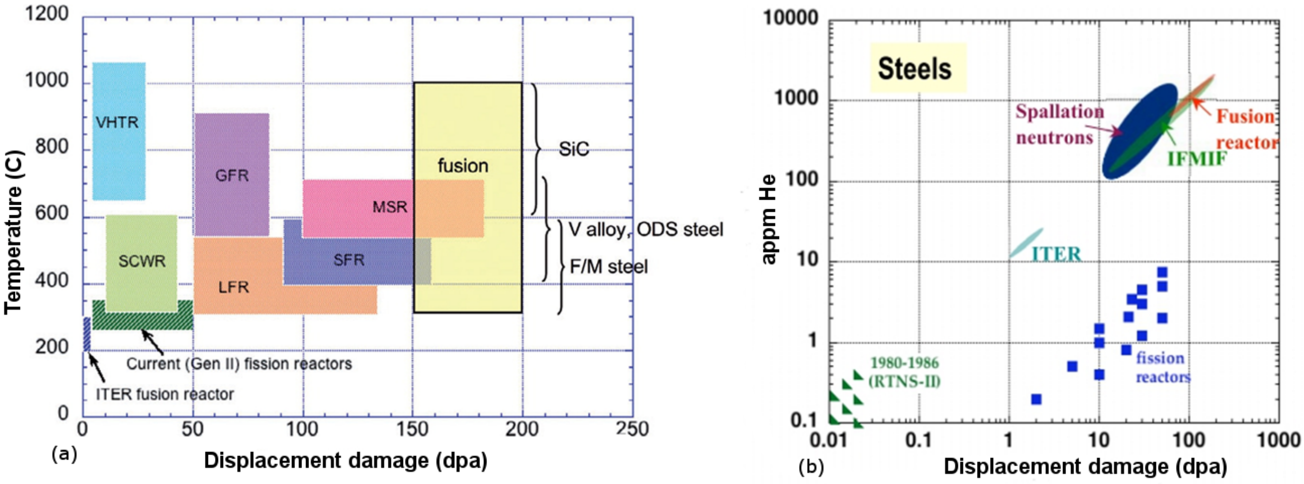

Figure 2.1: a). Temperature and dose requirements for in-core structural materials for the operation of the six proposed Generation IV advanced reactor concepts, fusion reactor concepts and the current generation of reactors. The dimensions of the colored rectangles represent the ranges of temperature and displacement damage for each reactor concept [14]. b). A comparison of helium and damage production in the future fusion reactors with the other systems [20].

As far as fusion reactor applications are concerned, the austenitic steels have been ruled out as structural materials for the plasma facing components. It is mainly due to swelling issue [1] . Since the neutron damage in fusion reactors are expected to be much higher than fast reactors (see figure 2.1), swelling in austenites could reach much higher values. Presently only three materials are considered as viable options:

SiC/SiC composites, vanadium alloys and reduced activation high chromium F-M steels [1]. For the first two candidates, joining technology still needs to be developed to form large structures. This makes F-M steels as the most promising candidates. As we saw earlier, it is also a material of interest for fission reactor applications. However, the key to success for ensuring a safe and satisfactory operation in extreme radiative environments lies in radiation response of these steels. The main points which merits their choice are summarized below:

High temperature and radiation response of F-M steels As mentioned earlier, in radiative environments, F-M steels exhibit good dimensional stability with resistance to void swelling as compared to austenitic steels. For example, their steady state swelling rate is expected to be around 0.2% /dpa as opposed to 1%/dpa for austenitic steels) [3]. A comparison of their swelling behaviour with different grades of austenitic steels is given in figure 2.2

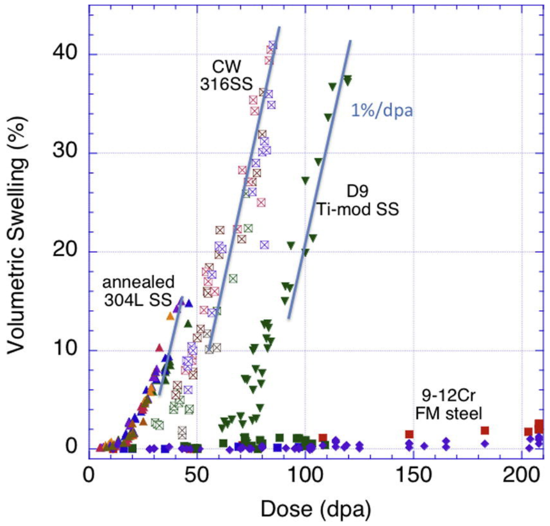

Figure 2.2: Comparison of the volumetric void swelling behaviour of different austenitic stainless steel grades with 9-12% Cr-tempered F-M steels following irradiation at 400-550 ^{o}C to high doses in a fast fission reactor spectrum summarized by Zinkle and Was. [21].

They also exhibit high thermal conductivity and relatively good thermal and irradiation creep resistance up to around 540-550^{o}C [22, 23]. However, they exhibit ductile to brittle transition (DBTT) which shifts to higher temperatures under irradiation [1]. They are prone to low temperature irradiation hardening for $T \leq 400$ ^{o}C [1]. Furthermore, at higher temperatures (beyond temperature 550^{o}C), their long term creep rupture strengths are low [1, 24]. This is the reason why F-M steels may not be directly used as cladding tubes of future SFRs, and austenites are still being used despite their higher swelling rate [2]. At present, F-M steels are only planned to be used for hexagonal tubes of the fast reactor fuel assemblies [2].

Nano-structured variant of these steels, known as Oxide Dispersion Strengthened (ODS) steels offer potential for high temperature applications ($T > 550$ ^{o}C) where conventional F-M steels can not be used due to low creep resistance [1]. A fine dispersion of hard nano-dispersoids can block the glide and climb of dislocations. The particle interfaces can act as sinks and reduce the portion of defects going to the dislocations which will reduce their climb, thereby, limiting creep. They may also improve the overall irradiation resistance of the steel. Currently, ODS ferritic steel is the primary candidate for the first wall material of the plasma facing components in fusion reactors and is considered for the cladding tubes of Gen. IV sodium cooled fast reactors with an extensive research programme centred in Europe, Japan, the USA and India.

Optimization of Cr concentration of F-M steels Most of the properties of F-M steels mentioned earlier are dependent on the chromium level of the steel. Higher chromium content is desirable for improvement in corrosion resistance. Lo and co-workers [25] have shown that a minimum of about 11 wt.% Cr is needed to form an effective passivation layer on the surface of these steels. In terms of radiation tolerance, 9 wt.% Cr is identified as the requirement for minimum DBTT shift [26]. As will be shown in Chapter 4, void swelling is also a non-monotonic function of chromium concentration. Thus, the selection would depend on a balance between optimum radiation tolerance and corrosion resistance required for the in-service conditions.

Apart from Cr level, the microstructure of the steels also needs to be optimized for the desired applications. In fusion environment, a martensitic structure is desirable due to its better irradiation tolerance than ferritic structure. This makes 9wt.% Cr tempered martensitic steel as the ideal candidate. In fission environment, a minimum of 14wt.% Cr is however essential to prevent corrosion and accidental breaking of clad especially during spent fuel treatment. But above 14wt.% Cr, the structure can not be martensitic. Thus, the interest is to develop ferritic steels for fission activities.

2.2 Radiation damage and its effect on microstructure

The main mechanism of radiation damage is by the elastic collision of energetic neutrons, ions or electrons with the lattice atoms of the structural materials. When the energy transferred is higher than the displacement threshold E_d[3] , the lattice atom is ejected out of its site leaving a vacancy behind. Such an interstitial-vacancy pair is termed as a Frenkel Pair. If the energy transferred is high enough, the ejected atom becomes itself a projectile (usually denoted as a primary knock-on atom PKA), and further induces the displacement of atoms generating displacement cascades, themselves divided into sub cascades. The time scales for displacement cascades are very small (few ps), and can not be observed experimentally with the present available characterization techniques. However, Molecular Dynamics (MD) simulations allow their study [27, 28].

In such cascades, a large fraction of the defect population is annihilated by mutual recombination and only few stable point defects (PDs) remain [27, 28]. Thereafter, the entire evolution of the irradiated microstructure depends on the properties of these PDs; principally on the formation energies, formation volume, binding energy with other type of defects and the migration energies.

The concentration of PDs adjacent to other larger PD clusters is low. This, therefore, creates a concentration gradient and hence a flux of PDs towards such clusters. The recombination rate is increased adjacent to them and they behave like sinks. Defect clusters also reduce the mobility of dislocations leading to hardening of the material [1].

The appearance of defect clusters, their size, density and morphology is strongly dependent on irradiation conditions.

In the following sub-sections, the main microstructural features arising as a result of clustering of PDs (mainly dislocation loops and cavities) and the effect of solute diffusion under irradiation are briefly presented.

---

[3] Displacement threshold is the minimum energy required to permanently displace an atom from its regular site and create a Frenkel Pair. It takes into account the volume of athermal recombination. Since it depends upon the direction of the velocity given to the PKA, it is averaged over all the possible directions.

2.2.1 Dislocation microstructure

Self-interstitial atoms (SIA) or their clusters are much more mobile compared to vacancies below 0.3T$_m$, where T$_m$ is the melting temperature of the material. Furthermore, the binding energy of self-interstitial clusters is higher as compared to vacancy clusters making them comparatively more stable [29]. A comparison of binding energy and migration energy between <110> oriented self-interstitials and small vacancy clusters in bcc Fe, calculated from ab-initio is given in figure 2.3. Thus, owing to high mobility and higher binding, self-interstitials or their small clusters during their migration, can combine to form bigger clusters and grow further to form 2D defects[4]: **the dislocation loops** of interstitial nature.

During prolonged irradiation, the dislocation loops grow in size while the new loop nucleation continues. The growth is much faster at higher temperatures owing to enhanced mobility. When the loops are sufficiently large in size, they lead to formation of complex loop networks due to interaction/impingement with other loops [30]. These network dislocations are typically randomly distributed and are often heavily jogged as opposed to the relatively straight dislocations found in unirradiated metals.

Dislocation loops influence the deformation behaviour and consequently the ductility and hardening of irradiated materials [31]. Furthermore, dislocation loops introduce distortions to the lattice which interact with the other distortion centres. They, thus, behave as biased point defect sinks: meaning that they exhibit preferential attraction for interstitials than for vacancies [31] and have a strong impact on the redistribution of the PDs and the evolution of the microstructure.

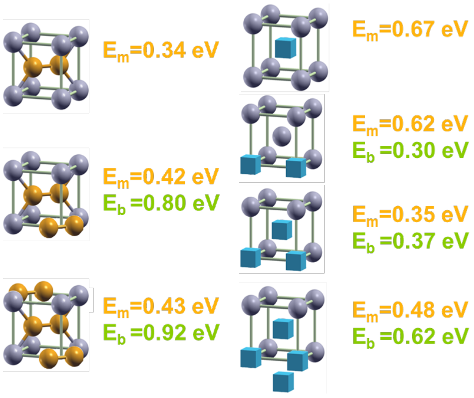

Figure 2.3: Ab-initio results of binding and migration energies of self-interstitial and vacancy clusters in bcc Fe, denoted as E$_b$ and E$_m$ respectively. Reconstruction from [29].

2.2.2 Cavity microstructure and swelling

Cavity nucleation and growth Vacancies attain mobility at relatively higher temperatures (beyond 0.3T$_m$) [31]. Supersaturation of vacancies under irradiation combined with their mobility could lead to

---

[4] We shall see in section 2.4.1 on page 19, recent theoretical calculations predict formation of 3D SIA clusters, known as C15 laves phases, in bcc Fe. They have, however, never been detected experimentally so far.

the nucleation of three dimensional (3D) vacancy clusters. These clusters could then grow further by vacancy absorption.

Vacancy clusters visible by TEM are given the names cavities, voids or bubbles. As mentioned by Zinkle [30], there is an important distinction between the definitions for these terms. Void refers to an object whose stability is not dependent on the presence of internal pressurization from a gaseous species such as He. Bubbles are defined as pressurized cavities. The term cavity can be used to refer to either voids or bubbles and is often used as a generic term for both cases. In our work, same definitions have been used.

It must be noted that the nucleation and growth of cavities is controlled by the dislocation bias. The required vacancy supersaturation is provided by the preferential absorption of interstitials by the dislocations. Thus, if there are no dislocations, there is no cavity nucleation and growth. Addition of gases like He help in stabilizing small vacancy clusters leading to early nucleation (see section 2.6 for more details).

Void swelling From macroscopic point of view, formation of cavities lead to the phenomenon of "void swelling" which induces dimensional instability by increase in the overall volume of the irradiated material [32, 3, 31] . For a given irradiation condition, this phenomenon achieves maximum value at an intermediate temperature known as the "peak swelling temperature" (see figure 2.4). For different grades of industrial F-M steels, this temperature is claimed to be between 425 - 550 ^{o}C upon ion irradiations [1]. Below this temperature, cavities are not formed due to dominant mutual recombination and slow diffusing vacancies; while at higher temperatures dominant vacancy evaporation from cavities take place due to low binding energy of vacancy clusters [1].

Peak swelling temperature is strongly dependent on the irradiation conditions, in particular on the damage rate [33, 34]. Its shift to higher temperatures is expected upon increase in damage rate. It is depicted, for example, in a comparison of void swelling in pure nickel irradiated by neutrons (10^{-7} dpa/s) and self-ions (3 x 10^{-3} dpa/s) by Packan and co-workers [34] in figure 2.4.

In experimental conditions, void swelling value is estimated by measuring the volume fraction of cavities using TEM imaging or by immersion density test [35, 36]. The later is based on Archimedes principal: the swelled material is dropped in a liquid, and the volume of the displaced liquid is estimated. However, in reality, immersion density measurements correspond not only to volume of voids but also to the volume of any precipitates that may have formed. Thus, it is a measure of total or net swelling. In certain cases, when no or very little precipitation has occurred, void swelling estimates are expected to be fairly similar by both the techniques. But when precipitation is large, there may be discrepancies between the two techniques. Precipitate formation can also lead to densification of the material. In this case, it appears as negative swelling value by immersion density [37]. This method is usually accurate to ± 0.2% [37]. Thus, if swelling is below this value, this technique should not be utilised. Such restrictions do not apply to TEM based observations. In this manuscript, wherever literature data obtained from immersion density technique is discussed, it is specifically mentioned.

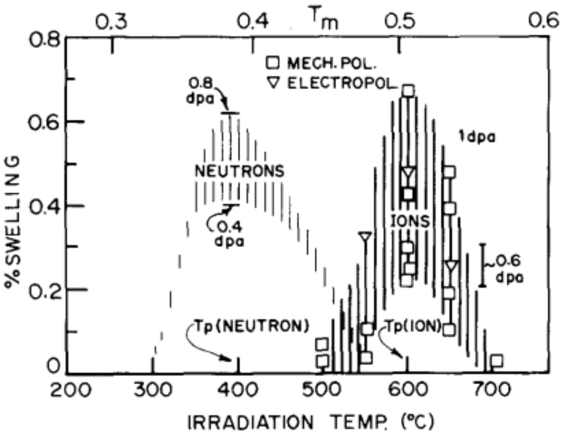

Figure 2.4: Shift in peak swelling temperature in pure Ni irradiated by neutrons (10^{-7} dpa/s) and self-ions (3 x 10^{-3} dpa/s) up to approximately 1 dpa [34]. T_m denotes the melting temperature.

It is interesting to note that the formation volume of vacancies are much smaller than those of interstitials. They can, thus, combine to form both 2D defects (vacancy platelets, vacancy type dislocation loops) or 3D cavities. However, in bcc Fe based alloys, cavities are energetically more favourable [38] - platelets are never observed and vacancy loops are observed only in very rare cases. This part is discussed in detail in section 2.4.

2.2.3 Solute diffusion under irradiation and its consequences

Radiation enhanced precipitation High vacancy concentration and mobile self-interstitial clusters accelerate the diffusion rate in irradiated materials. Enhanced diffusion can enhance the thermodynamically predicted phase transformation, i.e. it occurs at an increased rate, possibly at a temperature lower than the phase transformation temperature. This phenomenon is known as radiation enhanced precipitation. As we shall see in section 2.5.2.2 on page 29, a classic example is the appearance of Cr rich α' phase after irradiation in under-saturated concentrated FeCr alloys.

Radiation induced segregation/depletion and precipitation Radiation can also lead to solute segregation/depletion at the point-defect sinks [31]. This happens if there is a coupling between the point defect and solute fluxes leading to a re-distribution of the chemical elements in the material [31]. A permanent flux of point defects toward the sinks can result in a coupled transport of the solute atoms inducing a non-equilibrium segregation or depletion process at the sink known as radiation induced segregation/depletion (RIS/RID). It happens around $T_m/3$, where T_m is the melting temperature of the alloy [26, 39].

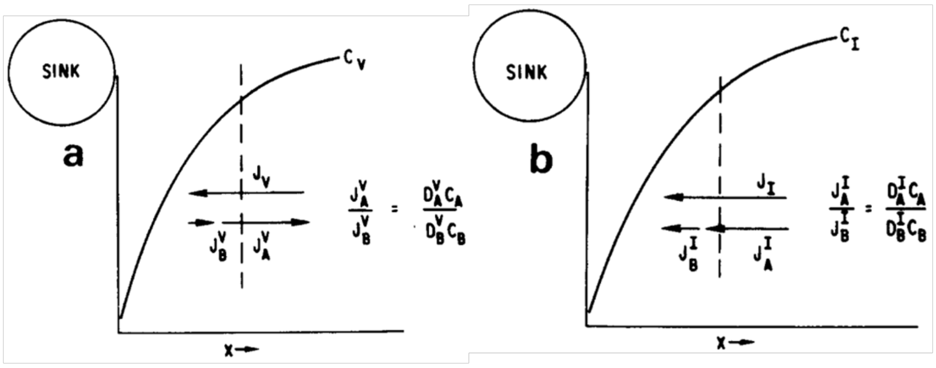

Figure 2.5: Schematic illustration of Inverse Kirkendall Effect induced by (a). Vacancy flux and (b). Interstitial flux [39].

If there is no strong binding between vacancy and solute atoms, the flux of vacancies towards the sinks would induce the flux of atoms in the opposite direction. In an A-B alloy, if A atoms diffuse faster than B ($D_B^V < D_A^V$), the sink will be depleted in A and enriched in B, and vice-versa. This phenomenon of RIS is referred as Inverse Kirkendall effect [39, 40]. In contrast, the sink will be enriched in A atoms by drag effect if they are bound to the self-interstitials which arrive at the sink [40]. Such a scenario is also possible if A atoms have strong binding with the mobile vacancy clusters. The mechanisms are schematically explained in figure 2.5

Furthermore, sometimes it is possible that by RIS, the concentration of solute could locally exceed the solubility limit at the irradiation temperature. This would lead to precipitation at sinks (radiation induced precipitation) in an overall under-saturated alloy [31]. The origin of this effect is purely kinetic and hence can induce non-equilibrium phases.

2.3 Comparison of radiation damage by neutrons, ions and electrons

Radiation damage can be induced in a material by using neutrons, energetic ions or electrons. In order to compare the damage by different types of irradiations, the standard exposure unit used is "**dpa**" standing for displacements per atom. It is the average number of times an atom has been displaced from its regular lattice site. The current widely accepted format is the NRT (Norgett, Robinson, Torrens) model [41] based on binary collision approximation with classical mechanics treatment.

However, there are fundamental differences in primary damage production based on the type of the particle chosen for irradiation, to which dpa value is insensitive. For instance, irradiation damage by neutrons is homogeneous along the target depth [31]. The primary damage consists of displacement cascades, point-defect clusters and Frenkel pairs. Neutron irradiations are relatively slow. Typical damage rate for neutron irradiations is between 10^{-6} to 10^{-10} dpa/s. Furthermore, neutrons also produce transmutation gases, in particular helium and also induce residual specimen activity [1, 31].

On the other hand, ions in ion irradiations act like PKA (primary knock-on atoms) in neutron irradiation. Unlike neutrons, ions are charged particles and they interact by electronic excitations and ballistic collisions [31]. In metals, it is the ballistic collision component which is responsible for material damage. The primary damage consists of displacement cascades, point defect clusters and Frenkel pairs. The damage is limited to small thickness and is not homogeneous. Faster damage rates between 10^{-2} to 10^{-4} dpa/s can be easily obtained. Although, the evolution of the microstructure at a given temperature depends on the primary knock-on atom (PKA) spectrum and the rate of damage, the ion irradiations can provide reliable information on fundamental mechanisms governing the radiation damage process, with an efficient command over the irradiation parameters: the irradiation temperature in particular. They are also cost effective, less time consuming with no issues of sample activation.

Concerning electron irradiations, the main difference is in the primary damage formation which consists of only Frenkel pairs [31]. Thus, the microstructural evolution is solely governed by point-defect diffusion. In this case, the damage rate is between 10^{-2}- 10^{-3}dpa/s for high voltage electron microscopes (HVEM).

The main differences among the three irradiation types are summarized in table 2.1. Considering these important differences into account, it is necessary to detail all the necessary irradiation parameters along with the dpa value while reporting experimental results.

Parameters	Neutrons	Ions	Electrons
Primary damage	Cascades, PD clusters and Frenkel pairs	Cascades, PD clusters and Frenkel pairs	Only Frenkel pairs
Damage rate	10^{-6} - 10^{-10} dpa/s	10^{-2} - 10^{-4}dpa/s	10^{-2} - 10^{-3}dpa/s
Style of damage	Homogeneous	Heterogeneous	Heterogeneous and localised
Samples	Bulk materials (no surface effects)	Few nm to ~100 μm (strong surface effects)	Few nm (TEM foils) to few mm
Energy	Depends on spectrum ~1 MeV for fast reactors 14 MeV for fusion	Few keV to ~100 MeV	1 MeV and higher
Transmutants	Yes	Yes, simulated by multi-beam irradiations	No
Sample activation	Yes	Low to none	No

Table 2.1: Fundamental differences between neutron, ion and electron irradiations [1, 31, 42]

2.4 Radiation damage in bcc Fe

In this section, bibliography on radiation damage in bcc Fe is given. Firstly, the theortical results are presented. Then, experimental results are given. The sections are divided into separate parts for interstitial and vacancy type defects.

2.4.1 Interstitial type defects

2.4.1.1 Theoretical Background

Recent advances in ab-initio and MD simulations have provided significant input into understanding the stability and migration of small SIA clusters which can not be seen experimentally [29, 43, 44, 45]. Based on the calculations of Fu and Willaime [29] it is known that a single SIA is the <110> dumbbell in bcc Fe. Up to four SIAs the most stable configuration is a cluster with parallel alignment of such dumbbells [46]. This is a specificity of Fe, since in other bcc transition metals the defect is aligned in, or close to, the <111> direction, forming a crowdion [47]. Long-distance migration of isolated dumbbells is by nearest-neighbour translation-rotation jump as shown in 2.6, with a migration energy of 0.34 eV which is coherent with experimentally obtained value of 0.3 ± 0.03 eV reported in [48] . This implies a three dimensional migration of SIAs.

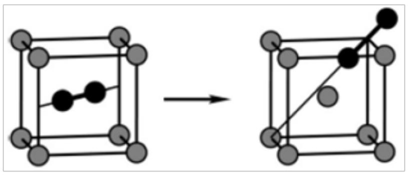

Figure 2.6: Migration mechanism of <110> dumbbells by translation-rotation [29]

Ab-initio studies also predict that the orientation of these dumbbells change from <110> to <111> above around five SIAs [46]. At larger scales these <111> oriented dumbbells can be packed together to form a/2<111> type dislocation loops, which are glissile [49]. However, very recent DFT (Density Functional Theory) calculations by Marinica and co-workers [50] revealed the existence of a metastable and sessile 3D morphology of defects in α-Fe, known as C15 Laves phase. The formation energies of these clusters is by far the lowest for four SIAs or more and is shown in figure 2.7.

Unpublished results from the same group also reveal that C15 phases eventually transform into <111> configuration after a certain size.

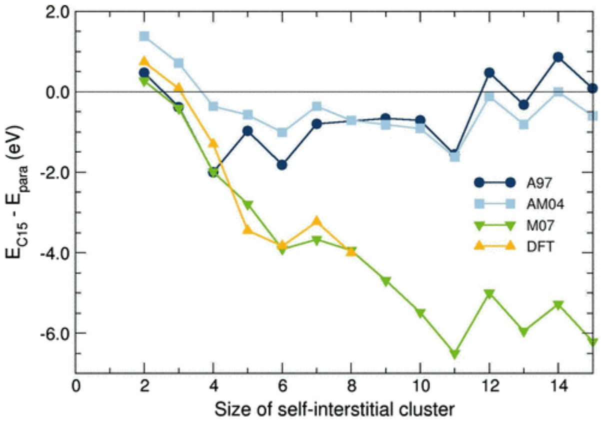

Figure 2.7: Results by Marinica and co-workers [50] showing the formation energies of the C15 SIA clusters in bcc Fe calculated with respect to the lowest energy parallel-dumbbell configurations, i.e., with a <110> orientation up to four SIAs and a <111> orientation at larger sizes. The green curve corresponds to Marinica's potential, named as M07. A97 [51] and AM04 [52] are the other two empirical potentials. The DFT results are compared to those from empirical potentials.

However, in the following sections which describes the experimentally observed evolution of dislocation loop microstructure in bcc Fe under different irradiation conditions, it will be shown that dislocation loops with Burgers vector a<100> are also observed in bcc Fe. The exact formation mechanism of this type of loop is still a debate. All the mechanisms proposed by many experimental and theoretical groups is discussed at the end.

2.4.1.2 Experimental Background

This section describes the experimental results available in literature on dislocation loops in irradiated bcc Fe. The section is divided into parts on neutron, ion and electron irradiated results. In all these cases, the microstructure was analysed by TEM.

Neutron Irradiation

Due to long penetration depth of neutrons, such irradiation experiments are performed on bulk specimens from which thin foil discs for TEM observations are punched out. As specimens are massive, there are negligible surface effects. Thus, the orientation of the grains for loop analysis by TEM is unimportant. The main results are the following:

- Interstitial type dislocation loops with burgers vector a/2<111> and a<100> are observed in neutron irradiated bcc Fe. Relative proportion between these two type of loops depend upon the irradiation temperature. The a/2<111> type population reduces upon increasing the temperature and almost becomes negligible beyond 300 ^{o}C. Beyond this temperature, a<100> perfect loops situated on $\{100\}$ planes are predominant [53, 54, 55, 56] .

- For a given neutron fluence, the average loop size increases and number density decreases with increase in the irradiation temperature. Horton and co-workers [54] observed 600 nm large loops at 500 ^{o}C, while the size dropped to 43 nm at 350 ^{o}C. Furthermore, three orders of magnitude increase in loop densities was noted when the temperature was lowered to 350 ^{o}C. Up to 0.9 dpa, the microstructure consisted of a homogeneous distribution of loops along with an entangled dislocation network.

- At relatively low doses (less than 1 dpa), both loop size and number density is seen to increase with dose. Zinkle and Singh [57] have shown that the visible defect cluster density increased from 1 x 10^{21} m^{-3} to 6 x 10^{22} m^{-3} when the dose increased from 0.001 dpa to 0.79 dpa at 70 ^{o}C. The corresponding average loop sizes increased from 1 nm to 4 nm. However, up to 0.0001 dpa, no visible defect clusters were observed by TEM. Irradiations at higher temperature (300 ^{o}C) by Hernandez and co-workers [56] show a similar behaviour.

- A tendency of small defect clusters to form rafts is known to exist. Irradiations at 70 ^{o}C by Zinkle and Singh [57], observed such rafts around 0.3 - 0.4 dpa. Most of the rafts were aligned along {111} habit plane; 15-20% of them were aligned along {110} habit plane and {100} alignment was less than 1 %. 80 % of the loops comprising the raft were pure edge a/2<111> type situated on {111} planes. However, a few a/2<111> loops were identified to be situated on {110} planes indicating that they may not be of pure edge character.

Since neutron irradiations are not in-situ type experiments, no direct observation of loop mobilities can be made. This information is obtained from ion and electron irradiation experiments mentioned in the next sub-sections.

Ion irradiations

For ion irradiations of few MeV energy, since the damage is limited to narrow depths (a few hundred nano-metres to few microns), the effect of free surfaces on damage accumulation is significant [13, 58, 59]. Surface effects can strongly induce a bias in the observed microstructure of dislocation loops. A comparison of ion irradiations performed at room temperature on thin foils and bulk specimens by Prokhodtseva and co-workers [58] showed a clear difference in the loop microstructure. For thin foils, 96% of the loops were a<100> type, while more than 75% of the loops in bulk specimen were a/2<111> type. Furthermore, the orientation of the surface can also induce differences in the dislocation loop microstructure for crystals irradiated under same conditions. TEM analysis of high purity bcc Fe irradiated at room temperature (RT) by 500 keV Fe^{+} [60] showed strong variation between the proportions of a<100> and a/2< 111> type loops between [225] and [115] oriented grain . In [225] orientation, a<100> proportion of 70% was observed, while only a/2<111> type loops were detected in [115] orientation. Such a grain orientation dependent defect yield was also reported by Jenkins and co-workers [59]. Thus, for comparative studies, it is essential to consider results obtained in same or similar grain orientations.

The main results are here under:

- Heavy ion irradiation experiments show a strong temperature dependent dislocation loop microstructure, which is qualitatively similar to results on neutron irradiated bcc Fe mentioned earlier. Interstitial type a/2<111> loops are in majority for $T < 300\ ^oC$, while for $T \geq 500\ ^oC$ only a<100> type loops of pure edge character situated on {100} planes are known to exist [13, 59, 61].

- The size of dislocation loops increases with the dose. In-situ self-ion irradiations at 500 ^oC by Brimbal and co-workers [13] observed an increase in average size from 6 nm to 43 nm between 0.1 dpa to 1 dpa . The increase in the size was slower between 0.5 to 1 dpa as opposed to the lower doses. Hernandez and co-workers [62] also observed similar behaviour at 300 ^oC up to 1.3 dpa. Loop size also increase with increase in irradiation temperature [59].

- Back-and-forth oscillatory motion of a/2<111> type loops and their sudden one dimensional jumps from one point to another over large distances (loop hopping) is seen under in-situ irradiations. Jenkins and co-workers [59] saw this effect more pronounced at 300 ^oC than at RT. Based on in-situ TEM heating experiments, Arakawa and co-workers [63, 64] attributed the back-and-forth loop motion to the effect of loop trapping by impurities in the material, in particular by carbon or nitrogen. Furthermore, loss of a/2<111> loops to free surface by glide along <111> direction is also common [59], due to which the total number of loops remaining at the end of the irradiation is less than what is produced by the irradiation. A grain orientation dependent defect yield mentioned at the beginning is essentially due to this effect.

- Recent studies at 500 ^oC by Brimbal and co-workers [13] observed mobility of a<100> loops, which were previously considered to be sessile. Loss of a<100> loops by glide to surface was seen, which increased from 0.25 dpa to 0.5 dpa. They were also seen to perform back-and-forth oscillatory motion.

- Work of Brimbal and co-workers also developed latest insights into kinetic effects on loop microstructure studied by in-situ ion irradiations. It was seen that for a given irradiation temperature, loop density increases with dose and then saturates [65]. The value corresponding to saturation dose is rather low. Transition from increasing loop density to saturation is not straightforward [13]. At 500 ^oC, the number density was seen to increase up to 0.2 - 0.3 dpa. This peak loop density corresponds to the time at which first mobile loops were observed. Thereafter, the density slightly decreased up to 0.5 dpa which was attributed to loop elimination to the free surface. Beyond that, an equilibrium was established between loop elimination and loop nucleation which stabilized the number density at a value of $1.5 \times 10^{14} cm^{-3}$ for <113> oriented grains at 0.5 - 0.6 dpa .

- At higher doses, very large dislocation loops accompanied with a dislocation network are known to exist. For example, a comparison of loops formed at 500 ^oC revealed sizes as large as 177 nm at 10 dpa and between 168 to 228 nm at 100 dpa [13]. Loop number density was less than $10^{13}\ cm^{-3}$ for both the doses (measured on same grain orientation). The dislocation line densities were also very similar, being $1.8 \times 10^9\ cm^{-2}$ at 10 dpa and between $1.1 \times 10^9\ cm^{-2}$ to $3.7 \times 10^9\ cm^{-2}$ at 100 dpa. A slight variation at high dose was an effect of different grain orientation. This observation further emphasizes the kinetic effect mentioned above, which induces an equilibrium between loop nucleation / growth and their elimination at the surface. Furthermore, we must also take into account that when loop networks are formed, the interaction of loops and their incorporation in the network can also stabilise the loop number density [66].

Electron Irradiations

As mentioned in section 2.3 on page 17, only Frenkel-Pairs are formed under electron irradiations. Thus, the dislocation loops are formed purely by the diffusion of point defects. Many studies have been performed on pure Fe by High Voltage Electron Microscopes (HVEM), with electron energy typically 1 - 3 MeV. Since the irradiations were in-situ type, the specimens were always thin foils. The kinetics of radiation damage process is more clearly noted in such experiments in terms of the role of temperature, dose and dose rate. The general conclusions are as follows:

- Similar to ion and neutron irradiations, loops with Burgers vector a<100> and a/2<111> are observed: a<100> type are pure edge type belonging to {100} habit plane [67] , while a/2<111> is seen to have both {111} and {110} habit planes.
- The size of loops increase with dose [68] . Their number density saturates very quickly after the appearance of first visible loops [68].
- The loop densities are higher when the irradiation temperature is reduced for the same dose levels [68, 69]. However, for very low temperatures below -70 ^{o}C, the density stays almost constant [68].
- For a fixed dose, the loop number density increases with increase in damage rate [68].
- Irregular shaped loops are also seen in electron irradiated Fe. For T < 300 ^{o}C, Yoshida and coworkers observed flower shaped loops [70]; while for T > 300 ^{o}C, they were regular in shape.
- Electron irradiations also show back-and forth loop motion of a/2<111> type loops and their glide along <111> direction between -153 ^{o}C to 394 ^{o}C [63, 68, 71, 64]. The frequency of loop motion is shown to drop upon increasing the irradiation temperature between -83 ^{o}C to 102 ^{o}C . Furthermore, thermal annealing between 187 to 427 ^{o}C of thin foil irradiated at -163 ^{o}C is also seen to induce glide of a/2<111> loops [71]. No motion of a<100> loops was detected.

2.4.1.3 Formation mechanisms proposed for dislocation loops observed in bcc Fe

In the previous sub-section, it is seen that both a/2<111> and a<100> loops are formed in bcc Fe. Their relative proportions depend strongly up on the irradiation temperature. However, theoretical calculations based on ab-initio and MD predict that for larger cluster sizes <111> configuration is the most stable (see sub-section 2.4.1.1 “Theoretical Background”). There is, thus, a clear discrepancy between experimental observations and theoretical predictions.

The exact formation mechanism of a<100> loops is still a debate. Eyre and Bullough [72] proposed a shear mechanism for the transformation of faulted <110> clusters to perfect loops with Burgers vector a/2<111> or a<100> as given below:

$$\frac{1}{2}[110]+\frac{1}{2}[00\bar{1}]=\frac{1}{2}[11\bar{1}]$$

$$\frac{1}{2}[110]+\frac{1}{2}[\bar{1}10]=[010]$$

Marian and co-workers [73] have proposed a similar mechanism based on the interactions they observed in their MD simulations. From elasticity calculations, Dudarev and co-workers [74] have shown that a<100> loops are not favourable below 350 ^{o}C, which is consistent with experimental observations described in sub-section 2.4.1.2.

It is also proposed that a<100> loops could stem from the mutual interactions between two a/2<111> type dislocation loops [75, 76, 60] by the mechanism:

$$\frac{1}{2}[111]+\frac{1}{2}[\bar{1}\bar{1}1]=[001]$$

But this argument lacks direct experimental evidence. In-situ TEM experiments by Arakawa and co-workers [77] observed collision between two a/2<111> loops. It was seen that the bigger loop absorbed the smaller one without transforming into a <100> loop. Another set of in-situ electron microscopy studies on irradiated iron performed by the same group [78] showed that upon heating to 300 ^{o}C, small dislocation loops spontaneously transform from a/2<111> to a<100> Burgers vector configurations without a collision between two loops. Furthermore, as quoted by Dudarev and co-workers [74], the argument is unsupported by the fact that a<100> loops are almost never observed in the other non magnetic bcc metals, where small prismatic a<111> loops are just as mobile as in bcc iron.

Thus, the unexplained occurrence of a<100> loops in bcc Fe (and Fe based alloys) makes this system unique compared to the other transition metals.

2.4.2 Vacancy type defects

2.4.2.1 Theoretical Background

As mentioned in section 2.2.2, vacancies can cluster together to form both 2D defects (vacancy platelets, vacancy type defects) or 3D cavities. But in bcc Fe, it is known by molecular static calculations performed with several inter-atomic potentials that a 3D structure of vacancies is much more stable compared to vacancy discs or vacancy type loops [15]. The later is unstable. They have a tendency to shrink under irradiation, ultimately disappearing completely, which can be due to the preferential absorption of interstitials by dislocation loops (effect of bias). Furthermore, vacancy type loops could also shrink and disappear by vacancy evaporation process due to which they have not been observed at high temperatures.

For the 3D clusters, MD simulations show that small vacancy clusters can be formed directly within the displacement cascades in bcc Fe [79] . However, as discussed in section 2.2, binding energy between vacancies or their clusters is much smaller compared to interstitials. Ab-initio calculations by Fu and Willaime [80] show that up to 4 vacancies, binding energy is less than 1 eV. Thus, vacancy clusters are unstable as compared to interstitial clusters and their formation / growth is strongly dependent upon the experimental conditions: the irradiation temperature in particular.

2.4.2.2 Experimental Background

Experimentally, small vacancy clusters containing up to three vacancies have been detected at very low doses (10^{-4} dpa) by positron annihilation spectroscopy (PAS) in neutron irradiated Fe between 50-70 ^{o}C [81]. Larger voids producing void swelling have been observed in many experiments by neutrons or ions. However, vacancy type loops have also been detected in a limited number of irradiation experiments. Such experiments have invariably been heavy ion irradiations performed at low temperatures.

A detailed description of experimental data available on vacancy type defects in bcc Fe observed after different type of irradiation experiments is detailed here:

Neutron Irradiation

- As mentioned in the previous paragraph, small 3D vacancy clusters were detected by Eldrup and co-workers at dose as low as 10^{-4} dpa by PAS. The number density and average size of these clusters increased with dose up to 0.23 dpa. Voids visible by TEM were observed only at 0.72 dpa, with average size and number density being 1.5 nm and 10^{24} m^{-3} respectively.

- Cavities visible to TEM are only observed in intermediate temperature ranges ($0.3T_m$ - $0.5T_m$). This corresponds well with the theory of peak swelling temperature discussed in section 2.2. TEM study performed by Horton and co-workers [54] on specimens irradiated to 0.9 dpa over a wide range of temperatures (180 ^{o}C to 740 ^{o}C) noticed that cavities were present only between 275 ^{o}C to 450 ^{o}C. The average void size varied from 5.7 nm at 275 ^{o}C to 12 nm at 400 ^{o}C. Larger cavities were usually faceted. A maximum swelling of 0.07 % was noted at 400 ^{o}C. Little and Stow [35] investigated swelling by immersion density measurement technique on specimens irradiated between 23 to 30 dpa over a temperature span of 380 ^{o}C to 615 ^{o}C. Two swelling peaks were reported: one at 420 ^{o}C and another one with less amplitude at 510 ^{o}C. For all the irradiation temperatures concerned, swelling remained low (less than 1%).

- Cold working is also seen to affect void swelling in pure Fe [82, 53]. Fast neutron irradiations in BR-10 reactor at 400 ^{o}C up to 26 dpa by Dvoriashin and co-workers [82] produced 4.5% swelling in 10 % cold worked Fe as opposed to 1.7% in annealed Fe. In a related study, Porollo and co-workers [53] observed 3% swelling at only 6.2 dpa in cold worked Fe.

- Heterogeneous distribution of cavities on dislocation lines and loops is known to exist. For the study by Horton and co-workers mentioned above [54], cavity association with small dislocation loops was systematically seen between 275 ^{o}C to 300 ^{o}C. However, beyond 350 ^{o}C, the distribution turned homogeneous. Dislocation lines decorated with cavities is observed by Farrell and Houston [83] at 415 ± 20^{o}C irradiated up to a fluence of 1.5 x 10^{21}neutrons/cm^{2}. In this case, no readily resolvable dislocation loops were observed.

To the best of our knowledge, no group has ever observed vacancy type dislocation loops in neutron irradiated bcc Fe. However, they have been observed in some ion irradiation cases and is detailed later, along with details on the cavity microstructure.

Ion irradiations

Unlike in neutron irradiation, both vacancy type loops and cavities have been observed in bcc Fe after ion irradiations. The section is, hence, divided accordingly to describe both the cases separately.

Vacancy type dislocation loops Dislocation loops of vacancy type have been observed in very rare cases : in thin foils irradiated with heavy ions at relatively low temperatures [84, 85, 86, 87]. Thus, the damage is very close to the surface. Moreover, owing to low temperature, the mobility of point defects is largely reduced. 80 keV W^{+}ion irradiation at RT by English and co-workers [84] observed that all the loops produced were vacancy type. They were perfect loops with Burgers vector a<100> and a/2<111> . A relative proportion between of these two kinds was dependent up on the foil orientation.Vacancy type a/2<111> loops were also claimed by Robinson and co-workers in pure Fe irradiated at -196 ^{o}C by 80 keV Xe^{2+}ions [86]. At relatively higher temperatures, only one group has reported vacancy type loops [85]. They were observed at 350 ^{o}C after 4 MeV Ni^{2+} ion irradiation : but were not detected at higher temperatures (450˚C and 500˚C).

Since vacancy type loops are unstable under irradiation, their presence in these cases is unexpected. By combining TEM experiments and MD simulations, Gilbert and co-workers [38] suggested that vacancy loops may form directly within the cascades. Although the most stable configuration is a spherical vacancy clusters, under certain favourable conditions, the transition of the vacancy loops to spherical voids by the process: vacancy loops →planar voids →spherical voids maybe hindered. It was suggested that when vacancy type a/2<111> loops are about 2 nm in size and a<100> loops are 3 nm, planar void configuration becomes less favourable than collapsed loops. The collapsed vacancy loops then can become metastable and remain for sufficiently long to be observed in the TEM experiments.

Cavities Most of the ion irradiation experiments have reported the presence of cavities, which supports the fact that 3D clusters is the principal phenomenon by which vacancies aggregate together in bcc Fe. Recent in-situ irradiations at RT of 20 nm thick Fe foils by Prokhodtseva and co-workers [60] have claimed the presence of tiny nano-metric voids imaged by TEM. Ex-situ self-ion irradiations at 500 ^{o}C on high purity bulk specimens by Brimbal and co-workers [13] observed relatively large cavities at 10 dpa. Those smaller than 10 nm were spherical, while the larger ones were with facets (predominantly cubic) aligned along [010] and [100] directions. Many cavities were associated with the dislocations lines and loops, which correspond well with the neutron irradiated results mentioned earlier. Upon increasing the dose to 100 dpa, cavities with complex shapes were observed, with certain cavities being elongated. Net void swelling estimated was 0.6 %. 4 MeV Ni^{2+} irradiation up to 50 dpa by Kuramoto and co-workers also observed faceted cavities between 450 ^{o}C to 500 ^{o}C [85]. At both the temperatures, void swelling was similar, close to 0.5 %. The average void size and number density were 33 nm, 3 x 10^{14} cm^{-3} and 39 nm, 1.8 x 10^{14} cm^{-3} at the two temperatures respectively.

Ohnuki and co-workers [12] irradiated pure iron at 525 °C to 118 dpa with 200 keV C^{+}ions. It produced 14 % swelling, which is very large compared to other ion irradiation experiments reported above. The average void size was 94 nm. Their facets were parallel to <100> directions, which is similar to results in reference [13] mentioned above. However, there was considerable carbon addition during the irradiation which lead to extensive formation of Fe_3C precipitates. The high swelling was argued to be an effect of carbon addition.

Electron Irradiation

Not a wide number of studies on cavities formed by electron irradiation in pure bcc Fe exist in the open literature. Kitajima and co-workers [88] have reported void swelling of 0.2 % at 10 dpa at 350 ^{o}C. The experiment was performed with high voltage electron microscope with 1.25 MeV electrons, at a damage rate of 1.9 x 10^{-3}dpa/s.

2.5 Effect of Cr on radiation damage in FeCr alloys

2.5.1 Basic properties of the FeCr system

The binary Fe-Cr phase diagram calculated with CALPHAD (CALculation of Phase Diagrams) approach is shown in figure 2.8 . For temperatures of technological interest, it predicts a phase separation reaction where ferrite decomposes into Fe rich α phase and chromium rich $\alpha^{'}$ phase. It predicts a very low solubility of Cr in Fe for low temperatures which is in disagreement with experimental data and recent theoretical calculations [89, 90] . Thus, modified phase diagrams are proposed. Bonny and co-workers [89] have proposed the new position of α domain as shown by the light gray line in figure 2.8, based on a review of experimental data in the literature dealing with phase transformations in FeCr binary alloys and steels under thermal ageing and irradiation exposure. They hypothesized that solubility limit is not modified under irradiation and there is no influence of additional alloying elements on the $\alpha-\alpha^{'}$miscibility gap. Experimentally, thermal ageing experiments coupled with APT characterization by Novy and co-workers [91] on Fe20%Cr revealed that the solubility limit of Cr in bcc Fe is 14 at.% at 500 ^{o}C. However, lower than this temperature, the experimental determination of solubility limit is problematic due to low mobility at lower temperatures.

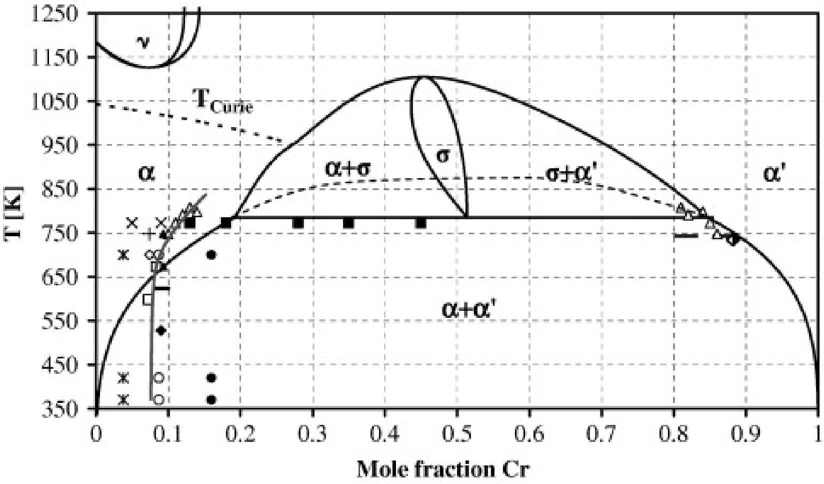

Figure 2.8: FeCr phase diagram calculated from CALPHAD and experimental data at lower temperatures taken from a review paper by Malerba and co-workers [92]. The new position of $\alpha - \alpha'$ miscibility gap proposed by Bonny and co-workers [89] is shown by the gray line. Please refer to [92] for more details.

The appearance of α' phase can induce hardening and embrittlement of the alloys [93] . FeCr system is also known to exhibit short range ordering (SRO) tendency for lower chromium contents (below ~ 5%) which can also affect the mechanical properties of steels. This transformation for the first time was noted by Mirebeau and co-workers [94] by neutron scattering experiments in an Fe5%Cr aged at 427 ^{o}C. The phenomenon is attributed to the change in the sign of enthalpy of mixing from positive to negative at lower Cr concentrations. Recent DFT results provide a physical explanation for this effect in terms of electron band and magnetic properties of Cr and Fe [95, 96, 97]. A single Cr atom prefers to be surrounded by Fe atoms which leads to lowering of the density of states at the Fermi level [96]. In addition, at the ground state, pure Cr is anti-ferromagnetic and pure Fe is ferromagnetic [97]. If a single Cr atom is inserted in an Fe matrix, its magnetic moment will be anti-parallel to that of Fe atoms. However, if a second Cr atom is introduced, a magnetic frustration is produced because either Cr atoms would tend to have its magnetic moment anti-parallel to the Fe atoms or to the other Cr atoms. As it is impossible to have moments anti-parallel to both, when there are many Cr atoms in the system, many magnetic configurations can result [97]. For low Cr concentrations, the most favourable situation is achieved when the Cr atoms are distributed sufficiently far from each other i.e. by ordering. However, when the Cr concentration is high it is impossible to avoid Cr-Cr interaction. This leads to positive formation enthalpy i.e. the tendency to cluster or segregate. .

2.5.2 Radiation damage in FeCr alloys

MD simulations of displacement cascades [98, 99] in FeCr system show that variation of Cr concentration from 0 to 15 at.% has no significant impact on the average number of surviving Frenkel Pairs and on the number of vacancies and interstitials within the defect clusters. Thus, Cr would not have an effect on the defect clusters formed directly within the cascades. However, it may have a role on the diffusion of defects. It would primarily depend upon the interaction between Cr atoms and defect clusters, which would then govern the evolution of the microstructure. This and the next sections are devoted to theoretical and experimental effects on this phenomenon to have an image of how Cr may influence the radiation damage scenario.

2.5.2.1 Interaction of Cr with defect clusters

According to the available data in the literature, it is to be believed that the main influence of Cr on microstructural evolution is primarily expected due to interaction with interstitials or interstitial clusters rather than vacancies. Theoretical calculations based on DFT show a very weak binding energy between Cr and vacancy in Fe matrix (≤ 0.1eV) [100]. Experimentally, muon spin rotation experiments by Möslang and co-workers [101] also show that the binding energy is below 0.1 eV . Resistivity recovery experiments have shown an absence of influence of Cr on the time of stage III which is the onset of vacancy migration [102]. Furthermore, Kwon and co-workers [103] have shown no presence of Cr-V complexes by PAS coincidence Doppler broadening measurements on electron irradiated Fe(5,9,15)%Cr at $T < 50\ ^{o}$C.

However, for the case of interaction with interstitials, DFT calculations and simulations using empirical potentials predict a noticeable interaction between SIAs and one or more Cr atoms [100, 104]. The interaction can be attractive or repulsive depending on the orientation of the dumbbell (<110> or <111>) or its nature (Fe-Fe, Fe-Cr or Cr-Cr). The attractive interaction highlights the trapping of SIAs by Cr atoms in concentrated alloys, with a binding energy between 0.2 to 0.5 eV [104] . Such a trapping effect by long-range interaction between Cr atoms and defects clusters is expected to reduce SIA cluster mobility [105]. It was seen by MD simulations that the diffusivity of SIA clusters modelled as <111> crowdions in FeCr system varied non-monotonically with Cr concentration [105]. In addition, the influence of Cr on the cluster diffusivity was claimed to gradually reduce for larger Cr contents due to a saturation of Cr-crowdion interactions.

It is worth noting that theoretical predictions of defect properties in Fe-Cr system still remains a challenge due to non-existence of a reliable potential that could describe the system satisfactorily. Thus, an in-depth understanding of the effect of Cr on the stability of type of defects or defect clusters and its influence on the long term microstructural evolution is limited. Due to this reason, experimental results coming from irradiation experiments are of primary importance. In the next sections, these experimental results are synthesised. To maintain a coherence with the survey on pure Fe, the sections are split in the same manner as in section 2.4 : the results on neutron, ion and electron irradiations with subsections describing the interstitial and vacancy type defects for each irradiation type.

2.5.2.2 Influence of Cr on interstitial type defects

Neutron Irradiation

- Most of the fast neutron irradiation data suggest an influence of Cr on the dislocation loop microstructure. A significant increase in loop number densities and drop in average size is known to exist upon Cr addition. Experiments performed at 400 ^{o}C in BR-10 fast reactor between 5.5 to 7.1

dpa show an jump in loop number density from 1.5 x 10^{21} m^{-3} for bcc Fe to 7.2 x 10^{22} m^{-3} just by addition of 2 %Cr [53]. The average size dropped from 28 nm to 7.2 nm. Thereafter, further addition of Cr did not seem to significantly modify neither the loop sizes nor their number density. Irradiations in FFTF-MOTA at 425 ^{o}C up to 140 dpa by Katoh and co-workers [106] show a non-monotonic variation of the number density of a<100> loops with Cr content. Starting from 3 % Cr, it reached a minimum value around 6 %Cr ; beyond that it increased again up to 12 % Cr where saturation was achieved.

- For the experiments in the BR-10 fast reactor mentioned above, an increase of a/2<111> loop population upon Cr addition to large concentrations was also observed [53] . For alloys containing less than 6 % Cr, predominantly a<100> loops lying on {100} planes were detected ; but for larger Cr concentrations, a mixed population of a<100> and a/2<111> loops was seen. Irradiations inside EBR-II fast reactor by Gelles and co-workers [107] at 400 ^{o}C also show similar results where up to 6 % Cr, only a<100> loops were detected and beyond this concentration both type of loop populations were present. However, reports of Katoh and co-workers [106] observed predominantly a<100> type loops for Cr level between 3% to 18%, with an exception at 12 % where a/2<111> loops in less density were also observed. Thus, it is evident that Cr may have an influence on the Burgers vector of dislocation loops, but a systematic trend of this effect is difficult to infer. At higher doses, an entangled dislocation network is usually observed [107].

- By far, to the best of our knowledge, no dedicated experimental results exist in the open literature by neutron irradiation on the effect of temperature, dose and dose rate on the evolution of dislocation loop microstructure.

- Precipitation of $\alpha^{'}$ phase has been invariably observed especially for higher Cr content alloys [32, 53, 106, 107, 108]. Irradiations in BR-10 fast reactor at 400 ^{o}C by Porollo and co-workers [53] mentioned above, observed $\alpha^{'}$ precipitation in alloys with 12 % and 18 % Cr. Their mean size and number density were 9 nm, 2.8 x 10^{22} m^{-3} and 6 nm, 2.8 x 10^{22} m^{-3} at 12 % Cr and 18% Cr respectively. In this case, the dose was between 5.5 - 7.1 dpa. Larger precipitates (between 10 - 14 nm, depending on cold work) were observed upon increasing the dose to ~ 26 dpa [108]. Precipitate free zones were seen adjacent to the grain boundaries [108]. Little and Stow [32] also mentioned the formation of $\alpha^{'}$ phase in Fe10.5wt.%Cr irradiated up to 30 dpa at 420 ^{o}C. In this case, the regions around voids were denuded.

Ion Irradiation

A rather significant proportion of ion irradiation data exists in the literature upon various aspects of radiation damage effects in FeCr alloys. The main results are detailed in this section.

- The most pronounced influence of Cr addition is the evolution of the loop microstructure on a finer scale, with small sizes and elevated number densities. This has readily been observed in almost all the known ion irradiation experiments [9, 60, 13, 62, 59, 87, 109], and is coherent with reports by neutron irradiation. In-situ irradiations by Hernandez and co-workers [62] at 300 ^{o}C by 150 keV Fe^{+} ions up to 13 dpa noted the average size and aerial loop number density to be 10.4 nm, 2.46 x 10^{14} m^{-2} in Fe and 5.5 nm, 9.68 x 10^{14} m^{-2} in Fe8% Cr. The maximum loops size was 224 nm in Fe and 24 nm in Fe8%Cr.

- Both a<100> and a/2<111> loops have been observed in Fe-Cr alloys for different irradiation conditions [9, 59, 87, 109, 110]. But the effect of Cr concentration on the relative population between a<100> and a/2<111> type of loops is not very clear due to the presence of contrasting results in the literature. For instance, in-situ self-ion irradiations by Jenkins and co-workers [59] at 500 ^{o}C up to 13 dpa observed only a<100> loops in Fe and Fe8%Cr. Experiment at 300 ^{o}C up to 1 dpa by Xu and co-workers [109] observed the proportion of a/2<111> loops to be 92 % in Fe, 30% in Fe5%Cr, 46% in Fe8%Cr and 37% in Fe11%Cr. . However, irradiations by 100 keV Fe^{+} ions at RT show 14 % a/2<111> loops in Fe and 37 % in Fe18%Cr [87]. Similar behaviour showing slightly higher a/2<111> loop population is also reflected in recent in-situ irradiations on high purity FeCr alloys at RT and 500 ^{o}C [60, 13].

- At high doses with elevated irradiation temperatures, a network of dislocations is usually observed [9, 13]. For instance, Horton and co-workers [9] saw a coarse distribution of network segments after triple ion beam irradiations (Fe + He + D) at ~ 577 ^{o}C up to ~10 dpa (with 100 appm He and 410 appm D).

- Similar to irradiations in pure Fe, the proportion between a<100> and a/2<111> loops seem to be dependent on irradiation temperature. Many experiments performed close to 500 ^{o}C show the presence of only a<100> loops situated on {100} planes [9, 59]. Whereas, for lower temperatures, the a/2<111> loop population is significant in proportion [87, 109]. An increase in temperature increases loop size and reduces their number density [87, 9, 110].

- Similar to irradiations in pure Fe, back-and-forth motion of small defect clusters is also known to exist in FeCr alloys [87]. But loop mobilities are strongly reduced in presence of Cr as opposed to pure Fe [13, 87]. Cr induced loop mobility drop is considered responsible for the development of a finer loop microstructure mentioned in section 2.5.2.2.

Electron Irradiation

The main points of electron irradiated FeCr alloys is mentioned here.

- Similar to neutron and ion irradiations, loop densities are generally higher in FeCr alloys than in pure Fe. At RT, Arakawa and co-workers [71] observed an order of magnitude of difference between loop densities in pure Fe and Fe9%Cr. But at very low temperatures (below 200 K), the loop microstructures were similar in Fe and FeCr alloys. Yoshida and co-workers [111] observed a long nucleation period of loops in Fe10%Cr as compared to Fe at 25^{o}C, with a saturation loop density much higher in the former.

- No clear result show an influence of Cr on the Burgers vector of dislocation loops. Both a<100> and a/2<111> interstitial type loops have been observed over a temperature range varying from RT to 500 ^{o}C [111, 112, 113].

- The effect of temperature on the relative population between a<100> and a/2<111> loops is also not well understood. Analysis of Fe10%Cr irradiated by 1 MeV electrons by Muroga and co-workers [114] observed mostly a/2<111> type loops at 300 ^{o}C and 500 ^{o}C; while both a<100> and a/2<111> types were seen with comparable densities at 400 ^{o}C. On the other hand, Wakai and co-workers [113] observed both the loop families in high purity Fe9%Cr and Fe18%Cr irradiated at 350 ^{o}C, 450 ^{o}C and 500 ^{o}C up to 1 dpa.

- It is interesting to note that the purity of the alloys may have an impact on the dislocation loops. For the studies by Wakai and co-workers mentioned above, both the loop families were observed in low purity alloys (with C content 100-110 wt. ppm), whereas in high purity alloys (C content 3-5 wt. ppm), only a<100> loops were detected.

- Back-and-forth motion of loops also exists, as reported by Arakawa and co-workers [71], for a/2<111> loops in Fe9%Cr between -83 ^{o}C to 102 ^{o}C. However, not a very clear picture of Cr effect on loop mobilities was seen. At -83 ^{o}C, more mobile loops existed in pure Fe, but at 22 ^{o}C, more loops in the latter were seen to be mobile. However, upon thermal annealing up to 687 ^{o}C of irradiated specimens, a clear reduction in the number of mobile loops was seen due to presence of Cr [71].

- Electron irradiation experiments also show evidence of Cr segregation on the dislocation loops [111, 113].

2.5.2.3 Influence of Cr on vacancy type defects

Vacancy type dislocation loops have never been observed in FeCr alloys under any type of irradiation. Only cavities are known to exist. Thus, this section describes mainly the cavities and void swelling behaviour in these materials. It must be noted that swelling can be measured by TEM (void swelling) or by densitometry (total swelling). A distinction has been made on the results based on the techniques used wherever found necessary.

Neutron Irradiation

- Cavities are observed in FeCr alloys after fast neutron irradiations. Many experiments performed in the last three decades have shown a complex modulation of void swelling behaviour with Cr content [35, 107, 115, 106]. Most of these swelling results are presented in a review paper by Garner and co-workers [3]. A collection of swelling data versus the Cr content taken from all these studies is depicted in figure 2.9. The results are split into dose range ~35 to 200 dpa and 15 to 30 dpa. Three studies up to 30 dpa by Little and Stow [35] indicate a reduction in swelling with addition of small quantity of Cr, at least up to 5% Cr level (see figure 2.9b). For instance, at 380

^{o}C, swelling in Fe was 0.85 % and Fe1%Cr swelled only 0.2%. But thereafter, the swelling trend is not very clear. Two out of three results at 30 dpa indicate that swelling may increase for higher Cr levels.

- Other data between ~35 to 200 dpa (see figure 2.9a) suggest a rather non-monotonic trend, with a swelling maximum around ~ 9%Cr, which becomes particularly prominent at very high doses (140, 200 dpa). Results obtained at 15 and 21 dpa also seem to suggest similar behaviour. Such discrepancy in swelling trend, when compared with the 30 dpa results, is difficult to interpret and calls for attention. Unfortunately, high dose experiments did not include any reference bcc Fe. So, it is difficult to say if swelling in Fe would remain, in the same conditions, significantly higher than in any FeCr alloy (producing a local minimum at about 3%Cr). There are, however, reasons to believe this may be the case due to the 30 dpa results by Little and Stow and due to some ion irradiation results which would be discussed in the next section.

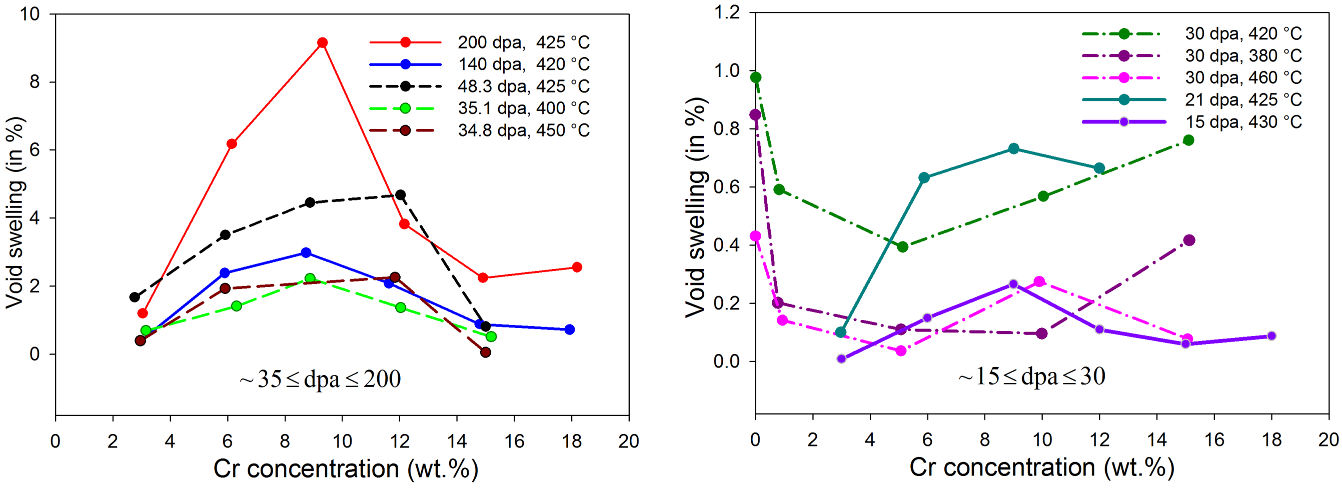

(a)

(b)

Figure 2.9: Variation of void swelling as a function of Cr concentration in fast neutron irradiated FeCr alloys. The irradiations were performed in fast neutron reactors. All these curves are reported in a review paper by Garner and co-workers [3]. The original work can be found in [32, 107, 115, 106].

- It appears that the major impact of Cr is on the duration of the incubation period before reaching the steady state swelling [3]. The shortest transient regime lies close to ~9 %Cr, which might explain a local swelling maxima seen around this concentration. When the steady state regime is reached, the swelling rate is ~ 0.2%/dpa, which doesn't seem to be strongly influenced by the Cr level [3] . It is shown in figure 2.10.

- The duration of the incubation period is strongly dependent on the irradiation conditions, especially on damage rate and He generation rate . For instance, a comparison of swelling data by Garner and co-workers in figure 2.10 [3] shows the dpa level for the onset of steady state swelling (in other words, the termination of incubation period) to be ~ 150 dpa in FFTF , which has a dpa rate and He generation rate equal to ~ 1.3 x 10^{-7}dpa/s and 2.2 x 10^{-7} appm He/s; while the same was identified around ~40 dpa in EBR-II with 1.2 x 10^{-6} dpa/s and 1.8 x 10^{-7} appm He/s . Beyond the incubation period, the steady state swelling rate is nearly independent of the irradiation conditions [3] .

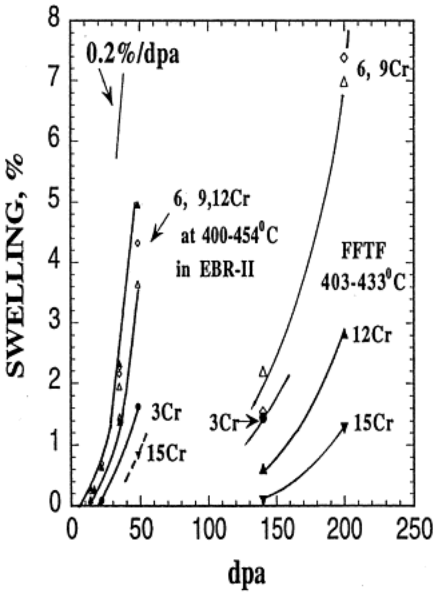

Figure 2.10: Comparison of swelling in FeCr alloys irradiated by fast neutrons in EBR-II and FFTF-MOTA [3]

- ○ Peak swelling temperature under neutron irradiation in FeCr alloys (also pure bcc Fe) is around 420^{o}C [35]. It seems unaffected by the Cr concentration of the alloy. A clear data on modification of the peak swelling temperature with changes in irradiation conditions is not available in the literature.
- ○ Negative swelling by densitometry measurements is also frequently observed, which is more pronounced at higher dpa levels and higher Cr levels [37] . This is considered most likely as an effect of densification primarily due to $\alpha^{'}$precipitation. In some cases, it may induce discrepancies between swelling deduced by this method and by TEM studies [106] .

It is important to remember that most operating nuclear reactor systems experience fluctuations in power and thereby, in temperature [116]. The temperature history of a reactor could strongly influence the observed results [117, 118]. Such fluctuations are more pronounced for reactors which do not have active temperature controls, for example the EBR-II [3] . Thus, neutron irradiated results are always difficult to interpret. For example, the discrepancies in the void swelling curve versus Cr concentration or the duration of the incubation period observed in the materials irradiated in EBR-II and FFTF may well be influenced by such fluctuations which could bias our comprehension. For this reason, the equivalent ion or electron irradiation experiments are important due to less variability in experimental parameters. But as we shall see in the next sections, due to lack of dedicated experiments and missing data, a plausible conclusion on most of the effects is difficult to derive.

Ion Irradiations

- Similar to observations after neutron irradiations, it is usually seen that void swelling reduces upon Cr addition [9, 12, 119]. Self-ion irradiations at 500 ^oC by Brimbal and co-workers [119] up to 95 dpa show 0.4% swelling in highly pure Fe and none in Fe5%Cr.

- From all the known studies which involve void swelling analysis in ion irradiated bcc Fe and FeCr alloys [9, 12, 119, 10] , the variation of void swelling trend with Cr level, in our opinion, is not clear. Except the work of Johnston and co-workers [10] by Ni^+ ions , no experiments were systematically performed including a reference bcc Fe and a wide range of FeCr alloys with varying Cr level to trace out the swelling curve. In this study, a somewhat non-monotonic behaviour was indeed observed with swelling peaking around ~15% Cr ; which is not what is observed after fast neutron irradiations (see previous section). Furthermore, the swelling in Fe remained low and almost comparable to the other FeCr alloys up to ~10%Cr. However, the authors were concerned about artefacts induced by deposition of 1.5 % of Ni ions close at the damage peak [3, 10] which might have modified the cavity distribution. Triple beam (D_2 , He , Fe) irradiation by Horton and co-workers [9] up to 10 dpa of annealed Fe and two FeCr alloys at 527 ^oC also seemed to indicate a similar non-monotonic trend as claimed after neutron irradiations, however with only 3 points. The levels of swelling were small (0.22% in Fe, 0% in Fe5%Cr and 0.16% in Fe10%Cr).

- Most of the ion irradiation experiments for Cr level between 10 to 15% show that the swelling peak is located between 500-580 ^oC [9, 10, 11]. However, as mentioned above, recent studies in very high purity Fe and FeCr alloys by Brimbal and co-workers [119] observed no swelling in Fe5%Cr at 500 ^oC for a dose as high as 95 dpa. Such observations question the peak swelling temperature range.

Electron Irradiations

Cavities have not been observed in electron irradiated FeCr alloys. For example, in the dual beam electron/helium irradiations by Gelles and co-workers [112] on Fe9%Cr up to 3.5 dpa at 425 ^oC, no cavities were detected.

2.6 Effect of He on radiation damage

2.6.1 Theoretical Background

He can be introduced in metals by transmutation induced by neutrons yielding α particles or implantation by ion accelerators [120]. Owing to its extremely low solubility, it induces a system far from equilibrium. Recent advances in ab-initio calculations have improved the understanding of the impact of He on the microstructure by studying the interaction of He with vacancies and self-interstitials. The simulation studies are mostly concerned in Fe due to difficulty of performing modelling in FeCr alloys. The main points are discussed below:

Position of He atoms

Relatively recent ab-initio based study by Fu and Willaime [29] on He behaviour in bcc Fe revealed that the most important positions for He atoms in a lattice are interstitial and substitutional sites. The latter is the most stable, followed by tetrahedral sites and then octahedral sites. The energy difference between these positions is, however, not very large : the difference between tetrahedral and substitutional position is 0.17 eV, and, between tetrahedral and octahedral position is 0.18 eV. Under experimental conditions, He produced by (n, α) reaction is initially at interstitial positions [80, 120].

He-Vacancy interactions

The primary influence of He atoms is to stabilize vacancy clusters. This is inferred from the ab-initio results in bcc Fe which show a strong binding energy of vacancies to He atoms and to He-vacancy clusters [80, 121]. A comparison is given in table 2.2. In experimental situations, this can lead to enhanced nucleation of cavities. Furthermore, the defect to cluster binding depends on the He density i.e., the n/m ratio of He_nV_m clusters [80]. Clusters may change their n/m ratio by, e.g., emitting He atoms or vacancies according to their respective dissociation energies. Vacancy dissociation energy increases with increase in n/m ratio, while the same for He decreases. The most stable clusters correspond to n/m ~ 1.3.

Reaction	E_b(eV)
$V_2 \rightarrow V + V$	0.30
$V_3 \rightarrow V_2 + V$	0.37
$V_1He_1 \rightarrow V + He$	2.3
$V_2He_1 \rightarrow V_1He_1 + V$	0.78
$V_3He_1 \rightarrow V_2He_1 + V$	0.83

Table 2.2: Binding energy of defects calculated from ab-initio [121].

He diffusion

The dominant migration mode of diffusion depends on preferential position of He atoms, temperature and the presence of other intrinsic or irradiation induced defects acting as traps: particularly in the presence of vacancies and He–vacancy clusters. As mentioned in the previous paragraph, the most important positions for He atoms are interstitial and substitutional sites, the latter being the most stable. For substitutional He atoms, migration is principally by vacancy or dissociation mechanism [80]. In vacancy mechanism, a transient He-vacancy complex containing one helium atom and two vacancies is formed in which He atom jumps from one vacancy to the other. In dissociation mechanism, a He atom in a vacancy is dissociated from its position and diffuses interstitially until re-trapped by another vacancy. Interstitial He migrates very fast with very low activation energies [80]. For instance, a tetrahedral He may migrate between two equivalent sites with migration energy of 0.06 eV. A fast migrating interstitial He can be deeply trapped by a vacancy and become a substitutional impurity.

He interaction with SIA and dislocations

Calculations using empirical potential reveal a positive energy of interaction between medium sized interstitial clusters (20 interstitials) and helium atoms [122]. Ab-initio approach also shows a positive interaction between <110> dumbbells and tetrahedral He atoms. The most favourable situation is found when the He atom resides in a third nearest tetrahedral site of the dumbbell. The corresponding binding energy is 0.26 eV and the dissociation energy being 0.32 eV. It is claimed that due to such a value of dissociation energy, SIAs could act as efficient traps for interstitial He atoms only when they are weakly mobile, for eg. at lower temperatures [80, 29] .

Fu and co-workers [29] show that substitutional He and SIA interaction occurs by a spontaneous recombination–replacement reaction known as "kick-out". In this mechanism, a substitutional He atom is ejected towards an interstitial site by an incoming Fe interstitial atom, i.e. He_{sub}+ SIA $\rightarrow He_{int}$, involving a large energy gain of 3.6 eV. This reaction is responsible for the substitutional He migration by replacement mechanism activated under irradiation [29].

Recent theoretical studies [123, 124, 125] have given more insight on the interactions between helium and dislocations. Heinisch and co-workers [123] have shown by atomistic simulations that both interstitial and substitutional He have a positive binding energy on the tension side of a a/2<1 1 1> edge dislocation in bcc iron. The binding energy of interstitial helium to an edge dislocation was determined to be 2.3 eV, and the migration energy of interstitial He along an edge dislocation is about 0.4 eV, higher than the migration energy in the matrix (about 0.08 eV), but allowing so-called ''pipe-diffusion'' at higher temperatures. Heinisch and co-workers [126] have also studied the interactions between He and screw dislocations in bcc iron, concluding that interstitial He atoms are also trapped in the dislocation core region in this case. Shim and co-workers [124] studied the interaction of He with dislocation loops containing 37 interstitials, with a/2<1 1 1> Burgers vector in bcc iron. It was seen that interstitial He strongly binds on the edge of such dislocation loops with a binding energy of about 1.4 eV. Substitutional He also binds to these dislocation loops with a lower binding energy of about 0.3 eV. These theoretical calculations justify that He can be trapped at the dislocation loop cores, and that interstitial helium atoms are mobile along dislocation cores.

2.6.2 Experimental Background

He induced void microstructure

Experimentally, many groups have observed that He strongly induces cavity nucleation (and hence an early onset of swelling) which is reflected in their increased number density [8, 13, 85]. Dual beam irradiations with 2 MeV Fe^{2+} ions and 2 MeV energy degraded He^{+} ions at 500 ^{o}C up to ~100 dpa, 26 appm He/dpa in bcc Fe by Brimbal and co-workers [13] observed an order of magnitude increase in cavity number density (and almost three times drop in size) as compared to single beam irradiations. Similar observations were made by Kuramoto and co-workers [85] by Ni ion irradiations co-implanted with He up to 10 appm He/dpa. It is interesting to note that in both these cases, a slight decrease in swelling was observed upon He co-injection. He is also claimed to induce bi-modal size distribution of cavities [127, 128]

For the sake of clarity, the effect of He on void swelling behaviour is given in much more detail in the discussion of results in chapter 6, section 6.1.

Thermo-desorption spectroscopy measurements show that He has strong affinity for grain boundaries and dislocations, probably due to presence of vacant space associated with them [129] . Presence of He induced cavities/bubbles along dislocation lines, martensitic laths and sub-grain boundaries and carbide-matrix interface has been reported by Henry and co-workers [5] in a 9%Cr martensitic steel implanted with 0.5 at.% He. Such observations are coherent with the theoretical calculation results mentioned earlier on He interaction with SIAs and dislocations. Cavitation along grain boundaries is in fact one of the most severe implication of He in the material as it results in their weakening and de-cohesion responsible for inter-granular cracking [5, 7].

Furthermore, recent dual beam in-situ studies (damage by self-ions and He co-implantation) in high purity bcc Fe and FeCr alloys revealed a strong heterogeneous distribution of cavities on dislocation loops [13]. For irradiations at 500 ^{o}C up to 1 dpa, 1000 appm He/dpa, cavities were present inside the a<100> type dislocation loops. They were smaller in size at the loop core than in the centre. The mechanism proposed by the authors to explain this behaviour is as follows: He atoms can be trapped at the dislocation core. The high mobility of the trapped He atom in the loop core can result in nucleation of small He-V clusters. As the dislocation loops grow by preferential absorption of self-interstitial atoms, it leaves the clusters behind. These clusters are expected to be stable as He is highly insoluble in Fe, as in most metals, and grow by absorption of vacancies and He atoms.

He influence on dislocation loops

Many experimental results indicate that He may have substantial interaction with SIAs or their clusters. For instance, in-situ irradiations at 500 ^{o}C by Brimbal and co-workers [13] show that He reduces considerably the mobility of dislocation loops in bcc Fe. It is perhaps due to the trapping of He atoms at the dislocation loop core. Such a drop in mobility results in higher loop number densities. Similar observations were made at RT irradiations on bcc Fe up to 0.45 dpa by Prokhodtseva and co-workers [60] where three fold increase in loop number density was observed upon He co-implantation up to 790 appm He/dpa .

Furthermore, study by Prokhodtseva and co-workers also claim that He stabilises glissile a/2<111> type loops in Fe. Analysis on bcc Fe irradiated to 0.45 dpa yielded 96% a<100> type loops and 99 % a/2<111> type loops without and with He co-implantation respectively. In both the cases, the results were reported for [111] oriented grain. In FeCr alloys, similar observations were indeed seen by the authors. Analysis on Fe(5, 10 , 14)%Cr irrdiated at RT to 1 dpa and 1000 appm He/dpa showed 50 - 60% a/2<111> loops when no He was present and the percentage increased to 80% in some cases when He was co-implanted.

2.7 Summary

In the following paragraphs, a summary and main conclusions derived from the bibliography review is given.

Currently, FeCr based F-M steels are candidates for structural materials of future fission and fusion reactors. Due to this reason, a lot of focus is given to basics of radiation damage studies on their matrix material i.e. the FeCr binary alloys. In these materials, the effect of Cr addition in a bcc Fe matrix on the radiation damage scenario is important to understand. This knowledge can only be obtained if, at first place, the behaviour of radiation damage in bcc Fe is understood. Thus, a wide variety of experimental and simulation results exist which compare the irradiation defects in bcc Fe with those in FeCr alloys. The key points are as follows:

Pure bcc Fe

The irradiation of pure bcc Fe generally leads to the formation of cavities and interstitial type dislocation loops with Burgers vector a/2<111> and a<100> [13, 53, 54, 55, 56, 57, 59, 61, 60, 87, 67, 69, 68].

The relative proportion between the two loop population is strongly dependent on irradiation temperature [54, 59]. The a<100> loop population increases with increasing temperature. From neutron and ion irradiation results, it is evident that a/2<111> population dominates when $T < 300\ ^{o}$C. At and beyond 500 ^{o}C, only a<100> loops exist. The presence of a<100> loops is unique to Fe as compared to the other transition metals. So far, no clear justification on their formation mechanism is present in the literature.

Many in-situ ion and electron irradiations have revealed that a/2<111> loops are highly mobile [59, 68, 63, 87]. The a<100> loops, which were long believed to be sessile, were also recently shown to be mobile [13].

The size of dislocation loops increase with increase in temperature [54, 59, 75] and with dose [13, 57, 62, 68]. However, their number density decreases with increasing temperature [54, 69, 68]. With increase in dose, the loop number density is initially seen to increase and then saturate [13, 68]. Furthermore, loop number density increases up on increase in damage rate [68].

Several experimental groups have given evidence of cavities, and hence void swelling, in irradiated bcc Fe [54, 35, 53, 82, 130, 13, 12]. Under neutron irradiations, the peak swelling temperature in bcc Fe is around 400 - 420 ^{o}C [35, 54]. An unexplained smaller magnitude swelling peak at ~510 ^{o}C is also reported [35]. However, under ion irradiations the position of swelling peak is not well known. A heterogeneous cavity distribution, usually associated with dislocation lines and loops, is also known to exist [13, 54, 83].

FeCr alloys

The solubility limit of Cr in bcc Fe matrix at 500 ^{o}C is 14at.% [91]. Under irradiations, similar to Fe, interstitial type dislocation loops with Burgers vector a/2<111> and a<100> are known to exist in FeCr alloys [9, 13, 60, 59, 87, 109, 110, 111, 112, 113]. Experimental evidences show strong impact of Cr on the dislocation loop microstructure. For instance, addition of Cr reduces loop size and increases their number density [13, 53, 106, 59, 60, 62, 87, 71, 111]. In-situ ion and electron irradiations reveal highly reduced loop mobilities as compared to bcc Fe [13, 87, 71]. It corresponds well with theoretical calculations which show a positive interaction between Cr atoms and SIA clusters, leading to a reduction on the diffusivity of these clusters [105].

Due to contradicting results in the literature, the effect of Cr on the relative population between a/2<111> and a<100> loops is not clear and, hence, needs a systematic study. Impurities like carbon may also influence the loop population. Thus, studies should be performed on high purity materials. Furthermore, temperature effect on the relative population between the two loop families is also not well known. A general view is that a<100> population increases with increase in temperature. It is derived from the observation of only a<100> loops when irradiations were performed close to 500 ^{o}C [59, 9], while more a/2<111> were seen at lower temperatures [87, 109]. Segregation of Cr on dislocation loops is also observed [111, 113].

Neutron and ion irradiations have revealed cavities responsible for void swelling in FeCr alloys [3, 35, 106, 107, 115, 53, 10, 12, 9, 119]. However, the variation of void swelling as a function of Cr content is not well understood, with some results indicating a non-monotonic variation having a swelling peak close to ~9% Cr and some other results indicating a more complex modulation [3]. In general, FeCr alloys seem to swell less compared to bcc Fe [35, 13]. Cavities have not been observed after electron irradiations.

Under fast neutron irradiations, the peak swelling temperature in FeCr alloys is around 420 ^{o}C [35], which is unaffected by the Cr level of the alloy. But the position of peak swelling temperature under ion irradiations is still a debate. Most experiments claim that the swelling peak is located between 500 - 580

^{o}C [9, 10, 11]. But recent self-ion irradiation experiments on high purity Fe5%Cr up to high doses (95 dpa) showed no cavities at 500 ^{o}C.

Neutron irradiations also show formation of α' precipitation [35, 53, 106, 107, 108] in higher Cr content alloys. But such precipitates have never been detected after ion or electron irradiations.

He effect

Ab-initio calculations on bcc Fe reveal that He stabilises small vacancy clusters [29]. In experimental situation, this leads to enhanced nucleation of cavities [13, 85], which can cause an early onset of void swelling. It is well-known that He causes heterogeneous cavitation along grain boundaries and interfaces [5]. Recent experiments reveal that He can also induce cavitation inside dislocation loops [131].

He is also seen to have impact on dislocation loop microstructure. Loop number densities were seen to be higher when He was co-implanted in bcc Fe [13, 60]. Loop mobilities in bcc Fe reduce when helium is co-implanted [13]. Recent studies at low temperatures (RT and below) also claim that He can induce higher a/2<111> loop population both in Fe and in FeCr alloys.

Chapter 3

Methodology

In our study, we have performed self-ion irradiations (i.e. using Fe ions) on a series of high purity FeCr binary alloys and a reference bcc Fe. The irradiations were performed in single beam mode (only ballistic damage due to Fe ions) and dual beam mode (damage plus co-implantation of He), to separate ballistic damage from gas implantation effects. Thereafter, the irradiated microstructure was analysed to see the radiation induced defects in the material. Based on the experimental results, a part of the study was complimented by numerical simulations based on cluster dynamics model.

This chapter, thus, describes the materials, experimental and numerical tools utilized for our study. At first, the materials and specimen preparation techniques are briefly described. This is followed by the details of the irradiation experiments. Then, the details of the microstructural characterization techniques used are given. In our analysis, the principal characterization tool was conventional transmission electron microscopy (TEM). This was complimented in a part of the study by analytical tools : energy dispersive X-ray spectroscopy (EDS) performed in scanning TEM (STEM) mode and atom probe tomography (APT). Then, the cluster dynamics model used in our study is presented.

3.1 Materials

The materials studied are a series of high purity FeCr alloys (with Cr level varying from ~3 wt.% to ~14 wt.%) and a reference bcc Fe. Their nominal composition is given in table 3.1. They were prepared by induction melting at Ecole des Mines at Saint Etienne, France, under the European Fusion Development Agreement contract EFDA-06-1901 [132]. The alloys were received as cylindrical rods of 1.1 cm diameter, in recrystallized state, after a cold reduction of 70%. They were then heat treated at different temperatures (for 1 hour, under pure argon flow), to reach high grain sizes and low dislocation density. Pure Fe was annealed at 700 ºC; Fe(3, 5)%Cr at 750 ºC; Fe10%Cr at 800 ºC and Fe(12, 14)%Cr at 850 ºC. This was followed by air cooling. The resulting grain sizes are also reported in the table 3.1. The dislocation densities in all the materials were of the order of 10^8 cm^{-2}[132].

Material	Cr wt.%	C wt. ppm	S wt. ppm	O wt. ppm	N wt. ppm	P wt. ppm	Mean grain size µm
Pure Fe	< 2 ppm	4	2	4	1	< 5	183
Fe3%Cr	3.05	4	2	6	2	X	390
Fe5%Cr	5.40	4	3	6	2	< 5	68
Fe10%Cr	10.10	4	4	4	3	< 5	82
Fe12%Cr	11.63	5	2	4	X	X	500
Fe14%Cr	14.25	5	7	4	5	< 10	141

Table 3.1: Nominal composition and mean grain size of the alloys, as reported in [132, 133].

The initial unirradiated microstructure of the materials was checked by TEM. Their images in unirradiated form can be found in appendix B. The specimens looked clean, without any sign of heterogeneities. They were, thus, suitable for performing irradiation experiments. The dislocation density was roughly checked. It was well within the order of magnitude of 10^8 cm^{-2}, in coherence with the value provided by the manufacturer.

3.2 Specimen preparation

The objective was to prepare specimens suitable for performing ion irradiation experiments, and observable for investigation using TEM. For this purpose, 1 mm thick circular slices were cut from the as-received cylindrical rods of the materials fabricated at Ecole des Mines. They were then mechanically polished by silicon carbide/diamond abrasives to ~100 µm[1] thickness using a Struers grinding/polishing machine. This polishing was done in a way to induce minimum work hardening of the surface by gradually decreasing the grain size of the abrasive discs; the finest grained disc used for the final polishing step. Then, discs of 3 mm diameter were punched out. When irradiation experiments were performed directly on TEM thin foils, the punched discs were jet-electro polished in a Tenupol-5 thinning device to obtain electron transparent thin zones (see Appendix A). When irradiations were performed on thicker or bulk specimens, electro-polishing was performed for a few seconds to obtain mirror finished thick dimpled discs (i.e. bulk specimens of ~ 100 µm thickness).

The irradiated samples were characterized after irradiation principally using conventional TEM. Two sort of samples were analysed: as-irradiated thin foils and transverse focused ion beam (FIB) specimens extracted from the thin foils or bulk samples. The later allows to have information on the depth distribution of damage in the material. FIB specimens were prepared by lift-out technique using a FEI Helios 600 dual beam FIB machine at University Paul Cézanne at Marseille and a FEI Helios 650 dual beam FIB at SRMA/CEA-Saclay. The initial lift-out was done with 30 keV Ga ions. While sampling, the energy of the ions was decreased progressively up to 1 - 2 keV to minimise defects induced by the preparation method.

A part of the study concerns analytical measurements using energy dispersive X-ray spectroscopy (EDS) in scanning TEM mode and atom probe tomography (APT). For these techniques additional specimens using FIB milling had to be prepared. Specimen preparation for EDS analysis using FIB followed a dedicated procedure. For the sake of simplicity it is mentioned directly in section 3.4.2, where EDS is discussed.

For APT analysis, specimens suitable for experiments were prepared as needles by FIB lift-out method in a Zeiss Nvision 40 dual beam FIB machine at the University of Rouen. They were annular milled up to 600 nm below the irradiated surface by Ga ions starting at 30 keV, down to 2 keV for the final milling step.

3.3 Ion irradiations

Self-ion irradiations, with and without He co-implantation, were performed at the JANNuS irradiation platform (Joint Accelerator for Nano-Science and Nuclear Simulations), located at CSNSM, Orsay and at CEA, Saclay, France [134] . This facility is a part of French EMIR (Étude des Matériaux sous Irradiation)

---

[1] Since the material is ferromagnetic, it is essential that specimens for TEM observations are thin enough (less than 100 µm) to reduce undesirable magnetic effects during the analysis.

network of accelerators. The irradiations were performed in batches of high, intermediate and low dose experiments. In all the cases, the irradiation temperature was fixed at 500 ºC. The detailed conditions of these three type of irradiations are given in the following paragraphs:

3.3.1 High dose irradiations

High dose irradiations were performed at the multi beam irradiation facility of JANNuS CEA/Saclay. Three ion accelerators (3 MV Pelletron accelerator, 2.5 MV single ended Van de Graaf, and a 2 MV tandem accelerator) are coupled to an irradiation chamber, for performing simultaneous multi-beam ion irradiations [134]. A pictorial description of beam lines in the facility is shown in figure 3.1. The specimens were irradiated in a triple beam chamber coupled to all three accelerator beam lines (see figure 3.2). The position of the specimen holder inside the chamber is such that each beam line is incident at 15º with respect to the normal of the specimen surface. Under regular operational conditions, the vacuum level inside the chamber is of the order of 10^{-7}- 10^{-8} torr. A combination of a baking plate and a cooler controlled by liquid N_2 permits a wide range of irradiation temperature from -170 ºC to 800 ºC. Seven Faraday cups on each beam line are used to monitor the beam current.

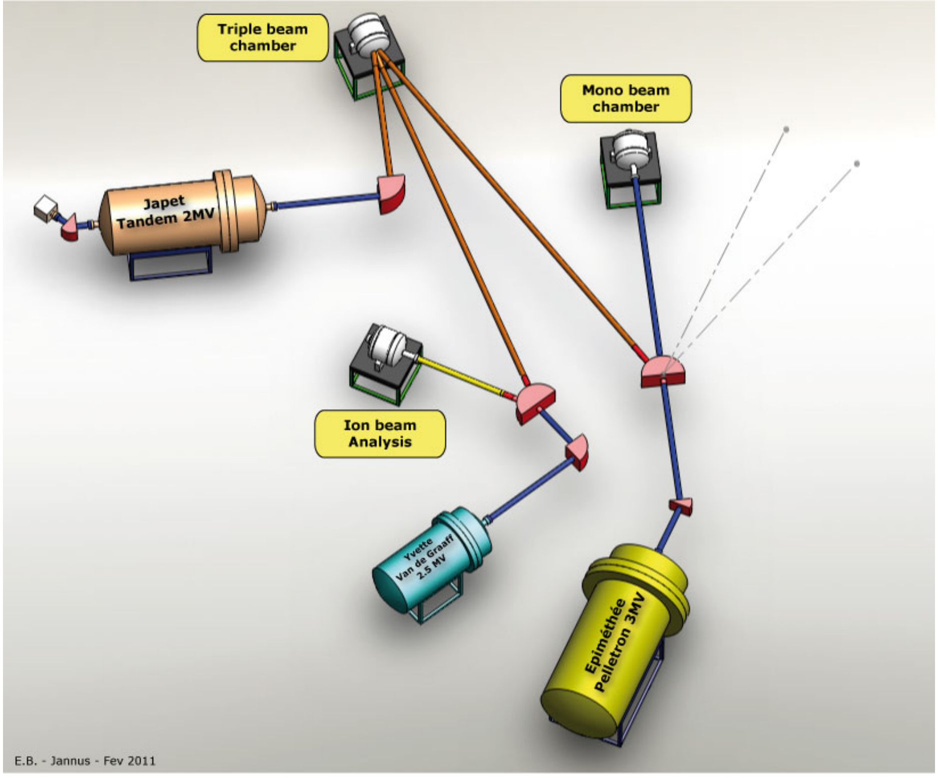

Figure 3.1: Schematic of JANNuS triple ion beam facility at CEA-Saclay, France.

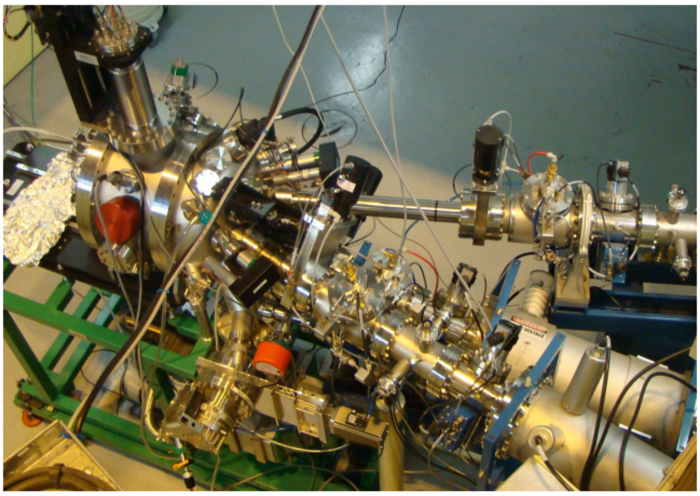

Figure 3.2: Irradiation chamber coupled to three accelerator beam lines at JANNuS, Saclay.

All the FeCr alloys and the reference bcc Fe specimens were irradiated at 500 ºC in single beam mode (Fe only) and simultaneous dual beam mode (Fe + He), as thin foils[2]. This study was primarily aimed to understand the void swelling behaviour of the alloys at high dose. 2 MeV Fe^{2+} ions were used to reach fluence equal to 1.38 x 10^{17} ions.cm^{-2}. The depth profile of the displacement damage is given in figure 3.3. It was estimated by SRIM [135] in a Fe matrix, using a displacement threshold of 40 eV and Kinchin-Pease calculation, as recommended by Stoller et al [136]. As the damage is not homogeneous within the material, for our convenience, the dose estimated in displacement per atom (dpa) is henceforth taken as the dose reached at the damage peak. We can see that the damage peak is located around 600 nm from the irradiated surface. The maximum dose at the peak is 157 dpa. As we shall see in the results section, the injected ions can have influence on the swelling behaviour where these ions are implanted. Due to this reason, the implantation profile of Fe ions is also shown in figure 3.3. For the dual beam irradiations, 2 MeV He^{+}ions were simultaneously injected along with the Fe beam, to reach 8.4 x 10^{16} ions.cm^{-2} ion fluence. To obtain a homogeneous He implantation along the target depth, an energy degrader consisting of a combination of rotating thin aluminium foils (see figure 3.4) were used on the He beam, as described in the appendix A of [13]. However, the He profile is not homogeneous because we have to take into account a significant ion loss due to divergence, after scattering in the foils. The implantation profile has been calculated after this correction and is given in figure 3.3. The He implantation with respect to the cascade damage obtained at the damage peak was 17 appm He/dpa. The irradiation conditions are summarized in table 3.2.

---

[2] After the irradiation, TEM observable FIB thin foils were extracted from the thicker zones (100 µm) of the specimen. We have thus considered this irradiation as irradiation on bulk specimens.

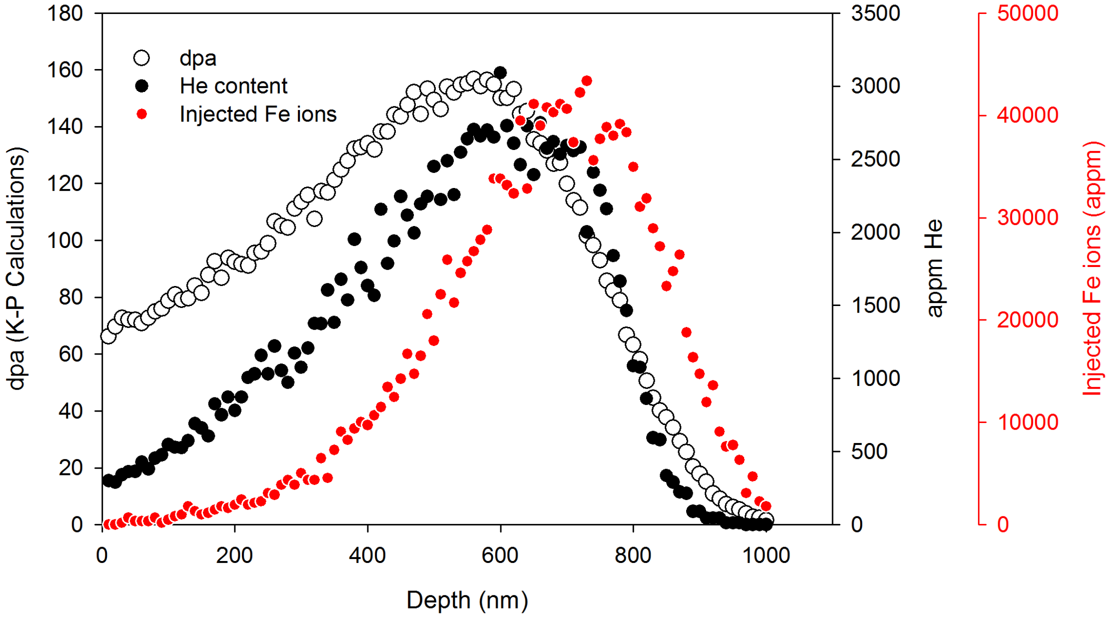

Figure 3.3: Depth profile of displacement damage, He implantation profile (in appm) and Fe injected ion implantation profile (in appm) obtained for Fe matrix by SRIM-2008 for the high dose irradiations. Kinchin-Pease calculations were utilized for estimating the damage in dpa.

Material	Sample	Fluence $ions.cm^{-2}$	Flux $ions.cm^{-2}.s^{-1}$	dpa *(at peak)*	He/dpa *(in appm)* *(at peak)*	Analysis Technique
All FeCr alloys and bcc Fe	TF	1.38 x 10^{17} **8.4 x 10^{16} (He)**	3 x 10^{12} **1.8 x 10^{12}(He)**	157	0/**17**	TEM

Table 3.2: Details of the irradiation conditions for the high dose irradiations performed at 500 ºC with and without He co-implantation. In this case, damage rate at the peak was 3.2 x 10^{-3}dpa/s. TF stands for thin foils.

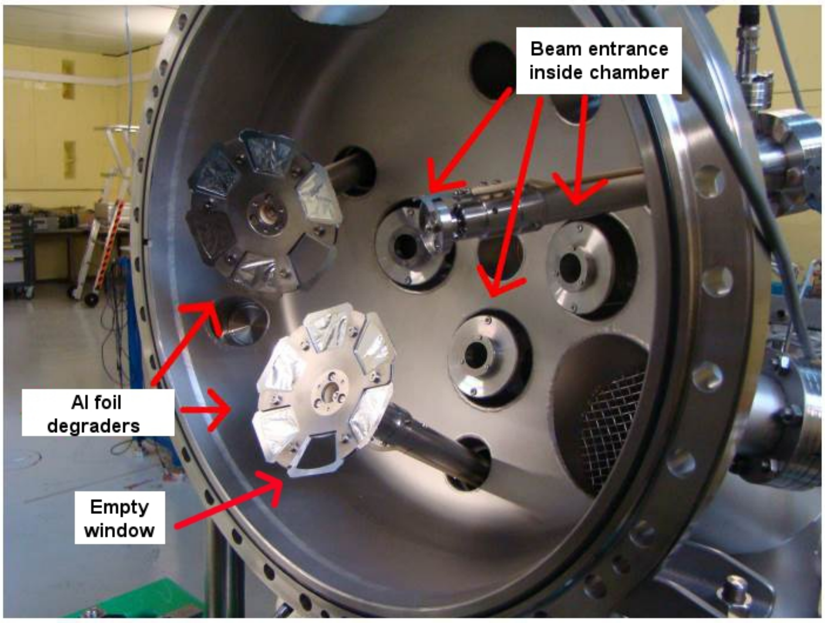

Figure 3.4: Position of degraders composed of Al foils with respect to the entry point of beam inside the triple beam chamber at JANNuS, Saclay.

For ion irradiations, the temperature control of specimens is crucial. Care should be addressed to avoid specimen heating due to the incident beam power. In our case, the temperature monitoring was performed using infra-red thermal camera and thermo-couples. The entire procedure of temperature control can be found in Appendix D.

It is important to remember that when the He beam was degraded using the degrader system, one slot was kept open without any Al foil (see figure 3.4). A geometry like this is necessary for performing beam current measurements. This means that even undegraded 2 MeV He^+ ions, which pass through this window, were deposited in the sample. However, the depth of this He implanted zone was 3.34 μm below the implanted surface. It was, thus, much further away from the dual beam zone of interest which was around 600 nm depth. It is hence considered in the analysis that there is no influence of these two zones on each other. Since there are five Al windows and one empty window, the He implantation fluence at this depth is one-sixth of the net fluence given in Table 3.2. These two zones are shown in a TEM image of transverse FIB thin foil of Fe10%Cr in figure 3.5. Maximum damage produced by this implantation was ~0.25 dpa, which is very less due to low atomic mass of He. More details about this zone can be found in Appendix E.

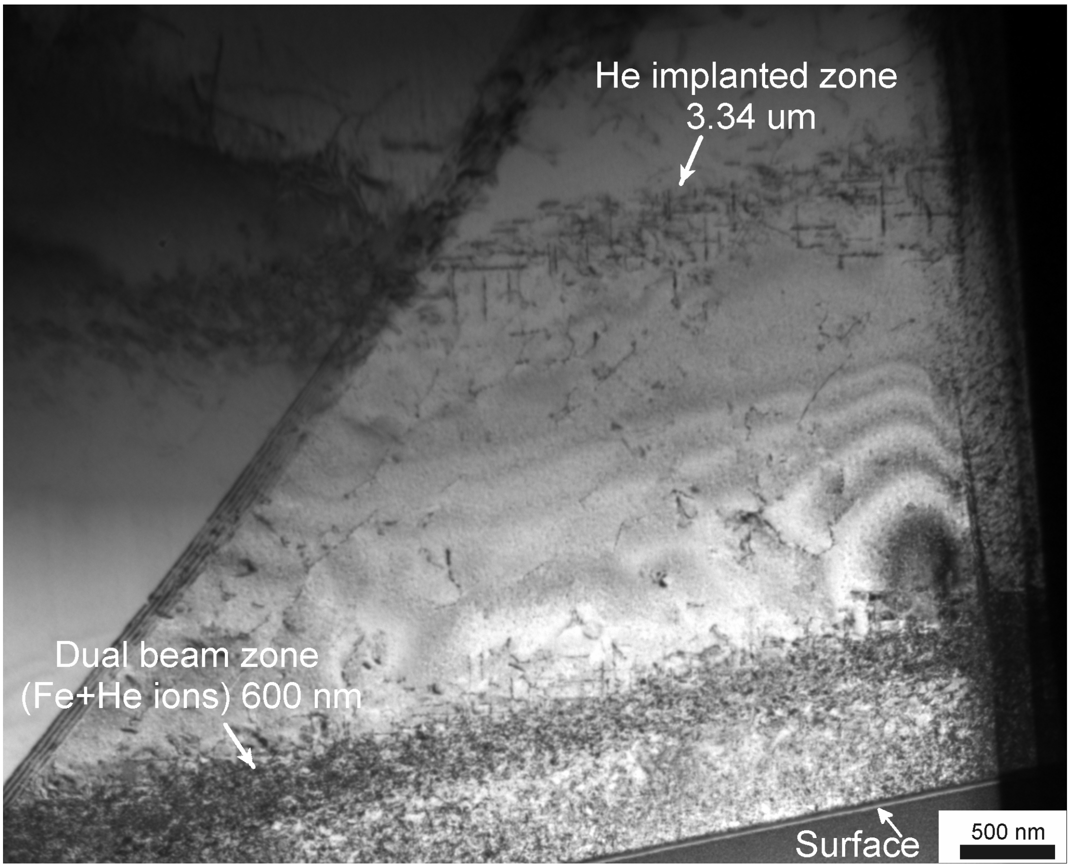

Figure 3.5: Transverse FIB thin foil of high dose dual beam irradiated Fe10%Cr showing the dual beam irradiated zone (Fe+He ions) at a depth of 600 nm and the He implanted zone arising due to empty degrader window at 3.34 μm below the irradiated surface.

3.3.2 Intermediate dose irradiations

Prior to our experiments, high purity FeCr alloys belonging to the same set of materials as ours, were irradiated to intermediate dose of 45 dpa (with and without He co-implantation) at 500 ºC at JANNuS Saclay facility. These irradiations were performed by D. Brimbal and co-workers [13] in a related thesis work. Owing to an access to these irradiated materials, we have utilised Fe5%Cr and Fe10%Cr in our study. The aim was to see the segregation/enrichment behaviour of Cr at the radiation induced dislocation loops. For such kind of studies, intermediate doses are ideal because the loops are expected to be larger which makes analysis relatively easier. On the other hand, they are not expected to be too large so that they get incorporated in a network which are always difficult to analyse. Details of the irradiation conditions are given below.

Similar to the high dose irradiations, 2 MeV Fe^{2+} ions were used. The fluence reached was 4.43 x 10^{16} ions.cm^{-2}. Estimation of the dose using SRIM Kinchin-Pease calculation gives maximum dpa at the peak damage zone, centered around 600 nm depth, to be 45 dpa. For the dual beam case, 2 MeV He^{+} ions degraded by Al foils was co-implanted to 8.8 x 10^{16} ions.cm^{-2}. The He implantation with respect to cascade damage obtained at the damage peak was 58 appm He/dpa. The dpa, He implantation and injected Fe ion profiles are given in figure 3.6. In this case, the microstructural characterization was performed using conventional TEM, EDS in STEM mode and APT. The irradiation conditions and the analysis technique used is given in table 3.3.

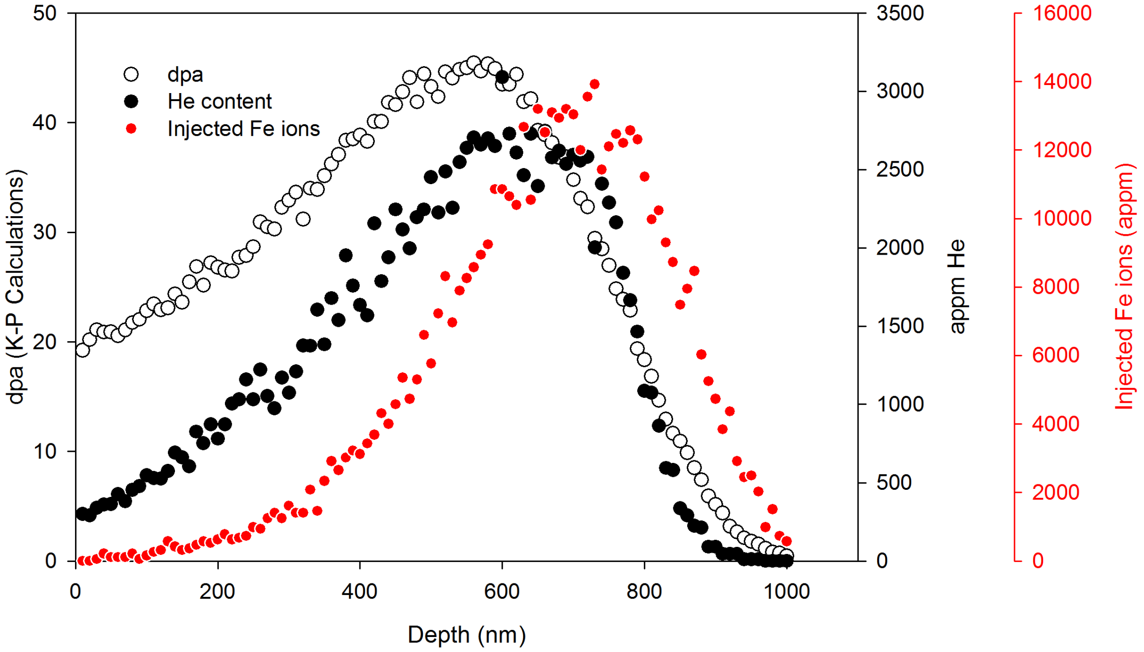

Figure 3.6: Depth profile of displacement damage, He implantation profile and Fe injected ion implantation profile obtained for Fe matrix by SRIM-2008 for the intermediate dose irradiations.

Material	Sample	Fluence *ions.cm*$^{-2}$	Flux *ions.cm*$^{-2}$*.s*$^{-1}$	dpa *(at peak)*	He/dpa *(in appm)* *(at peak)*	Analysis Technique
Fe5%Cr Fe10%Cr	TF, DD TF, DD	4.43 x 10^{16} **8.8 x 10^{16} (He)**	7 x 10^{11} (Fe) **14 x 10^{11}(He)**	45	0/**58**	TEM TEM, EDS, APT

Table 3.3: Details of the irradiation conditions for the intermediate dose irradiations performed at 500 ºC with and without He co-implantation. In this case, damage rate at the peak was 7.1 x 10^{-4}dpa/s. TF and DD stands for thin foils and dimpled disc (of 100 µm) thickness.

3.3.3 Low dose irradiations

Low dose irradiations were performed in the in-situ dual beam JANNuS Orsay facility on the Fe14%Cr alloy. This facility is equipped with a LaB_6 based 200 keV FEI Tecnai $G^2$20 TEM. The TEM is coupled to a 2 MV tandem accelerator, which allows ion energy between 500 keV to 15 MeV, and to a 190 kV ion implanter, which allows ion energies up to 570 keV [134] (see figure 3.7). A photograph of the beam lines coupled to the TEM is shown in figure 3.8.

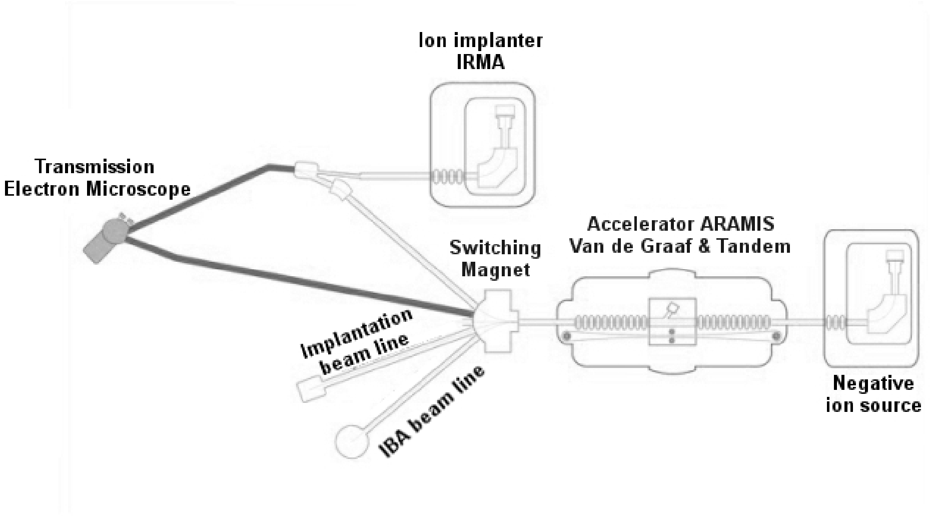

Figure 3.7: Schematic of the JANNuS dual beam in-situ irradiation facility at CSNSM, Orsay.

The angle of incidence of the beam lines is 22° with respect to the TEM specimen holder position as shown in figure 3.9. Moreover, there is a 45° angle between the two beam lines. The specimens inside the holder are necessarily tilted to be in optimum conditions for irradiations and for performing simultaneous TEM imaging. The ion flux is determined by the incident angle between the beam and the specimen surface. Further details about this can be found in [13].

Similar to earlier irradiations, the experiments were performed in single beam (Fe ions only) and simultaneous dual beam mode (Fe + He) to separate ballistic damage from gas implantation effects. In this case, the incident angle was 45° for the He beam and 61° for the Fe beam. For the single beam case, the microstructure was followed in-situ. However, in-situ observations were not possible for the dual beam case. It was due to the problem of divergence of He beam (or in general, light ion beams) because of interaction with the magnetic field of the TEM objective lens. Thus, while performing the experiment, the objective lens was switched off. Nevertheless, the microstructure of both specimens was analysed after the irradiation.

Figure 3.8: Two accelerator beam lines coupled to 200 keV FEI Tecnai $G^2$20 Twin TEM at JANNuS, Orsay.

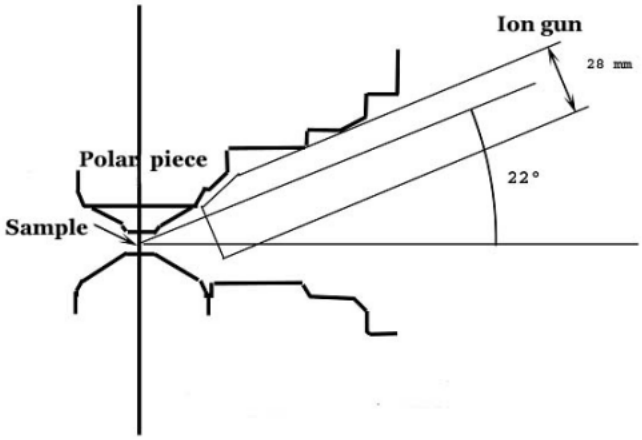

Figure 3.9: Position of beam with respect to the position of specimen holder of TEM at JANNuS, Orsay [13].

The irradiations were carried out at 500 ºC on specimens as TEM thin foils using the Gatan heating double tilt specimen holder. In this case, 1 MeV Fe^+ ions were used to reach fluence equal to 3 x 10^{14} ions.cm^{-2}. For the dual beam case, the specimen was simultaneously implanted with He, using 15 keV He^+ions to 1.46 x 10^{15} ions.cm^{-2}. Taking the incident angle of the Fe beam into account, SRIM Kinchin-Pease calculation provided a dose equal to 0.33 dpa at the damage peak, while the He injection was equal to 3030 appm He/dpa. The depth profile of the damage and He implantation is shown in figure 3.10 . The irradiation parameters are summarized in table 3.4.

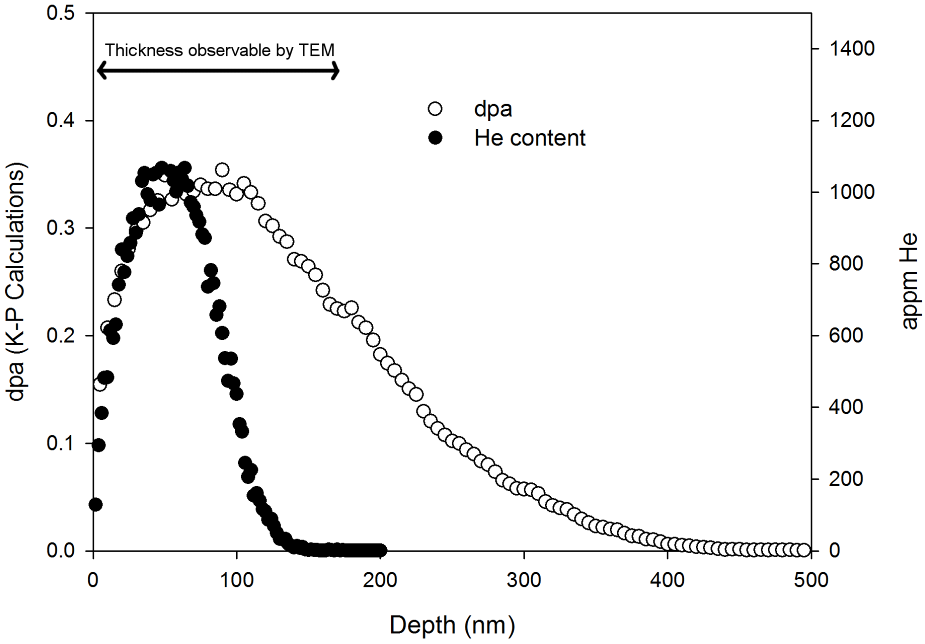

Figure 3.10: Depth profile of displacement damage and He implantation profile obtained for Fe matrix by SRIM-2008 for the low dose irradiations.

Material	Sample	Fluence *ions.cm*$^{-2}$	Flux *ions.cm*$^{-2}$*.s*$^{-1}$	dpa *(at peak)*	He/dpa *(in appm)*	Analysis Technique
Fe14%Cr	TF	3 x 10^{14} **1.46 x 10^{15} (He)**	1.33 x 10^{11} **4.2 x 10^{11}(He)**	0.33	0 **3030**	TEM

Table 3.4: Details of the irradiation conditions for the low dose in-situ irradiations performed at 500 ºC with and without He co-implantation. In this case, damage rate at the peak was 1.6 x 10^{-4}dpa/s. TF stands for thin foils.

3.4 Microstructural characterization techniques

For all the irradiation conditions, the microstructure of the materials was characterized before and after the irradiation. Only during the in-situ experiment, the evolution was followed in real time. In all the cases, the principal characterization technique used was conventional TEM, to analyse the radiation defects such as dislocation loops and cavities. A part of the results concern analytical measurements of Cr enrichment on radiation induced dislocation loops. For this study, other complimentary experimental techniques were used in tandem with conventional TEM. These were energy dispersive X-ray spectroscopy (EDS) in scanning TEM mode (henceforth called as STEM/EDS) and atom probe tomography (APT). A brief description and experimental details concerning these characterization techniques are given in this section.

First, the details of conventional TEM investigation are given. Thickness measurement of thin foils performed using conventional TEM and EELS is also given. Then, analytical techniques : STEM/EDS and APT are briefly detailed.

3.4.1 Transmission electron microscopy (TEM)

TEM utilises energetic electrons which traverse very thin zones of a material and forms an image of the microstructure in which the material defects or their clusters can be directly seen[3]. This ability of direct visualisation of microstructure is by far the principal advantage of TEM over other characterization techniques. The interaction of the electron beam with the material gives a “contrast”, which depends on the nature of the defect and imaging conditions.

In our case, conventional TEM imaging was used to perform post irradiation analysis of the dislocation loop microstructure and cavities. The characterization work was shared between three TEM machines available at CEA-Saclay : 200 keV Philips CM20 and Jeol 2100 equipped with a thermionic LaB_6 cathode, and a FEG (Field Emission Gun) based 200 keV Jeol 2010F. The dislocation microstructure was characterized using mainly the first two TEMs. It was due to the possibility of reaching higher tilt angles in these TEMs which are essential for loop analysis. Dislocation loops were characterized by diffraction contrast in 2-beam kinematic bright-field (KBF) and weak beam dark field (WBDF) imaging techniques [137] using <110> reflections (see the next section). The analysis of cavities (voids or bubbles) was mainly performed on the FEG based TEM using through-focal imaging technique [137]. In all the cases, Gatan Orius SC200 and Gatan Orius SC200 D camera with a resolution of 2000 x 2000 pixels were used for recording images.

Apart from conventional imaging, in-situ sequential annealing of the irradiated specimen was also performed. It was the case for Fe10%Cr intermediate dose irradiated thin foil (45 dpa, 58 appm He/dpa). This dedicated experiment was performed by using the Philips CM20 TEM and a Gatan tilt-heating specimen holder, which is capable of withstanding temperatures up to 1000 °C. During this experiment, KBF conditions were used to analyse the evolution of the dislocation loop microstructure. The loop evolution was observed by staying fixed at discrete temperature steps for certain durations, up to 627 °C (see Chapter 5, section 5.2.3). As heating causes local bending of the thin zones in a specimen, the imaging conditions were frequently adjusted to provide an optimum visible loop contrast.

Since dislocation loops and cavities were mostly the features of interest in our study, we present a brief detail of the imaging condition utilized for these two cases.

3.4.1.1 Dislocation contrast

Dislocations (lines and loops) are imaged by using diffraction (or strain) contrast imaging technique [137]. By virtue of the elastic strain field of the dislocations, they introduce local changes to the diffrac-

---

[3] For obtaining images, it is necessary to reduce specimen thickness to a value for which they become electron transparent. In general, the specimen thickness is of the order of a few tens of nanometres.

tion conditions. For instance, introduction of edge dislocations in a perfect matrix causes the diffracting planes to bend locally, causing changes in the amplitude of the diffracted beam which is used to form their image. The image characteristics are sensitive to the imaging conditions used. As indicated earlier, in our case we have utilized 2-beam kinematic bright field imaging (KBF) and weak beam dark field (WBDF) imaging modes. Both these methods are briefly discussed here:

2-beam kinematic bright field condition In our study, 2-beam KBF technique was the most utilized imaging condition for analysing the dislocation microstructure. This imaging condition is achieved by tilting the TEM thin foil to a well-defined diffraction condition by ensuring that only one set of diffracting planes is close to the Bragg condition (also called 2-beam condition). The diffraction condition is specified by the 'deviation parameter', s_g, which is the distance of the reciprocal lattice point $\vec{g}$ from the Ewald sphere. In this case, s_g is kept slightly positive by tilting sufficiently away from the exact Bragg condition (which corresponds to $s_g = 0$). The Ewald sphere[4] construction for this condition, taken from [137], is shown in figure 3.11b. Bright field (BF) image is obtained by selecting the transmitted beam spot using an objective aperture situated at the back focal plane of the objective lens. Since the dislocation core diffracts differently as compared to the matrix, this intensity is lost from the transmitted beam. This makes dislocations appear dark in BF kinematic images. KBF imaging technique has the advantage that the dynamic interactions between the two beams, which happens at exact Bragg condition (i.e. $s_g = 0$), is avoided and image contrast is simpler to interpret [137].

Weak beam dark field condition Weak beam images are dark field images obtained using a weakly excited beam. In this imaging condition, the foil is tilted so that the diffracting planes are sufficiently far from the exact Bragg condition (see figure 3.11c). Thus, the magnitude of the deviation parameter s_g is large. However, in regions adjacent to the dislocation cores, the local strain field may bend the diffracting planes back towards the Bragg condition. Therefore, weak beam images have a substantial enhancement of the defect peak intensity relative to the surrounding background [137]. The dislocations appear bright in a darker background.

The main advantage of WBDF images is that the dislocation peak widths are much narrower than in KBF imaging conditions because of large s_g [137]. Thus, the image of dislocation microstructure is on much finer scale, which makes it easy to resolve individual objects. Due to this reason, this technique is favoured when characterizing very small dislocation loops or in general a dense dislocation microstructure.

---

[4] In the figure, the curvature of the sphere has been increased for clarity; it is actually rather flat (with radius $k = \lambda^{-1}$, where λ is the electron wavelength; thus $k >> g$).

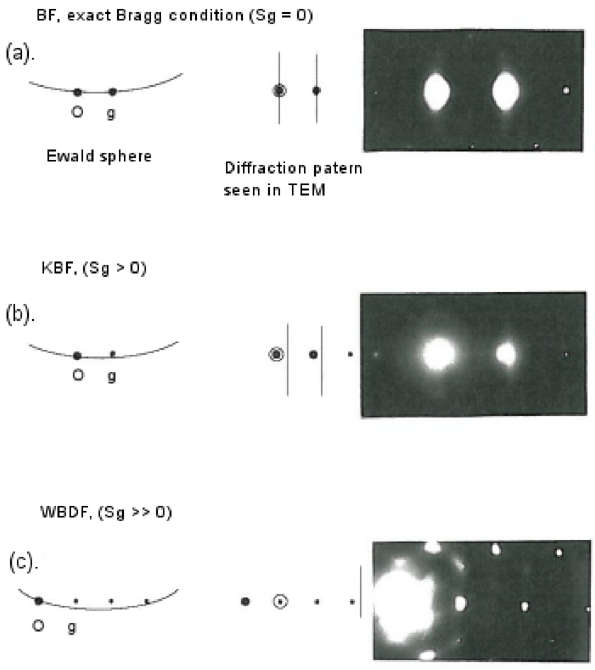

Figure 3.11: Representation of different diffraction contrast imaging techniques. (a). Bright field condition on exact Bragg condition (s_g = 0), (b). 2-beam kinematic bright field condition (s_g > 0), and (c) weak beam dark field condition ($\vec{g}$, n$\vec{g}$) and s_g >> 0. For each condition, the Ewald sphere construction is on the left, 2-beam diffraction condition with Kikuchi lines in the centre and the experimentally observed diffraction pattern on the right. The circular selection indicates the spot selected using objective aperture for obtaining images. Adapted from [137].

3.4.1.2 Determination of Burgers vector of dislocation loops

Dislocation loops are characterized by their Burgers vector $\vec{b}$ and dislocation line direction $\vec{u}$. In our case, we have determined the Burgers vector of loops for the low dose in-situ irradiated materials (0.33 dpa). The invisibility criteria $\vec{g} \cdot \vec{b} = 0$ [137, 138] was utilised. In this criteria, since the value of dot product is already known, then by knowing $\overrightarrow{g}$, we can find out $\overrightarrow{b}$. It is known from chapter 2 “Bibliography” that in bcc Fe and FeCr alloys, only a/2<111> and a<100> type loops are observed. Thus, by selecting a set of appropriate $\vec{g}$ (and the corresponding images), a set of visibility/invisibility criteria for the loops was generated. The combinations were unique to each loop family. Using these combinations, the Burgers vector identification was made. In our analysis, <110> and <200> type reflections were used. A detailed example is shown in Chapter 5, section 5.1.1.2)

It must be taken into account that in reality, the invisibility criteria originates from $\vec{g} \cdot \vec{R} = 0$, where $\overrightarrow{R}$ is the net displacement induced by a defect. As mentioned by Williams and Carter [138], for an isotropic solid, it is given as

$$\overrightarrow{R} = \frac{1}{2\pi}\left(\overrightarrow{b}\phi + \frac{1}{4(1-\nu)}\left\{\overrightarrow{b_e} + \overrightarrow{b} \times \overrightarrow{u}(2(1-2\nu)ln(r) + cos2\phi)\right\}\right)$$

where $\vec{b}$ is the Burgers vector, $\vec{b_e}$is the edge component of Burgers vector, $\overrightarrow{u}$ is unit vector along dislocation line (the line direction) and ν is the Poisson's ratio. For pure edge dislocations,

$$\vec{b} = \overrightarrow{b_e}$$

and

$$\overrightarrow{b_e} \times \overrightarrow{u} \neq 0$$

Full invisibility of loops will occur only when $\vec{g} \cdot \vec{b_e} = 0$ and $\vec{g} \cdot \vec{b_e} \times \vec{u} = 0$. However, we can have situations when $\vec{g} \cdot \vec{b_e} = 0$ and $\vec{g} \cdot \vec{b_e} \times \vec{u} \neq 0$. The second term, hence, produces a faint contrast of the otherwise invisible loops, usually referred as residual contrast. This contrast is however much weaker in intensity compared to the visible loops. It is, thus, neglected.

We have not attempted to determine whether the loops were interstitial or vacancy in type. This information is obtained by utilising the inside-outside contrast technique using " First Start Right Hand (FSRH)" rule [137, 139]. However, for our irradiation conditions, i.e. irradiation using self ions at 500 ºC, the loops are not expected to be vacancy type. As seen in Chapter 2 "Bibliography", vacancy loops in bcc Fe are a very rare feature, usually seen at low temperatures (RT or below) when irradiated with very heavy ions. At elevated temperatures, loops in Fe are much larger in size (almost of the order of 100 nm) even for dose of the order of 1 dpa [13]. Such large loops should not be vacancy type because they have a tendency to shrink with irradiation. Thus, its a fair supposition on our part that all the loops are interstitial in nature.

3.4.1.3 Determination of specimen thickness

For quantitative information about the number density of defects, the thickness of the TEM samples is necessary. In our experiments, this measurement was performed by counting thickness fringes (obtained at exact Bragg condition) in specimens where these could be formed. However, we must note that for obtaining thickness fringes, the specimen should have a uniform thickness gradient. This situation is not always met, for example in FIB samples and for bent electro-polished thin foils. Thus, for the later two cases, thickness was determined by electron energy loss spectroscopy (EELS). We detail these two techniques briefly in this section:

Thickness fringes When a wedge-shaped TEM thin foil is imaged under exact Bragg condition ($s_g = 0$), fringes are observed which contain information about the thickness of the specimen. Each fringe corresponds to a part of the specimen having the same thickness. From Howie-Whelan equations [138], the intensity of the Bragg diffracted beam I_d and the transmitted beam I_t can be written as,

$$I_d = \left(\frac{\pi t}{\xi_g}\right)^2 . \frac{sin^2\left(\pi t s_{eff}\right)}{\left(\pi t s_{eff}\right)^2} = 1 - I_t$$

where t is the distance travelled by the diffracted electron beam which can be approximated as specimen thickness, ξ_g is the extinction distance and s_{eff} is the effective excitation error given as

$$s_{eff} = \sqrt{\left(s_g^2 + 1/\xi_g^2\right)}$$

From the intensity equation, it readily follows that for $s_g = 0$, the intensity of the transmitted beam is zero (i.e. a dark fringe) for thickness $t = (1/2 + n)\xi_g$, where n is an integer. Consequently, the wedge shaped specimen would show dark fringe for region of thickness $\xi_g/2$, $3\xi_g/2$, etc. for bright field condition. Thus, just by counting the number of dark fringes and knowing the value of the extinction distance ξ_g, the foil thickness can be determined. A schematic description of formation of thickness fringes is shown in figure 3.12. In our case, the value of the extinction distance ξ_g was taken to be 35 nm for $\vec{g}$ = <110> for Fe and for accelerating voltage of 200 keV.

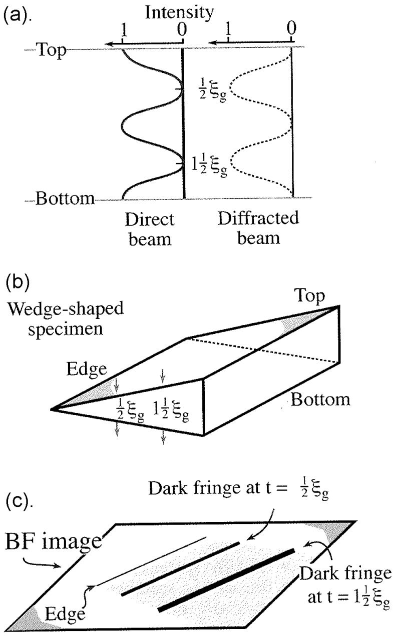

Figure 3.12: Origin of thickness fringes in wedge-shaped specimens. (a) Intensity oscillation of direct and diffracted beam at Bragg condition ($s_g = 0$). (b). Representation of the wedge-shaped specimen. (c). Representation of fringes in a TEM BF image (the fringe separation is determined by extinction distance ξ_g and the angle of the wedge). Adapted from [138].

As indicated by Brimbal and co-workers [13], the error in thickness estimation by this method is around 30%. An example of such fringes is shown in figure 3.13, where low dose irradiated Fe14%Cr is imaged using <110> reflection at exact Bragg condition. The thickness value of each dark fringe is mentioned in the image.

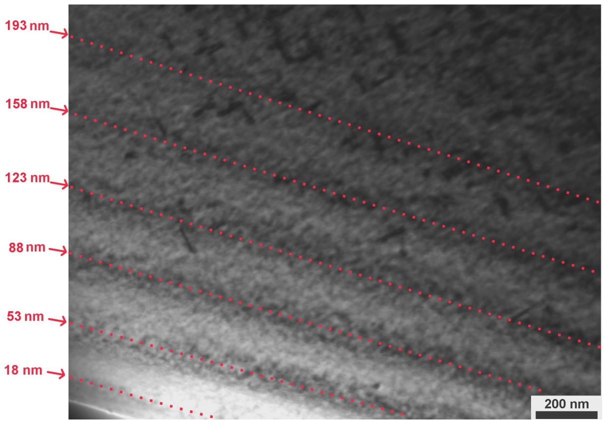

Figure 3.13: Example of thickness fringes in single beam irradiated Fe14%Cr to 0.33 dpa obtained. (BF, $\overrightarrow{g} =< 110 >$, zone axis = (001), $s_g = 0$).

Thickness determination by EELS In some electro-polished thin foils, thickness fringes could not be obtained. It was mainly due to local bending of the foil. Furthermore, such fringes are not obtained for FIB specimens owing to almost homogeneous thickness. In these cases, the thickness was determined by using EELS in TEM mode.

This method is based on the loss of the kinetic energy of electrons after undergoing inelastic Coulombic interactions with the atomic electrons of the constituent elements in the specimen [140]. Based on the interactions, the transmitted beam of electrons constitute an energy spectrum, which is analysed using a magnetic spectrometer and an EELS CCD camera. A basic schematic of a conventional TEM equipped with an EELS system is shown in figure 3.14.

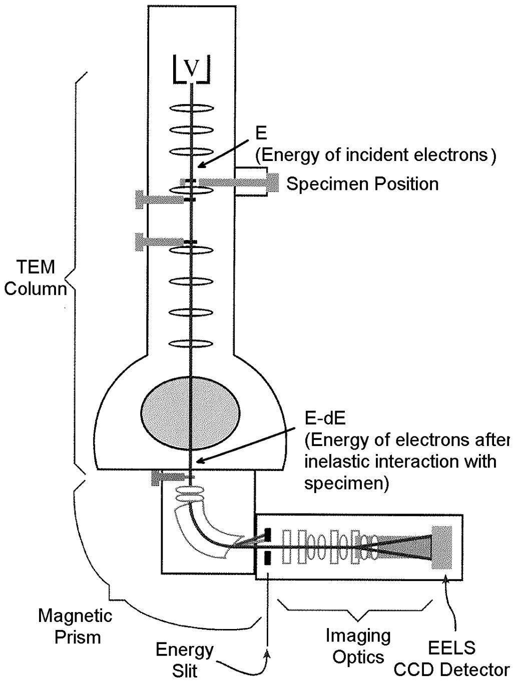

Figure 3.14: Schematic representation of EELS set-up coupled with a conventional TEM. Adapted from [138].

An example of typical energy spectrum obtained by EELS is shown in figure 3.15. In this case, it corresponds to bcc Fe single beam irradiated to 157 dpa at 500 ºC. The most prominent feature corresponds to an intense peak at 0 eV, termed as zero-loss peak. It represents electrons that did not undergo inelastic scattering but might have been scattered elastically (with atomic nuclei) with an energy loss too small to measure. Other features arise from inelastic scattering by conduction or valence electrons. For instance, the peak centered around 22 eV in figure 3.15 results from plasma resonance of the valence electrons, known as plasmon peak. The shape of the spectrum is strongly dependent on the structure of the irradiated material, TEM accelerating voltage, semi-angle of convergence of the beam denoted as α, and the semi-angle of collection β (see figure 3.16).

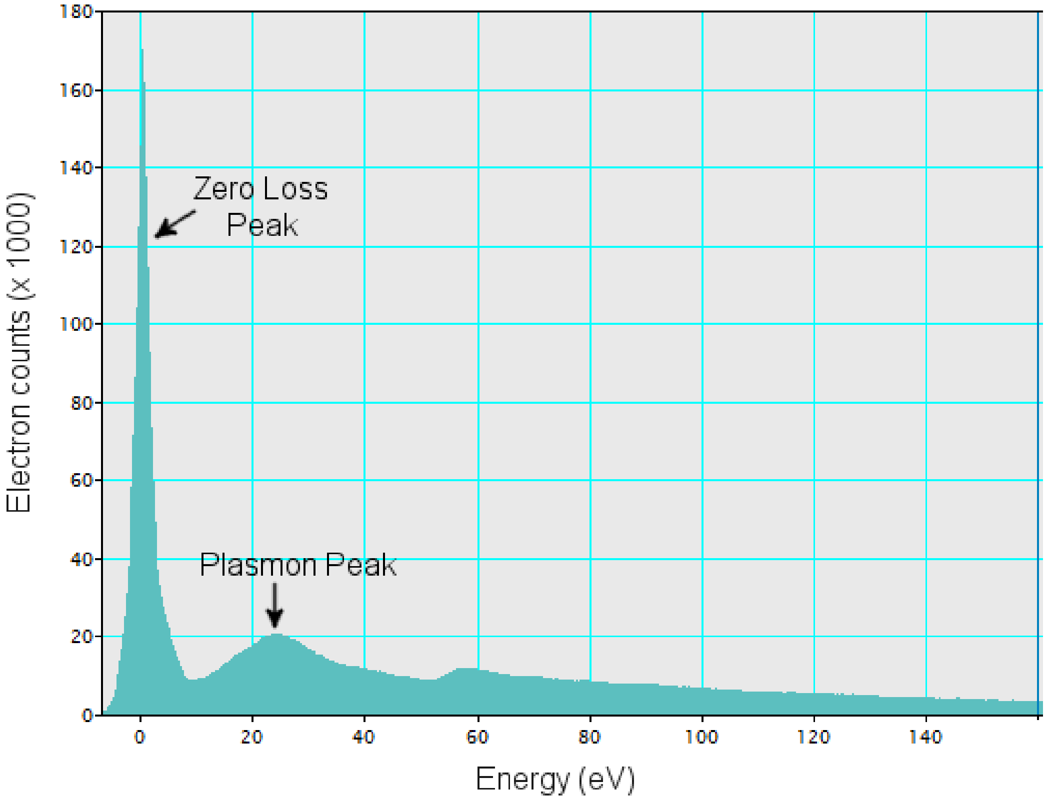

Figure 3.15: EELS low-loss spectrum from our FIB thin foil specimen of bcc Fe irradiated to 157 dpa at 500 ºC, obtained using Gatan EELS software. The zero loss peak and Fe plasmon peak at 22 eV are indicated.

Thickness information is present in such spectrums because the intensity of inelastically scattered electrons increases with specimen thickness [138]. The most common procedure for estimating specimen thickness within a region defined by the incident beam (or an area-selecting aperture) is to record a spectrum in low-loss regime and compare the area under the zero-loss peak (I_0) with the total area under the whole spectrum (I_t) using the “Log-Ratio Model” [140]. Using this model, the thickness can be estimated using the relation

$$\frac{t}{\lambda} = ln(\frac{I_t}{I_0})$$

where λ is the mean free path of electrons for inelastic scattering in the material.

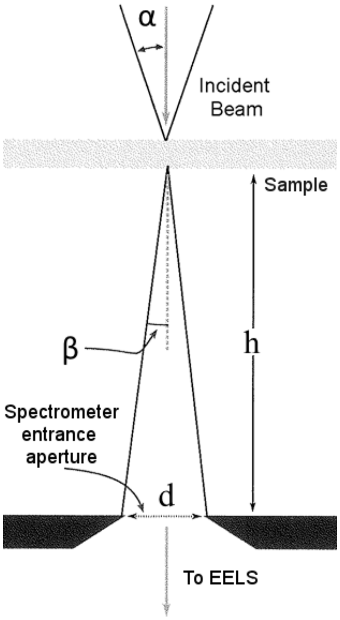

Figure 3.16: Schematic diagram showing the definition of semi-angle of convergence and semi-angle of collection for EELS analysis [138].

In our case, we have performed the analysis using a 200 keV Jeol 2100 TEM equipped with a Gatan GIF EELS spectrometer. The "compute thickness" option of Gatan EELS software permits us to measure the specimen thickness. For Fe excited with 200 keV electrons, the mean free path for inelastic scattering λ was taken as 110.4 nm, as estimated in a relatively recent report on a comparison of various TEM based thickness measurement techniques performed at SRMA/CEA-Saclay [141]. As recommended in this report, we have worked in diffraction mode with a large collection angle (typically > 100 mrad) for which electron intensity is maximised and λ becomes independent of β and α. The Gatan EELS software directly provides us the value of log of the intensity ratios. These values were multiplied by λ to obtain foil thickness values. More details about this technique can be found in [140].

Usually the error in thickness determination under ideal user conditions by this method is ~20% [141]. Ideal user conditions mainly implies that the beam alignment is perfect and sample is completely uniform in thickness and composition with no contamination. In our case, we have taken a conservative approach and have considered the error to be 30%. We believe its a reasonable estimate by considering the fact that we are dealing with irradiated specimens where contamination may be difficult to avoid. Repeated measurements on the same zone of specimens were also performed and the values obtained were well within the 30% error range.

3.4.1.4 Determination of loop size and number density

The size of the dislocation loops were measured using the KBF images obtained using <110> reflections. The longest distance within the loops was taken as the size. Based on a relatively important statistics of loops considered, wherever possible, the maximum, minimum and average loop size was estimated. If there were two very different loop distributions visible in the microstructure (which can happen when both a<100> and a/2<111> loops are present), the average size was calculated for each distribution separately. Error bars were calculated on size by performing repeated measurements on the loops. It was dependent on the loop size. For smaller loops less than 5 nm in size, it was around 15%. Between 5 - 20 nm, it was ~ 7.5%. For larger loops more than 20 nm in size, the error was 2 - 3%.

A histogram of loop sizes was also performed where the number of occurrences (i.e. frequency) of loops belonging to a certain size bin was plotted. The bin widths were selected appropriately depending on the sizes measured. The error bars for the histograms were also estimated, which is only the statistical error on the loop count. For the sake of simplicity, the error in their size measurement was ignored.

Loop number density was determined by counting loops on images obtained using <110> reflections in KBF mode and estimating the volume of the analysed zone (which is area of the zone visible in the image multiplied by sample thickness). The relationship is given as

$$Number\, density\, of\, loops = \frac{Number\, of\, loops\, counted\, in\, the\, zone}{Volume\, of\, the\, analysed\, zone}$$

The values were corrected for the invisibility of some loop families by utilising the results of $\vec{g}.\vec{b}$ analysis. The error bar on the number density was estimated using a combination of statistical error on the number of loops counted in the zone of analysis and the error in sample thickness. However, the later is the major contributor. The error in loop count depends on the number of loops included for the analysis. In our case, this value was around 10%. Whereas the uncertainty associated with the methods of thickness measurements mentioned in the previous sub-section, is around 30%. Similar to size estimation, if two very different loop distributions were visible, number density was estimated for each separately.

3.4.1.5 Cavity microstructure

Cavities were analysed in the materials irradiated to high dose (157 dpa). Through focal series imaging technique was utilized to image them[5] [137]. The basic principle of this technique is the phase shift in the column of electrons which traverse the cavity with respect to the electron column which passes through the adjacent perfect crystal. This gives rise to Fresnel fringes near the edge of the cavity which can be seen when the objective lens is out-of-focus. For under-focused objective lens, the cavities appear bright with a dark fringe around. For over-focused condition, they appear dark with a bright fringe around. The effect depends sensitively on the degree of out-of-focus. The imaging is performed in KBF conditions with thin foil tilted sufficiently far from Bragg condition. This is done to avoid overlap of diffraction

---

[5] For irradiation with simultaneous He implantation, cavities contain some quantities of He inside. Nevertheless, the imaging technique stays the same.

contrast with the contrast of cavities. However, in some cases we have performed cavity imaging not too far from Bragg condition to see loop microstructure and cavities on the same image.

3.4.1.6 Determination of cavity size, number density and void swelling

For spherical cavities, which were usually smaller than 5 nm, their size was represented by the diameter. As recommended in [137], the inner diameter of first dark fringe in under-focus condition was taken as the cavity size. For faceted cavities, their longest distance was taken as the size. Error on size was determined by repeated measurements on the microstructure.

The maximum and average cavity size was estimated for each case. Minimum cavity size was also estimated, but it is not mentioned because its value is biased by the resolution the microscope. Based on measured sizes, frequency distribution of cavity size was also plotted in some cases. The error bars in this case were purely the statistical error arising from the cavity count.

Cavity number density was calculated by counting the number of visible cavities in a given zone by comparing the under and over focused images. The relationship is given as

$$Cavity\,number\,density = \frac{Number\,of\,cavities\,counted\,in\,the\,zone}{Volume\,of\,the\,analysed\,zone}$$

Void swelling was estimated for the high dose irradiated materials by calculating the volume fraction of cavities with respect to the volume of the analysed zone. The relation is given as

$$S = \frac{Net\,volume\,of\,cavities}{Volume\,of\,zone - Net\,volume\,of\,cavities} \times 100\%$$

Since void swelling is dependent on the volume of cavities, care was taken to consider the cavity shapes (wherever possible) while calculating their volume.

The error bars were also calculated on the value of void swelling and number density. The main sources of error were in (i). thickness determination, (ii). statistical error in number of cavities in the analysed zone and (iii). the error in determining cavity size (only important for swelling estimation).

As seen in the previous section on dislocation loops, the error in thickness was about ±30%. Statistical error on cavity count was minimised by analysing a larger zone to have sufficient number of cavities to consider. This is, however, strongly dependent on the microstructure. If the number density of cavities is high, as we shall see is the case for FeCr alloys, this error is largely reduced. For the high dose dual beam irradiations, this was between 6 - 9% (depending on how many cavities were considered for the analysis). However, when cavity number density is low, which was the case for single beam irradiated bcc Fe, this error increases - it was between 30 - 57% along the damage depth in the FIB foil. The other source of error is in the size of cavities. It was estimated by making repeated size measurements on the microstructure. The error was strongly dependent on the size - large errors for small cavities. For instance, when the size was less than 5 nm, the error was 20%. For 5 to 20 nm sized cavities, it was ~11%. Larger cavities beyond 20 nm had error in the range of 3 - 5%. All these errors were included for calculation of each swelling data. Size histogram of cavities was also represented in certain cases. In this case, for the sake of simplicity, the error was estimated as statistical error in each size bin, without taking into account the error in size determination.

3.4.2 Energy dispersive X-ray spectroscopy (EDS)

Analytical EDS measurements were performed in scanning TEM (STEM) mode on the Fe10%Cr irradiated to intermediate dose (45 dpa, 58 appm He/dpa). The main aim was to see the enrichment/depletion of Cr on the dislocation loops. The analysis was performed using Jeol JED-2300T EDS spectrometer in a spherical aberration (Cs) corrected high resolution Jeol ARM200F analytical STEM at the University of Rouen, equipped with a FEG Schottky electron gun. The advantage of this instrument is that the detection area of X-ray detector is large (up to 100 mm^2), which increases the detection sensitivity. Furthermore, sub-angstrom probe size could be reached using this microscope in STEM mode, which enabled us to record X-ray line spectras on a very fine scale (resolution = 0.2 nm). The energy resolution of this system is 138 eV.

The basic principle of this technique is based on the emission of characteristic X-rays from the specimen produced by the incoming energetic electron beam [138]. These characteristic X-rays contain information about the chemical elements present in the material. The most intense are the X-rays emitted due to the de-excitation of K-shell electrons (K_α and K_β lines). A quantification of X-ray counts could provide the compositional information about a material. It is estimated by measuring the area under the peak of the characteristic X-ray of a desired chemical element to the total area under X-spectrum [138]. This value is directly provided by the EDS softwares coupled to the detection system. A general set-up of EDS measurements in a TEM is shown in figure 3.17.

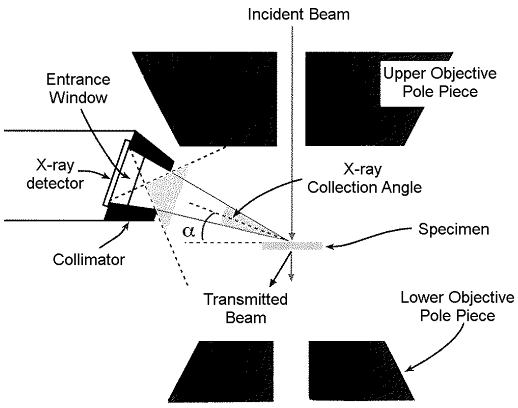

Figure 3.17: Schematic representation of EDS system coupled to TEM [138].

A detailed description of this technique can be found in [138]. In our case, the error bars on the concentration measurements were also given. They were estimated from the standard deviation of the X-ray counts registered by the detector.

The sample used for the EDS analysis was a FIB thin foil prepared from the irradiated dimpled disc. However, unlike other FIB specimens, it was prepared by following a special procedure. Prior to FIB preparation, an orientation map of the grains was obtained by electron back-scatter diffraction (EBSD), using a FEG-based JEOL 7001F LV scanning electron microscope. This map is shown in figure 3.18. The objective was to select a (001) grain orientation to have the a[100] and a[010] dislocation loops on edge for analytical measurements. The foil was prepared using a FEI Helios 600 dual-beam FIB at the University Paul Cézanne, Marseille. The initial lift-out was done with 30 keV Ga ions. While sampling, the energy of the ions was decreased progressively up to 2 keV to minimise defects induced by the preparation method.

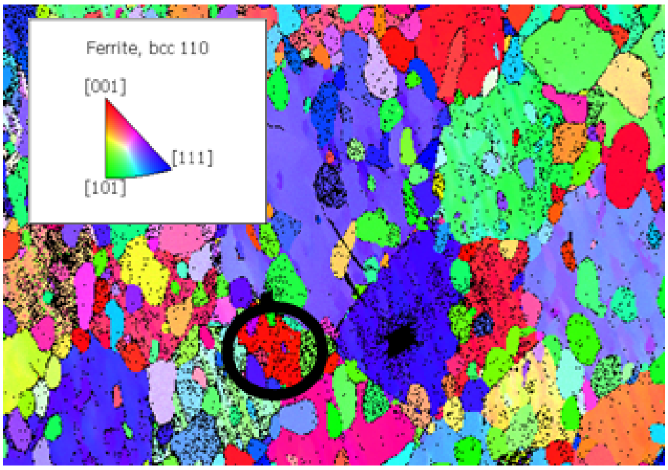

Figure 3.18: EBSD orientation map of the grains in Fe10%Cr disc irradiated to 45 dpa, with 58 appm He/dpa. The black circle shows the selected grain on the (001) orientation.

3.4.3 3D Atom probe tomography

APT experiment was performed as a complimentary analytical tool to EDS for quantitatively studying Cr segregation/depletion behaviour at the dislocation loops. Intermediate dose dual beam irradiated (45 dpa, 58 appm He/dpa) Fe10%Cr was analysed in this case. In this section, firstly we describe the basics of the technique, then the experimental conditions and the details of atom probe data analysis is given.

The basic principle of this technique is based on the field evaporation of atoms within a needle-shaped specimen [142]. The evaporation field, typically 30 - 50 V/nm, is provided either by electric or by femto-second laser pulses applied in addition to a standing DC voltage. The field evaporation system is coupled to a time-of-flight (TOF) mass spectrometer equipped with a position sensitive detector[6]. A representation of atom probe tomography technique is shown in figure 3.19.

---

[6] The signal of a single atom is very weak. Due to this reason, the atom signal is converted into an amplified electron signal using an amplifier known as a micro-channel plate. More details about the system instrumentation can be found in [142].

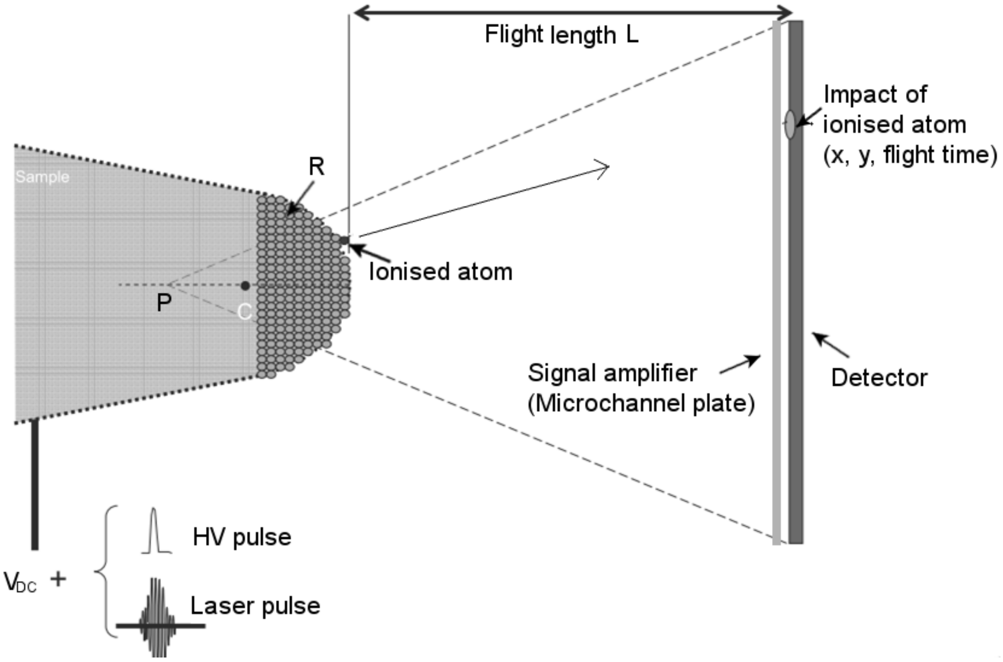

Figure 3.19: Schematic representation of APT system equipped with a position sensitive detector. Figure adapted from [143]. R is the radius of the needle tip, C is the geometric centre of sphere with radius R and P stands for the projection point.

The measurement of the time of flight of evaporated ions allows the mass over charge ratio (m/n) to be known, which hence determines the chemical nature of the species. It is estimated using the energy conservation relation,

$$neV = \frac{1}{2}mv^2$$

where m is the mass of the ion (in a.m.u), v is ion velocity, n is the charge state, e is charge of electron and V is the potential applied to the specimen.

Ion velocity v is measured by knowing the ion flight time t and the flight length L (i.e. sample to detector distance) by the relation $v = \frac{t}{L}$. Thus, the mass to charge ratio can be deduced as

$$\frac{m}{n} = 2eV\frac{t^2}{L^2}$$

The data obtained by the detector is presented as a mass spectrum where for each mass over charge ratio, the related counts of detected events is given. An example of mass spectrum from the intermediate dose dual beam irradiated (45 dpa, 58 appm He/dpa) Fe10%Cr is shown in figure 3.20. Each peak is associated with a particular chemical element. The concentration of each element in the analysed volume (in atomic percent) is then given as $C_x = {}^{N_x}/_{N_t}$, where N_x is the number of atoms of a given element and N_t is the total number of detected atoms in the analysed volume. The uncertainty on the concentration value of a given element is given by the standard deviation:

$$\sigma = \sqrt{\frac{C_x(1-C_x)}{N_t}}$$

However, for some materials, some peaks in the mass spectrum can not be unambiguously assigned to elements because of the overlap of two or more isotopes of different species having same mass-over-charge ratio. For FeCr alloys, it is the case for $54Cr^{2+}$and $54Fe^{2+}$ isotopes. In this case, the natural isotopic abundance of the elements is used to correct the concentration values [142].

3.4.3.1 3D Reconstruction

The position sensitive detectors coupled to the TOF mass spectrometry system records the (X,Y) information of the atoms. Once these positions are known, the co-ordinates of the atoms on the needle surface can be found out using inverse stereographic projection [142], which considers that all the atoms seem to be originating from a fixed projection point P, (denoted in figure 3.19). The magnification, which is dependent on specimen shape, is given by

$$G = \frac{L}{(m+1)R}$$

where L is the ion flight length, R is the specimen end radius - which is related to the voltage and electric field by the relation $R = \frac{V}{E\beta}$,where β is the specimen shape related factor; m is the compression factor, E is the evaporation field. The value of $m+1$ is empirically taken as 1.45.

Once magnification G is determined, the co-ordinates of atoms on specimen surface can be deduced using the relations

$$x = \frac{X}{G}$$

and

$$y = \frac{Y}{G}$$

The third dimension z, which corresponds to the depth, is obtained from the total number of evaporated atoms. For each detected atom, the analysed depth is incremented by $\triangle z = \frac{G^2 V_{at.}}{QS}$, where V_{at} is the atomic volume; Q is the detection efficiency of an atom probe and S is the detector surface area. As the depth investigation of the material proceeds, an atom-by-atom reconstruction of the analysed volume can be undertaken which allows us to have a 3D visualisation of the specimen.

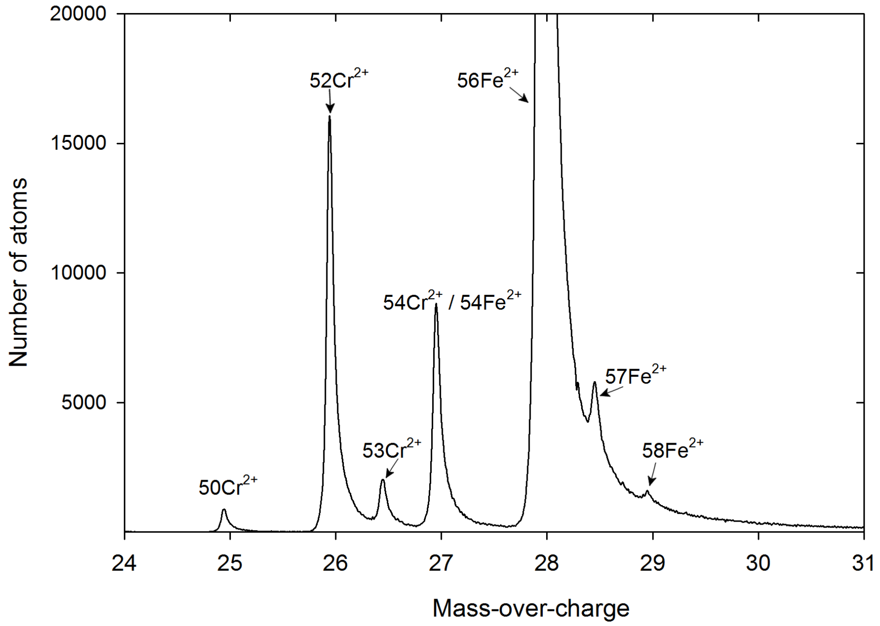

Figure 3.20: Mass spectrum of Fe10%Cr irradiated at 500 ℃ to 45 dpa, 58 appm He/dpa. Analysis was performed using laser assisted wide angle tomographic atom probe (LaWATAP).

3.4.3.2 Experimental conditions

In our case, the experiment on dual beam irradiated Fe10%Cr was performed with a laser-assisted wide-angle tomographic atom probe (LaWATAP), developed by CAMECA, at the University of Rouen. It uses femto-second laser pulses to cause field evaporation and is equipped with a position sensitive advanced delay line detector (aDLD), which minimises the loss of information due to impact superposition [144]. The surface area of the detector is 0.004656 m^2. The detection efficiency of LaWATAP is 60%. An ultraviolet laser beam of 343 nm wavelength was used during the experiment, with a pulse repetition rate of 100 kHz and a power set up of the laser representing 20% of the standing potential. During the experiment, a high vacuum, 10^{-9} to 10^{-10} Pa was maintained.

Since the evaporation field of Cr is lower than that of Fe [142], the experimental conditions must be optimised to obtain accurate measurements, especially for chemical compositions. Thus, the specimen was cooled down to 40 K, to avoid artefacts due to preferential evaporation of Cr atoms. More details about atom probe artefacts can be found in [142].

3.4.3.3 Data treatment

After the atom probe experiment, the analysis of the data recorded by the detector is necessary to obtain quantitative information about the compositional changes, clustering, segregation etc., which may have happened during the irradiation. This data treatment was performed using the standard tools available for the atom probe characterization developed at the University of Rouen. The main option of the tool utilized for the analysis is briefly discussed below:

Identification of clusters As we mentioned earlier, the aim of this experiment was to see segregation/depletion of Cr on the dislocation loops. In case if excess Cr is present on the loops, these enriched areas which can be called as clusters, should necessarily be distinguished from the rest of the matrix. In the current work, we have used the algorithm of identification of clusters based on sphere of maximum radius R_{max} [143]. In this algorithm, a user defined threshold concentration C_{min} is chosen. Then a sphere of radius R_{max} is centered on each atom in the analysed volume and the concentration C_s of the solute atoms is estimated. If $C_s > C_{min}$, this atom is considered as belonging to the cluster. Else, it is labelled as a matrix atom. Furthermore, if the atoms considered as cluster atoms are situated closer than R_{max}, they are considered as atoms of the same cluster size. Else they belong to different clusters. A minimum number of atoms is also defined for a cluster. For groups of atoms that contain less than this fixed minimum value, they are removed from the cluster.

In this algorithm, the choice of the threshold concentration for clusters C_{min} is critical. If it is too low, then even the matrix atoms may be considered to be belonging to clusters. On the other hand, if it is too high, then real clusters may be undetected. In our case, this threshold was set at 13 at.%, because the matrix concentration is ~10% Cr. This value is then estimated around each atom, within a 1 nm diameter sampling sphere. Thus, the sampling volume is adapted accordingly for the Cr enrichment measurement within the clustered zones.

The error bars on the concentration measurement are given in the analysis. It corresponds to a statistical error estimated from the number of atoms included within the sampling volume, which is directly provided by the characterization software.

3.5 Cluster dynamics modelling by CRESCENDO

A part of void swelling results obtained in bcc Fe irradiated to high dose are discussed by performing simulations using CRESCENDO. It is a cluster dynamics model based on mean field approach, developed at SRMP/CEA-Saclay and EDF R&D [145]. It aims at simulating the evolution of defect clusters formed under irradiation up to large doses, which are difficult to be reached with the other simulation techniques like Monte-Carlo. For instance, the end-of-life doses of the structural materials in the nuclear power plants could be reached. In this code, the clustering of defects is considered to take place in an effective environment where all the physical microstructural heterogeneities in a material are homogenised. This means there is no spatial correlation between the studied objects like defect-clusters, dislocations, grain boundaries etc.

Defect-clusters are defined by their size and composition. It can contain only interstitials, only vacancies, and interstitial-He/vacancy-He complexes. The model, then allows to observe the evolution of these clusters as a function of irradiation time by solving a system of ordinary coupled differential equations. A detailed description of the model can be found in [145, 146].

In our case, CRESCENDO was utilised only for the study concerning the effect of injected ions on void swelling. We have not considered the presence of He. The calculations were performed in a homogeneous system with spatial discretization along one direction. The details are given in the next sub-sections.

3.5.1 Master equation for a homogeneous system

The simulation method consists of solving a system of coupled differential equations on the number density of clusters C_j, where j is the cluster type defined by the number of elementary components which constitute the cluster, such as interstitials, vacancies, and solute or gas atoms. A general form comes from a master equation, written as

$$\frac{dC_j}{dt} = \sum_{i \in \mu_b} J_{j-i,j} - \sum_{i \in \mu_b} J_{j,j+i} \tag{3.5.1}$$

where μ_b is the set of mobile species. C_j is the concentration of the cluster of class j. In this equation, j is immobile and i is mobile. $J_{j,j+i}$ is the flux of defects from class j towards the class $j+1$ and is given as

$$J_{j,j+i} = \beta_{j,i} C_j C_i - \alpha_{j+i,i} C_{j+i} \tag{3.5.2}$$

Under steady-state conditions equation 3.5.2 will be equal to zero, $\beta_{j,i}$ is the absorption rate of a defect i by a cluster of concentration j, by assuming that j is not mobile. It is given as

$$\beta_{j,i} = 4\pi D_i Z_{j,i} \left(r_j + r_i + d_{j,i} \right) \tag{3.5.3}$$

where D_i is the diffusion coefficient of cluster i, r_i and r_j are the effective radius of the clusters, $d_{j,i}$ is a reaction distance and $Z_{j,i}$ is an efficiency factor which accounts for the geometrical shape of the clusters and for elastic effects.

$\alpha_{j+i,i}$ is the emission rate and it is deduced from the steady-state condition $J_{j,j+i} = 0$. By applying this condition, the emission rate can be written as

$$\alpha_{j+i,i} = \frac{\beta_{j,i}}{V_{at}} exp(-\frac{E^b_{j+i,i}}{k_B T}) \tag{3.5.4}$$

where V_{at} is the atomic volume, $E^b_{j+i,i}$ is the binding energy of cluster i to cluster j, k_B is the Boltzmann constant.

However, isolated point-defects and their clusters are also produced directly in the cascades. For this reason, the production rate of clusters of class j, denoted as G_j (also known as source term) is added. The clusters created in the cascades are distinguished from the other types: if no clusters are formed in cascade, the source term is zero. In our case, it is assumed that only mono-interstitials and mono-vacancies are formed during irradiation. Furthermore, if cluster j is mobile, it would eliminate on sinks like grain boundaries, dislocations, surfaces etc. Thus, their elimination rate on fixed sinks $-K_j$ is also added to the master equation. Lastly, mobile clusters can also be trapped by all the other clusters (which may be mobile or immobile). If all these terms are added to equation 3.5.1, then it becomes:

$$\frac{dC_j}{dt} = \sum_{i\in\mu_b} J_{j-i,j} - \sum_{i\in\mu_b} J_{j,j+i} - \sum_{a\in\Omega} J_{a,a+j} - K_j + G_j \tag{3.5.5}$$

where Ω is the set of all the clusters mobile or immobile.

The solution of equation 3.5.1, depends on the cluster size considered to be mobile. In our case, for a simplified approach, it was considered that only mono-interstitials and mono-vacancies are mobile. In that case, the master equation can be written as

$$\frac{dC_j}{dt} = \sum_{i\in\{-1,1\}} J_{j-i,j} - \sum_{i\in\{-1,1\}} J_{j,j+i} \tag{3.5.6}$$

By convention, $i = 1$ is taken for interstitials and $i = -1$ is taken for vacancies. Thus, from the above equation, it is evident that the fluxes involve two terms: one for vacancy and other for interstitials. They can be written as

$$\sum_{i\in\{-1,1\}} J_{j-i,j} = J_{j-1,j} + J_{j+1,j} \tag{3.5.7}$$

$$\sum_{i\in\{-1,1\}} J_{j,j+i} = J_{j,j+1} + J_{j,j-1} \tag{3.5.8}$$

Physically these terms imply a net contribution to a cluster of class j by other clusters of class $j+1$ and $j-1$. Then, using equation 3.5.2, the individual fluxes can be written as

$$J_{j-1,j} = \beta_{j-1,1}C_{j-1}C_1 - \alpha_{j,1}C_j \tag{3.5.9}$$

$$J_{j+1,j} = \beta_{j+1,-1}C_{j+1}C_{-1} - \alpha_{j,-1}C_j \tag{3.5.10}$$

$$J_{j,j+1} = \beta_{j,1}C_jC_1 - \alpha_{j+1,1}C_{j+1} \tag{3.5.11}$$

$$J_{j,j-1} = \beta_{j,-1}C_jC_{-1} - \alpha_{j-1,-1}C_{j-1} \tag{3.5.12}$$

For a better understanding, these terms are pictorially represented in figure 3.21, which explains the evolution of a cluster of class j, by assuming that only mono-interstitials and mono-vacancies are mobile,

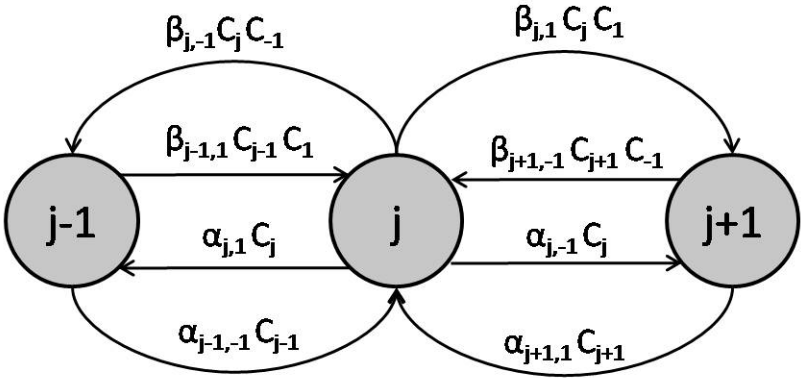

Figure 3.21: Schematic representation of all the flux terms describing the evolution of a cluster of class j, by assuming that only mono-interstitials and mono-vacancies are mobile.

3.5.2 Continuous mode of calculation

The rate equations in the previous sub-section are solved at discrete steps in terms of cluster size using numerical methods. However, the maximum size of the cluster that can be considered is limited by the number of differential equations. It is because if we wait till the clusters evolve to sizes where they become visible, for example, by TEM, the number of equations to solve becomes huge. Thus, to reduce the number of equations and hence the computation time, equations governing the concentration of clusters till second order are used. In this case, the evolution of the cluster is controlled by a Fokker - Planck type equation, in which the cluster concentration is made dependent of a continuous variable x, as shown below

$$\frac{dC(x)}{dt} = \frac{\partial}{\partial x}[f(x)C(x)] + \frac{\partial^2}{\partial x^2}[d(x)C(x)] \tag{3.5.13}$$

where $C(x)$ is the concentration, $f(x)$ and $d(x)$ are functions of absorption rate $\beta(x)$ and emission rate $\alpha(x)$.

3.5.3 Spatial Discretization

In the simplest case, cluster dynamics equations are ordinary coupled differential equations, in which the microstructure of the simulated material is considered homogeneous. However, for ion irradiations, the damage is not homogeneous along the target depth. Same applies for irradiations on thin foils where the effect of free surfaces can be very important. To solve this problem, one-dimensional spatial dependency of the rate equations is used. In this approximation, the specimen thickness is divided into slices considered to be locally homogeneous. Within each slice, the rate equations are solved with mean-field formalism. But in these rate equations, a diffusion term is added which takes care of the interaction between the two adjacent layers through the mobile clusters which can diffuse between the layers. In this way, the entire non-homogeneous depth distribution of defect clusters can be simulated for irradiations by ions or in thin foils. As suggested by Jourdan and co-workers [146], the partial differential equations

(PDE) for a mobile cluster to solve over the specimen thickness t_{foil} is given as

$$\frac{\partial C_i}{\partial t} = R_{homo,i}\left(z, \tilde{C}(z,t)\right) - \frac{\partial \phi_i(z,t)}{\partial z} \tag{3.5.14}$$

and

$$\phi_i(z,t) = -D_i(z)\frac{\partial C_i(z,t)}{\partial z} \tag{3.5.15}$$

where C_i is the concentration of the mobile species i which is a part of the vector of concentrations $\tilde{C}$, D_i is the local diffusion coefficient, $\phi_i(z,t)$ is the diffusion flux and $R_{homo,i}$ is the master equation (equation 3.5.1).

This PDE system is solved on a non-uniform grid. The grid points are indexed from k = 1 to k = N_{grid} and the distance between two grid points z_k and z_{k+1} is h_k. The formulation is depicted in figure 3.22.

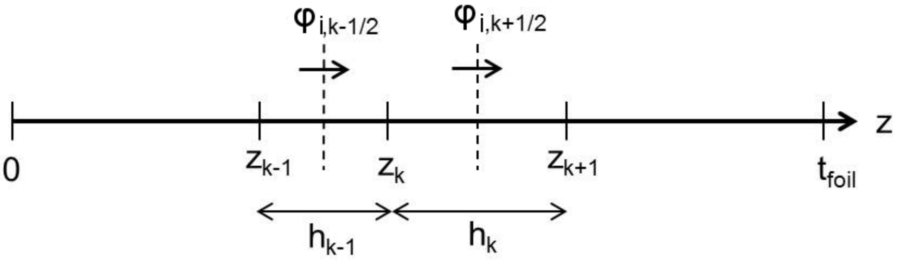

Figure 3.22: Schematics showing the spatial grid for incorporating spatial dependency of cluster dynamics equations. Notations are explained in the text. Adapted from [146].

By dropping the dependence on t, the equation for a given species in a slice k can be written as

$$\frac{\partial C_{i,k}}{\partial t} = R_{homo,i,k}\left(\tilde{C}_k\right) - 2\frac{\phi_{i,k+1/2} - \phi_{i,k-1/2}}{h_{k-1} + h_{k+1}} \tag{3.5.16}$$

$$J_{d,k+1/2} = -D_{i,k+1/2}\frac{C_{i,k+1} - C_{i,k}}{h_k} \tag{3.5.17}$$

$$= -\frac{1}{2}(D_{i,k+1} + D_{i,k})\frac{C_{i,k+1} - C_{i,k}}{h_k}$$

and

$$\phi_{i,k-1/2} = \phi_{i,(k-1)+1/2} \tag{3.5.18}$$

In our case, the specimen thickness was taken as 5 μm and was divided into 40 slices.

Chapter 4

Irradiated microstructure at high dose

In this chapter, the experimental results on the evolved microstructure after single and dual beam high dose irradiations at 500 ºC are presented. The irradiation conditions in terms of the depth variation of the damage in dpa and He implantation profile obtained from SRIM-2008 is shown in figure 4.1. The implantation profile of the self-ions used as a source of ballistic damage is also shown in the same figure. The maximum dose at the damage peak was 157 dpa . For the dual beam case, He was co-implanted to 17 appm He/dpa at the damage peak.

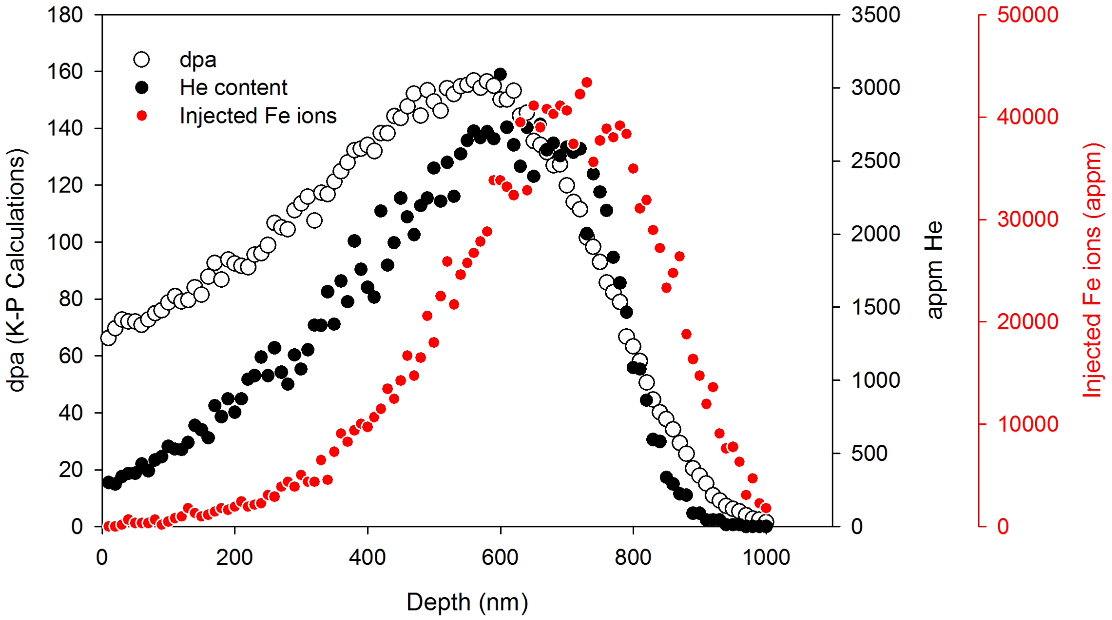

Figure 4.1: Depth profile of the displacement damage in dpa (Kinchin-Pease calculations), He implantation profile and the injected Fe ion implantation profile for the high dose irradiations. The damage at the peak was 157 dpa and He implantation was 17 appm He/dpa at the damage peak. The irradiations were performed at JANNuS ex-situ irradiation facility at CEA/Saclay.

In the first section, the results on bcc Fe irradiated in single and dual beam mode is presented. It revealed the role of He on void swelling. Then, the cavity microstructure in FeCr alloys and its comparison with bcc Fe is presented to see the influence of Cr on void swelling. As discussed in chapter

2, “Bibliography”, section 2.5.2.3, this trend is still not clear from the fast neutron irradiated studies on FeCr alloys performed in last three decades. Moreover, no dedicated well controlled ion irradiation results exist which have thoroughly probed this effect. An analysis of the depth distribution of cavities and heterogeneous cavity nucleation in FeCr alloys is also shown in this section. Thereafter, the dislocation loop microstructure is briefly detailed. In all these cases, the microstructure was studied by conventional TEM on FIB specimens.

4.1 Cavity microstructure in bcc Fe - effect of He

In this study, bcc Fe irradiated in single beam mode (no He) and dual beam mode (co-implanted He) were analysed to understand the influence of He on the cavity microstructure. Cavities were observed for both the irradiation conditions. Their distribution was homogeneous. TEM image of the irradiated zone, taken on (001) zone axis, is shown in figure 4.2. Most of the cavities were cubic in shape with facets aligned along <100> direction. An interesting thing to notice from figure 4.2 is that cavities look much larger in size when He is not co-implanted. Such a behaviour was seen to have important consequence on void swelling, which is detailed in this section.

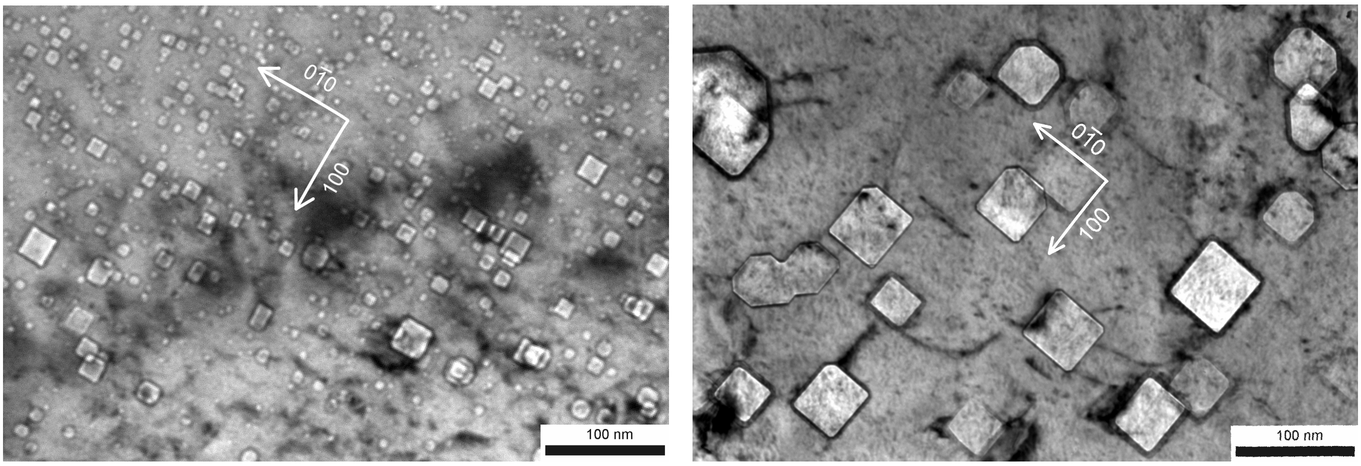

(a) (b)

Figure 4.2: Cavities in irradiated bcc Fe after irradiation at 500 ºC to 157 dpa. (a) He co-implanted to 17 appm He/dpa at the damage peak and (b) without He. Imaging performed on (001) zone axis (BF, under-focus = -1136 nm).

The entire depth distribution of cavities was studied for the two irradiation experiments to understand the influence of He on void swelling. The corresponding TEM images are shown in figure 4.3. Quantitative information on void swelling, cavity size and number density variation, extracted from the TEM images, is shown in figure 4.4 and 4.5 respectively. These figures denote a denuded zone up to ~100 nm below the irradiated surface for both the irradiation conditions. Beyond that, the addition of He was seen to reduce cavity size and increase their number density drastically (see figure 4.5). This induced a very strong reduction of void swelling upon He co-implantation all along the damage depth (figure 4.4) . For instance, in the zone between 300 - 400 nm, void swelling was estimated to be 8.5 % for the single beam case, which tumbled to only ~1% when He was co-implanted. In this case, the average cavity size was 67 nm for the former and 6.8 nm for the later, with almost two orders of magnitude higher number density. Maximum difference of swelling in the two cases was noted for the regions between 200 - 300 nm. Both average size and void swelling gradually tapered off at larger depths, but stayed always higher for the single beam case.

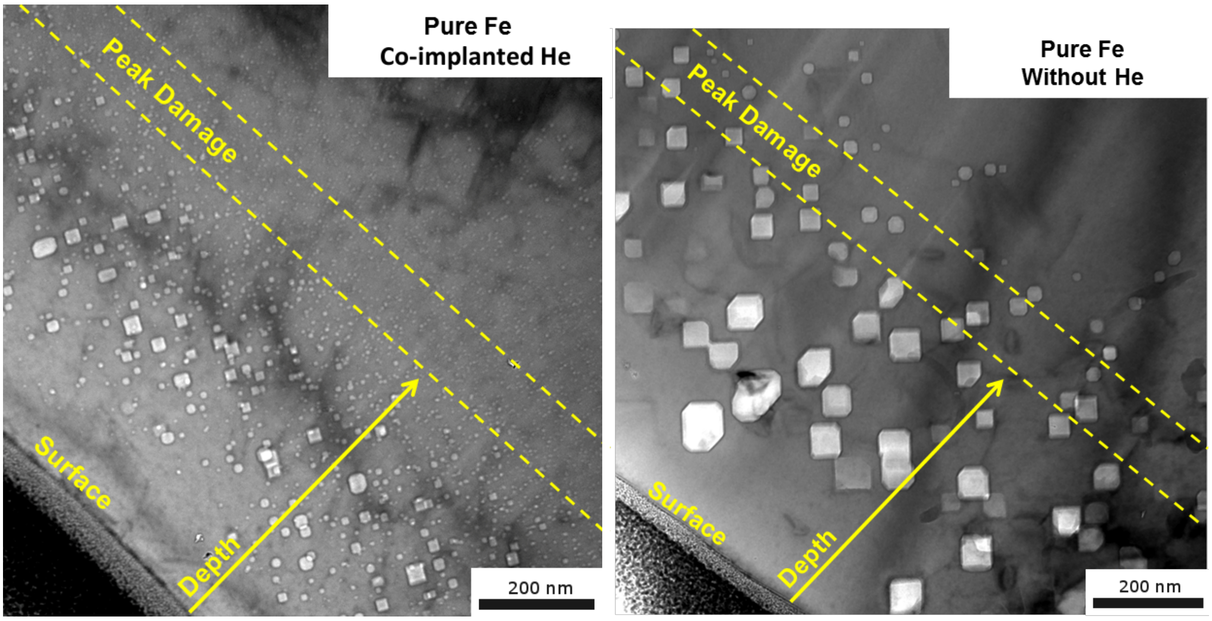

(a) (b)

Figure 4.3: TEM images of the depth distribution of cavities in irradiated bcc Fe. (a) Cavity microstructure when He was co-implanted and (b) when He was not present. (BF, $s_g >> 0$, under focus = -1136 nm).

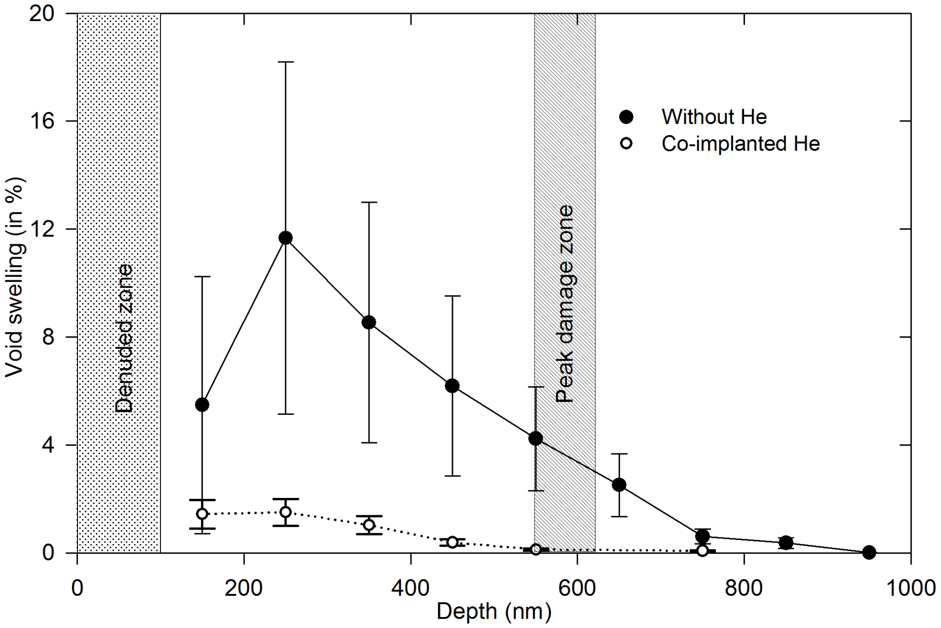

Figure 4.4: Comparison of depth distribution of void swelling in bcc Fe irradiated without and with co-implantation of He.

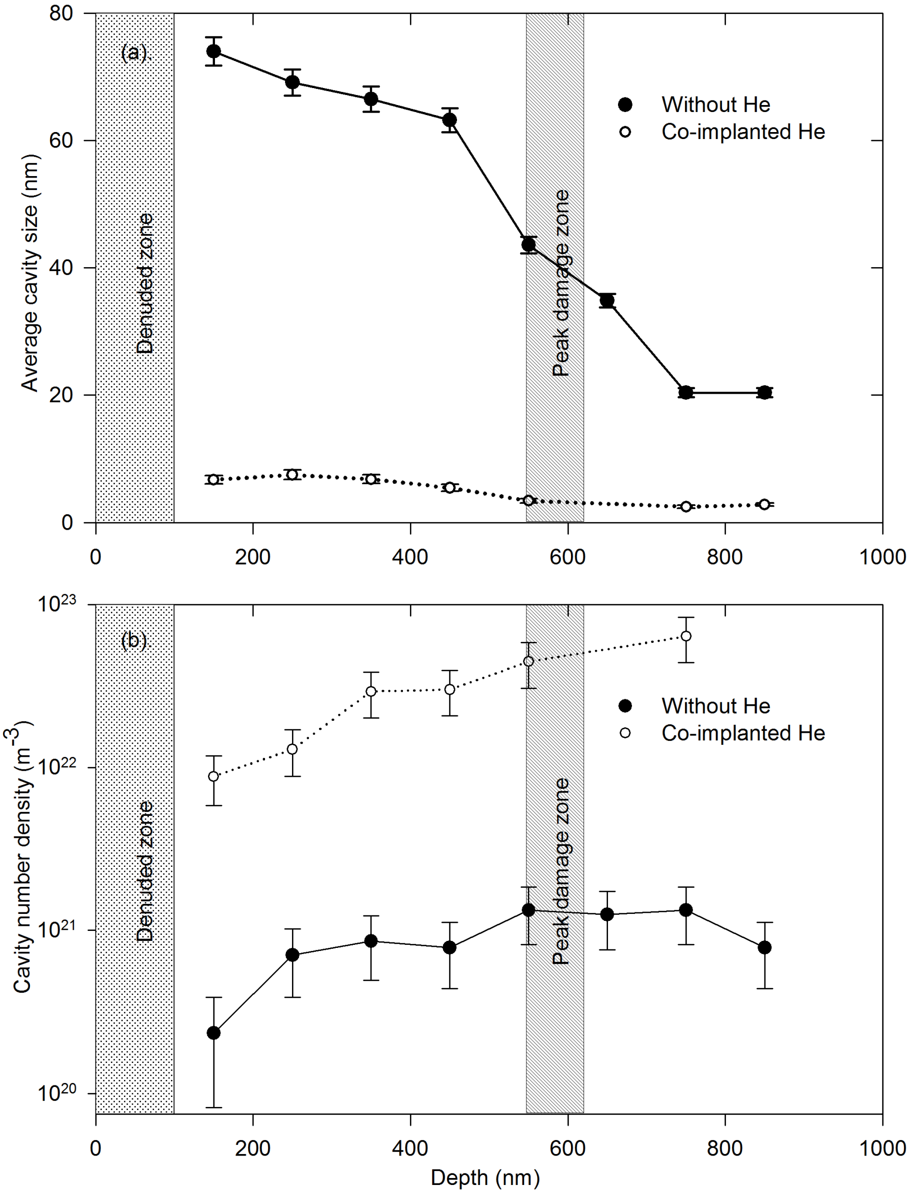

Figure 4.5: Average size and number density of cavities in bcc Fe irradiated without and with co-implantation of He

To understand better the microstructure at each depth, a histogram of cavity size is presented in figure 4.6 for the case with He co-implantation. The corresponding TEM images, taken from a part of the analysed zone, are also attached. They show a broad distribution for the areas 100 - 500 nm below the irradiated surface. Large cavities, more than 20 nm in size, were detected up to 400 nm deep zones. Largest cavity sizes, between 40-50 nm, were observed in zones closer to the surface. Smaller cavities, between 2 - 4 nm, were present in significant proportion all along the specimen depth, which suggests that the nucleation phase of cavities was still not over. The distribution became narrow at larger depths upon approaching the peak damage area around 600 nm. At the damage peak and up to 800 nm, most of the cavities were between 2 - 4 nm in size.

A similar size histogram could not be drawn for the single beam irradiated Fe due to much less statistics of cavities in the FIB foil (owing to lower number density). However, from the TEM image in figure 4.3b, it is clear that the cavity sizes are not vastly different, at least prior to the peak damage area. They all were between 63 - 74 nm up to ~450 nm depth. Similar to the dual beam case, largest voids were detected in zones closer to the surface . However, there was no presence of very small cavities. This indicates that the nucleation phase has terminated and microstructure was controlled by cavity growth.

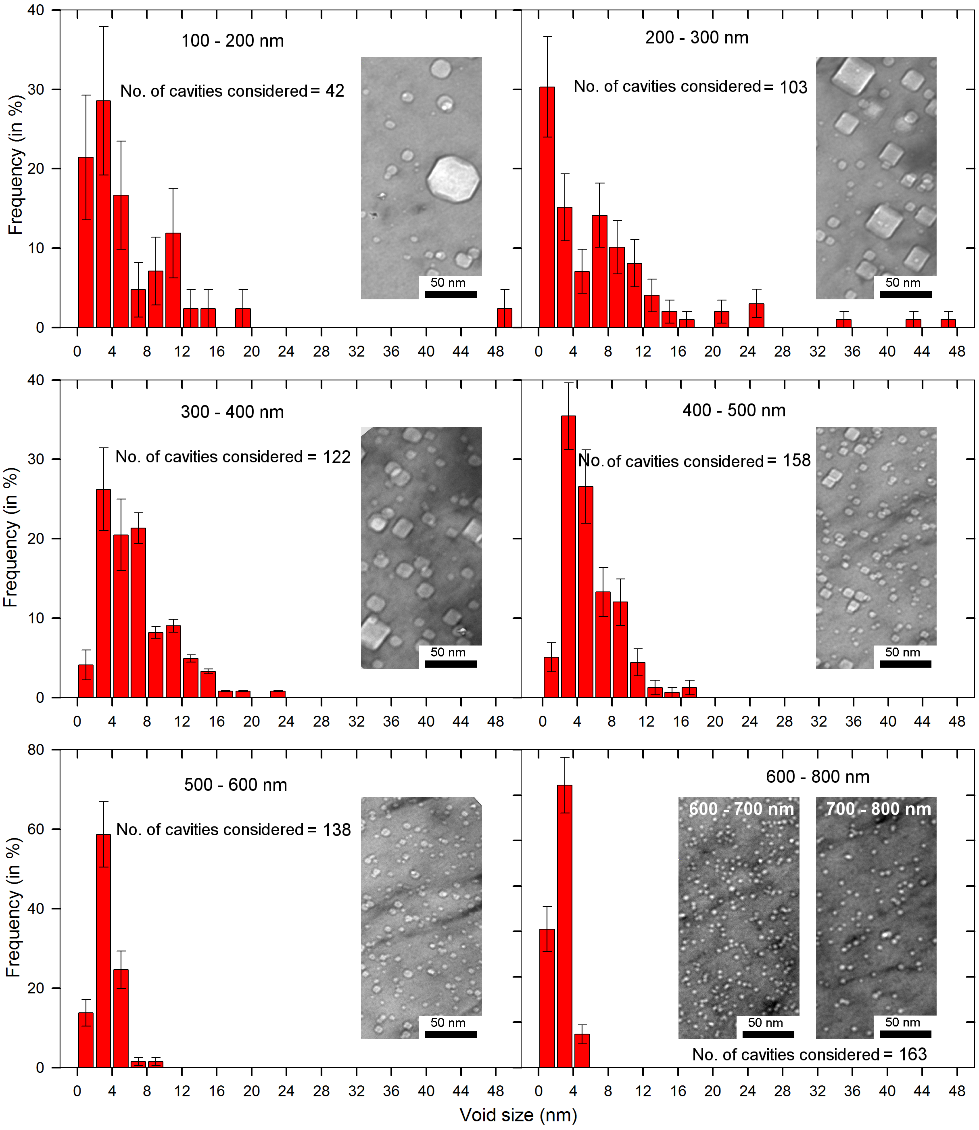

Figure 4.6: Size distribution of cavities in bcc Fe co-implanted with He. TEM images showing cavities in a small part of each analysed zone are also presented. (BF, $s_g >> 0$, under focus = -1136 nm).

It is interesting to note that for both the irradiation conditions, average cavity size and void swelling fell off close to the region around 550 - 600 nm depth where damage was maximum. For the single beam irradiated Fe, swelling at the beginning of this zone was nearly one-third of the value in the intermediate depths. Incidentally, it is also the region where ions injected by the accelerators come to rest in the material. It may be possible that these injected ions could behave as injected interstitial atoms and thereby artificially suppress swelling in this region. This issue of injected ions has been specifically addressed in the discussion of the results.

4.2 Cavity microstructure in FeCr alloys

4.2.1 Effect of Cr on void swelling

Dual Beam Irradiation

Cavities were observed by TEM in both bcc Fe and FeCr alloys. A comparison of the cavity microstructure extracted from a zone 300 - 400 nm below the irradiated surface[1], (corresponding to a damage of 128 dpa at 2.6 x 10^{-3}dpa/s, co-implanted with 13 appm He/dpa), is shown in figure 4.7. It revealed a strong diminution of cavities, and hence, void swelling upon Cr addition to bcc Fe matrix. This was primarily achieved by the reduction in cavity sizes. In Fe, the average cavity size was 6.8 nm. Thereafter, just by the addition of 3% Cr, the average size reduced to 0.9 nm, which did not change significantly at higher Cr levels. A decrease in cavity size was accompanied with an order of magnitude increase in their number density between Fe and the FeCr alloys. In Fe, it was estimated to be 1.32 x 10^{22} m^{-3}, which increased to 4.5 x 10^{23} m^{-3} for Fe3%Cr. In this zone, the distribution was homogeneous.

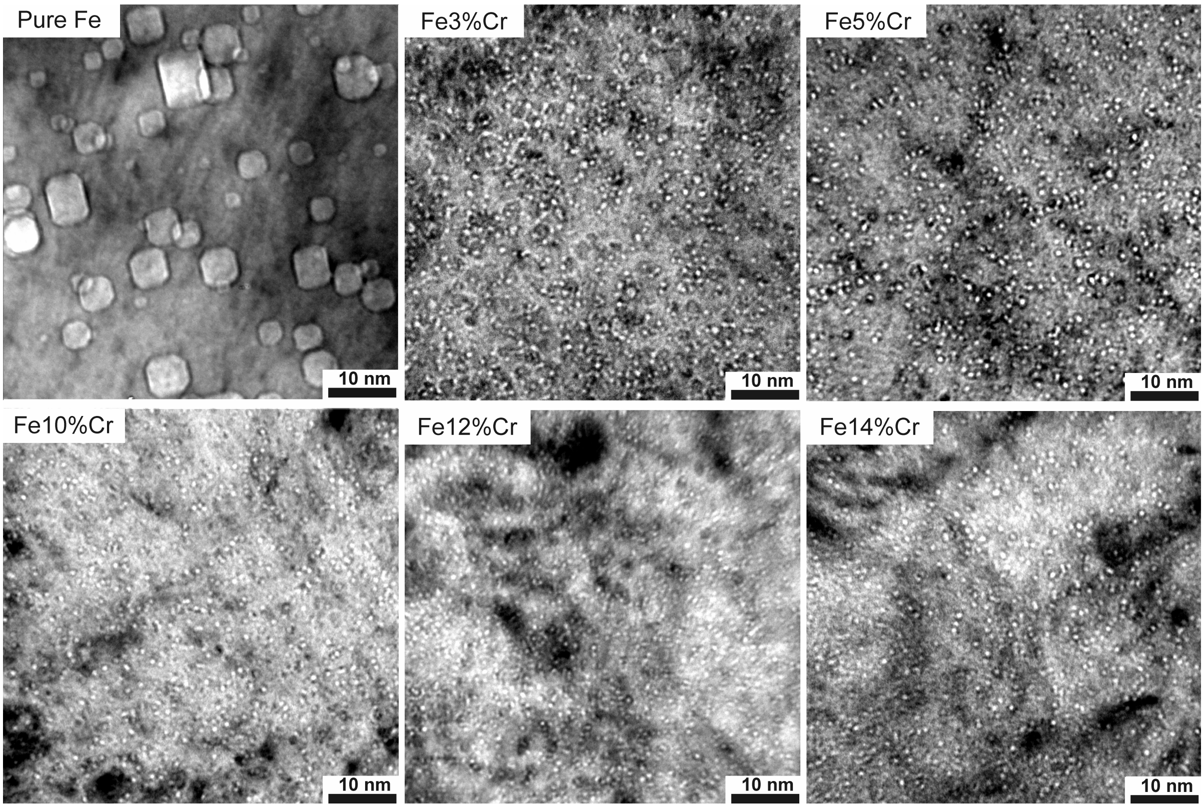

Figure 4.7: TEM images of cavities in irradiated bcc Fe and FeCr alloys at 500 ºC. The images were taken from an area 300 - 400 nm below the irradiated surface, corresponding to 128 dpa (2.6 x 10^{-3} dpa/s), 13 appm He/dpa. (BF, $s_g >> 0$, under-focus = -1136 nm).

A variation of cavity size and number density extracted from this zone of observation is plotted as a function of Cr level in figure 4.8. Based on this, the estimated void swelling is also plotted in the same

---

[1] This intermediate depth was chosen to avoid surface effects and to stay away from the peak-damage area where, as we saw in bcc Fe in section 4.1, a strong reduction in cavity population was noted.

figure. It clearly shows the initial swelling reduction by small Cr addition between 3 - 5%. Thereafter, the variation was non-monotonic with a local swelling maxima peaking around 10% Cr, followed by a reduction at 12% and 14% Cr. This maxima appeared due to higher number density of cavities in Fe10%Cr as compared to the other alloys. In all the cases, the absolute swelling values remained low : between 0.02 to 0.09 % for FeCr alloys and ~1% for Fe. No α' precipitation was observed in any of the alloys[2].

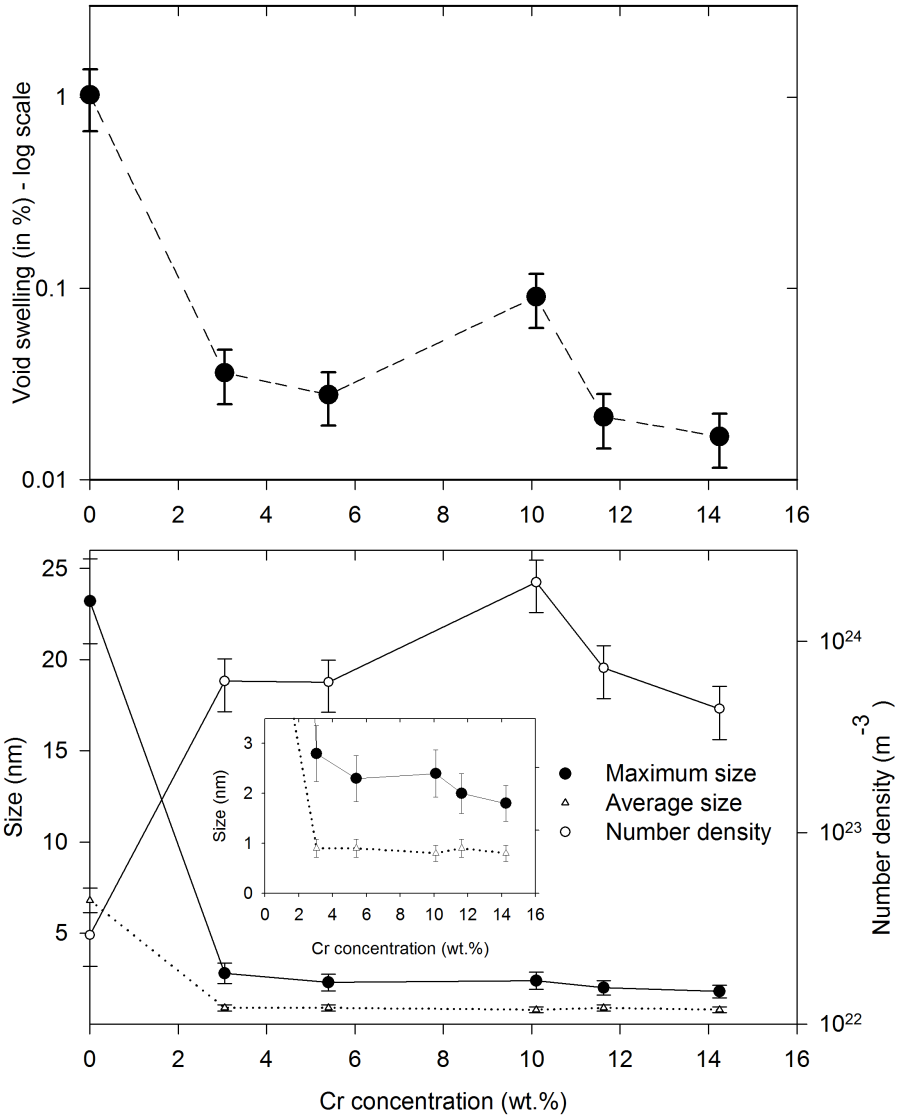

Figure 4.8: Variation of the void swelling, cavity size, and the number density as a function of Cr concentration for dual beam irradiated FeCr alloys and bcc Fe up to 128 dpa, 13 appm He/dpa at 500 ºC. Void swelling varied non-monotonically with Cr concentration. A zoomed graph showing the maximum and average cavity size in FeCr alloys is separately given in the centre of the figure. The maximum cavity size corresponds to the largest cavity observed in the image; while average cavity size corresponds to the mean value calculated using all the measured sizes. We can see that the difference between the maximum and average cavity size is very less for all the FeCr alloys, while the difference is important for bcc Fe.

---

[2] Due to very close atomic number of Cr and Fe, it is difficult to observe Cr-rich α' precipitates by TEM, especially if they are small in size. Hence, it is possible that they are formed but remain undetected.

Single Beam Irradiation

Specimens irradiated without co-implantation of He were also studied to compare the cavity microstructure. In this case no cavities were observed in any FeCr alloys. However, they were indeed seen in Fe as detailed in section 4.1 on page 76. For a zone between 300 - 400 nm depth, swelling in Fe was estimated to be 8.5%. Such a large swelling level dropped to zero upon Cr addition beginning at 3%Cr. An example of the microstructure of two FeCr alloys with maximum and minimum Cr level (Fe3%Cr and Fe14%Cr) is shown alongside bcc Fe in figure 4.9. We can see that voids in Fe. However, none can be seen in the other two materials. This result emphasizes further the extent of swelling diminution by Cr.

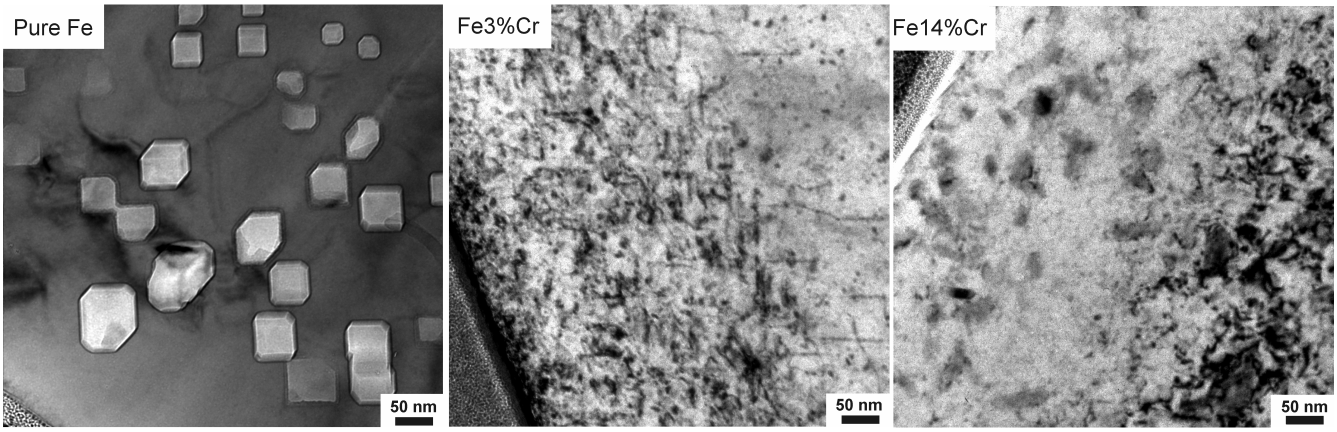

Figure 4.9: Microstructure of pure Fe and Fe(3,14)%Cr after irradiation at 500 ºC to 157 dpa, without He co-implantation. Large voids were present in Fe and none were detected in FeCr alloys. (BF, underfocused = -1136 nm). For Fe3%Cr, imaging was performed close to (001) zone axis not too far from Bragg condition due to which the dislocation forest is also in contrast. In Fe14%Cr, the dark blotches visible in the image are due to specimen contamination. We believe its mainly carbon deposition occurring during the irradiation.

4.2.2 Depth distribution of cavities

Dual beam irradiated FeCr alloys were studied to observe the entire depth distribution of cavities. A thorough quantitative analysis was performed on the Fe14%Cr alloy. Then, a qualitative description is given for the other FeCr alloys. In this study, very different cavity microstructures were noted in areas prior to the damage peak as compared to the zones which are after the damage peak. Thus, the results are presented firstly for the former and then for the later for each material.

Fe14%Cr

Figure 4.10 shows TEM images of cavities taken at different depths beneath the irradiated surface up to the peak damage zone (around 600 nm deep) in Fe14%Cr. The first thing to notice is that there is almost no denuded zone close to the surface (0 - 100 nm), as seen in Fe in section 4.1. However, the number density is small at this depth. It increased upon going deep in the material. No significant change in their size can be seen in the TEM images. All along these areas, the distribution was seen to be homogeneous.

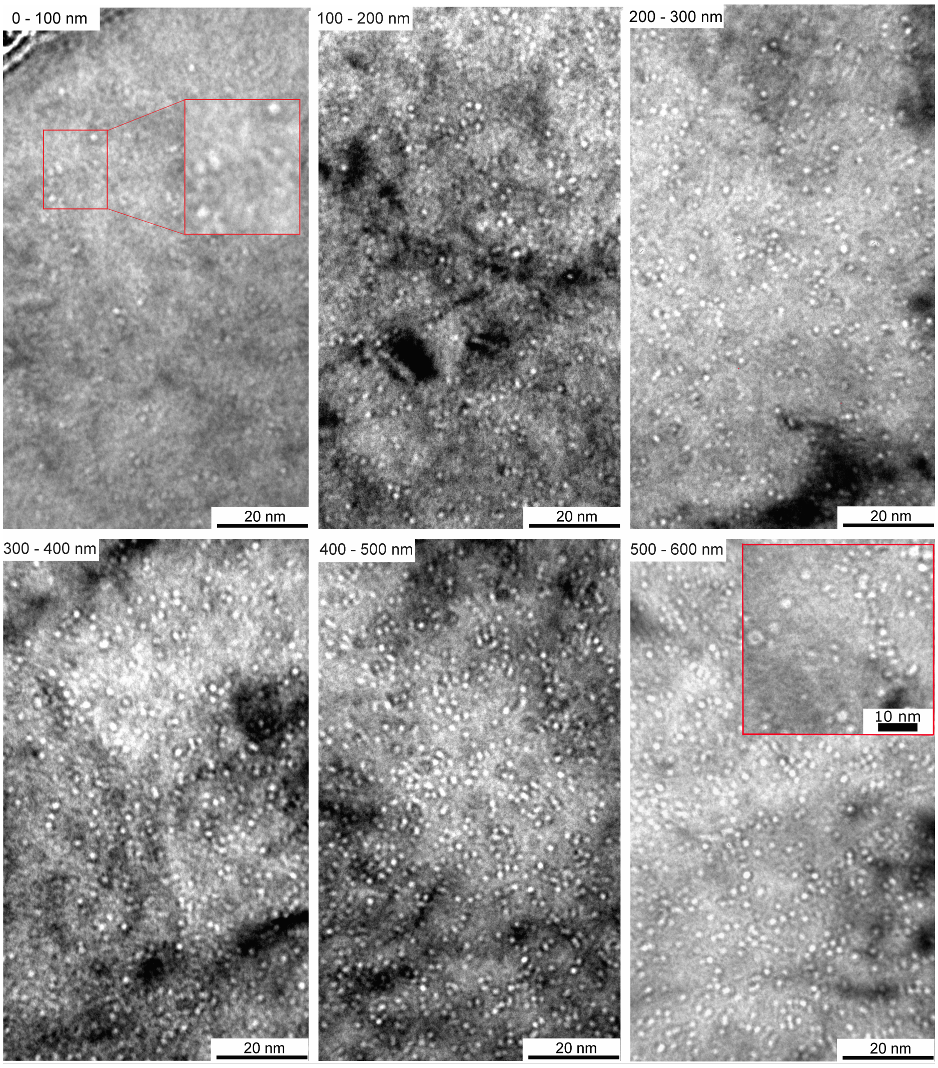

Figure 4.10: Depth distribution of cavity microstructure in Fe14%Cr irradiated at 500 ºC to 157 dpa with 17 appm He/dpa. Areas up to the peak damage (around ~ 600 nm depth) are shown. A few large cavities 4 - 5 nm in size were also observed between 500 - 600 nm depth. They are shown separately in the image at this depth, marked by red boundaries. (BF, $s_g >> 0$, under-focus = -1136 nm).

Quantitative information on cavity sizes and number density estimated from these images is plotted in figure 4.11. It revealed that the number density increase was almost linear up to ~ 450 nm deep areas. Compared to the surface, it was about six times higher at this depth. No significant difference between the maximum, minimum and average size was noticeable. A variation of depth distribution of void swelling is also plotted in figure 4.11. Similar to the number density, it showed an increasing trend prior to the peak damage zone. But the absolute swelling values remained low (less than 0.02%).

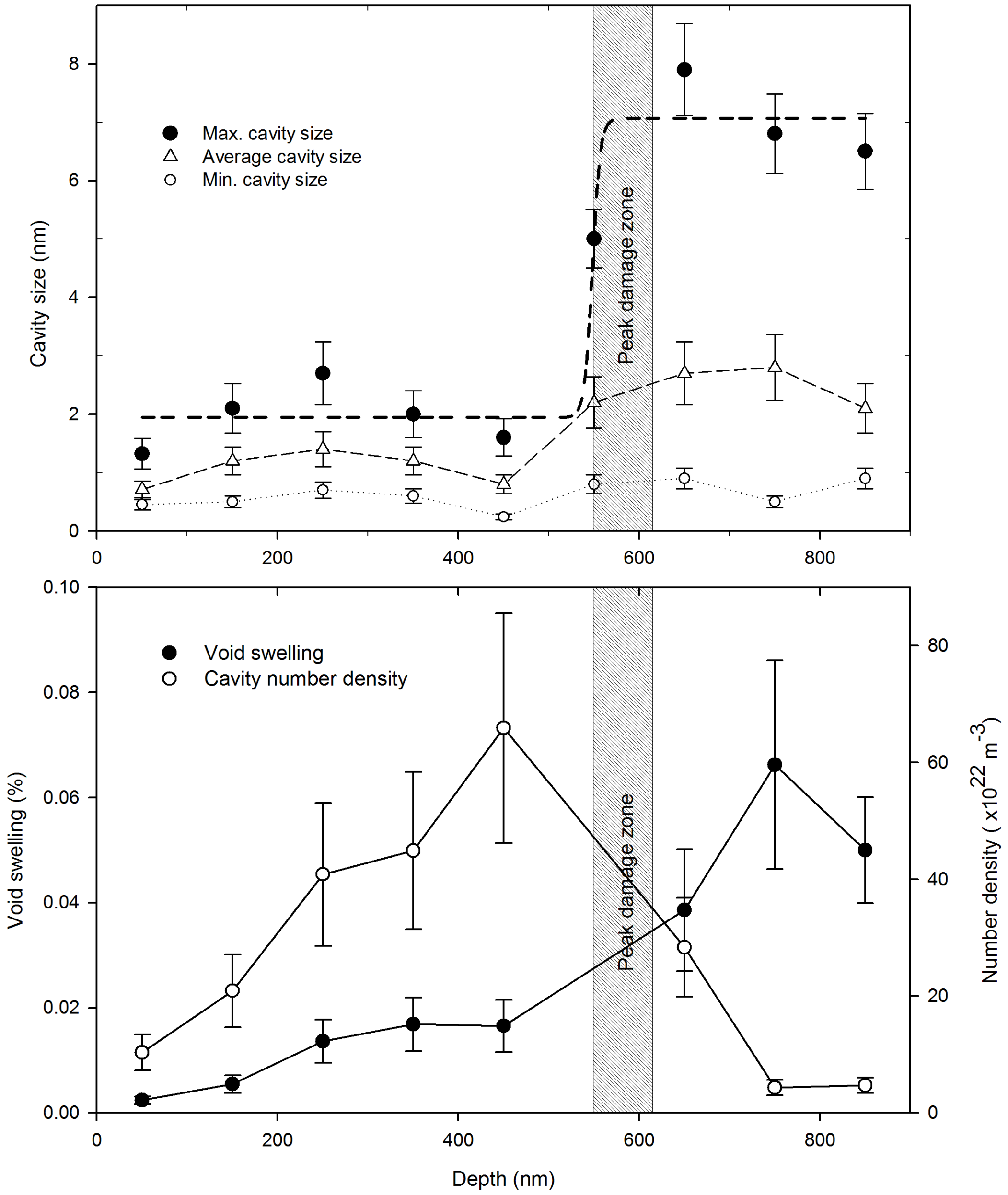

Figure 4.11: Depth variation of cavity sizes, number density and the corresponding void swelling in Fe14%Cr.

Upon reaching the damage peak and the zones beyond, the cavity microstructure changed drastically. The spatial distribution was a mixture of heterogeneously nucleated cavities associated with the dislocation loops, combined with a low density of freely nucleated cavities in the matrix. It is shown in figure 4.12, which was imaged not far from (001) zone axis. In this image, we can see the cavities on the plane of the loops in open configuration, and their linear arrangements on the loops which are on-edge. The freely nucleated cavities in the matrix were always the larger ones with facets. Whereas, those inside the loops seemed to have a rather broad distribution in size. However, no correlation could be inferred in terms of cavity size and its position inside the loop. Quantitative results on depth variation plotted in figure 4.11 shows that in these zones, cavity size increased sharply as compared to the areas prior to damage peak. Such an increase in cavity size is contrary to what was observed in bcc Fe in section 4.1. However, their number density dropped substantially. Void swelling, on the other hand, continued to increase. It followed the same trend as the average cavity size, with a sharp initial increase followed by a slight drop. Rate of swelling increase was faster compared to prior peak damage zones. Another thing to note is that there was a significant difference between the minimum and maximum cavity size, indicating that the distribution in size broadened up.

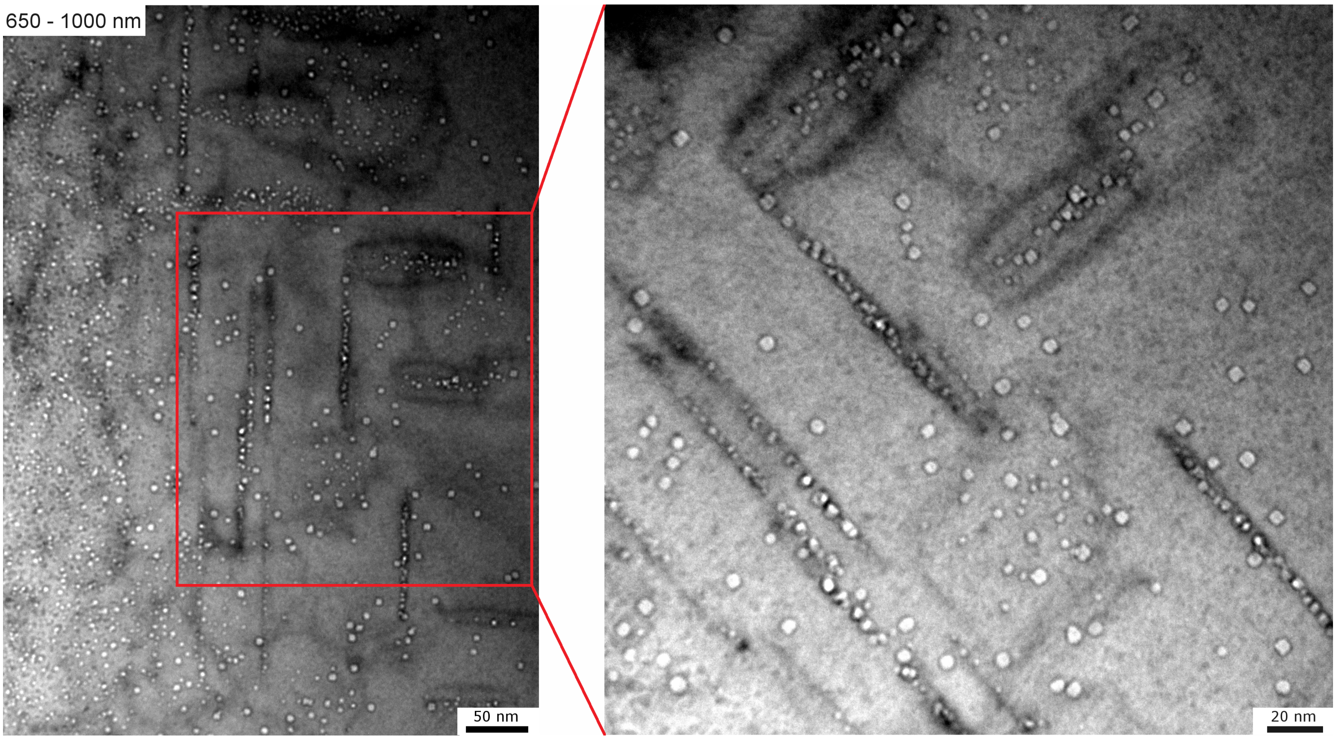

Figure 4.12: Cavity distribution beyond the peak damage area in Fe14%Cr. Imaging was performed not far from (001) zone axis, due to which <100> type loops are slightly in contrast. To see the dislocation loops and the cavities on the same image, out-of-focus imaging was performed not too far from KBF conditions. ($s_g > 0$, under-focus = -930 nm).

To understand better the cavity microstructure, a histogram of cavity sizes was also estimated. It is shown in figure 4.13. It shows a narrow distribution up to ~ 400 nm deep areas. Such a behaviour is also indirectly depicted in figure 4.11 where we can see that there is no important difference between maximum, minimum and average cavity size. The most probable cavity size was close to 2 nm. The distribution began to broaden upon approaching the damage peak region, with average and maximum size of 2 nm and ~8 nm respectively. Beyond that, the distribution was significantly broad due to a wide range of sizes present in the microstructure. As mentioned previously, it is the zone where microstructure comprised of heterogeneously nucleated cavities inside the loops and freely nucleated cavities in the matrix.

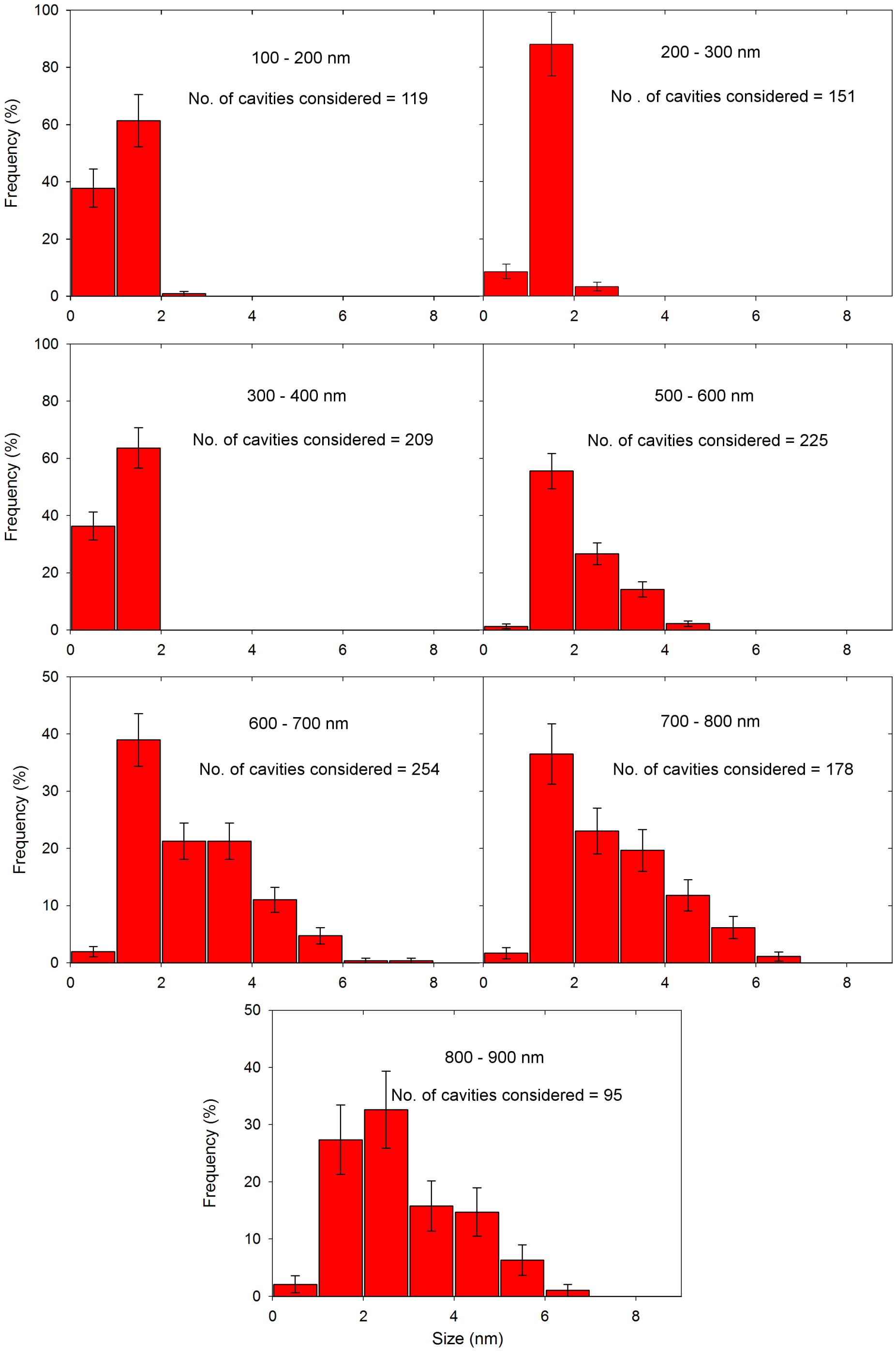

Figure 4.13: Size distribution of cavities, estimated at different depths below the irradiated surface in Fe14%Cr.

Fe(3, 5, 10, 12)%Cr

A qualitative TEM based study was performed on the other FeCr alloys as well. For Fe3%Cr and Fe5%Cr, the entire depth was scanned. However, for Fe10%Cr and Fe12%Cr, only the zones beyond the damage peak were observed. The details are as follows:

For Fe3%Cr and Fe5%Cr, images of cavities taken at various depths below the irradiated surface are shown in figures 4.14 and 4.16 respectively. They revealed very similar evolution of the microstructure as seen previously for Fe14%Cr. It is evident that the number density increased from near surface areas (100 - 200 nm depth) to deeper zones. Cavity size did not seem to vary significantly in areas prior to the damage peak. However, at and beyond the damage peak, it increased, which might be accompanied by a drop in the number density. It is shown in the TEM image of the zone between 600 - 700 nm depth in figures 4.14 and 4.16. Furthermore, similar to Fe14%Cr, the spatial distribution of cavities was homogeneous prior to the damage peak, followed by a mixed distribution beyond (i.e. heterogeneous nucleation inside dislocation loops plus freely nucleated cavities in the matrix). For Fe3%Cr, it can be seen in figure 4.15, where a cluster of cavities is marked in dashed lines. In this case, the dislocation loop in residual contrast is not visible. But from the manner the cluster is present, it is perhaps sufficient to believe that these cavities are nucleated inside a loop. Linear arrangement of cavities, possibly nucleated on a dislocation line, can also be seen above this cavity cluster in the same figure. The zone corresponds to 800 - 1000 nm depth below the irradiated surface. Similar features are depicted in figure 4.17 for Fe5%Cr at 700 - 1000 nm depth..

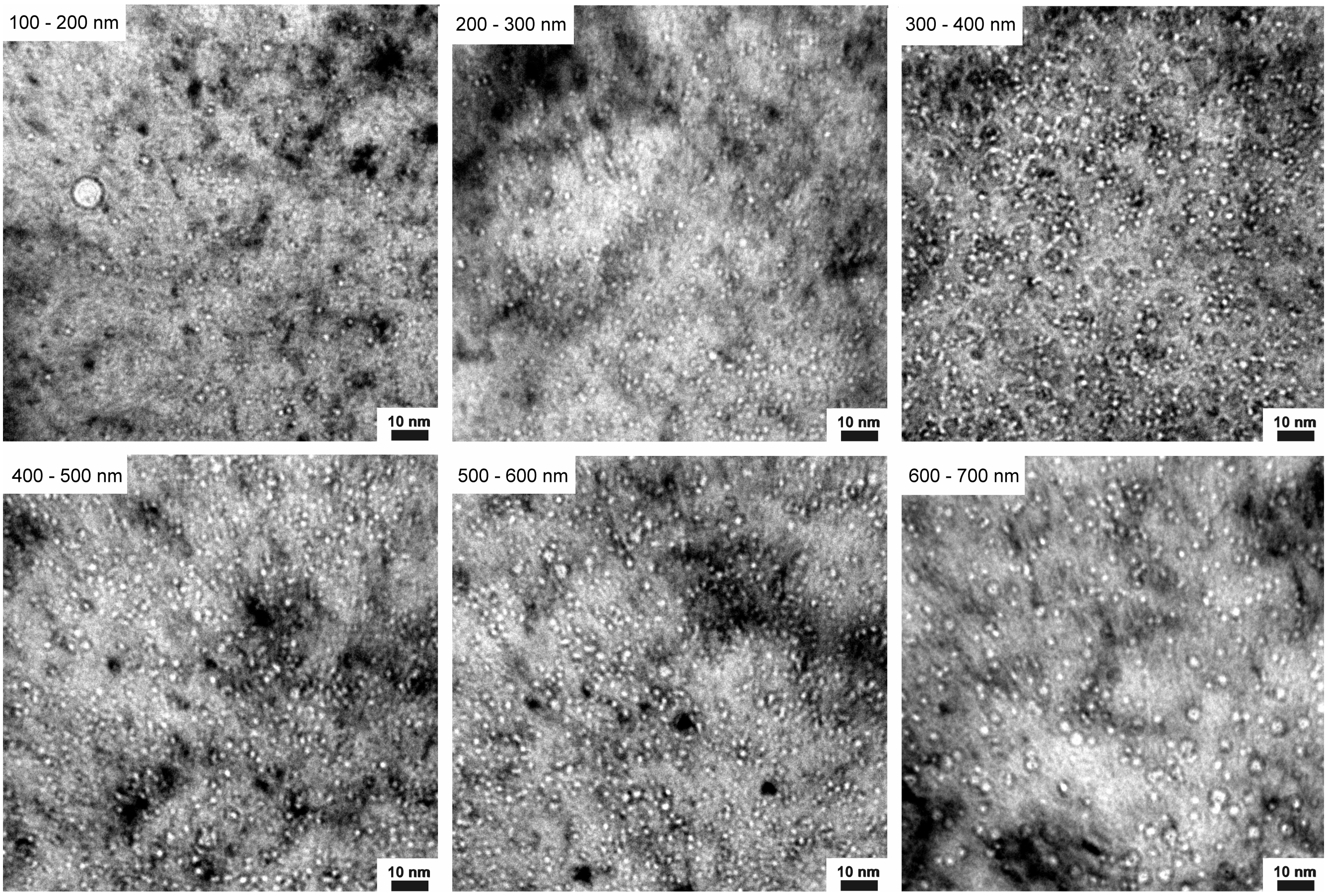

Figure 4.14: Depth distribution of cavity microstructure in Fe3%Cr. (BF, s >> 0, under-focus = -1136 nm)

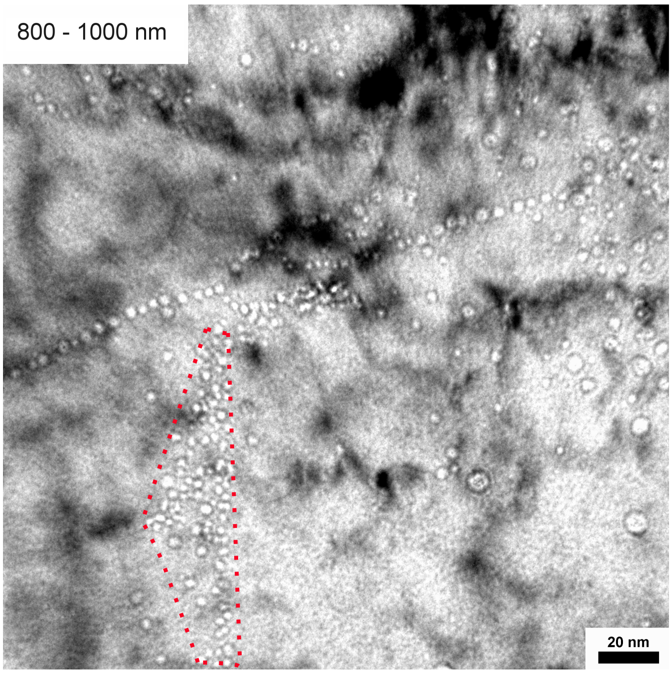

Figure 4.15: Cavity microstructure beyond the damage peak in Fe3%Cr. A cluster of cavities nucleated perhaps inside a dislocation loop is marked by dotted lines. (BF, s_g >> 0, under-focus = -1136 nm)

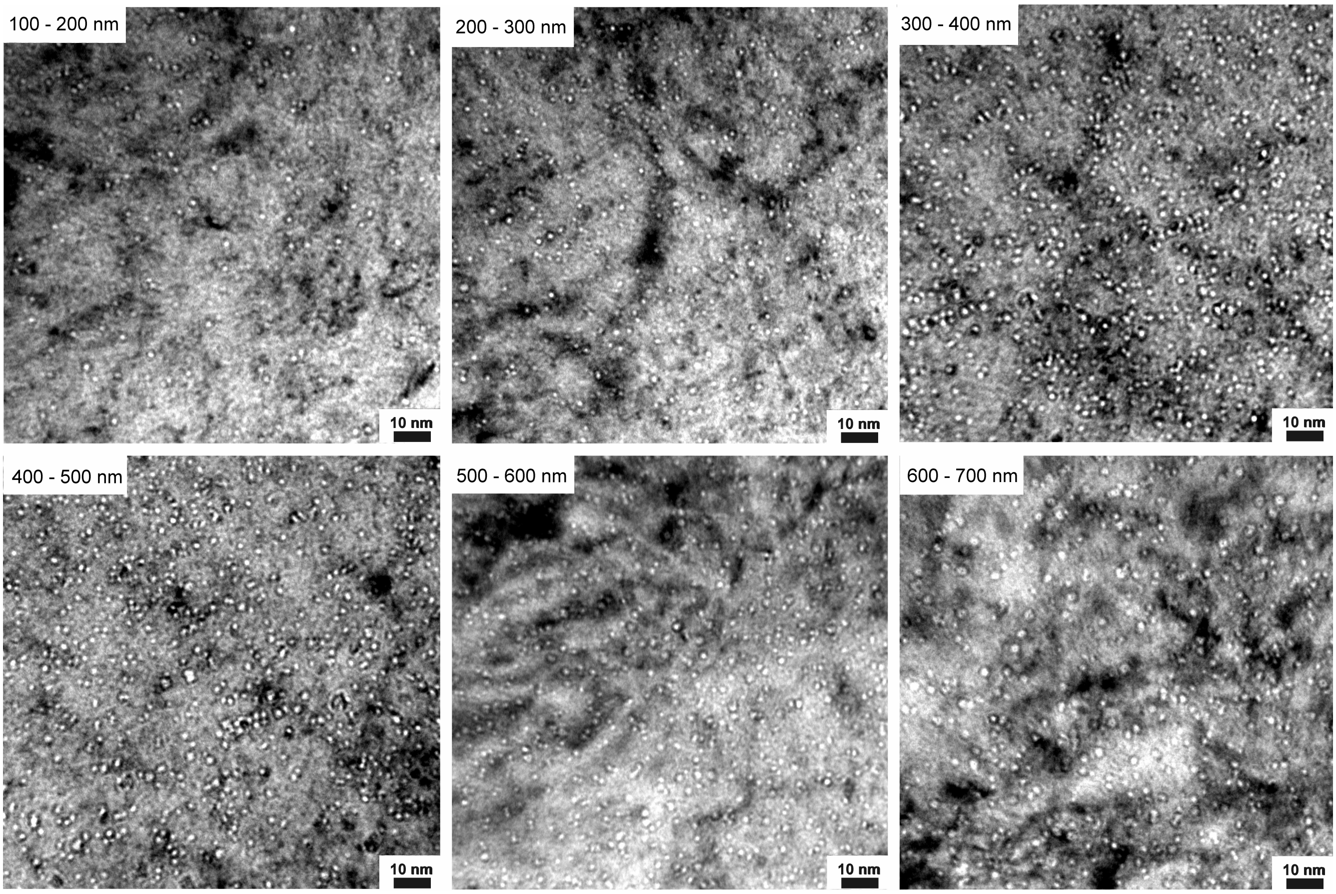

Figure 4.16: Depth distribution of cavity microstructure in Fe5%Cr. (BF, s_g >> 0, under-focus = -1136 nm)

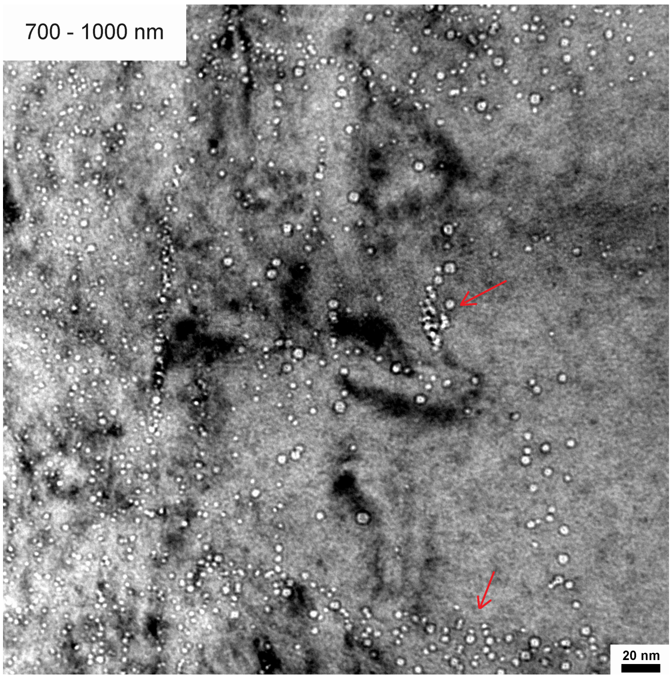

Figure 4.17: Cavity microstructure beyond the damage peak in Fe5%Cr. Cavity clusters, possibly associated with the dislocation loops, are indicated by the arrows. (BF, $s_g >> 0$, under-focus = -1136 nm)

For Fe10%Cr and Fe12%Cr, the entire depth was not systematically seen. However, there are reasons to believe that the microstructure evolution followed similar trend as observed in the other FeCr alloys. For instance, figure 4.18 shows the cavities beyond peak damage area (between 800 - 1000 nm depth) in both these materials. We can see that the majority of the cavities are associated with the dislocation loops, which was a regular feature in the other studied materials. For Fe10%Cr, the loops are on-edge, which made the cavities appear linearly aligned. In Fe12%Cr, loops are in open configuration and cavities can be seen inside them. It is also visible that the freely nucleated cavities in the matrix are relatively larger in size. Distribution prior to peak damage was studied only for the 300 - 400 nm depth in section 4.2.1. From the corresponding TEM images (figure 4.7), we can conclude that in this region, the distribution was homogeneous. Thus, a similar transition in cavity microstructure from homogeneous distribution to a mixed distribution beyond the damage peak is evident for these two materials as well.

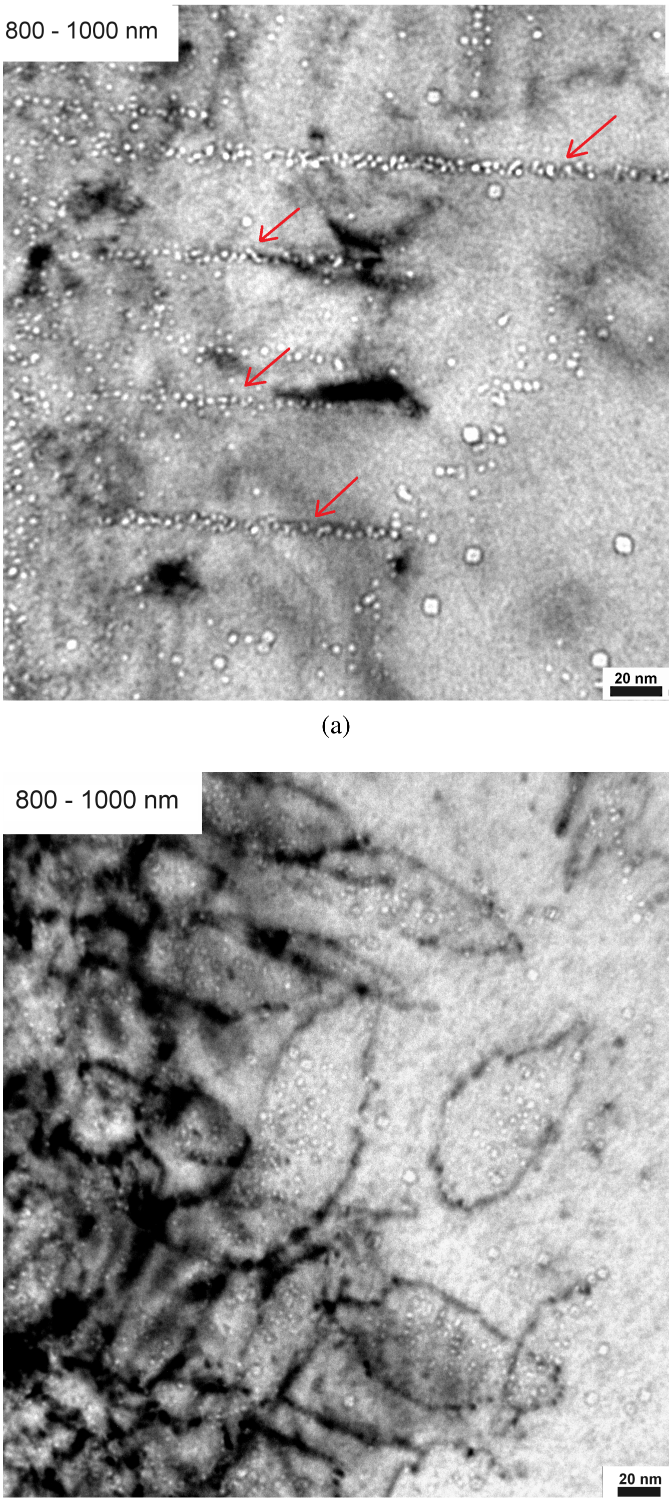

(a)

(b)

Figure 4.18: Heterogeneously nucleated cavities inside the dislocation loops in FeCr alloys. (a). Cavities on edge-on dislocation loops in Fe10%Cr. Imaging was performed close to (001) zone axis. (BF, $s_g >> 0$, under-focus = -1136 nm) and (b). Cavities inside the dislocation loops which are in open configuration in Fe12%Cr. Imaging was performed close to (011) zone axis. In this case, to see both cavities and the dislocation loops at the same time, KBF conditions with an out-of-focus objective lens was used. ($s_g > 0$, under-focus = -1136 nm)

4.2.3 Heterogeneous cavity nucleation on dislocation lines and grain boundaries

Dislocation lines

Beyond the peak damage area, apart from the nucleation inside the dislocation loops, linear arrangement of faceted cavities was regularly observed in the irradiated FeCr alloys[3]. A few examples are shown in figures 4.19 and 4.20a for Fe10%Cr, and figure 4.20b for Fe14%Cr. These are expected to be heterogeneously nucleated cavities on the pre-existing dislocation lines in the matrix. Such a behaviour can act as a pinning force on the dislocation motion, forcing them to climb before they could glide freely. It is depicted in the arrangement A, B and C in Fe10%Cr in figure 4.20 and in arrangement A, B in figure 4.19. In these images, the cavity arrangement is indicated by filled arrows and the position of the associated dislocation is indicated by dashed arrows. For A and B in figure 4.20, we can see that the dislocation has perhaps partially climbed; while the arrangement C shows a situation where dislocation seems to have climbed fully and then glided away, leaving the void arrangement behind. In these micrographs, the imaging was performed in out-of-focus conditions slightly far from Bragg condition. Due to this, the dislocation contrast is not strongly visible.

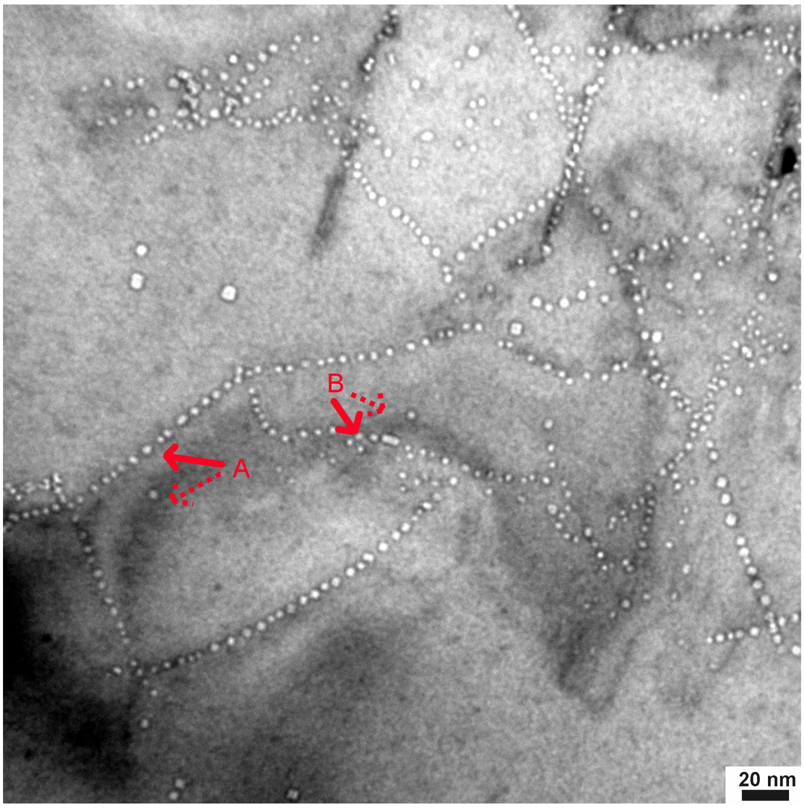

Figure 4.19: Decoration of the pre-existing dislocation lines by faceted cavities in Fe10%Cr. The micrograph corresponds to a zone beyond the damage peak between 1000 - 1300 nm. (BF, $s_g >> 0$, underfocus = -960 nm). A and B represent a situation where the associated dislocation seems to have partially climbed.

---

[3] According to SRIM calculations, He implantation ends at 1000 nm depth. But still we see cavities at depths beyond 1000 nm. We believe it maybe attributed to diffusion of He under irradiation at 500 °C. We have not probed this effect in detail.

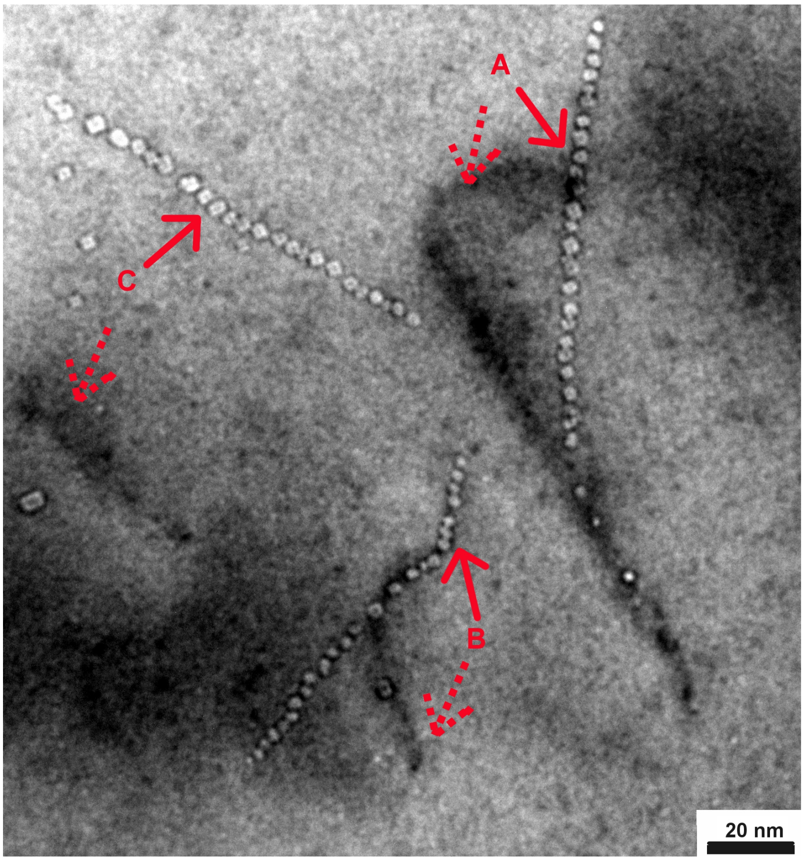

(a)

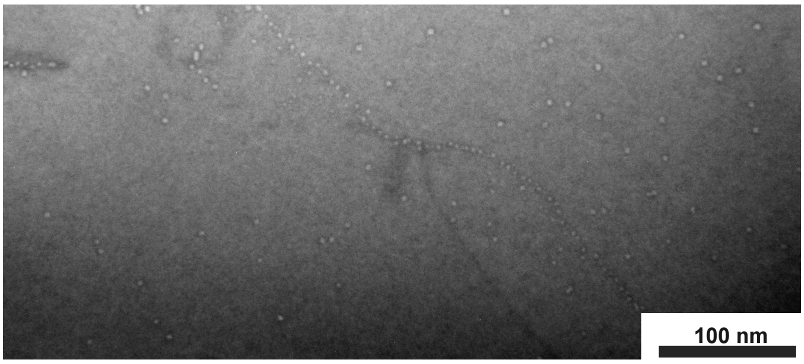

(b)

Figure 4.20: Another example of cavity nucleation on dislocation lines. (a) Zone at the tail end of dpa damage (1100 - 1300 nm) showing three almost linear arrangement of faceted cavities and their associated dislocations (indicated by dashed arrows) in Fe10%Cr. A and B represent a situation where the associated dislocation seems to have partially climbed; and in arrangement C, the associated dislocation has glided away. (b). Similar type of cavity nucleation observed in Fe14%Cr. (BF, $s_g >> 0$, under-focus = -890 nm)

Grain Boundaries

TEM analysis revealed strong He induced cavitation along the grain boundaries in Fe12%Cr and Fe3%Cr. These were the only FIB specimens which had intercepted a grain boundary. The corresponding TEM images are shown in figures 4.21 and 4.22 respectively. The manner in which the cavities were nucleated was largely different in the two specimens. For instance, we can see in Fe12%Cr that the cavities show an alignment. It could be due to heterogeneous nucleation on the dislocations constituting a grain boundary. On the other hand, in Fe3%Cr, such alignment did not exist. In this case, cavities along the grain boundary were significantly larger in size as compared to those in the matrix. We could argue that the nature of the grain boundary in this case was different from that in Fe12%Cr, which yielded a different style of cavity nucleation. Due to the complexity of the study, we have not attempted to perform a detailed analysis to identify the grain boundary disorientation in both the cases.

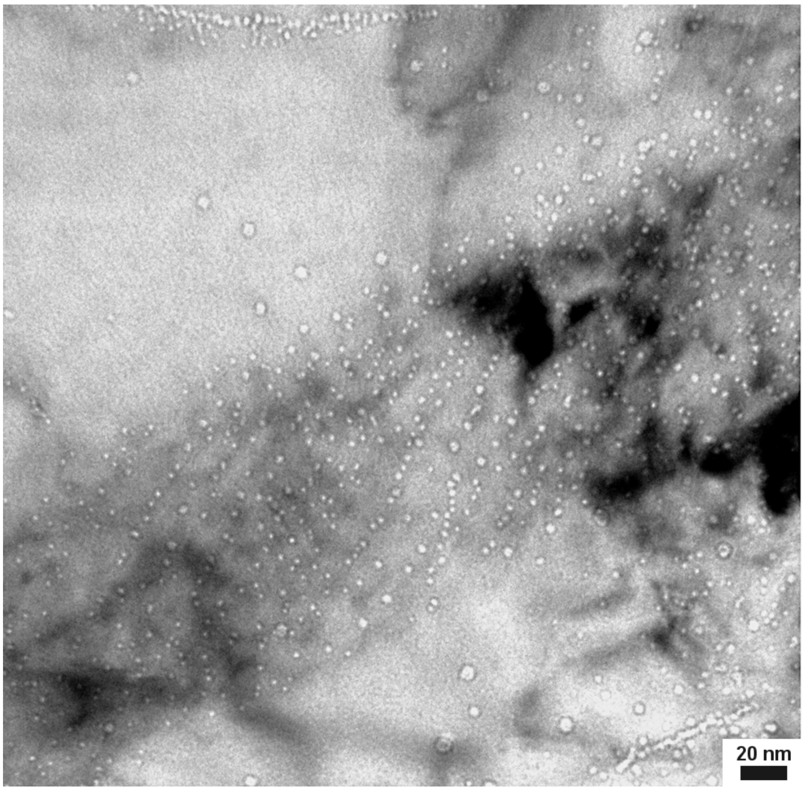

Figure 4.21: Heterogeneous nucleation of cavities on a grain boundary in Fe12%Cr. The arrangement of cavities seems to show an alignment indicating that nucleation may have taken place on the dislocations constituting the grain boundary. (BF, $s_g >> 0$, under-focus = -1136 nm)

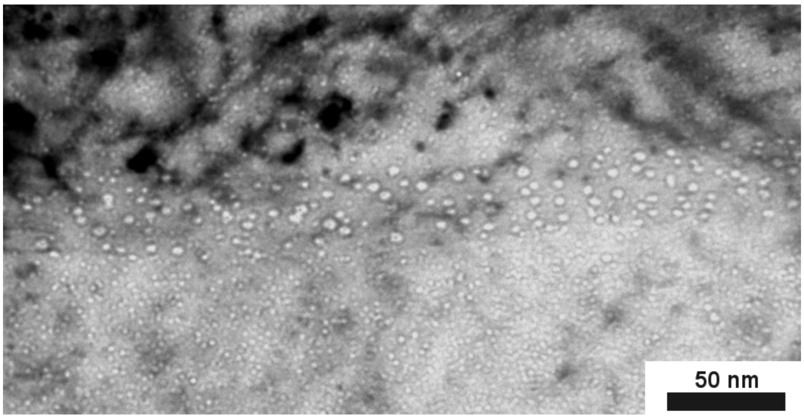

Figure 4.22: Cavities on grain boundary in Fe3%Cr. In this case, no alignment of cavities was seen. (BF, $s_g >> 0$, under-focus = -1136 nm)

4.3 Dislocation loop microstructure in bcc Fe and FeCr alloys

The dislocation loop microstructure induced after the high dose irradiations in bcc Fe and FeCr alloys was also investigated. The study was performed on the same FIB specimens on which cavities were studied. In this section, firstly the details on Fe are given and then the results are shown for FeCr alloys.

Bcc Fe

Single beam irradiated bcc Fe

In single beam irradiated bcc Fe, very few dislocation loops were detected in the entire damage depth. Even no existence of a dislocation network was seen. Such a network is usually expected at such high doses due to interaction and coalescence of dislocation loops. TEM image of the damage zone imaged in KBF conditions close to (001) zone axis is shown in figure 4.23a. The only two objects identified as loops are shown by an arrow. Apart from that, the dislocation density seemed similar to that of a virgin non-irradiated material [4].

Note that in the same image voids can also be seen. It is due to their very large size which makes them visible even when the image is in-focus.

Dual beam irradiated bcc Fe

For the dual beam case, it was difficult to obtain clear micrographs of the microstructure due to significant proportion of damage created by FIB milling in the sample[5]. Such damage, which are small interstitial clusters in the form of dislocation loops, seemed to have masked the original microstructure[6]. The corresponding TEM image is shown in figure 4.23b. Thus, no direct conclusions could be made. However, between the single beam and the dual beam case, the main difference is the presence of He. But the major fraction of matrix damage is induced by Fe self ions and not by He ions. Therefore, it would be reasonable to assume that the loop microstructure for the dual beam case may not be drastically different from the single beam case, if we neglect the effect of He on the loops.

---

[4] In FIB thin foils, the observable zones of interest are much smaller as compared to, for example, electro-polished TEM thin foils. Thus, the statistics of objects detected is always lower. It is, hence, possible that we do not see dislocation loops in significant numbers owing to low statistics.

[5] Due to experimental difficulty in preparing FIB specimens, all the samples did not have the same surface quality. In this particular case, the Ga ion source was fully consumed before arriving at the final polishing step of 2 keV. Thus, polishing at lower energies could not be performed. Because of this, the FIB damage (produced at higher energy milling steps) was not successfully removed.

[6] Since FIB damage are small interstitial clusters, they are in contrast in kinematic conditions which are used for imaging dislocation loops. However, they are less restrictive in masking cavities as they are generally imaged using through-focal imaging technique away from Bragg condition. No cavities were detected beyond the damage peak which which indicates that FIB milling did not produce any cavities.

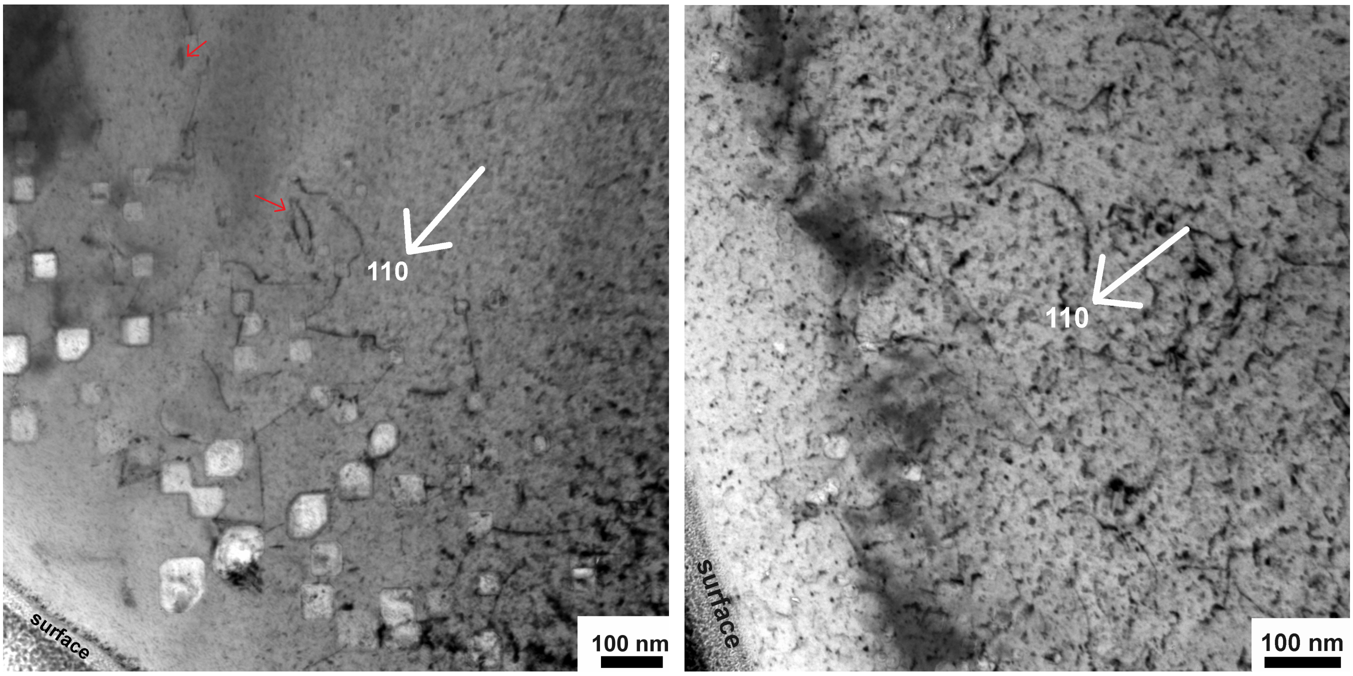

(a) (b)

Figure 4.23: TEM KBF images of irradiated bcc Fe. (a) Single beam irradiated and (b). Dual beam irradiated. In both the cases, the imaging was performed close to (001) zone axis.

FeCr alloys

A systematic observation of the dislocation loop microstructure for both the types of irradiations was performed for Fe14%Cr and Fe3%Cr alloys. The details are given below:

Dual beam and single beam irradiated Fe14%Cr

An analysis of dual beam irradiated Fe14%Cr alloy revealed a strong network of dislocations all along the specimen depth, which is expected to have formed by the interaction and coalescence of the dislocation loops. It started from the irradiated surface. The corresponding TEM image obtained in KBF conditions close to a (001) zone axis is shown in figure 4.24. A zoomed image of the dislocation network at an intermediate depth in the specimen is shown in the same figure, indicated by B. This network broke down into individually resolvable loops at larger distances where dpa damage falls of rapidly (mentioned as A in the image). Most of these loops are on-edge aligned along <100> directions, which is the peculiarity of a<100> type loops. Due to the complexity of the microstructure, we have not attempted to estimate quantitative information about the number density or Burgers vector of the dislocations incorporated in the network. This observation is in striking contrast to what was observed in bcc Fe.

Figure 4.24 also shows a part C which corresponds almost to the end of the damage zone. It shows two dislocations which are partially not linear. It is due to segregation of cavities on them which was mentioned in the previous section. The non-linear part, indicated by an arrow, is where the dislocation is perhaps trying to climb. A zoomed out-of-focus image of one of the dislocations decorated with small cavities is shown in the same figure, indicated by D. These small cavities appear black as the image is in over-focus condition.

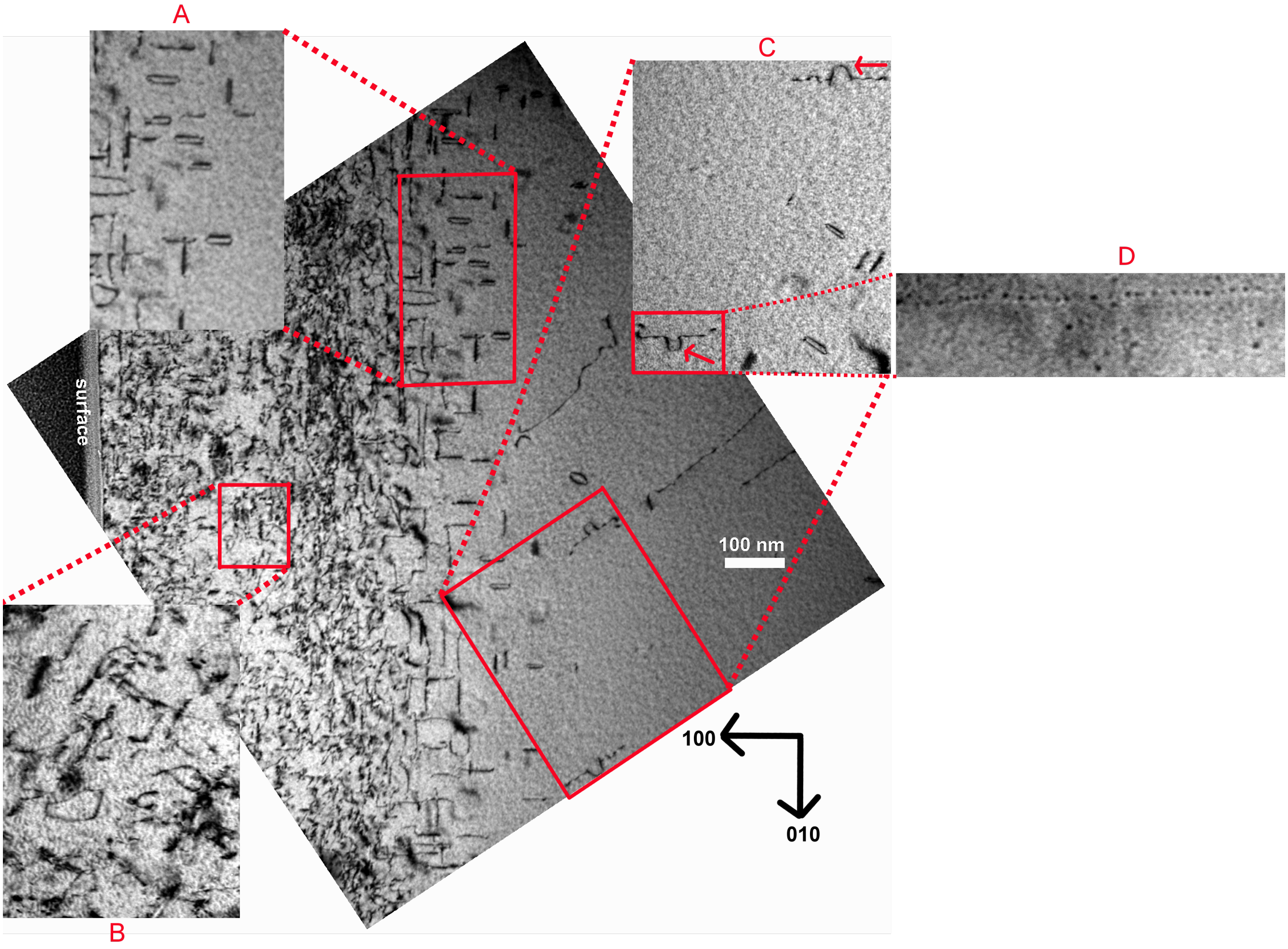

Figure 4.24: TEM image of dislocation network in dual beam high dose irradiated Fe14%Cr. Imaging was performed in KBF conditions close to (001) zone axis. “A” represents resolvable loops at the end of the damage zone. “B” represents the dislocation network at an intermediate depth, “C” shows two dislocations which seem partially trying to climb. “D” shows small cavities decorating the dislocation line (BF, over-focus = +1000 nm). The cavities appear dark because the image was obtained in over focus condition.

For the single beam case, unfortunately due to the presence of large amount of FIB damage[7], no conclusion could be obtained. The TEM image is shown in figure 4.25 . We can see the FIB damage in small streak like features. However, as it was said for bcc Fe, the microstructure is not expected to be very different from the dual beam case because the only difference is the presence of He which does not contribute significantly to the matrix damage.

---

[7] In this case, polishing at lower energies (5 keV and lower) could not be performed because the Ga ion source was completely utilised. Because of this, the FIB damage, produced at higher energy milling steps, was not successfully removed.

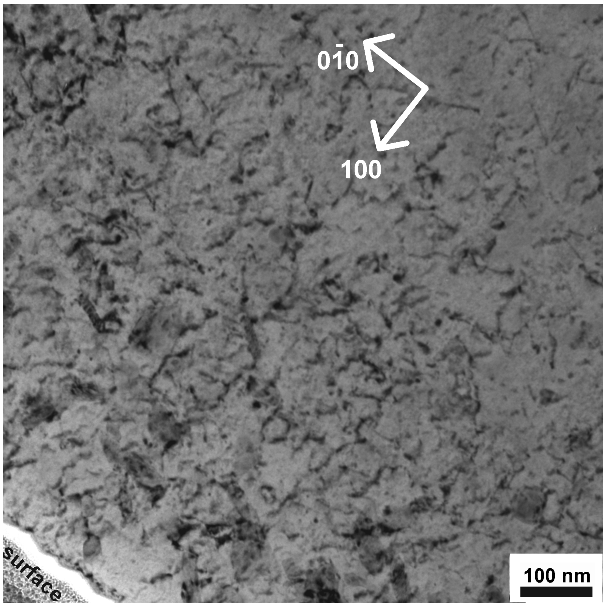

Figure 4.25: Microstructure of the single beam irradiated Fe14%Cr imaged in KBF conditions close to (001) zone axis.

Dual beam and single beam irradiated Fe3%Cr

TEM image of both dual and single beam irradiated Fe3%Cr, obtained close to (001) zone axis is shown in figure 4.26 . From both these images, a dislocation network can be seen in the damage region. There seems no remarkable difference between the single and dual beam irradiated specimens. Some edge-on individually resolvable loops can be seen in both the images. However, the mircostructures are not readily resolvable due to the presence of FIB damage in the specimen.

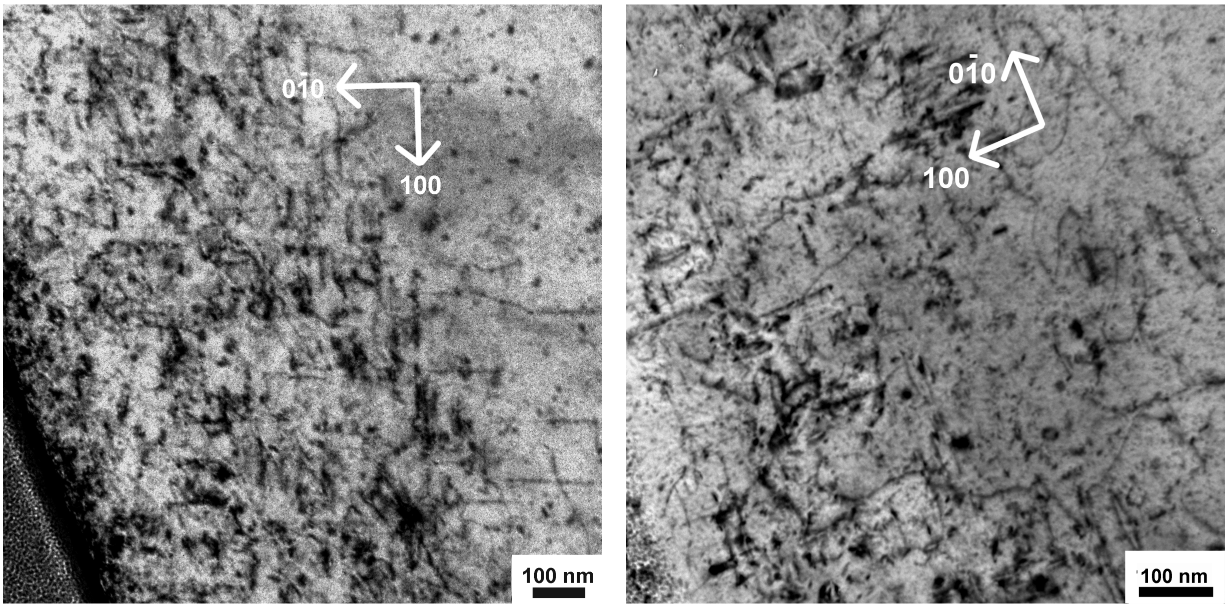

(a) (b)

Figure 4.26: Dislocation network in the high dose irradiated Fe3%Cr. (a). Single beam irradiated and (b). Dual beam irradiated. Imaging performed close to (001) zone axis in KBF conditions.

No such analysis was attempted for the remaining FeCr alloys (Fe5%Cr , Fe10%Cr and Fe12%Cr). However, from the study of the depth distribution of cavities in sub-section 4.2.2 on page 89, the dislocation loops were indirectly seen in these materials due to the presence of heterogeneously nucleated cavities associated with them.

From these observations, a general qualitative conclusion can be made that in presence of Cr, the dislocation density after irradiation is much higher as compared to bcc Fe. Such transition from bcc Fe begins just by addition of small Cr concentration (3% in our case).

It has to be noted that at such high doses, extracting quantitative information is difficult because the dislocation loops are incorporated into a network. For this reason, we have performed intermediate and low dose irradiations where dislocation loops can be identified as individually resolvable species. A detailed analysis can be seen in the next chapter where precise quantitative findings on the influence of Cr on the dislocation loop microstructure are presented.

4.4 Summary

High dose irradiations up to 157 dpa at 500 ºC were performed in single beam mode (only ballistic damage by self Fe ions) and in dual beam mode (co-implantation of He up to 17 appm He/dpa) on a series of FeCr alloys with Cr level varying from 3 to 14wt.% and a reference bcc Fe. Post-irradiation microstructure was studied by TEM on FIB specimens.

In bcc Fe, the entire depth distribution of cavities was thoroughly studied. A comparison of specimens irradiated with and without He revealed strong reduction in void swelling all along the damage depth when He was co-implanted. For instance, in the zone between 300 - 400 nm, void swelling was estimated to be 8.5 % for the single beam case, which reduced to only ~1% for the dual beam case. In this case, the average cavity size was 67 nm for the former and 6.8 nm for the later (with almost two orders of magnitude higher number density). This result urges to re-consider our established idea that He may always increase void swelling in irradiated materials.

A depth distribution of cavity sizes revealed a rather broad size distribution for the case of He co-implantation. Small cavities between 2 - 4 nm in size were always present all along the depth of damage, which imply that the nucleation of cavities was not over yet. In contrast, the size of voids in single beam irradiated Fe were not widely different atleast up to the damage peak and were very large (63 - 74 nm). This suggests that the microstructure for the single beam case was controlled by void growth rather than nucleation.

Analysis of the single and dual beam irradiated Fe also revealed strong diminution of cavities close the peak damage area, around 550 - 600 nm below the irradiated surface. For instance, swelling at the beginning of this zone dropped to nearly one-third its value at the intermediate depths. It is also the region where the implanted Fe ions come to rest in the material. This suggests perhaps implanted ions behave as injected interstitials which could artificially suppress the cavities.

All the results are thoroughly discussed in chapter 6. The effect of injected ions on void swelling is discussed specifically using cluster dynamics code CRESCENDO.

In FeCr alloys, it was revealed that the behaviour of void swelling as a function of Cr concentration is non-monotonic. The data was extracted from an intermediate depth of 300 - 400 nm (corresponding to 128 dpa, 13 appm He/dpa), to avoid surface effects and possible effects of injected ions near the damage peak. Initially, a strong swelling diminution was seen just by the addition of 3wt.% of Cr as compared to the swelling in bcc Fe. Thereafter, swelling slightly increased at 10wt.%Cr , and then started to decrease for higher Cr levels up to 14wt.% Cr. This, hence, produced a local swelling maxima at 10wt.%. In all the FeCr alloys, void swelling was considerably less (0.02 - 0.09%) as compared to bcc Fe (~1%). Strong void swelling diminution by Cr was also evident from the single beam irradiations where very high swelling level was noted in bcc Fe all along the damage depth, whereas no cavities were detected in any FeCr alloys.

The depth distribution of the cavities was also studied in FeCr alloys. A detailed analysis was performed on dual beam irradiated Fe14%Cr. In the areas prior to the damage peak, the cavities were small (the average size was slightly less than 2 nm). They were homogeneously distributed. Upon reaching the damage peak, a drastic change in cavity microstructure was noted. It consisted of a mixture of homogeneously nucleated cavities in the matrix, and heterogeneously nucleated cavities inside the dislocation loops. The size distribution became broader because of the presence of larger cavities in the microstructure (between 4 - 8 nm in size) in this region. Homogeneously nucleated cavities were mostly the larger ones, with facets. An increase in cavity size at and beyond the damage peak is contrary to what was observed in bcc Fe. Qualitative analysis performed on the other FeCr alloys showed similar behaviour.

Apart from heterogeneous cavity nucleation inside the dislocation loops, He induced heterogeneous cavitation along grain boundaries and dislocations was also observed in zones just beyond the damage peak in the dual beam irradiated FeCr alloys.

Dislocation loop microstructure was also analysed for the irradiated materials. It revealed the presence of an entangled dislocation network in FeCr alloys. The specimen studied were Fe(3, 12 ,14)%Cr. Individually resolvable loops were observed only at the end of the damage zone. In contrast, no dislocation network was observed in bcc Fe. The number of identified loops were also considerably less. Thus, it can be concluded that the dislocation loop density is, in general, higher in FeCr alloys as compared to bcc Fe.

Chapter 5

Irradiated microstructure at low and intermediate dose

This chapter is devoted to the interesting findings on the irradiated microstructure in FeCr alloys after in-situ low dose (0.33 dpa) and ex-situ intermediate dose (45 dpa) irradiations. In both the cases, the irradiations were performed in single beam mode and dual beam mode. The primary focus was the study of the dislocation loops induced by the irradiation, which are difficult to be studied at very high doses where the loop microstructure evolves into complex entangled dislocation networks. Fe14%Cr alloy was concerned by the low dose irradiations. Firstly, the details of the in-situ observation of the loop microstructure is given. Then, the determination of the Burgers vector of the dislocation loops is presented. Then, a comparison of the results is done with those obtained in bcc Fe irradiated under similar conditions by Brimbal and co-workers [13], to understand the effect of Cr on the dislocation loop microstructure. This is followed by the analysis of the dislocation loops in the dual beam irradiated Fe14%Cr, to see the effect of He on the dislocation loop microstructure.

Finally, a dedicated study performed on the analysis of Cr enrichment on the habit plane of the dislocation loops in low and intermediate dose irradiated FeCr alloys is presented. The materials concerned were Fe(5,10,14)%Cr. This analysis was performed using complimentary state-of-art characterization techniques: conventional TEM, EDS in STEM mode and APT.

5.1 Dislocation loop microstructure in low dose irradiated Fe14%Cr

In the previous chapter, we saw that Cr seems to have an important effect on the dislocation loop microstructure induced after the high dose irradiations. It was revealed that very less dislocation loops were detected in pure bcc Fe. In contrast, all the FeCr alloys ranging from 3 to 14% Cr consisted of a strong dislocation network along the depth of the damage zone. This network was expected to be formed due to the interaction and coalescence of dislocation loops induced by the irradiation. Resolvable loops were seen only at the tailing end of the damage zone. Thus, it seemed apparent that in the presence of Cr, an intense dislocation loop microstructure with high density develops. However, precise quantitative informations (eg. Burgers vector of dislocation loops, number density and size) could not be extracted from such networks at high dose.

For this reason, we have performed self-ion irradiations at low doses (~ 0.33 dpa) where loops are expected to be sufficiently large and can be resolved individually. Fe14%Cr alloy was concerned by this study. Similar to high dose experiments, the irradiations were performed at 500 ºC in single beam mode (damage by Fe ions) and dual beam mode (damage by Fe ions and co-implantation of helium). In these two cases, the aim was to understand the effect of Cr and a combined influence of Cr and He on the dislocation loops.

The irradiation parameters are given in table 5.1 and in figure 5.1[1]. For the single beam irradiation, the parameters are the same but without He.

Material	Temperature ºC	Dose dpa	He / dpa
Fe14%Cr	500	0.33	3030 (only for dual beam)

Table 5.1: Summary of irradiation parameters for Fe14%Cr

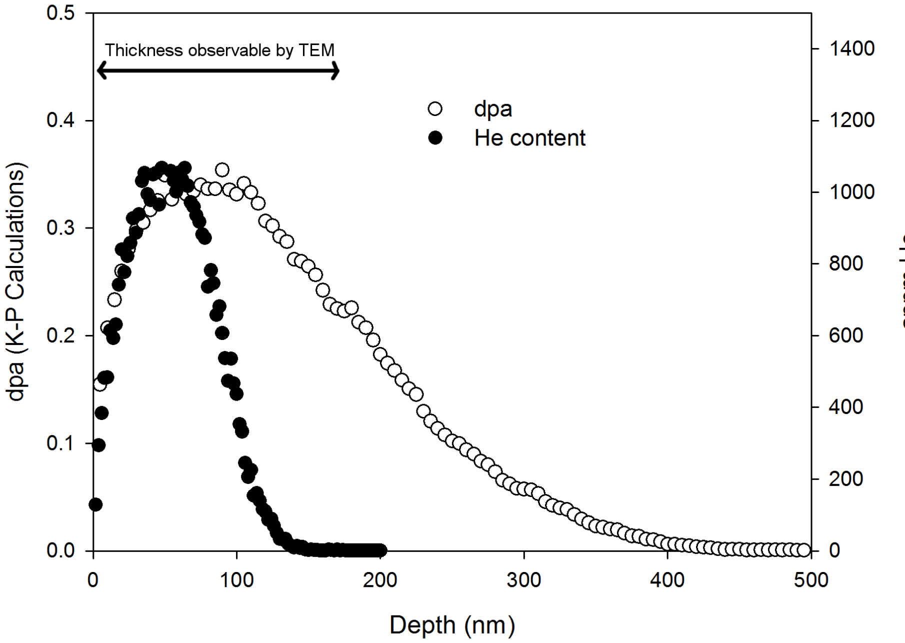

(a)

Figure 5.1: Self ion irradiations of Fe14%Cr without and with co-implantation of He at 500 ºC. The dose reached was 0.33 dpa. For the dual beam case, He was co-implanted to 3030 appm He/dpa. The irradiations were performed at JANNuS in-situ irradiation facility at CSNSM, Orsay.

---

[1] Additional information on the irradiation conditions can be seen in Chapter 3 “Methodology”.

5.1.1 Single beam irradiation

In this section, findings on the dislocation loop microstructure induced after single beam irradiation of Fe14%Cr are presented. Firstly, the results from the in-situ observations are given. Then, the determination of the Burgers vector of the dislocation loops is presented. Then, the results are compared with those available in literature on bcc Fe irradiated under similar conditions (results of Brimbal and co-workers [13]).

5.1.1.1 Mobility of loops - Kinetic effects

Single beam irradiation was an in-situ type irradiation which permitted to follow the evolution of the dislocation loops in the specimen. However, for the major part of the experiment, the zone of observation selected was relatively thin (less than ~90 nm). Due to this, almost no nucleation of loops took place in this zone. A measurement of the thickness performed using "thickness fringes method" (shown in figure 5.2) confirmed that up to ~123 nm, (corresponding to 4^{th} dark fringe), almost no nucleation occurred. It was probably due to large surface effects in the thin foil. Thus, the dose at which the first visible defect appears could not be estimated. When the observation zone was changed to a relatively thick area (>158 nm), dislocation loops were indeed visible[2]. It corresponded to 32 minutes after the start of irradiation (dose ~0.2 dpa) . Thereafter, upon following the microstructure evolution, no mobility of the dislocation loops was detected. Image sequences extracted from the recorded video showing the loop evolution from ~ 0.2 dpa to the end of irradiation (0.33 dpa) can be seen in figure 5.3 . It was imaged close to (001) zone axis using <110> diffraction vector. We can see that the positions of the loops stay fixed (they are slightly shifted downwards due to specimen drift during the irradiation). Only their growth was seen. A few examples of loop growth are indicated by circles in the figure. In addition to that, new loop nucleation was also visualized. It is marked with a dotted rectangle in the first image, where no loop was seen. Upon reaching 0.24 dpa, we can see a loop appearing at this place (see figure 5.3b), which eventually grows at larger doses . It appears to be on-edge at the end of the irradiation. Nucleation adjacent to a previous loop, giving rise to a small raft structure was also noted. Such occurrences can be seen by following the evolution of the loops indicated by an arrow in figure 5.3. No instances of loop elimination to surface was noted.

A total suppression of loop mobilities in Fe14%Cr is in striking contrast to the results in bcc Fe where the loops are known to be highly mobile (see chapter 2 "Bibliography"). Such a behaviour is also seen by other experimental groups as discussed in chapter 2. In their cases, the Cr level was less than 14%.

---

[2] As we can see from figure 5.1, that although the damage peak is located around 100 nm, there is still damage at larger thickness. It is due to this reason, we are seeing loops in thicker zones which are beyond the peak damage area.

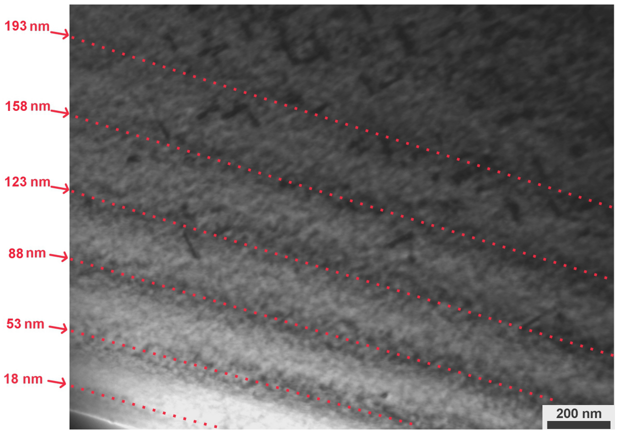

Figure 5.2: Fe14%Cr irradiated to 0.33 dpa (without helium co-implantation) imaged on exact Bragg condition to reveal the thickness fringes (BF, $\overrightarrow{g}$ = <110>, zone axis = (001), $s_g = 0$, grain orientation ~ (001)). For thickness below 88 nm, no loops were present. Majority of loop were seen beyond 158 nm thickness.

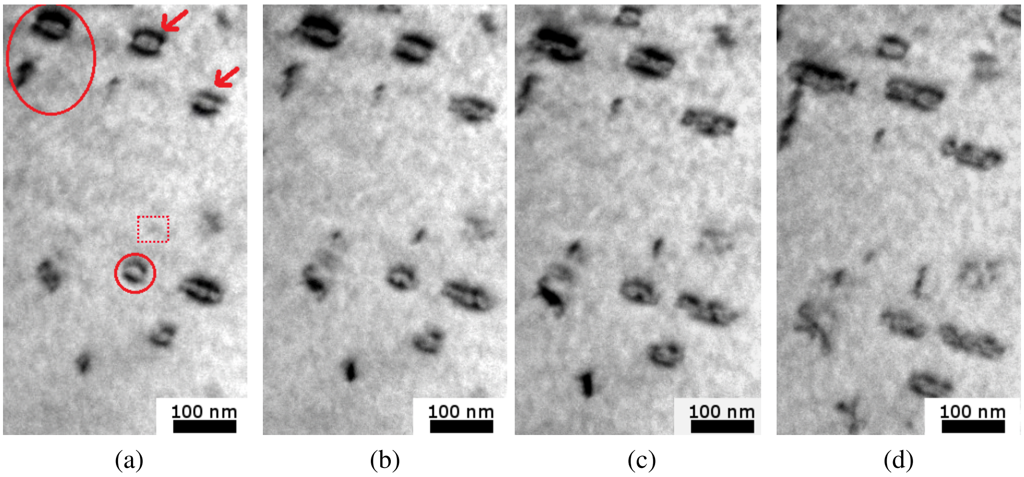

(a) (b) (c) (d)

Figure 5.3: Image frames extracted from the video of the evolution of the dislocation loops during in-situ irradiation of Fe14%Cr (BF, $\overrightarrow{g}$ = [110], zone axis = (001), $s_g > 0$). Loops at (a). 0.2 dpa (32 minutes after the start of irradiation), (b). 0.24 dpa, (c) 0.27 dpa and (d) end of irradiation corresponding to 0.33 dpa. No mobility of loops was seen. Loop nucleation in the matrix can be seen by following the evolution in the dashed box. Loop growth can be seen by following the sequence of encircled loops. Raft formation can be seen by following the evolution of loops indicated by the arrows.

5.1.1.2 Burgers vector of dislocation loops

Burgers vector of the dislocation loops formed after the irradiation up to 0.33 dpa was analysed using $\overrightarrow{g}.\overrightarrow{b}$ analysis (see chapter 2 “Methodology”). It was performed on a grain oriented close to (001) zone axis. The region selected was relatively thick (beyond 193 nm) to have good statistics. Since, the thickness fringes were not present beyond this depth (see figure on the current page), it was assumed that the thickness of the region corresponds to 193 nm.

A combination of <110> and <200> type $\vec{g}$ was used to image a fixed zone, but with different tilts. The set of visibility/invisibility criteria of a<100> and a/2<111> type dislocation loops for each selected diffraction vector is shown in Table 5.2, which allows us to determine their Burgers vector. As seen in chapter 2, section 2.4.1, initially small <110> oriented SIA clusters are expected to be formed in bcc Fe up to around five SIAs. Then, they are expected to transform to a/2<111> loops. But a<110> loops were never detected experimentally by TEM studies. Thus, in the determination of the Burgers vector of the loops, we have not included a<110> loops. Furthermore, as mentioned in Chapter 3, section 3.4.1.2, loops in residual contrast can arise if $\vec{g} \cdot \vec{b} \times \vec{u} \neq 0$. In our analysis, we have considered that such loops are not in contrast.

Diffraction vector $\vec{g}$	$[\bar{1}10]$	[110]	$[\bar{2}00]$	[020]	$[0\bar{1}1]$
a[010] (family A)	V	V	I	V	V
a[100] (family B)	V	V	V	I	I
a[001] (family C)	I	I	I	I	V
a/2[111] (family D)	I	V	V	V	I
a/2$[\bar{1}11]$ (family E)	V	I	V	V	I
a/2$[1\bar{1}1]$ (family F)	V	I	V	V	V
a/2$[11\bar{1}]$ (family G)	I	V	V	V	V

Table 5.2: Table showing the set of visibility/invisibility criteria of different families of a<100> and a/2<111> type dislocation loops, based on the "scalar product" of $\vec{g}.\vec{b}$: when $\vec{g}.\vec{b} = 0$, loop is invisible (I), if $\vec{g}.\vec{b} \neq 0$, loop is visible (V). Since none of the loop families satisfy the same criteria for a selection of different $\vec{g}$, it allows us to distinguish them on the basis of their Burgers vector.

A detailed analysis is shown in figure 5.4, where each image is obtained by tilting the zone of study at different angles to select the appropriate diffraction vector $\vec{g}$. It revealed that both a<100> and a/2<111> type dislocation loops were present in the microstructure. All the identified families are indicated in the image using the nomenclature given in table 5.2. Figures 5.4a to 5.4d were imaged on (001) zone axis. Families A and B with Burgers vector $\vec{b}$ = ±a[010] and ±a[100] respectively can be seen on edge[3]. Their projections were contained along the plane of projection of (010) and (100) planes. Since a<100> loops are known to be perfect loops of pure edge character, it can be concluded that (010) plane is the habit plane of ±a[010] loops (family A) and (100) plane is the habit plane of ±a[100] loops (family B). Family C with Burgers vector ±a[001] does not satisfy the visibility criteria on this zone axis, and is hence invisible. However, it is in contrast in figure 5.4e taken on (011) zone axis. Its habit plane was not determined. But from the observations of family A and B, it is sufficient to believe that family C would be contained in (001) planes. a/2<111> type loops were present in significant proportions. Their different families (D, E, F and G) can be seen marked on Figure 5.4. For the images taken on (001) zone axis, all the loops which are in contrast and not on edge are the ones belonging to a/2<111> category. The habit plane of a/2<111> loops was not determined.

A statistics on the total number of identified loops belonging to different families of a<100> and a/2<111> category is shown in table 5.3. It shows that the percentage of a/2<111> type is higher (46% as opposed to 35% of a<100> type). A relative proportions of all the families of both dislocation loop categories is also shown in table 5.3. It is evident that a<100> category is almost equally distributed in proportion among its three families (a[100], a[010] and a[001]) ; a/2<111> category also seems almost equally divided except for a/2[$1\bar{1}1$] which was found to be slight less in number (7% of the total population).

There were a certain number of unidentified loops as well. Due to their very small size, it was difficult to locate them on images with different tilts. They contributed to 19% of the net loop population (see table 5.3). However, none of them seemed to be aligned on edge along <100> projections. Thus, it would be reasonable to say that they were also a/2<111> type. This would eventually increase further the percentage of the a/2<111> loop category in the analysed zone. In estimating the number density of a/2<111> loops given in table 5.4, these were taken into account. Additionally, these unidentified loops may also explain slightly low proportion of a/2[$1\bar{1}1$] family mentioned above: it is possible that a part of their proportion may correspond to a/2[$1\bar{1}1$] family. It would mean that the relative proportion between the four a/2<111> loop families is very similar. This is expected because during the in-situ irradiation experiment, none of the loops were seen to be mobile.

In terms of loop size, it is evident from the figure 5.4 of Burgers vector analysis, that a<100> loops were invariable the larger ones[4]. To understand this effect clearly, a size distribution of the dislocation loops is presented in figure 5.5. We can see that the majority of the loops are varying from a few nanometres in size to about 30 nm. They were mostly a/2<111> type. Larger loops beyond 40 nm, up to 100 nm were always a<100> type. The average size of both these loop populations and their number density

---

[3] It is interesting to note from the above observations that imaging of dislocation loops on <100> type zone axis provides a quick means of identifying the loops on the basis of their Burgers vector just by looking at their image projections: a<100> type loops would be on edge and anything else which is not on edge would be a/2<111> type. It is helpful technique when loops are sufficiently large in size, and reduces the need of performing a complete $\vec{g}.\vec{b}$ analysis.

[4] It must be noted that the measured size is not the true size of the loops. Its their projection, in this case, on (001) zone axis.

is given in table 5.4. The maximum and the minimum loop size observed in the microstructure and the total loop density is also given in the same table.

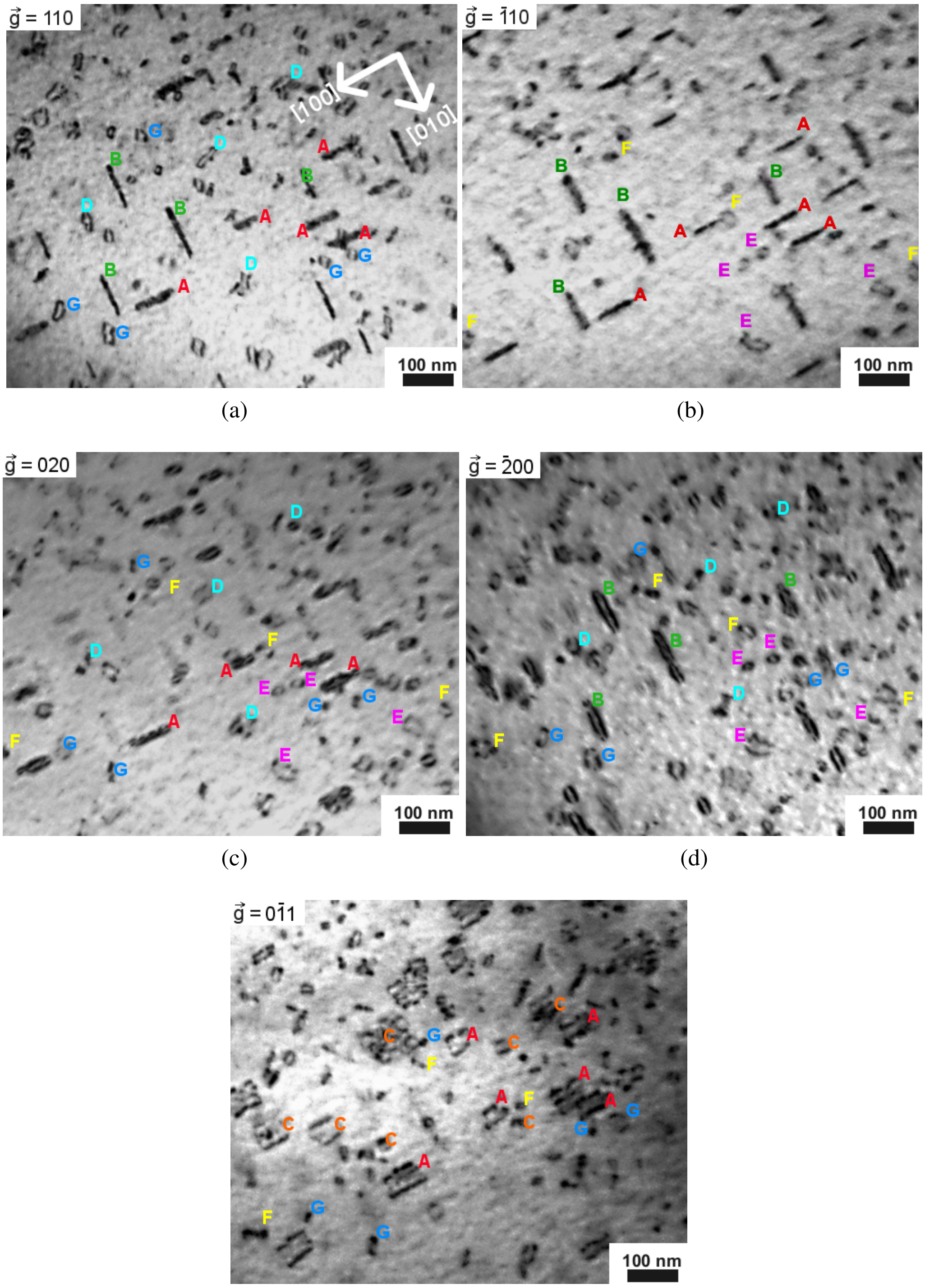

(a) (b)

(c) (d)

(e)

Figure 5.4: Determination of Burgers vector of dislocation loops in Fe14%Cr irradiated to 0.33 dpa without helium co-implantation (KBF, grain orientation = (001)). The imaging was performed on a fixed zone with different tilts to select the appropriate $\overrightarrow{g}$. (a). $\overrightarrow{g}$ = [110], zone axis = (001); (b). $\overrightarrow{g}$ = [$\bar{1}$10], zone axis = (001); (c). $\overrightarrow{g}$ = [020], zone axis = (001); (d). $\overrightarrow{g}$ = [$\bar{2}$00], zone axis = (001); (e). $\overrightarrow{g}$ = [0$\bar{1}$1], zone axis = (011).

Loop family	Number of identified loops	Percentage of identified loops
a[100]	12 ± 1	11 ± 1 %
a[010]	11 ± 1	10 ± 1 %
a[001]	16 ± 2	14 ± 2 %
a/2[111]	17 ± 2	15 ± 2 %
a/2[$\bar{1}11$]	12 ± 1	11 ± 1 %
a/2[$1\bar{1}1$]	8 ± 1	7 ± 1 %
a/2[$11\bar{1}$]	15 ± 1	13 ± 1 %
Net a<100> loops	39 ± 4	35 ± 4 %
Net a/2<111> loops	52 ± 5	46 ± 5%
Total number of loops studied	90 (identified) + 22 (unidentified) = 112	
Percentage of unidentified loops	19%	

Table 5.3: Relative proportion between a<100> and a/2<111> type dislocation loops in the analysed zone close to (001) grain orientation. The error bars are estimated from the statistical error in the number of loops considered for the analysis.

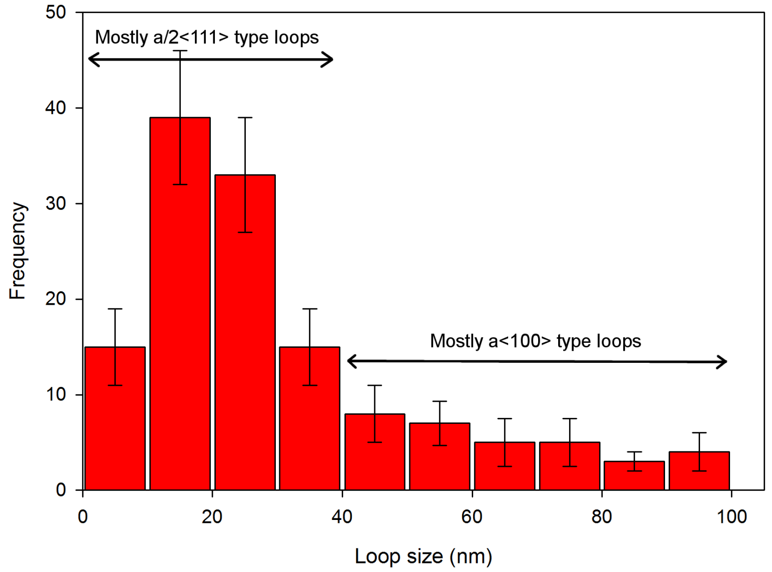

Figure 5.5: Size distribution of dislocation loops in Fe14%Cr irradiated in single beam mode to 0.33 dpa. Larger loops more than 40 nm in size were mostly a<100> type while smaller ones were predominantly a/2<111> type.

Maximum loop size	98 ± 2 nm
Minimum loop size	3 ± 0.5 nm
a<100> type Average loop size	65 ± 2 nm
a/2<111> type Average loop size	20 ± 2 nm
Net average (both a<100> and a/2<111>)	22 ± 2 nm
Number density of a<100> loops	(4.5 ± 1.4) x 10^{20} m^{-3}
Number density of a/2<111> loops	(8.5 ± 2.5) x 10^{20} m^{-3}
Total number density	$(1.3 \pm 0.4\ )$x 10^{21} m^{-3}

Table 5.4: Quantitative results on size and number density of the dislocation loops in single beam low dose irradiated Fe14%Cr.

5.1.1.3 Comparison with bcc Fe

The presence of a large proportion of a/2<111> type dislocation loop category in single beam irradiated Fe14%Cr is in contrast to results known in bcc Fe. Indeed, at 500 ºC by ion irradiations, a/2<111> type loops have never been observed in Fe [13, 59]. This reveals that the addition of Cr (14wt.% in our case) in bcc Fe matrix helps in stabilising the a/2<111> type dislocation loops.

A comparison of the loop number density and average loop size in this case to the results in bcc Fe obtained by Brimbal and co-workers [13], who performed the experiments under similar irradiation conditions, is shown in figures 5.6 and 5.7 respectively. It shows that the microstructure in Fe14%Cr developed at a finer scale as compared to Fe, with more than one order of magnitude higher total loop number density. The major difference was induced by the a/2<111> type loops. It is evident because between these two materials, the concentration of a<100> loops was not drastically different (see figure 5.6). Furthermore, the average size of a<100> loops was slightly larger in Fe14%Cr than those in Fe, but not vastly different. Thus, the finer loop microstructure in Fe14%Cr was an effect of a/2<111> type loop stabilization by Cr.

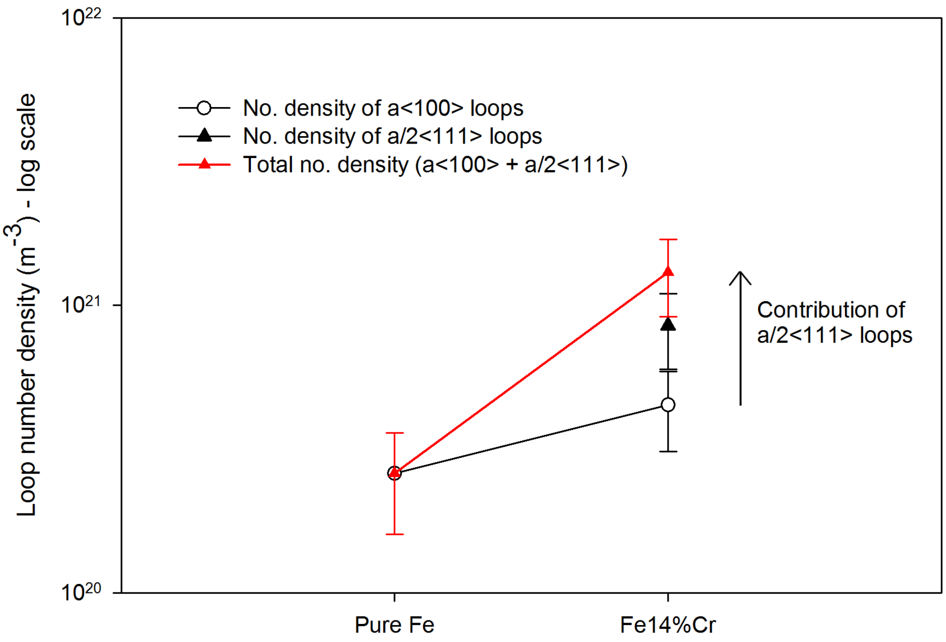

Figure 5.6: A comparison of number density of the dislocation loops observed in Fe14%Cr with bcc Fe irradiated under similar irradiation conditions. Fe data is taken from the study of Brimbal and co-workers [13].

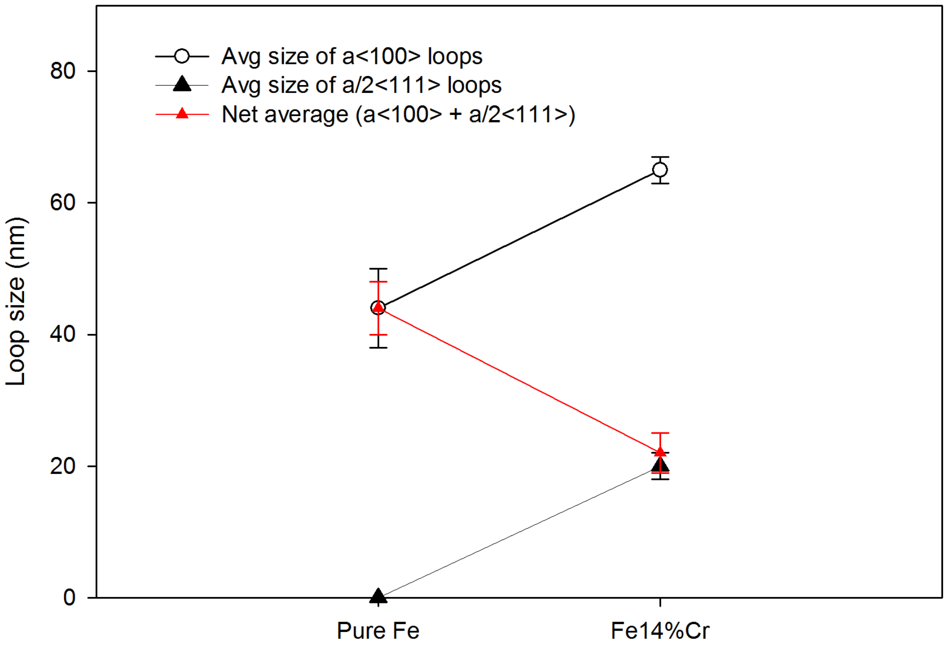

Figure 5.7: A comparison of average loop size of the dislocation loops observed in Fe14%Cr with bcc Fe irradiated under similar irradiation conditions. Since a<100> and a/2<111> type loops were observed in Fe14%Cr, the data is represented separately for both. Fe data is taken from the study of Brimbal and co-workers [13].

5.1.2 Dual beam irradiation: He effect on the dislocation loops

Fe14%Cr was also irradiated in dual beam mode (with co-implantation of He) to the same dose level as in the previous section. He implantation at the damage peak was 3030 appm He/dpa. The aim was to see the combined influence of Cr and He on the dislocation loops. In this case, due to strong deviation of light ion beams (He in our case) by the objective lens of the TEM, microstructure could not be followed in-situ. Thus, the specimen was analysed post-irradiation. The results are shown in this section.

5.1.2.1 Burgers vector of dislocation loops

Similar to the single beam irradiation case, the dislocation loops induced by the irradiation were observed by performing TEM analysis on the irradiated thin foil specimen. Burgers vector of the loops was analysed using $\vec{g}.\vec{b}$ analysis. In this case, the grain orientation was (011). The set of visibility/invisibility criteria of dislocation loops for each selected diffraction vector is shown in table 5.5.

Diffraction vector $\overrightarrow{g}$	$[01\bar{1}]$	$[\bar{2}00]$	$[1\bar{1}0]$	$[10\bar{1}]$	$[110]$
a[001] (family A)	V	I	I	V	I
a[010] (family B)	V	I	V	I	V
a[100] (family C)	I	V	V	V	V
a/2[111]	I	V	I	I	V
a/2$[\bar{1}11]$	I	V	V	V	I
a/2$[1\bar{1}1]$	V	V	V	I	I
a/2$[11\bar{1}]$	V	V	I	V	V

Table 5.5: Table showing the set of visibility/invisibility criteria of different families of a<100> and a/2<111> type dislocation loops, based on the “scalar product” of $\overrightarrow{g}.\overrightarrow{b}$. If $\overrightarrow{g}.\overrightarrow{b} = 0$, loop is invisible (I), if $\overrightarrow{g}.\overrightarrow{b} \neq 0$, loop is visible (V).

The determination of the Burgers vector performed on a fixed zone is shown in figure 5.8. It revealed that only a<100> type dislocation loops were present in the microstructure. The corresponding three loop families are marked in the images. This observation is striking because the only difference in this case as compared to the single beam irradiated Fe14%Cr is the presence of He. Thus, it appears that He can have significant impact on the dislocation loop microstructure. In figure 5.8a and b, the zone axis is (011). Using a $[01\bar{1}]$ type diffraction vector $\overrightarrow{g}$, a[010] and a[001] family can be seen in open configuration , while a[100] family is invisible (in residual contrast). Upon selecting $\overrightarrow{g} = [\bar{2}00]$, a[100] family was seen on-edge aligned along the projection of $[\bar{2}00]$ planes.

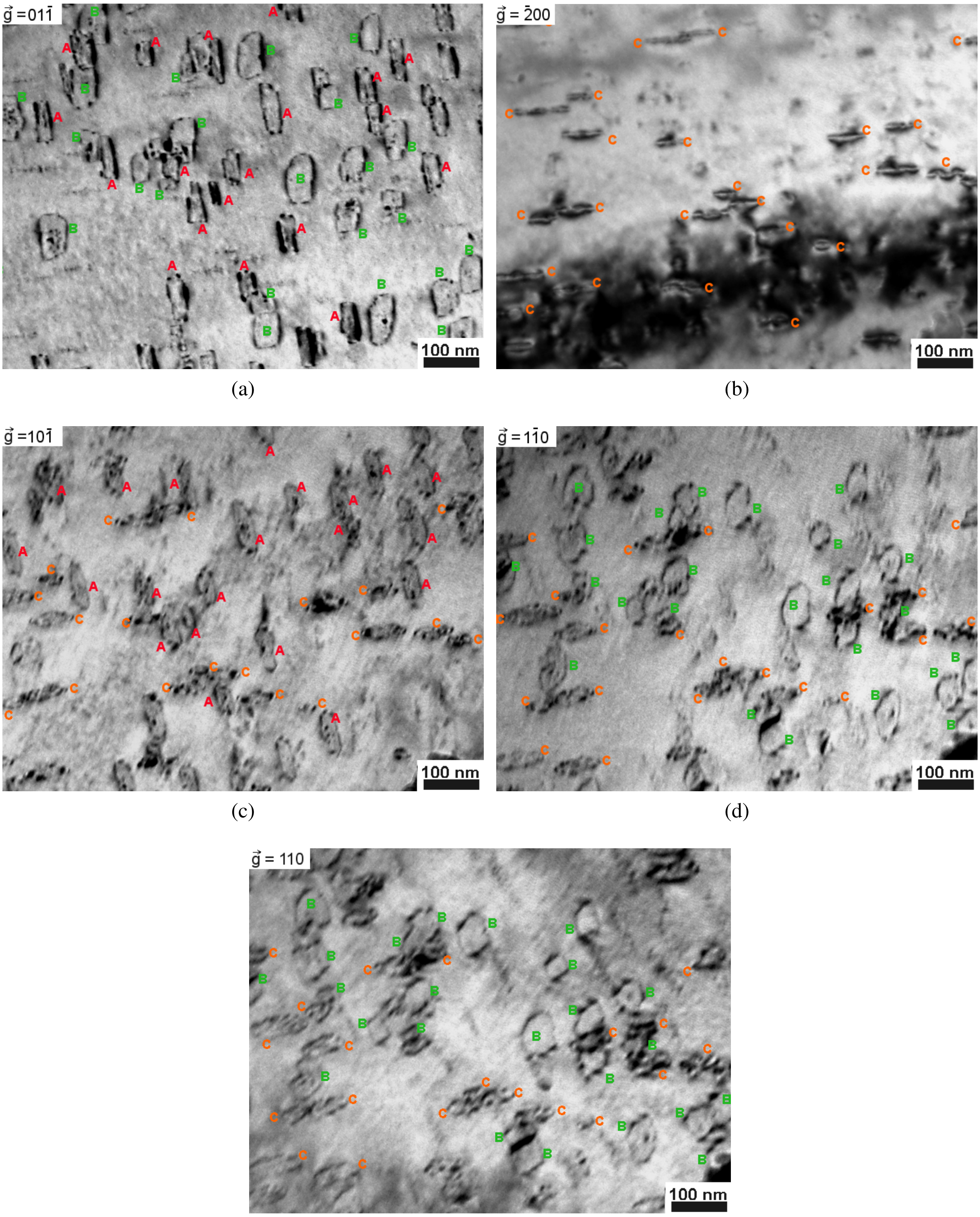

(a) (b) (c) (d) (e)

Figure 5.8: Determination of Burgers vector of dislocation loops in Fe14%Cr irradiated to 0.33 dpa co-implanted with 3030 appm He/dpa (KBF, grain orientation = (011)). The imaging was performed on a fixed zone with different tilts to select the appropriate $\vec{g}$.(a). $\vec{g}$ = $[01\bar{1}]$, zone axis = (011); (b). $\vec{g}$ = $[\bar{2}00]$, zone axis = (011); (c). $\vec{g}$ = $[10\bar{1}]$, zone axis = (111); (d). $\vec{g}$ = $[1\bar{1}0]$, zone axis = (111); (e). $\vec{g}$ = [110], zone axis = $(\bar{1}11)$.

A relative proportion between the different families of the dislocation loops is shown in table 5.6. We can see that a[100], a[010] and a[001] families are present in almost similar proportions. This is similar to the results in the single beam case (see table 5.3).

Loop family	Number of identified loops	Percentage of identified loops
a[100]	34 ± 3	31 ± 3 %
a[010]	37 ± 4	33 ± 4 %
a[001]	40 ± 4	36 ± 4 %
a/2[111]	0	0
a/2[$\bar{1}$11]	0	0
a/2[1$\bar{1}$1]	0	0
a/2[11$\bar{1}$]	0	0
Net a<100> loops	111	100%
Net a/2<111> loops	0	0
Total number of loops studied	111	

Table 5.6: Relative proportion between a<100> and a/2<111> type dislocation loops observed in the low dose dual beam irradiated Fe14%Cr. Only a<100> loop category was observed. The errors bars are estimated from the statistical error in the number of loops considered for the analysis.

Size distribution of dislocation loops is shown in figure 5.9. It revealed that the majority of the loops were relatively larger in size as compared to the single beam case, spanning over a range between 30 nm to 110 nm. The average, minimum and maximum loop size and their number density is shown in table 5.7. We can see that the average loop size was 70 nm. This value is very similar to the average size of a<100> loops seen in the single beam case (65 nm). Furthermore, the total loop number density was also similar in both the cases.

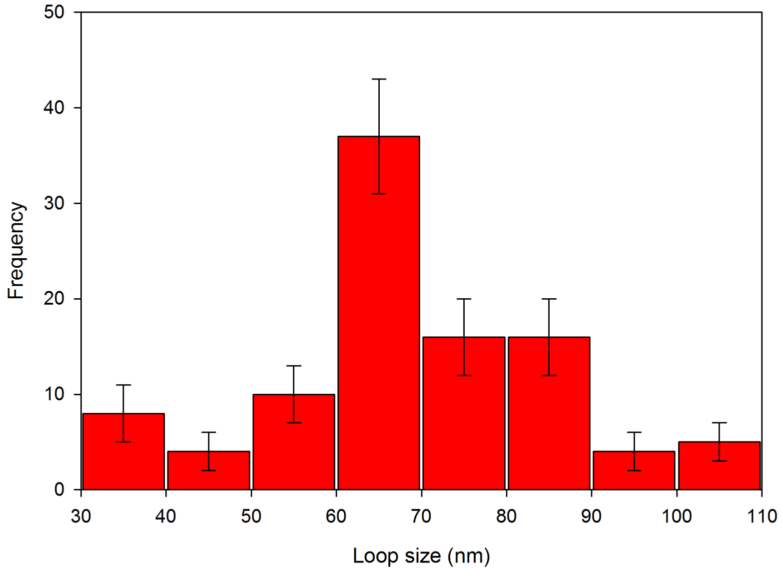

Figure 5.9: Size distribution of the dislocation loops in the dual beam irradiated Fe14%Cr. All the loops were a<100> type.

Maximum loop size	108 ± 2 nm
Average loop size	70 ± 2 nm
Minimum loop size	35 ± 1 nm
Number density of <100> loops	(1.1 ± 0.3) x 10^{21} m^{-3}

Table 5.7: Size and number density of the dislocation loops in low dose dual beam irradiated Fe14%Cr.

5.1.2.2 Comparison with Fe

The results on the dislocation loops observed in the low dose dual beam irradiated Fe14%Cr were compared to those obtained in bcc Fe by Brimbal and co-workers [13], who performed irradiations under similar irradiation conditions. In both the cases, only a<100> loops were seen. A comparison of their average size and number density is given in figure 5.10. It reveals that the microstructure in Fe14%Cr was on finer scale, with smaller loop sizes and elevated loop number density.

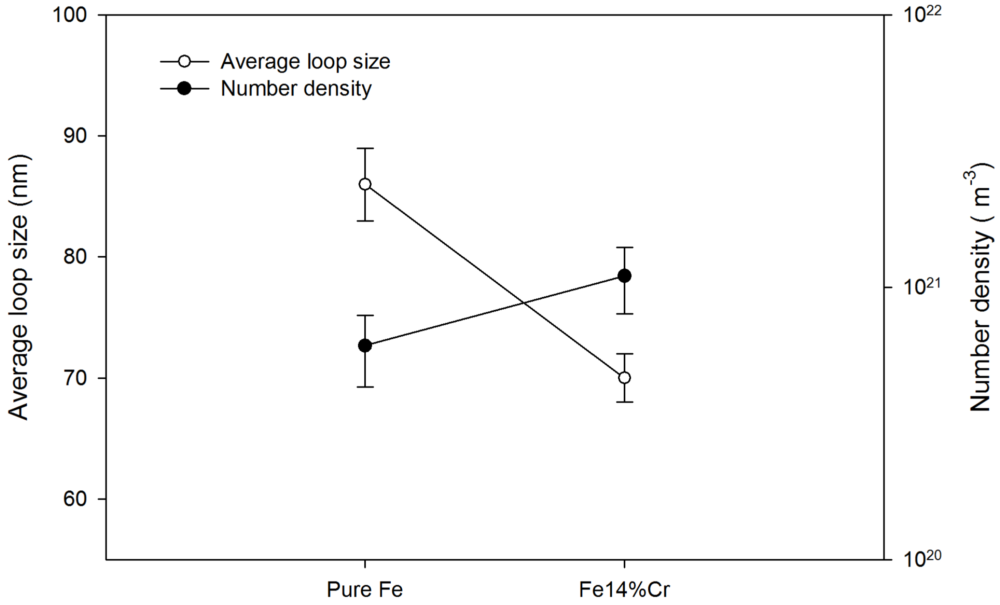

Figure 5.10: Comparison of the average loop size and number density of the dislocation loops between the low dose dual beam irradiated Fe14%Cr, to those obtained in bcc Fe irradiated under similar irradiation conditions. Only a<100> loops were observed in both the cases. Fe data is taken from the study of Brimbal and co-workers [13]

Another thing to note is that, if we look carefully on the images of loops in figure 5.8, they show a slight contrast on the loop plane. It can also be seen in the single beam irradiated Fe14%Cr in figure 5.4e (imaged using $\vec{g}$ = $[0\bar{1}1]$ on (011) zone axis). When these loops were imaged in weak beam dark field conditions, it turned out that the habit plane of the loops were decorated with a fringe pattern (which was weakly visible in KBF conditions). A comparison of images obtained using these two techniques on same cluster of dislocation loops in dual beam irradiated Fe14%Cr is shown in figure 5.11. We can see the slight contrast on loop plane in KBF image turning into fringes in the WBDF image. Such fringe patterns are usually associated with faulted dislocation loops (Franck loops) in fcc austenitic steels. However, it is well known that stacking fault energy in bcc Fe (and hence in bcc Fe based alloys) is high. Thus, dislocation loops are not expected to be faulted. This observation was very curious and has been thoroughly analysed separately in the next section. For this study, a coupling of other state-of-art characterization techniques (EDS in STEM mode and APT) was utilised along with conventional TEM.

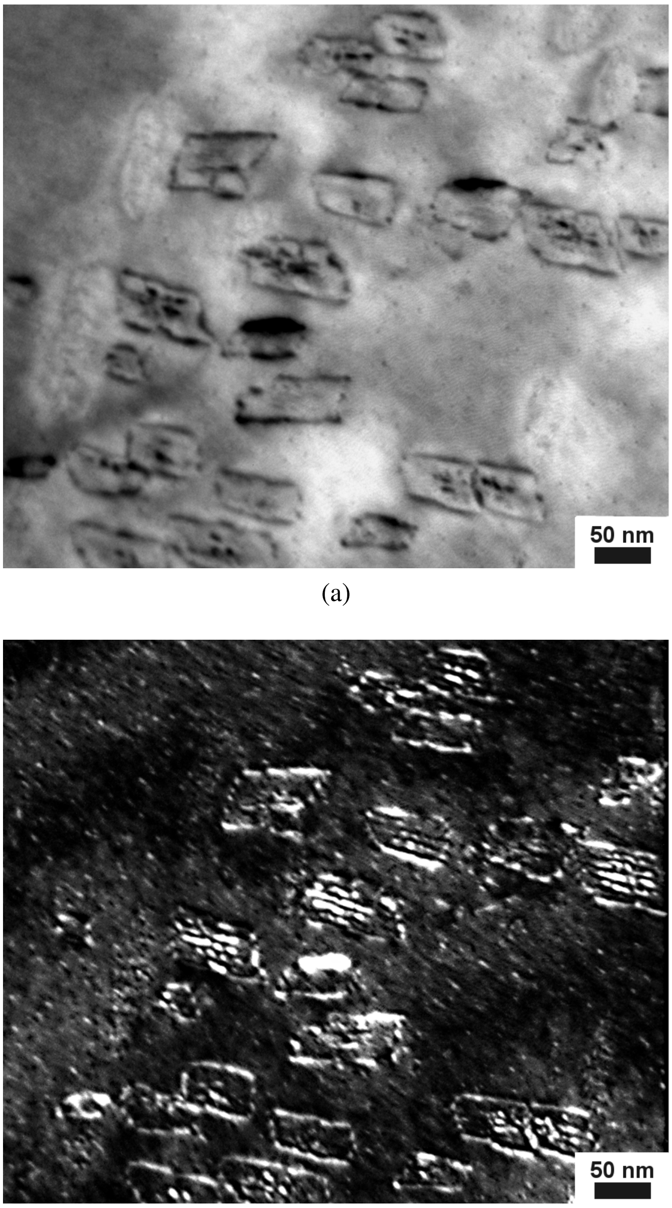

(a)

(b)

Figure 5.11: A comparison of dislocation loops in Fe14%Cr imaged in (a). KBF conditions ($\vec{g}$ = $[0\bar{1}1]$ on (011) zone axis, $s_g > 0$) and (b). weak-beam dark field conditions ($\vec{g}$, $5\vec{g}$). Weak beam image revealed fringes on the plane of the dislocation loops.

5.2 Chromium enrichment on habit plane of dislocation loops in FeCr alloys

As indicated in the previous section, fringes were seen inside the dislocation loops in dual beam irradiated Fe14%Cr. This observation was curious and striking because the stacking fault energy in bcc Fe is high. So, the loops in bcc Fe based alloys are not expected to be faulted. To probe this effect into more detail, intermediate dose irradiated (up to 45 dpa) Fe5%Cr and Fe10%Cr specimens were thoroughly analysed in addition to the low dose irradiated Fe14%Cr. The irradiation conditions for the former are given in figure 5.12. The specimens were both electro-polished thin foils and dimpled discs (of 100 μm thickness). After the irradiations, FIB specimens were extracted from the dual beam irradiated dimpled discs. Atom probe needles were also prepared, using FIB annular milling.

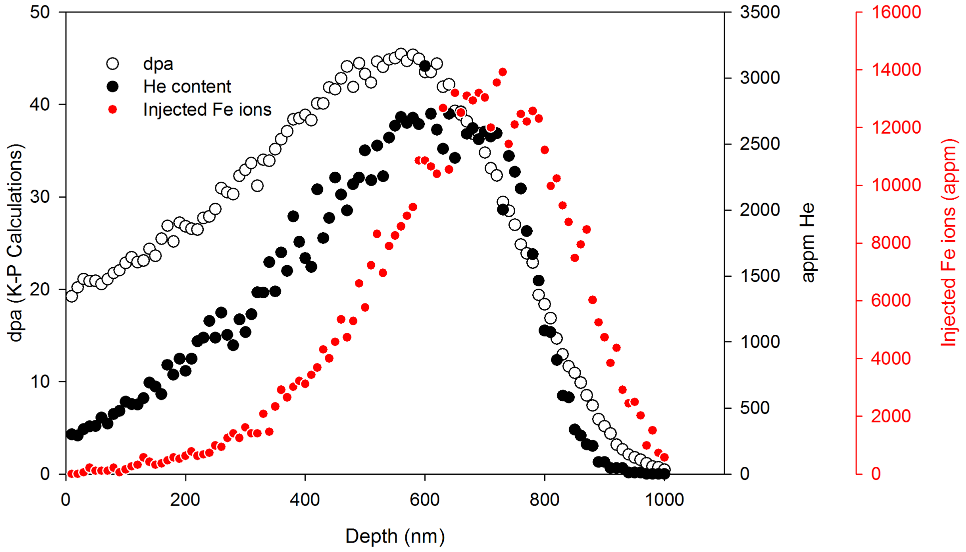

Figure 5.12: Irradiation conditions for the intermediate dose irradiations at 500 °C. The dose at the damage peak was 45 dpa. For the dual beam case, He was co-implanted to 58 appm He/dpa (at the damage peak). The irradiations were performed at JANNuS ex-situ irradiation facility at CEA/Saclay.

Post-irradiation microstructure was characterized by conventional TEM (on as irradiated electro-polished thin foils and on FIB specimens extracted from the bulk dimpled discs). Analytical tools: EDS in STEM mode (on FIB specimens) and APT were utilised on the dual beam irradiated Fe10%Cr. All these details can be found in this section. A summary of the specimens for each material, precise irradiation conditions and the characterization technique used can be seen in table 5.8.

In this section, the compositional measurements performed using EDS and APT are given in atomic percent for the sake of simplicity.

These results are recently published in Acta Materialia : $A.Bhattacharya\, et\, al.\, Acta\, Materialia$, 2014; 78 : 394 – 403

Materials	Specimen	Fluence *($ions.cm^{-2}$)*	Peak dpa	appm He/dpa	Peak dpa / s	Analysis technique
Fe5%Cr	TF and DD	$4.43\text{x}10^{16}$ (Fe) **$8.8\text{x}10^{16}$ (He)**	45	0 / **58**	$7.1\text{x}10^{-4}$	TEM
Fe10%Cr	TF and DD	$4.43\text{x}10^{16}$ (Fe) **$8.8\text{x}10^{16}$ (He)**	45	**58**	$7.1\text{x}10^{-4}$	TEM, STEM/EDS, APT
Fe14%Cr	TF	$3\text{x}10^{14}$ (Fe) **$1.46\text{x}10^{15}$ (He)**	0.33	**3030**	$1.6\text{x}10^{-4}$	TEM

Table 5.8: Summary of the investigated ion irradiation conditions at 500 °C and the characterization technique used. TF is thin foil; DD is dimpled disc of 100 µm thickness, prepared by jet electro polishing for a few seconds.

5.2.1 Fringes on dislocation loop planes in Fe5%Cr, Fe10%Cr and Fe14%Cr alloys: TEM analysis

All the samples (Fe5%Cr, Fe10%Cr and Fe14%Cr) were analysed by conventional TEM. Radiation-induced prismatic dislocation loops were noted in each case. KBF and WBDF TEM images of the loops in these materials are shown in figure 5.13.

In the Fe14%Cr dual beam irradiated up to 0.33 dpa, as seen in the previous section, large a<100> type prismatic loops were observed. The mean size was equal to 70 nm. Their habit planes were decorated with fringes (see figure 5.13a). This fringe pattern was neither very pronounced, nor very regular. For many of the loops, the fringes were partially visible and did not cover the entire loop plane. This is visible on the loops at the bottom left side in figure 5.13a, indicated by arrows.

On the contrary, in the dual beam irradiated Fe10%Cr up to 45 dpa, the fringes were much more pronounced (see figure 5.13 b). However, their shape was still rather irregular. Such fringes were also observed in the single and dual beam irradiated Fe5%Cr (figures 5.13c and 5.13d). They look similar to those in Fe10%Cr, and cover the entire loop plane.

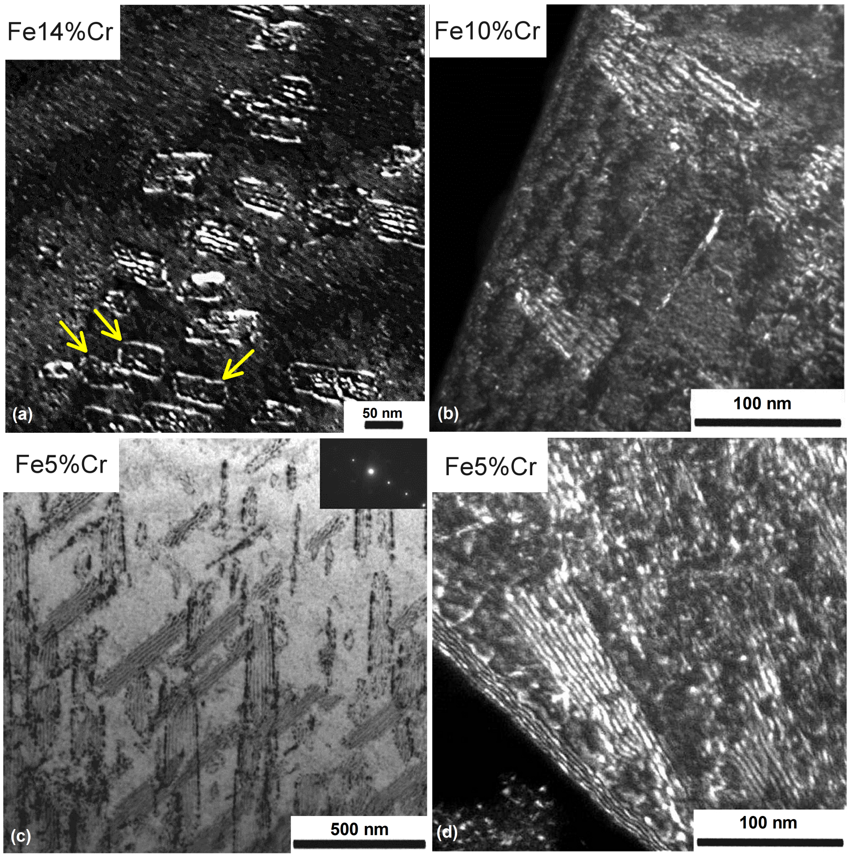

Figure 5.13: Characterization of the dislocation loop microstructure by TEM. Fringes inside the dislocation loops in (a). Fe14%Cr, dual beam irradiated to 0.33 dpa (thin foil disc) - WBDF image; (b). Fe10%Cr, dual beam irradiated to 45 dpa (FIB specimen) - WBDF image ; (c),(d). Fe5%Cr, single and dual beam irradiated to 45 dpa respectively (thin foil disc and FIB specimen) – KBF and WBDF images.

5.2.2 Analytical measurements on loops with fringes in dual beam irradiated Fe10%Cr

5.2.2.1 STEM/EDS analysis

EDS measurements were performed in STEM mode on the dislocation loops in Fe10%Cr dual beam irradiated up to 45 dpa. For reliable estimates by EDS on two dimensional objects (dislocation loops in our case), it is essential that the normal to the features of interest be exactly perpendicular to the electron beam direction. Hence, only a<100> type loops were analysed for the sake of simplicity. As mentioned in chapter 2 “Methodology”, section 3.4.2, in this case, the thin foil by FIB was prepared by selecting a (001) oriented grain determined by EBSD analysis. Due to this, the two a[100] and a[010] type families were perfectly on edge, and hence, aligned with the electron beam. Down axis convergent beam diffraction [138] was used to image the loops, in Low Angle Annular Dark Field (LAADF) [147] and High Angle Annular Dark Field (HAADF) imaging modes [138] . Images from the former are attained with electrons scattered through angles just outside the bright field region. Both elastically and in-elastically scattered electrons contribute to the detected signal. Due to the elastic contribution (Bragg scattering), diffraction contrast is visible in such images. While images from the latter are obtained by large angle inelastic, incoherent scattering of electrons, and hence can provide Z-contrast [138]. LAADF images of the irradiated zone of the specimen showing the four edge-on loops considered for EDS measurements are shown in figures 5.14a and 5.14b, and an HAADF image of one of these four loops is shown in figure 5.14c. The spectroscopy measurements revealed that there is Cr enrichment at the loops. A scatter plot of Cr concentration across the four selected dislocation loops, obtained with an electron beam of 2 Å spatial resolution is shown in figure 5.14d. The values are between 23 to 35 at.%. These values are well below the chromium content expected for the Cr-rich α′ phase at 500 °C (> 80% Cr).

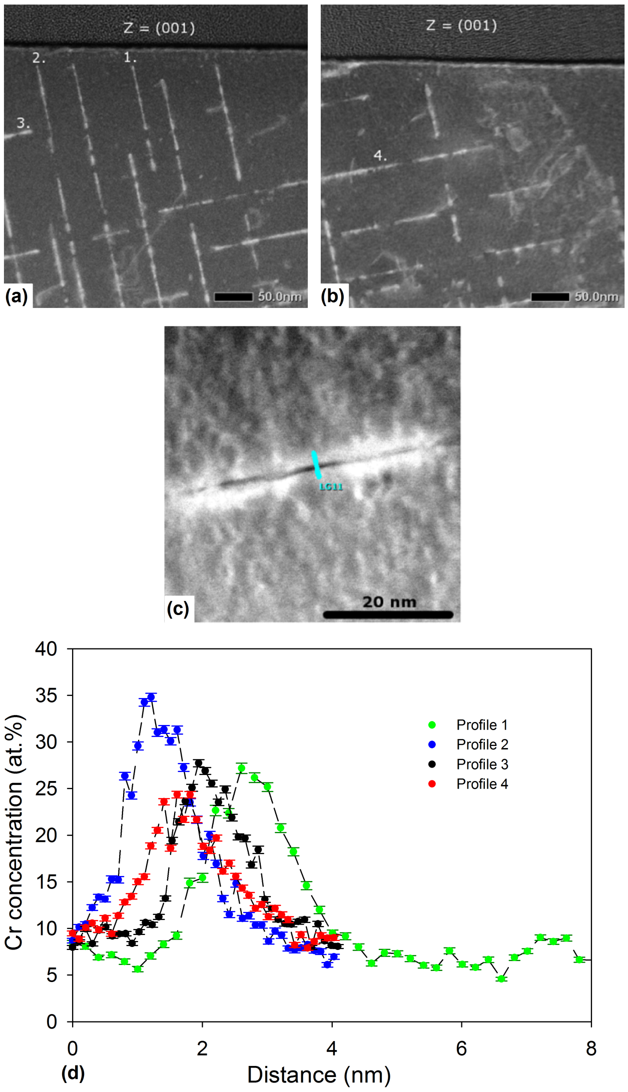

Figure 5.14: Characterization of Fe10%Cr, irradiated to 45 dpa, with 58 appm He/dpa. (a), (b) STEM-LAADF image of edge-on a<100> type dislocation loops in FIB thin foil oriented to (001) zone axis. (c) STEM-HAADF of loop number 3; the blue line represents the trace of the line scan for EDS measurement. (d) Enrichment profiles of Cr in atomic percent on the dislocation loops obtained by EDS analysis (resolution: 2 Å) using a Cs corrected Jeol ARM200F scanning TEM.

5.2.2.2 APT analysis

APT experiment was performed to gain insight about the distribution of Cr enriched areas within the dislocation loops. One out of the three APT needles prepared by FIB intercepted a planar object in the matrix. It could be a grain boundary or a dislocation loop. It was identified as a dislocation loop by noting the same position of the zone axis across the intercepted object. A 3D reconstruction of the needle, showing the loop on edge is depicted in figure 5.15a, where each dot represents a Cr atom. For the sake of clarity, the other chemical elements present in the specimen are not shown here. As described in chapter 2 "Methodology", section 3.4.3.3, a data filter was employed to select only the atoms belonging to areas for which the Cr content is higher than 13 at.%. The result is shown in the figure 5.15b. It reveals that Cr enriched areas are present on the loop plane and are not homogeneously distributed. A concentration profile of Cr extracted from an enriched region within the dislocation loop (marked by a red square) is given in figure 5.15c. The value obtained is 22 ± 2 at.%, which is coherent with those obtained by STEM/EDS analysis. Since the dislocation loops are very large as compared to the diameter of the needle, we believe that only a part of it has been intercepted. The oval shaped 3D reconstruction is due to the shape of the needle, and should not be confused as the actual shape of the loop.

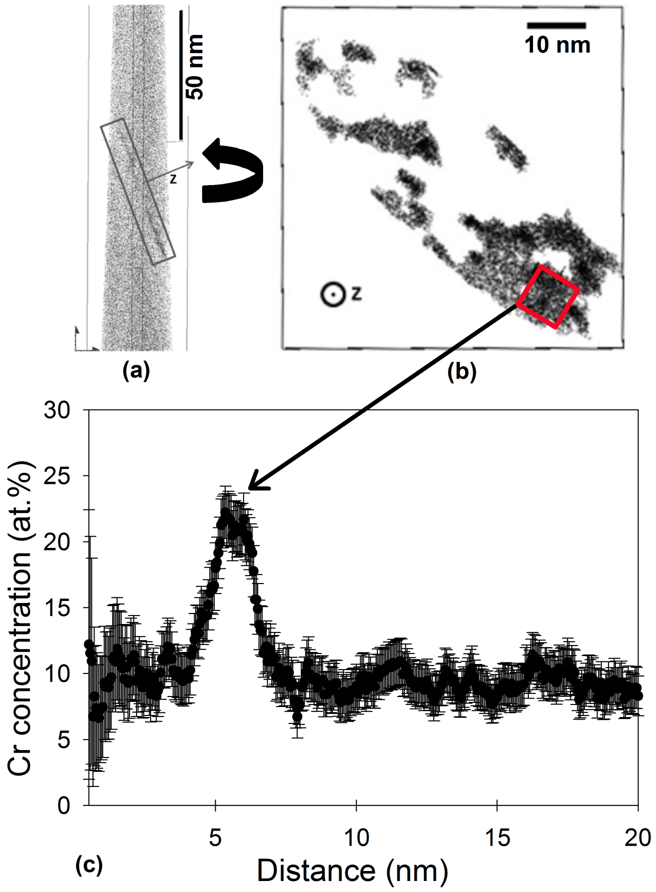

Figure 5.15: APT study on Fe10%Cr, irradiated to 45 dpa, with 58 appm He/dpa. (a). 3D reconstruction of the needle shaped specimen showing only the Cr atoms; the dislocation loop is marked in a box. (b). The dislocation loop showing regions enriched in Cr on the habit plane. (c). Profile of Cr in atomic percent obtained from an enriched region marked in square.

5.2.3 Loop and fringe disappearance upon in-situ annealing in TEM upto 627 ºC in Fe10%Cr

The dual beam irradiated Fe10%Cr was sequentially annealed inside the TEM. The specimen temperature evolution as a function of time is shown in figure 5.16a . For T < 627 ºC, no significant evolution of the dislocation loops took place. Only surface oxidation occurred. At 627 ºC, they began to shrink in size, ultimately disappearing completely by shrinkage. No loop mobility and subsequent elimination to surface was observed. A sequence of images extracted from the recorded video showing their evolution at this temperature is depicted in figure 5.16b , where the loops of interest are encircled. The first image corresponds to the time when the loop began shrinking, and is taken as t = 0. Thereafter, the image frames were recorded with respect to this time. Due to specimen drift during the experiment, these loops have moved towards the top of the image frame. The fringes were present as long as the loops were present. After the loops disappeared, no evidence of a secondary phase particle was observed at their position.

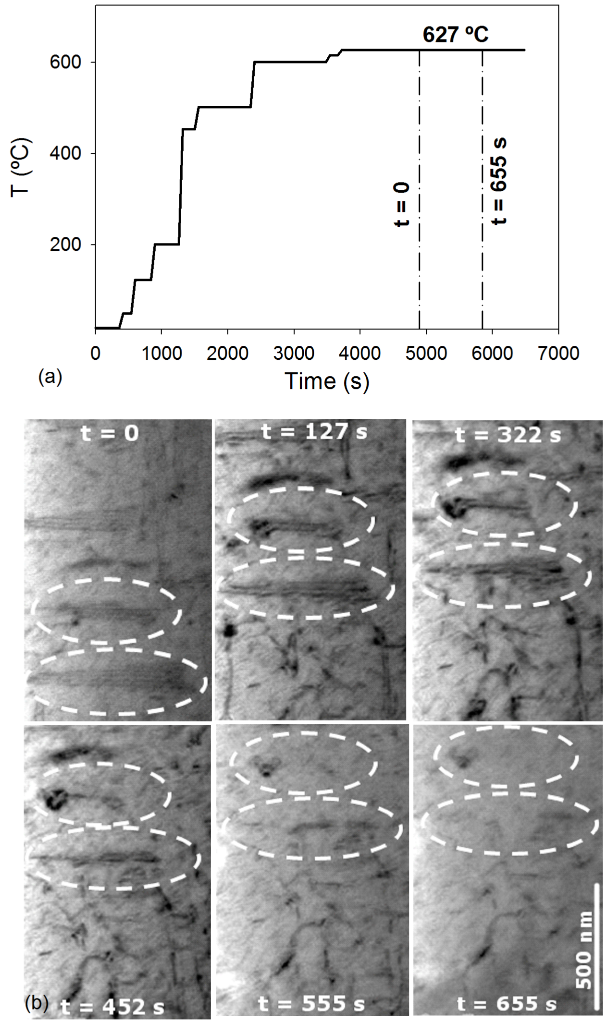

Figure 5.16: Evolution of the dislocation loops upon in-situ annealing in Fe10%Cr irradiated to 45 dpa, with 58 appm He/dpa (KBF images). (a). Temperature evolution profile of the specimen; loop evolution began at 627 ºC. (b) Evolution of the loops; t = 0 is the time when loops began to shrink. The time in the following images are with respect to this time.

5.3 Summary

Low dose in-situ irradiations at 500 ºC up to 0.33 dpa were performed on Fe14%Cr in single beam mode (only damage by self-ions) and dual beam mode (damage plus He co-implantation). For the later, He was co-implanted to 3030 appm He/dpa.

For the single beam case, no dislocation loop mobility was observed during the in-situ irradiation. Post-irradiation analysis revealed a mixed population of a<100> and a/2<111> type loops. However, at 500 ºC, only a<100> loops are known to be formed in bcc Fe. We can, thus, conclude that Cr addition (14wt.% in our case) to bcc Fe stabilises a/2<111> type dislocation loops.

The stabilisation of a/2<111> loop population was responsible for the higher loop number density in Fe14%Cr as compared to bcc Fe irradiated under similar conditions.

When irradiation was performed under same conditions, but with co-implantation of He, the microstructure comprised of only a<100> type loops : no a/2<111> type loops were detected. The average size was smaller and the loop number density was higher as compared to bcc Fe irradiated under similar conditions.

The plane of the dislocation loops was decorated with a fringe pattern for the dual beam irradiated Fe14%Cr. This was puzzling because stacking fault energy in bcc Fe is high. So, the dislocation loops are not expected to be faulted. To probe this effect into more detail, intermediate dose single and dual beam irradiated (up to 45 dpa) Fe5%Cr and Fe10%Cr specimens were thoroughly analysed in addition to the low dose irradiated Fe14%Cr. The presence of Cr enriched zones on the habit plane of the dislocation loops was shown by complementary experimental techniques: conventional TEM, APT and analytical STEM/EDS.

When imaged by TEM using the classical diffraction contrast imaging techniques, these enriched zones produced fringes on the loop plane. For the low dose case, these fringes were not completely developed, while at 45 dpa the pattern was much more pronounced.

A quantitative estimate of this enrichment was deduced by STEM/EDS and APT. The Cr content in these areas was between 23 to 35 at.% by EDS measurements performed on four edge-on loops, while it was estimated to be 22 ± 2 at.% by APT. These values are well below the chromium content of the Cr rich α' phase. The values obtained are coherent between these two techniques.

Upon in-situ annealing at 627 ºC, these loops disappeared by shrinkage without leaving any secondary phase particle. The fringes were present as long as the loops were present.

A detailed discussion is given in chapter 6.

Chapter 6

Discussion of results

We have performed self-ion irradiations, with and without simultaneous implantation of He, to different doses on a series of high purity FeCr alloys along with a reference bcc Fe, to understand the behaviour of these model materials in high temperature radiative environments. In all the cases, the irradiation temperature was fixed at 500 ºC. The first step was high dose irradiations, more than 100 dpa, with and without He co-implantation. The main objective of this irradiation was to see the cavity microstructure and swelling behaviour in these materials. For FeCr alloys, the swelling data was extracted from an intermediate depth corresponding to 128 dpa and 13 appm He/dpa. This is close to the fusion reactor conditions for which F-M steels are the primary candidates. While for bcc Fe, the entire depth distribution of cavities was thoroughly studied. In the second step, low dose irradiations (0.33 dpa with 0 and 3030 appm He/dpa) were performed to see the evolution of the dislocation loop microstructure. The focus was on the quantitative information in terms of Cr and He effect on the dislocation loops, which are difficult to derive from the high dose irradiated microstructures due to the formation of entangled dislocation networks. In the third step, intermediate dose irradiated (45 dpa, 0 and 58 appm He/dpa) materials were analysed to have more information about the dislocation loop microstructure. The study was structured to understand the distribution of Cr adjacent to radiation induced the dislocation loops in FeCr alloys. This analysis was prompted by an unexpected fringe pattern inside dislocation loops observed by conventional TEM in FeCr alloys. In all the cases, the microstructure was analysed by conventional TEM. STEM/EDS and APT were used when analytical information on Cr distribution was needed.

Here, a detailed discussion of the results is presented along with the relevant available data in the literature. We have also used the cluster dynamics code CRESCENDO to discuss a part of our results. In this case, it was the analysis of injected ions which can act as interstitials with a consequence of an artificial void swelling suppression around the damage peak area.

The chapter is divided into two broad sections to discuss results separately in Fe and in FeCr alloys. For Fe, the role of He and injected ions on void swelling is discussed. Then, a discussion of the cavity microstructure and swelling observed in FeCr alloys is presented. This is followed by the discussion on the effect of Cr and a combined effect of Cr and He on the dislocation loops. Finally, the discussion of the enrichment of Cr on the prismatic dislocation loops in FeCr alloys is presented.

6.1 Pure bcc Fe

6.1.1 Swelling diminution by helium co-implantation

High dose irradiations, up to 157 dpa, at 500 ºC were performed in high purity bcc Fe in dual beam mode (He ions injected simultaneously) and single beam mode (no He) to see the influence of He on the cavity microstructure. For the dual beam case, He content at the damage peak was 17 appm He/dpa. An analysis of the microstructure by TEM on FIB thin foils revealed a strong void swelling reduction when He was co-implanted all along the damage depth. For instance, in an intermediate depth of 300 - 400 nm (corresponding to 128 dpa, 13 appm He/dpa at 2.6 x 10^{-3}dpa/s), swelling reached 8.5% for the irradiation without He as compared to only ~1% when He was co-implanted. This strong diminution was induced by large reduction in cavity sizes (67 nm when He was not present as opposed to only 6.8 nm when He was present), but with almost two orders of magnitude increase of the number density. An analysis of the cavity sizes revealed that for the dual beam case, size distribution was very broad. Smaller sized cavities (2 - 4 nm in size) were present all along the target depth. On the other hand, in single beam case, no such small cavities were present which means that the nucleation phase of the cavities was over and the microstructure was controlled by void growth.

Such a behaviour makes us re-think about our established notions of He influence on swelling. It is long believed that He causes swelling. However, from these results, it is clear that this may not always be the case. Thus, caution must be addressed when interpreting or analysing the existing literature results or future experimental results on swelling behaviour of steels in terms of He. In the following paragraphs, we have thoroughly discussed this effect.

Reduced swelling due to He in high purity bcc Fe was also seen in the recent work of Brimbal and co-workers [119]. But swelling remained low. For irradiations at 500 ºC up to 45 dpa, they observed 0.40% swelling when no He was present; which then dropped to 0.31% and 0.2 % by co-implantation of 250 appm He and 2500 appm He respectively. The average size was seen to drop from 24 nm to 7.2 nm for the highest He implantation dose (accompanied with increase in number density). These results show similar behaviour to our results. Apart from this study, other relevant works available in the literature is not on bcc Fe, but usually on fcc austenitic steels. For example, in a relatively old study performed by Packan and Farrell [8] on the influence of the method of gas implantation on void swelling of 316 stainless steel, similar results were seen when He was co-implanted. At 627 ºC up to 70 dpa, swelling reached 18% when no He was present, and dropped to 11% when He was simultaneously injected (1400 appm He corresponding to 20 appm He/dpa). The corresponding images of the void microstructure taken from this paper is shown in figure 6.1. More details of the microstructure are published by the authors in [148] where once again it was seen that He reduced cavity sizes (90 nm without He and 49 nm with He) and increased number density (4.2 x 10^{20} m^{-3} without He and 1.3 x 10^{21} m^{-3} with He). Thus, the drop in net swelling was due to the reduction of the cavity sizes. In a related study, the authors observed this reduction over a wide range of temperature (567 ºC to 827 ºC) [149]. Furthermore, pre-injection of helium was also seen to strongly suppress swelling (only 4% and 1% for hot-preinjection (at 627 ºC) and cold pre-injection (at RT) respectively; see figure 6.1).

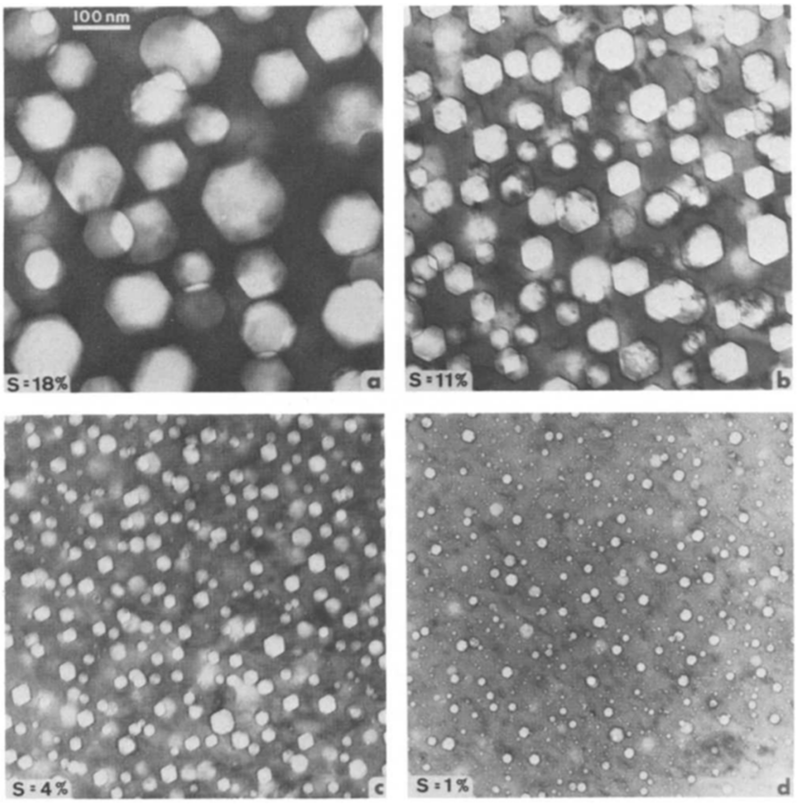

Figure 6.1: Study by Packan and Farrell [8] on the effect of different ways of helium incorporation on the void microstructure in austenitic stainless steel. Irradiation performed by 4 MeV Ni ions at 627 ºC to 70 dpa (swelling given on each microstructure). (a). No added gas; (b). simultaneous injection of a cumulative 1400 appm He; (c). pre-injection of 1400 appm He at 627 ºC; and (d). pre-injection of 1400 appm He at RT.

From a theoretical point of view, it is well known that He stabilises small vacancy clusters. Ab-initio studies [29, 121] of He interaction with defects in bcc Fe (discussed in Chapter 2 "Bibliography") show much higher binding energy between He-V complexes as compared to vacancy clusters. This means that He would induce much higher nucleation of cavities as compared to the situations when He is absent. This phenomenon is indeed seen in experimental results (including ours) where number density of cavities is higher when He is co-implanted. Apart from that, within the framework of the "dislocation bias model", it is known that swelling is induced by the effect of bias (i.e. preferential migration of interstitials at dislocations which leaves vacancy super-saturation in the matrix) [150, 31]. The cavity begins to grow more rapidly in response to an excess flux of vacancies over interstitials. However, this excess flux of vacancies, and hence cavity growth, is strongly dependent on the relative point defect sink strengths of the microstructural features including cavities themselves [150]. But cavities are unbiased or neutral sinks because they do not have any associated strain fields (which means no preferential absorption for any kind of defect). If the number density of cavities increase sufficiently in the irradiated material due to He, it is possible that they can become the dominant sinks for the point defects instead of the dislocations (lines or loops). In that case, the relative interstitial flux towards the dislocations would be reduced, reducing the vacancy flux towards the cavities due to enhanced recombination. Cavities would then be unable to grow, thereby, restricting swelling. The quantitative term to explain this behaviour is the ratio between the sink strengths of the dislocations and cavities [150] shown by

$$Q = \frac{Z^d_{i,v} L}{Z^c_{i,v} 4\pi r_c N_c}$$

In this equation, $Z^d_{i,v}$ and $Z^c_{i,v}$ are the bias factors of the dislocations and cavities (for interstitials and vacancies) respectively ; L is the total dislocation length; $r_c N_c$ is the product of the average cavity size and number density. For neutral sinks (like cavities), bias factor $Z^c_{i,v}$ is taken as unity.

Based on this Q-value, an experimental data set on steady state swelling in austenitic stainless steels and F-M steels is collected by Mansur and Lee [150]. It shows that the swelling rate shows a peak when $Q = 1$ (i.e. when the bias by dislocations and cavities is equal). If $Q > 1$, the dislocation density is high enough to significantly reduce the vacancy supersaturation needed to cause swelling. This leads to swelling decrease. When $Q < 1$, the bias is controlled by the cavities which are in high number density. In that case, swelling drops again. In our case, as seen in Chapter 4 “Irradiated microstructure at high dose”, the dislocation loop microstructure for single beam and dual beam irradiated bcc Fe was similar. Due to this, it would be reasonable to assume that the dislocation bias for both these irradiation conditions should also be similar. Then, Q and hence swelling would be inversely proportional to the cavity sink strength:

$$Q \propto (Z^c_{i,v} 4\pi r_c N_c)^{-1}$$

Taking $Z^c_{i,v}$ equal to unity, the depth variation of the cavity sink strength for the single beam and dual beam irradiated bcc Fe is shown in figure 6.2. We can see that in the entire damage depth, the sink strength of the cavities is higher when He is co-implanted (essentially due to a higher cavity number density). This, hence, explains why swelling is less when He is present all along the specimen depth.

Furthermore, an influence of He/dpa on void swelling is also known to exist from studies performed in austenitic steels. It is shown by Katoh and co-workers and by Stoller that swelling peaks at intermediate He/dpa ratios [151, 152] . The corresponding results taken from these references are shown in figures 6.3 and 6.4. This behaviour was explained by Stoller [151] using similar arguments based on the variation of the sink strength ratio Q mentioned earlier: the initial increase in swelling is due to early nucleation induced by He, which continues to increase until the dislocation and cavity bias are equal; beyond that, the excessive nucleation changes the bias towards cavities due to which swelling decreases. In our case, He/dpa varied from ~ 5 appm He/dpa in near surface areas to 17 appm He/dpa at the damage peak. But all along the depth, swelling was less when He was present. We did not see a similar peak in swelling appearing at a given He/dpa. We attribute this to the irradiation conditions (in terms of dpa, dpa rate and PKA spectrum) which vary strongly upon following the damage depth. Thus, a direct comparison with the He/dpa effect, as seen for austenitic steels, can not be made due to large variability of the parameters. However, it is possible that for each swelling data point which corresponds to a unique irradiation condition along the target depth, we may be at the falling part of the curve at higher He/dpa values in figure 6.4. In this way, we are always in the condition where void swelling is less when He is added.

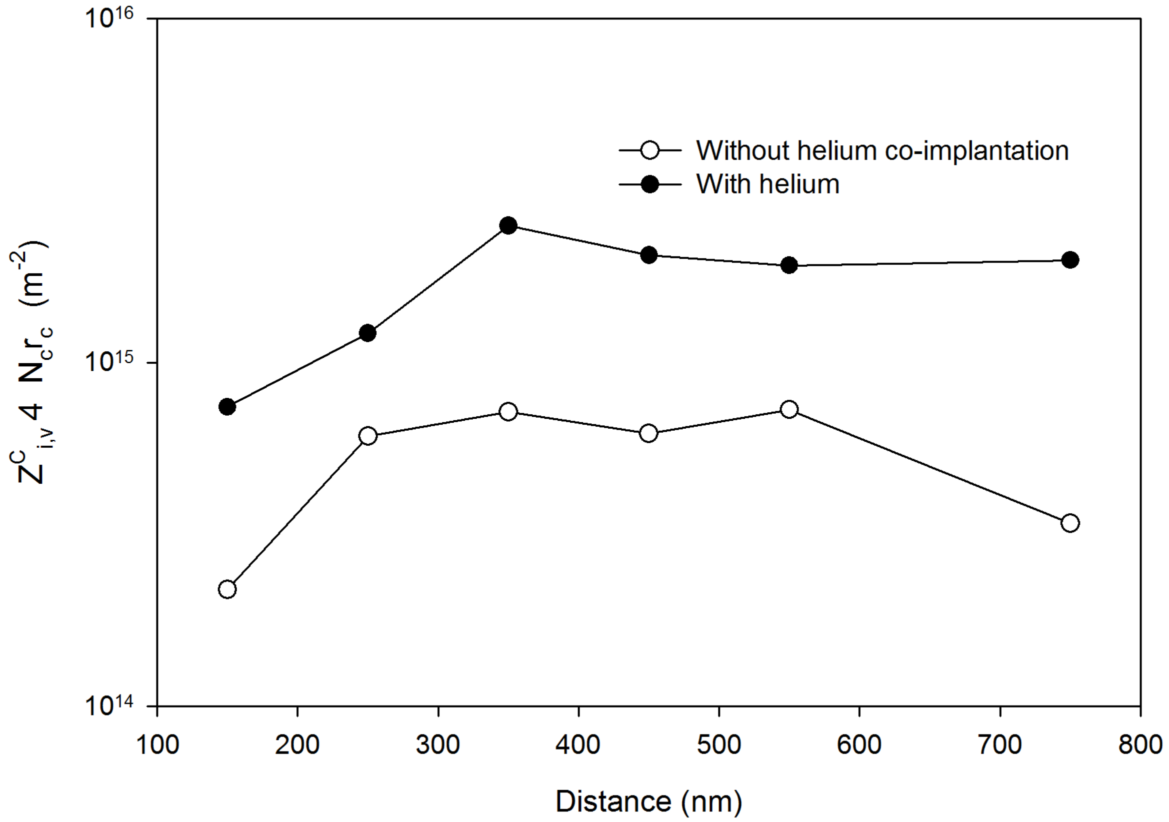

Figure 6.2: Depth variation of the cavity sink strength estimated in the single and dual beam irradiated bcc Fe to 157 dpa (at the damage peak). For the dual beam case, He was co-implanted to 17 appm He/dpa at the damage peak .

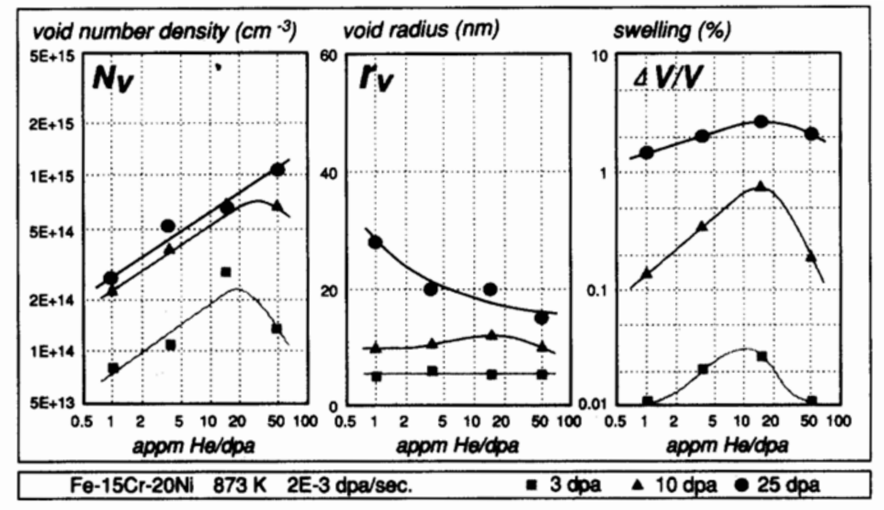

Figure 6.3: Study of Katoh and co-workers [152] on He/dpa dependence of the characteristics of void microstructure in Fe-l5Cr-20Ni austenitic steels. Irradiations were performed at 600 ºC up to 3, 10 and 25 dpa (at 2 x 10^{-3}dpa/s) using 4 MeV Ni^{3+} ions and co-implanted with energy degraded 1 MeV He^{+} ions.

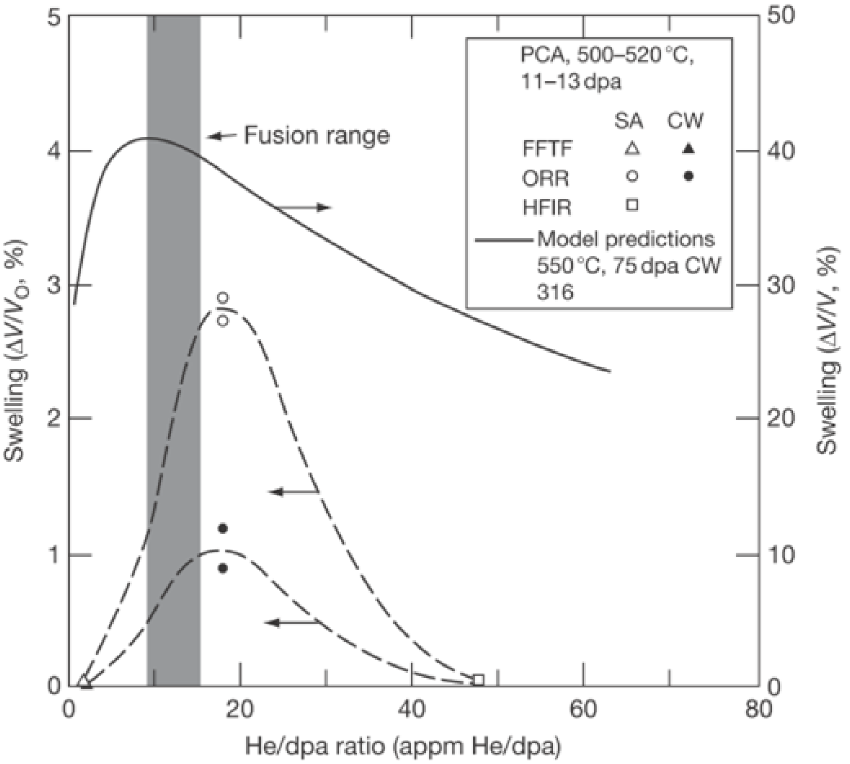

Figure 6.4: Data from Stoller [151] on the neutron irradiations of cold worked and solution annealed austenitic stainless steels at 500 - 520 ºC suggesting that swelling peaks at an intermediate He/dpa ratio.

6.1.2 Cavity facets

In both single beam and dual beam irradiations at high dose, large cavities in bcc Fe were faceted with cubic or cuboidal geometry (see figure 4.2). Their facets were mostly aligned along {100} planes. This suggests that the addition of He, at least up to the level as in our case, does not have any impact on the orientation of the facets of the cavities in bcc Fe. However, the smaller cavities (less than 4 nm) formed in the presence of He were not faceted. But it is possible that in these cases, facets were close to the resolvable limits of a conventional TEM for observations using Fresnel contrast [137]. Horton and co-workers had also mentioned that the largest cavities they observed in bcc Fe were with facets after neutron irradiation [54]. Ohnuki and co-workers [12] had reported observations of cavity facets contained along {100} planes for irradiations using C^+ ions up to 10 dpa. More recently, studies by Brimbal and co-workers [13] also observed cavity facets for irradiations up to 45 dpa. However, in this case, facets were identified to be along {100} and {110} planes. Based on this result, if we carefully observe the cavities once again in our case, it seems to suggest that we may be in similar situation as of Brimbal and co-workers. For instance, if we look at the images of larger voids in single beam irradiated Fe in figure 4.2, we realize that for many cubic cavities, the structure is not "perfectly cubic". They have a small facet (or sometimes more than one small facet) at the edge of the void, which seems aligned along {110} planes. For the case of Brimbal, cavities with {110} facets were octagonal in shape, but not cubic with an additional small {110} facet as in our case. This observation is, thus, curious and to the best of our knowledge, it has never been reported before. At present, we do not have a concrete explanation for such shape of voids. However, it might be the case that these are occurring due to shape transitions to the most stable structure upon irradiation. It seems that the shape is trying to evolve to a cubic geometry which earlier might have been octahedral or vice-versa, and what we observe is the transient phase where facets of both geometries (the new cubic geometry and the old octahedral geometry) are visible. It can also be linked to the surface energy of the facets. If {110} and {100} facets are close in energy, we would expect to have both populations represented.

6.1.3 Effect of injected ions on void swelling

In both single and dual beam high dose irradiated bcc Fe, it was noticed that void swelling dropped significantly in the areas close to the damage peak (at 157 dpa). For instance, in the single beam case, void swelling estimated by TEM just at the beginning of the damage peak (around 550 - 600 nm depth) was nearly one-third its value at the intermediate depths. Since the damage level is maximum at the damage peak, less swelling in this zone than in the areas prior to the damage peak, is not expected. However, during ion irradiation experiments, the ions deposited in the material lie very close to the damage peak. In our case, the implantation peak of 2 MeV Fe ions was nearly at ~700 nm depth, with a long tail extending towards the damage peak region around 550 - 600 nm. At the implantation peak, the amount of injected Fe ions was ~40000 appm (4 at.%). It reduces to between 20000 - 30000 appm at the damage peak. We speculate that these injected ions could behave as "injected interstitials" which may artificially reduce cavities around the damage peak. If it is the case, this would be an artefact of ion irradiation experiments which we should be aware of especially for void swelling studies.

To probe and discuss this effect, we simulated the irradiation conditions up to 157 dpa on bcc Fe using the cluster dynamics code CRESCENDO. The approach was restricted to the simple case without

He. The spatial discretization feature of the code, mentioned in Chapter 3, section 3.5, permitted us to follow the heterogeneous damage evolution by the Fe ions. A simplified cascade condition for 2 MeV Fe self-ions was utilised in which it was considered that only mono-interstitials and mono-vacancies are produced. Indeed, this approximation is far from reality, but allows for quick qualitative estimates without having to go into details of the displacement cascades and point-defect cluster formation directly within cascades. SRIM estimates of the depth variation of dpa rate and the injected ion implantation rate are shown in figure 6.5. These were given as inputs for the simulation. We can see that the rising part of the injected ion peak overlaps with the peak damage area. The dpa rate at the damage peak was ~3.5 x 10^{-3} dpa/s, while the ion injection rate at the implantation peak was ~1 appm/s . Information about void swelling can be known if the concentration and size of vacancy clusters can be obtained. For this, inputs on defect binding and migration energies in bcc Fe were necessary. They were taken from ab-initio based results available in the literature [29]. The parameters related to the material (grain size, dislocation density, sample thickness), irradiation time and dose correspond to our actual experimental conditions. All the input parameters are summarized in table 6.1. In our case, it was considered that only mono-interstitials and mono-vacancies are mobile.

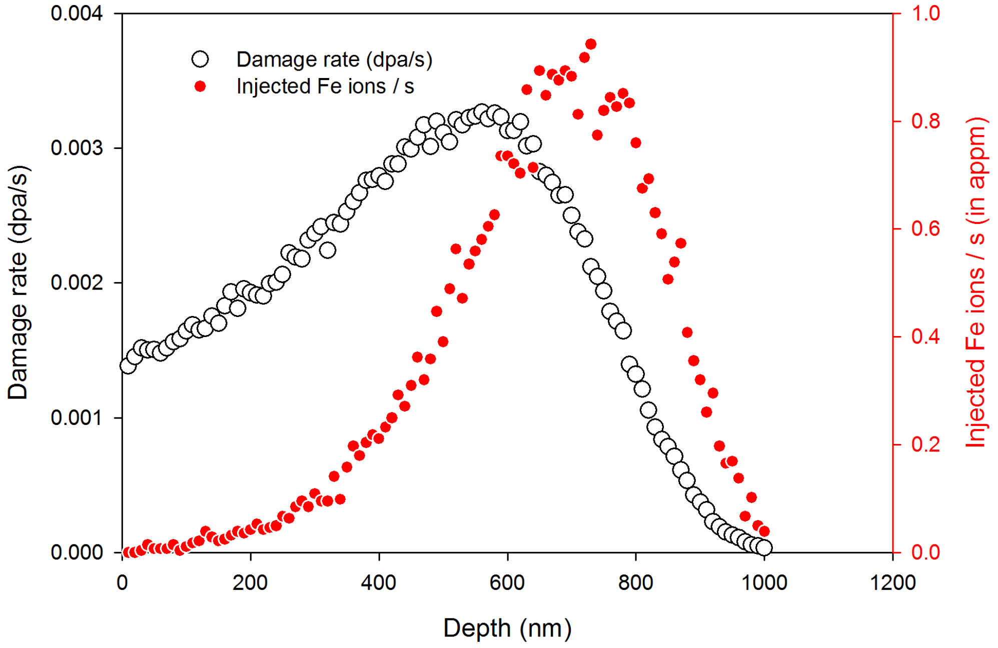

Figure 6.5: Depth distribution of damage rate in dpa/s and rate on Fe ion implantation (in appm/s) obtained from SRIM for Fe matrix.

Temperature	500 ºC
Irradiation dose and time	157 dpa (at peak) 4.57 x 10^4 s
Sample thickness	5 μm
Number of slices	40
Pre-exponential diffusion coefficient	8.2 x 10^{-3} $cm^2.s^{-1}$
Migration energies of monomers E_i^m, E_v^m	0.34 eV ; 0.67 eV (larger clusters are immobile)
Formation energy of monomers E_i^f, E_v^f	2.12 eV ; 3.77 eV
Binding energy of vacancy clusters (up to 4) E_v^b (2V, 3V, 4V)	0.3 eV ; 0.67 eV ; 1.29 eV
Binding energy of interstitial clusters (up to 4 interstitials) E_i^b (2I, 3I, 4I)	0.8 eV ; 1.72 eV ; 3.36 eV
Dislocation bias	Z_i= 1.1 Z_v= 1
Sinks	Grain boundaries (grain size = 200 μm) Initial dislocation density = 10^8 cm^{-2}

Table 6.1: Parameters used for simulations using CRESCENDO. *i* and I stands for interstitial and *v* and V stands for vacancy.

After supplying all the necessary parameters, the simulations were run for three cases to perform a comparative study: without any injected ions (0 appm/s injection rate), 1 appm/s (the actual experimental condition) and 100 appm/s (hypothetical case). For the last case, the actual injected ion profile was simply multiplied by 100 to obtain the new profile. The analysis was performed at two depths : 221 nm below the surface (far from the injected ion peak) and 700 nm below the surface (close to the damage peak) We should note that for the sake of convention, vacancy clusters are taken with minus sign for size.

The vacancy cluster distribution for the three cases of injected ions at two depths: 221 nm below the surface and 700 nm below the surface is shown in figures 6.6 and 6.7 respectively. We can see that for all the three cases, firstly there is a very high concentration of small vacancy clusters, mainly mono-vacancies. This is expected because vacancy concentration is always higher in materials after the irradiation. Thereafter, for 221 nm depth, there is no significant difference between the three vacancy cluster distribution curves: 0 appm/s and 1 appm/s curve coincide completely and 100 appm/s curve is shifted very slightly (see figure 6.6). It implies that this zone is unaffected by the presence of the excess interstitials around the damage peak. At 700 nm depth (figure 6.7), 0 appm/s and 1 appm/s curve once again coincide. But for 100 appm/s, the impact of injected ions was clearly visible. We can see that both the size and concentration of vacancy clusters dropped significantly. This readily implies that void swelling in this zone would be lower than the areas prior to the damage peak.

It should be noted that for the actual irradiation conditions corresponding to 1 appm/s, simulations show no effect of the injected ions. But, experimentally, we indeed saw swelling suppression around the damage peak. We believe this is a discrepancy that could arise from our definition of the primary damage production in the simulations. As mentioned earlier, to simplify our calculations we assumed that only mono-interstitials and mono-vacancies are formed by the ions, whereas displacement cascades are formed in reality. Furthermore, the mobility of larger clusters was also not taken into account. These results, therefore, do not provide quantitative evidence of the phenomenon. But they are qualitatively robust.

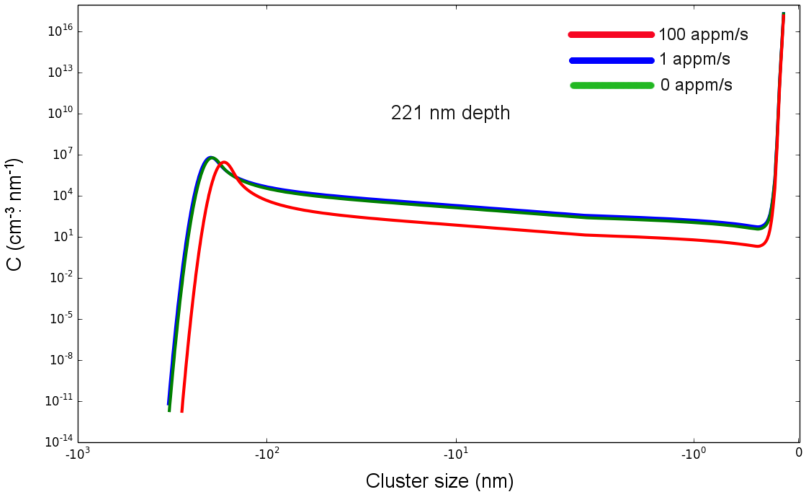

Figure 6.6: Vacancy cluster distribution as a function of cluster size at 221 nm depth, far from the zone where injected ions come to rest. Three cases were considered: 0, 1 and 100 appm/s injected Fe ions. By convention, vacancies are taken with a negative sign in CRESCENDO. Thus, for sizes, we must ignore the negative sign.

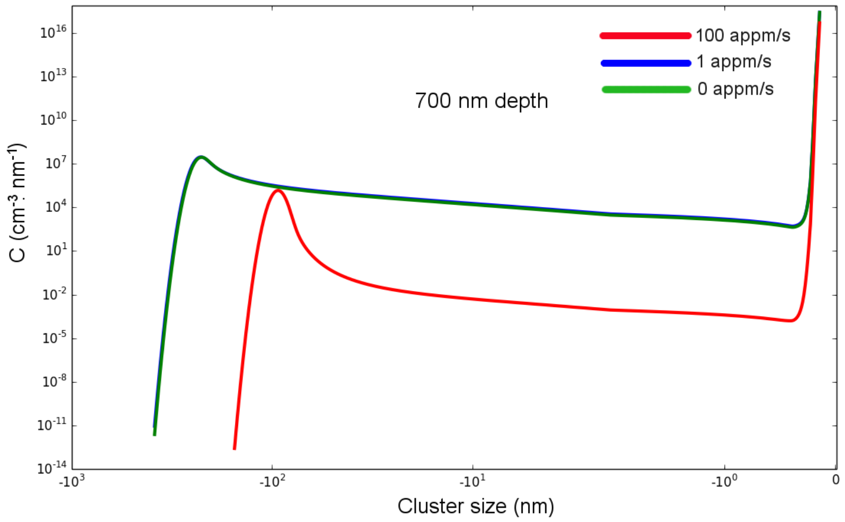

Figure 6.7: Vacancy cluster distribution as a function of cluster size at 700 nm depth where injected ions come to rest. Three cases were considered: 0, 1 and 100 appm/s injected Fe ions. By convention, vacancies are taken with a negative sign in CRESCENDO.

For added information, the interstitial cluster distribution at 221 nm and 700 nm depth is also plotted (see figures 6.8 and 6.9). By convention, interstitial cluster size is taken as positive. We can see that for 221 nm depth, not a strong difference exist between all the curves. But at 700 nm, the size of the interstitial clusters was higher when excess interstitials were injected into the system. This is expected because injected interstitials could also contribute to the interstitial clusters and eventually to the dislocation loop microstructure.

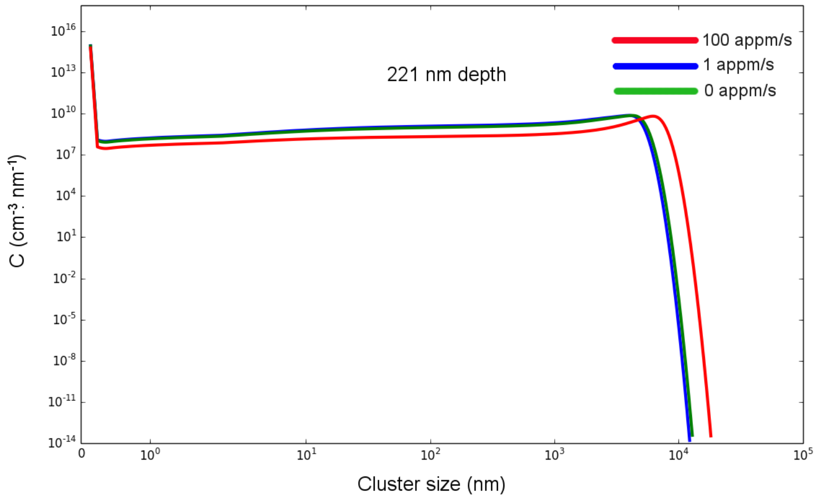

Figure 6.8: Interstitial cluster distribution as a function of cluster size at 221 nm depth. Three cases were considered: 0, 1 and 100 appm/s injected Fe ions

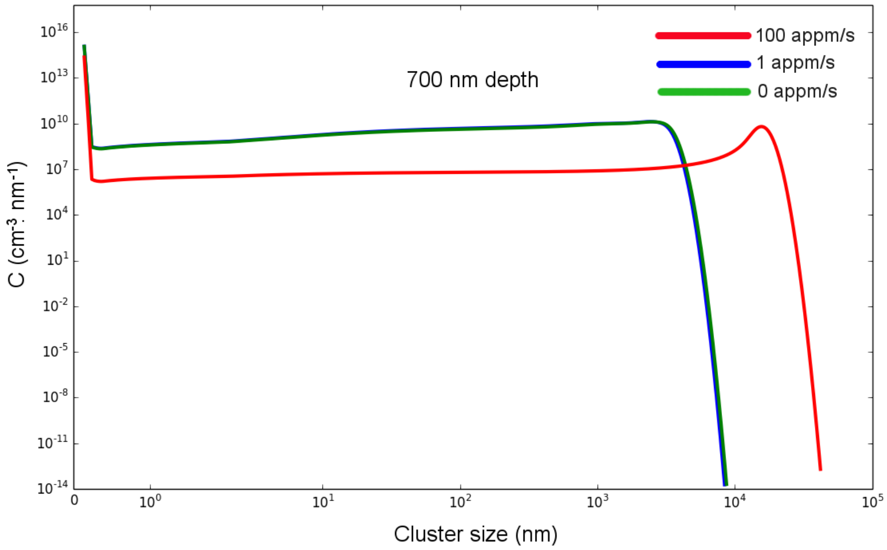

Figure 6.9: Interstitial cluster distribution as a function of cluster size at 700 nm depth. Three cases were considered: 0, 1 and 100 appm/s injected Fe ions

Many previous ion irradiation experiments, some coupled with simulation studies on a variety of metallic materials, have also reported similar behaviour of highly reduced void swelling around the peak damage area [153, 154, 155, 156, 157, 158, 159, 160]. For instance, Tanigawa and co-workers [153] irradiated reduced activation F82H (8%Cr - 2%W-V-Ta) in dual beam mode by 4 MeV Ni^{3+} ions and 1 MeV He^{+} ions at 450 ºC up to 100 dpa - 10 appm He/dpa. They observed a strong drop in void swelling at the damage peak compared to areas before. In this case, the damage peak was located around 1000 nm and Ni implantation peak was located around 1200 nm. Nearly 2 at.% of Ni was estimated at the implantation peak. Based on this, the authors considered injected Ni ions to be responsible for reduced voids in this zone. Lee and co-workers [155] performed ion irradiations using 4 MeV Ni ions on pre-neutron irradiated 316 stainless steels. The neutron irradiation was performed at 450 ºC and 584 ºC up to ~43 dpa. Following that, ion irradiations were performed up to 60 dpa at 600 ºC (for 450 ºC neutron irradiated sample) and 625 ºC (for 584 ºC neutron irradiated sample). They observed swelling peak at ~450 nm depth and not at 700 nm where the damage peak was located. The effect was more pronounced for the specimen pre-conditioned by neutrons at 584 ºC. In these cases, the ion implantation peak was located at 800 nm depth. Based on these results and combining it with rate equations, the authors suggested that void growth is suppressed by injected interstitials. Rate theory calculations by Brailsford and Mansur [158] indicated void growth suppression by injected ions at all the temperatures considered in their simulations (400 - 600 ºC). The effect was more visible at low temperatures, where recombination is dominant. Furthermore, similar rate theory study by Plumton and Wolfer [156] showed that void nucleation rate also decreases drastically due to injected ions close to the damage peak. In this case, the simulations were performed on Ni irradiated by 5 MeV Ni ions for a temperature range of 300 - 600 ºC. The effect was highly pronounced at 300 ºC. The ratio of excess interstitials to the interstitials produced by irradiations was about three times higher for 5 MeV case as compared to 14 MeV case, which yielded much higher suppression of void nucleation rate in the former.

From the coupling of our experimental results with cluster dynamics simulations, and from all the available literature data mentioned above, it is sufficient to conclude that injected ions can artificially suppress void swelling around the damage peak in ion irradiation experiments. Thus, for studying cavities in irradiated materials, the damage peak should always be avoided.

6.2 FeCr alloys

6.2.1 Effect of Cr on void swelling

Dual beam irradiated bcc Fe and FeCr alloys with Cr level varying from 3wt.% to 14wt.% were studied to see the influence of Cr on cavity microstructure and swelling at 500 ºC. The analysis was performed at an intermediate depth of 300 - 400 nm below the irradiated surface to avoid surface effects and artefacts of injected ions (as discussed in the previous section). This zone corresponds to a dose of 128 dpa (2.6 x 10^{-3}dpa/s) and 13 appm He/dpa. TEM characterization on FIB thin foils revealed a very strong reduction of void swelling just by the addition of 3wt.% Cr. This was due to a drastic reduction of cavity sizes (however number density in FeCr alloys was an order of magnitude higher). Beyond this concentration, swelling stayed almost the same for Fe5wt.%Cr; it increased at Fe10wt.% Cr, followed by a decrease at higher Cr levels. The behaviour is, thus, a non-monotonic function of the Cr content. For the sake of clarity, the swelling curve is shown once again in figure 6.10c. All the other literature results of swelling in FeCr alloys versus Cr content obtained after fast neutron irradiations are also shown. If we compare our results with these results, it can be seen that the initial drop in swelling by addition of 3wt.% Cr observed in our case is consistent with the neutron irradiated results at 30 dpa at three different temperatures (380 ºC, 420 ºC and 460 ºC) [35] (see figure 6.10b). However, in this study, a complex modulation of the swelling trend was noted beyond 5wt.% Cr: at 420 ºC swelling increased at higher Cr levels and at 380 ºC it first decreased slightly, followed by a rather steep increase. In the third set of data at 460 ºC, the variation became non-monotonic with swelling peaking at 10wt.%Cr. Due to these three contrasting results, the trend was not clear. We have not attempted to understand why there were such irregularities in the 30 dpa studies present in the literature. Nevertheless, it must be noted that neutron irradiations in reactors are prone to temperature fluctuations due to power fluctuations [117]. These results may, thus, be biased due to this effect. The discrepancy is clarified by our study where it is seen that the trend is non-monotonic with a local swelling maxima around ~ 10wt.% Cr. It correspond well with the other low dose (15 dpa and 21 dpa [107]) and high dose neutron irradiated data (between ~ 35 to 200 dpa [3, 106, 115]) where a swelling maxima was indeed noted at 9wt.% Cr (see figure 6.10a and b). But most of these neutron irradiated studies did not include a reference bcc Fe, due to which it was not possible to conclude about the transition from Fe to FeCr alloys. In an separate neutron irradiated study by Porollo and co-workers at 400 ºC to dose range 5.5 - 7.1 dpa [53], a reference bcc Fe was indeed studied. In this case, the initial swelling drop from Fe to Fe2wt.%Cr was pronounced. Beyond that the trend faintly resembled a non-monotonic variation. However, in our opinion, this may not be the best example because the dose was not exactly the same for each specimen. Therefore, based on our results and a few of older results present in the literature after irradiations in a fast reactor, it is now possible to conclude that Cr suppress void swelling when added to bcc Fe matrix and that swelling variation is non-monotonic with a local maxima around the intermediate Cr levels of 9 - 10wt.%.

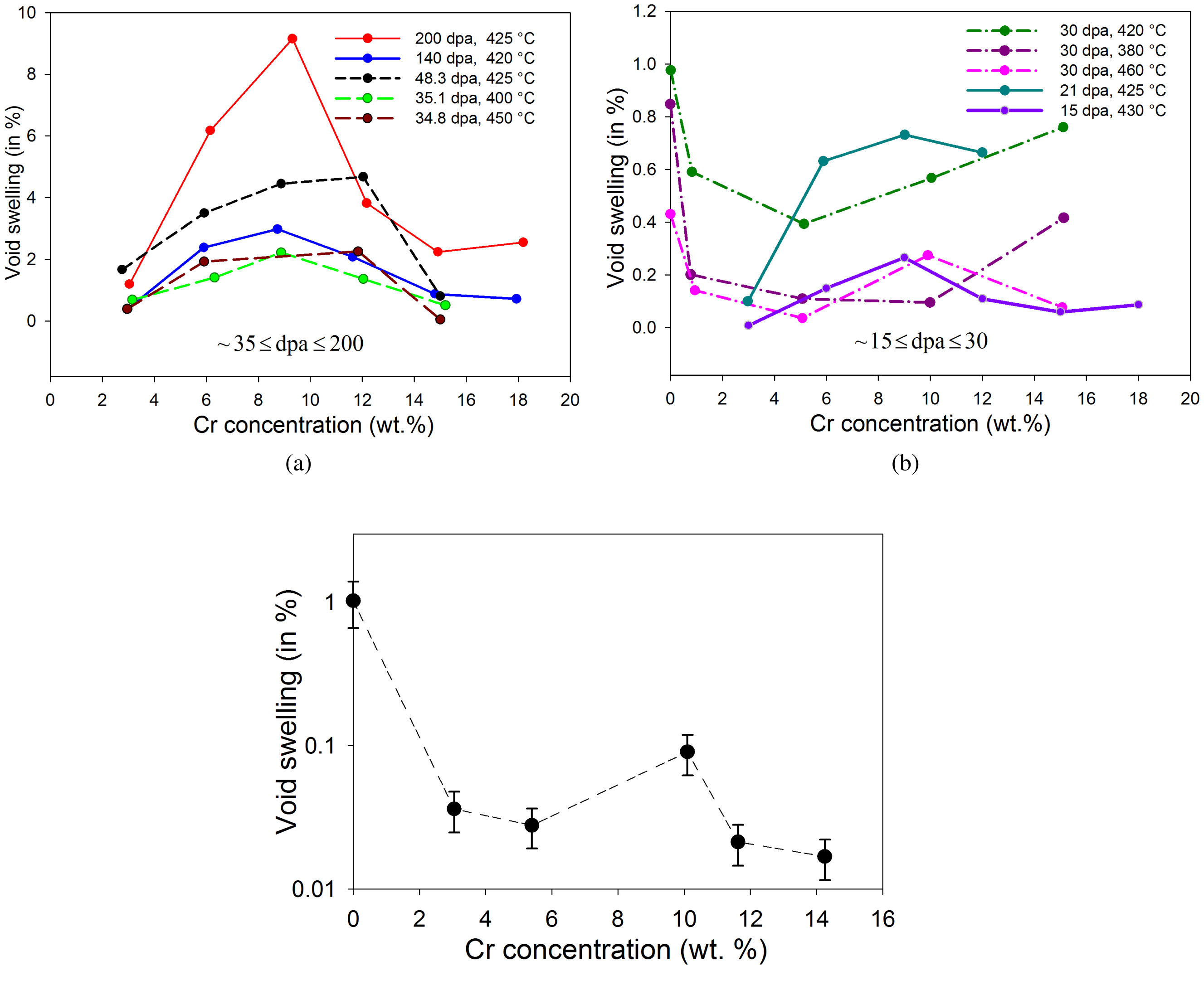

(a)

(b)

(c)

Figure 6.10: Variation of void swelling with Cr concentration in FeCr alloys. (a). Fast neutron irradiated results at relatively high doses. (b). Fast neutron irradiated results at low doses. (c). Ion irradiated results at 500 ºC to 128 dpa (2.6 x 10^{-3}dpa/s) with 13 appm He/dpa implanted simultaneously.

The observation of void swelling reduction by the addition of Cr in our case also corresponds well with some studies performed by the other experimental groups by ion irradiations [9, 119, 161]. But in their cases, a systematic study involving many Cr concentrations was not performed. Thus, a complete swelling curve was not obtained. As discussed in section 2.5.2.3, the only ion irradiation study involving a reasonable number of FeCr alloys was by Johnston and co-workers [10] who carried out irradiations using 5 MeV Ni^+ ions up to 116 dpa at 550 ºC. In this case, a somewhat non-monotonic trend was indeed seen. But the peak appeared at 15wt.% Cr, which is not what we have observed. Furthermore, swelling in Fe was strongly suppressed compared to the FeCr alloys. However, there were concerns that Ni ion deposition close to the peak damage area may have distorted the swelling trend.

It is interesting to see that when the same irradiation was performed without co-implantation of He in our case, no cavities, and hence swelling, was noted in any FeCr alloys. But as mentioned in the section 4.1, swelling was indeed seen in bcc Fe (it was in fact larger than the dual beam case): for the zone of study between 300 - 400 nm, estimated swelling was 8.5%, which is very large. Such a high swelling value is brought to zero by Cr levels as low as 3wt. %. This observation further glorifies the strong tendancy and extent of swelling diminution due to Cr addition in bcc Fe.

A plausible mechanism which can explain the observed swelling behaviour is difficult to give. It is mainly because of the absence of dependable theoretical results on FeCr alloys due to the complexity of modelling this system. From an experimental point of view, some conclusions may be made by analysing the dislocation loop microstructure and utilising the ideas from dislocation bias model. For instance, if we compare the dislocation loop microstructure of bcc Fe and Fe3%Cr, it can be seen that a strong network of dislocations existed in Fe3%Cr (see figures 4.24 and 4.26). This network is expected to be formed due to interaction and coalescence of dislocation loops in the damage region. On the other hand, loop density in bcc Fe was drastically lower. No dislocation network existed. Very few objects were identified as loops in the FIB thin foil. The strong initial diminution of swelling by addition of few percent of Cr may be explained from this phenomenon. Dislocations (lines and loops) act as sinks for point defects [31]. If their density is too high, then the vacancy super-saturation needed to nucleate cavities will drop. Thus, in this case, swelling will decrease. But what happens at higher Cr levels which yields a non-monotonic swelling behaviour is an open question. As seen in section 4.3, the network of dislocations was present in all the FeCr alloys. Although, obtaining proper TEM images of the same was a challenging task in many samples due to excessive damage produced by FIB preparation, it appeared that the network was not widely different in extent and morphology. However, precise quantitative informations (on density, Burgers vector etc.) are difficult to obtain from such highly entangled networks. Thus, if there is any subtle influence of the variation of some parameters of the dislocation forest on void swelling, it can not be obtained from such dislocation microstructures at high doses. Based on the neutron irradiated results up to different doses in EBR-II and FFTF-MOTA, Garner and co-workers [3] predicted that the major impact of Cr is on the duration of the incubation period. The shortest transient regime lies close to 9wt.%Cr, which may explain a local maxima around this concentration. Theoretically, Terentyev and co-workers had tried to give an explanation of this trend based on the positive interactions predicted in their calculations between Cr atoms and small SIA clusters modelled as arrangement of <111> crowdions using ab-initio and MD simulations [105]. It was claimed that the diffusivity of such clusters in FeCr alloys decrease non-monotonically with increasing Cr concentrations as compared to bcc Fe, with a minimum at 9 - 12%Cr. The larger the cluster size, the lower is the Cr level where this minima is located. In addition, the Cr effect on cluster diffusivity is gradually seen to disappear at larger Cr levels (~ 12% Cr), which is claimed to be due to saturation of Cr-crowdion interactions. Such strong interactions can lead to high loop densities which is experimentally known to exist in FeCr alloys (see section 5.1 and

[13, 105, 111, 59]). These clusters in high density provide additional recombination sites for freely migrating vacancies and small vacancy clusters, which would reduce swelling compared to bcc Fe. The hypothesis is similar to what we have proposed earlier based on experimental results as a reason of initial swelling reduction, i.e. high dislocation forest in FeCr alloys compared to Fe reduces the vacancy super saturation, and hence, swelling. Furthermore, using the argument of diffusivity minima around 9 - 12% Cr, the authors had tried to rationalise a swelling minima around 10 % Cr at lower doses which would shift to lower Cr concentrations as the dose is increased. But we have already seen previously, that experimental results do not show a minima at 10%Cr , except one study up to 30 dpa at 380 ºC by Little and Stow [3] (see figure 6.10), which we believe can be a consequence of non-isothermal irradiations in nuclear reactors. Furthermore, modelling of the FeCr system stays questionable due to non-existence of a reliable potential that could satisfactorily describe the system involving all the relevant physics.

For higher concentrations (12% and beyond), void swelling showed a decreasing trend (figure 6.10c). Most of the neutron irradiated results had also shown this behaviour (see figure 6.10), which the authors attributed to the formation of Cr rich α' precipitates. These precipitates would act as additional recombination sites which would increase the recombination rate. Similar mechanism was hypothesised by the theoretical studies of Terentyev and co-workers mentioned earlier. But in our TEM analysis on the FIB specimens, we have not seen an evidence of such precipitates in any of the FeCr alloys. However, the atomic number of Cr and Fe are very close. Due to this, even if such precipitation had happened, they may remain undetected by TEM especially when they are small. In such situations, other techniques like APT may be utilised as a complimentary tool. We must recall from the bibliography chapter that besides our study, α' precipitates have never been detected in any other ion or electron irradiation experiments on FeCr alloys performed by many experimental groups. They were only seen after neutron irradiations. Terentyev and co-workers even mentioned that swelling may decrease for larger Cr levels (beyond 16 wt.%) due to coalescence of these precipitates leading to lower number density. In our experiment, we did not have samples having Cr level more that 14wt.%. Thus, we can not conclude what happens beyond this concentration.

Another feature of interest to be noted is the absolute magnitude of swelling in all the FeCr alloys in our irradiations. If we compare this value with the fast neutron data (see figure 6.10), we realise that swelling levels reached in the ion irradiation experiment is significantly lower. This is despite of the fact that the dose is very high (128 dpa for the zone of analysis). In fact, the orders of magnitude of swelling was comparable (or even lower) to the neutron irradiations data with the lowest dose level of 15 dpa (see figure 6.10). Such an observation throws a light on the irradiation temperature used for the study. For neutron irradiation experiments, peak swelling temperature for FeCr alloys is at 420 ºC [35], which does not vary with the Cr level of the alloy. This temperature is higher in ion irradiated experiments to compensate for higher dose rate. It is claimed to lie in the range between 500 - 580 ºC [9, 10, 11]. Due to this reason, we had selected 500 ºC for the swelling analysis. But void microstructure (and hence the peak swelling temperature) are strongly dependent on the dose rate. It is hence possible that for our dose rate (2.6 x 10^{-3} dpa/s), we may not be exactly at the peak swelling temperature due to which we end up having very low swelling. If we look at the dislocation microstructure of the FeCr alloys after the high dose irradiation in section 4.3, we observed a very high density of entangled dislocation network. Such networks are usually not observed after high dose irradiations at peak swelling temperature. In fact, it resembles to a microstructure irradiated at a lower temperature where the loops are in high concentration. Thus, it would be reasonable to say that we may be below the peak swelling temperature in our case. Apart from studies in [9, 10, 11], other experimental works to determine peak swelling temperature also exist in the literature for a wide range of industrial high Cr F-M steels. Indeed, their matrix is an FeCr alloy. A large data set is tabulated in [1], which shows that the variation is between 425 - 550 ºC. Thus, lower temperatures below 500 ºC are also claimed by some studies. However, in our case, it is difficult to develop an analogy with these results due to the fact that they are not “high purity model FeCr alloys”, but are industrial steels with many additional impurity elements which may have a significant role on the evolution of the cavity microstructure.

6.2.2 Distribution of cavities

In this section, the results on the distribution of cavities along the damage depth in FeCr alloys are discussed. The first section concerns the evolution of cavity size, number density and swelling along the depth. The second section mostly describes the manner in which cavities are distributed in the matrix.

6.2.2.1 Depth distribution

Similar to bcc Fe, depth distribution of cavities was studied in the FeCr alloys. All the alloys were analysed by TEM, but a detailed quantitative analysis was performed only on Fe14%Cr. This study had revealed a very narrow size distribution of cavities in the zones prior to the peak damage area around 550 - 600 nm depth (see figure 4.13). The average size was slightly less than 2 nm (figure 4.11). There was not a strong difference between the maximum, minimum and average size. Almost no cavity denuded zone existed close to the irradiated surface, which was seen in bcc Fe. The number density of cavities increased almost linearly up to the damage peak from near surface areas. Swelling followed the trend of number density, although absolute swelling values remained low. Cavities were homogeneously distributed in the matrix. Upon reaching the damage peak and the zone beyond, microstructure showed drastic change. The maximum cavity size increased significantly. The size distribution became broad. Number density of cavities showed a sharp drop. But estimated swelling continued to increase, thereby, following the trend of the average cavity size in this zone. Furthermore, the microstructure consisted of a mixture of freely nucleated cavities in the matrix and heterogeneously nucleated cavities inside the dislocation loops. Freely nucleated cavities were the larger once (and usually with facets), whereas those inside the loops had a broad size distribution (see figure 4.12). This observation is in striking contrast to the results in bcc Fe where strong void suppression was noted adjacent to the peak damage zone because of the injected Fe ions. However, it must be noted that small cavities in rather larger numbers were indeed seen beyond the peak damage area in the dual beam irradiated Fe as well. To understand this behaviour, a variation of average void size, re-plotted this time on same scale, in dual beam irradiated bcc Fe and Fe14%Cr is shown in figure 6.11 . We can see that, unexpectedly, the average cavity size in both materials reached almost the same value beyond the peak damage area (shown by a circle in figure 6.11) . In Fe14%Cr, it was attained by increasing the size from the previous zones, whereas, in Fe it was due to the decrease in cavity size as compared to the pre-peak damage regions. A careful speculation makes us believe that this unanticipated behaviour could be due to a combination of artefact of injected ions (discussed for bcc Fe in section 6.1.3) and the methodology of the dual beam irradiations. In chapter 3, "Methodology", it was detailed that dual beam irradiations were performed using an energy degraded He beam whose initial energy was 2 MeV. The degradation was performed using a combination of thin aluminium foils with varying thicknesses. The foil thicknesses were chosen to reduce the He beam energy to an extent that it is deposited in the damage zone. Thus, at the peak damage zone and a little beyond that, He is indeed deposited. At the same time we learnt from the results in bcc Fe, that in this zone, cavities were strongly suppressed due to injected Fe ions. It would be reasonable to say that injected interstitial effect would also exist in all the FeCr alloys and may not be perturbed by different Cr levels of these materials. Hence, it is possible that cavities which we see beyond peak damage areas are not due to the ballistic damage by Fe ions. They are the cavities (or even bubbles) formed simply by He implantation. This hypothesis goes well with the observation that the average size of these cavities or bubbles was same in both these materials (because they were implanted with the same He concentration). In Fe14%Cr, the size variation looks increasing near the peak damage zone because the cavities prior to this region were smaller in size. Had there been no He present, we would anticipate that the variation would look similar to the one in bcc Fe (if there are cavities in the matrix).

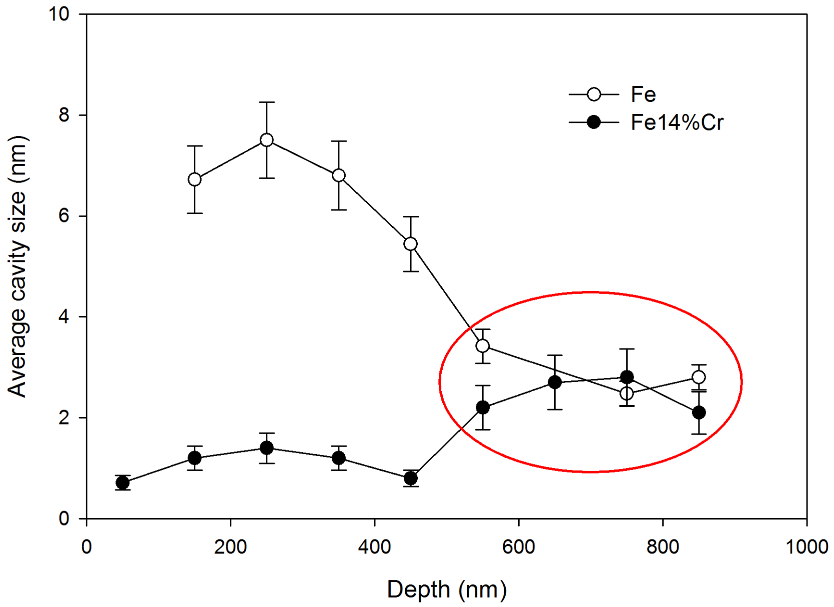

Figure 6.11: A comparison of depth distribution of average cavity size in dual beam irradiated bcc Fe and Fe14%Cr up to 157 dpa at the damage peak. He implantation corresponding to the damage peak was 17 appm He/dpa. The irradiation was performed at 500 ºC.

6.2.2.2 Spatial distribution

Another feature of interest to be noted is the spatial distribution of cavities in FeCr alloys which was not the same in pre- and post-peak damage zones. As mentioned earlier, in the regions prior to the damage peak, cavities were homogeneously distributed in the matrix. On the other hand, in regions just after the peak damage, the microstructure consisted of a mixture of freely nucleated cavities in the matrix and heterogeneously nucleated cavities inside the dislocation loops. The later were in relatively high proportion. This trend was systematically present in all the FeCr alloys irrespective of the Cr content. We believe, this difference in the cavity microstructure before and after the damage peak is due to the presence of different dislocation loop microstructure existing in these two regions. In the zones beyond the damage peak, the dpa level falls of rapidly (and also the dpa rate). Due to this, the dislocation loop density is not very high and individually resolvable loops are indeed present in this region. Thus, the correlation between the cavities and the dislocation loops is straightforward to see by TEM. On the other hand, in the regions before the damage peak, the microstructure consisted of an entangled dislocation network. Thus, if any correlation existed between the cavities and the loops, it can not be seen because individually resolvable loops do not exist any more. We could argue that when the microstructure began to develop at the early stage of the irradiation prior to the development of the dislocation network, a similar cavity-dislocation loop correlation may well have existed even in this region.

The presence of cavities inside the prismatic dislocation loops have been reported in a recent in-situ irradiation study in bcc Fe by Brimbal and co-workers [131]. In this case, the irradiation was performed on an electro-polished TEM thin foil at 500 °C up to 0.92 dpa, implanted simultaneously with ~ 540 appm He. Thus, we can conclude that the trend is similar between bcc Fe and FeCr alloys[1]. This behaviour is solely induced by the presence of He. Brimbal and co-workers had proposed a mechanism based on their observation which is as follows: He atoms can arrive at the core of the dislocation loops during irradiation where they can be trapped. The mobility of these trapped He atoms can result in the formation of He-V clusters at the loop core. As the loop grows by preferential absorption of interstitials, these clusters are left behind. Since He is insoluble in Fe matrix, these clusters are stable which can grow by absorption of He atoms and vacancies and are then observed in TEM imaging as cavities on the loop plane.

Apart from heterogeneous nucleation inside dislocation loops, strong segregation of cavities was seen on the grain boundaries and pre-existing dislocation lines. For the grain boundaries, the segregation seemed dependent on its orientation. For instance in Fe12%Cr, the cavitation showed an alignment reflecting that nucleation took place heterogeneously on the dislocation lines constituting a grain boundary. On the other hand, no such alignment existed in the grain boundary intercepted in Fe3%Cr. Moreover, all the pre-existing dislocations beyond the peak damage zone were also decorated with cavities: a phenomenon induced by He which can block dislocation motion and, thereby, increase hardening of the materials. In many cases, the associated dislocation was seen perhaps trying to climb before it could glide freely. These are expected results : it is well known that in metals irradiated at high temperature,

---

[1] In our case, we could not compare the microstructure with the reference Fe because almost no loops were seen in the FIB thin foil (owing to significantly lower loop number density in Fe).

germination of cavities take place at different interfaces and on dislocations due to He [120]. This phenomenon is observed in many industrial F-M steels [5, 162, 163]. For example, Henry and co-workers [5] studied 9%Cr martensitic steel after implantation with 23 MeV α-particles at 550 ºC up to a He concentration of 0.5 at.%. In this experiment, cavities were detected in many different defects in the materials: pre-austenitic grain boundaries, lath boundaries, dislocations and matrix-carbide interfaces. It corresponds well with the fact that, in general, grain boundaries act as neutral sinks to point defects, but the presence of He makes them as preferred nucleation sites for He-V clusters.

6.2.3 Effect of Cr on dislocation loop microstructure in FeCr alloys

The ion irradiation experiments have revealed a significant impact of Cr on the dislocation loop microstructure in FeCr alloys as compared to bcc Fe. In high dose experiments, a strong development of an entangled dislocation network was observed in all the FeCr alloys ranging from 3 - 14wt.% Cr. Individually resolvable loops which were not incorporated in the network were noted at the tailing end of the damage where dpa and dpa rate was low. However, in bcc Fe, such a network was not noticed. Only a few objects were identified as loops. This readily implies that dislocation loop density is much higher when Cr is added in Fe matrix[2]. The observation corresponds well with many other previous neutron, electron and ion irradiation experiments where similar behaviour was noted [53, 106, 59, 60, 62, 13, 9, 111, 109, 107, 71]. But the true origin of this behaviour is still unknown. Formation of network was observed by Gelles and by Horton and co-workers [107, 9] at relatively high doses.

When the low dose irradiation was performed on Fe14%Cr, similar result was obtained. The loop microstructure developed at a finer scale with higher number density as compared to bcc Fe irradiated to similar irradiation conditions in the study by Brimbal and co-workers [13]. In this case, since the irradiation was up to low dose (0.33 dpa), loops were not incorporated in a network which enabled us to extract informations on their Burgers vector, number density and size. A detailed analysis revealed that the microstructure consisted of both a<100> and a/2<111> type dislocation loops. However, from the results in bcc Fe at 500 ºC, it is well known that only a<100> loops are formed at this temperature [59, 164]. This implies that Cr addition (14wt.% in our case) in bcc Fe matrix stabilises the a/2<111> type dislocation loops.

After breaking up the loop number density into a/2<111> and a<100> category, it was realised that between Fe and Fe14%Cr, the concentration of a<100> loops was in fact not largely different (although a bit higher in Fe14%Cr). Furthermore, even the average size of a<100> loops in both these materials was not widely different . The main difference was induced by the population of a/2<111> loop. If we look at the distribution of loops in figure 5.5, we can see that majority of the loops are a/2<111> type (46%) and they are the smaller ones (20 nm average size). The less frequent, but relatively larger ones are the a<100> type (65 nm average size). Thus, the higher loop number density observed in Fe14%Cr

---

[2] Low loop density could also explain why no dislocation network was observed in Fe FIB foil. Indeed, a network must have formed in Fe because the dose is relatively high. However, when this microstructure is intercepted by a thin FIB foil, owing to low density of loops or network dislocations, it is possible that only a few objects are intercepted.

alloy can be attributed to the stabilisation of a/2<111> loops by the Cr atoms. Furthermore, higher loop density because of Cr also explains the observed entangled network in FeCr alloys irradiated at high doses, whereas none was observed in Fe. Due to the complexity of performing in-situ irradiations and the unavailability of time, other FeCr alloys with lower Cr levels were not irradiated in the present study.

A true physical explanation of stabilisation of a/2<111> loops by Cr (14wt.%) is not straightforward. One explanation may be derived from the theoretical studies performed on FeCr system mentioned in Chapter 2 “Bibliography” in section 2.5.2: DFT calculations and simulations using empirical potentials predict a strong interaction between Cr atoms and SIAs [100, 104]. The attractive interaction highlights a tendency of trapping of SIAs by the Cr atoms [104]. Furthermore, ab-initio and MD simulations also claim a mobility decrease of SIA clusters (modelled as parallel arrangement of <111> crowdions) by Cr due to this trapping effect. Experimentally, a reduction in loop mobility in FeCr alloys is indeed seen in in-situ type irradiation experiments [87, 13, 71], including ours where no loop motion was seen (see section 5.1). If we believe these arguments, we can hypothesize that Cr atoms can trap the otherwise “glissile” a/2<111> type dislocation loops. In this way, these loops are prevented from escaping to free surfaces where they can be eliminated and are hence visible to us in the post irradiation microstructure analysis[3].

Prior to our study, many other experimental groups had also analysed Burgers vector of dislocation loops in FeCr alloys. However, no clear trend was noticed due to contrasting results present in the literature. For instance, neutron irradiated studies by Porollo and co-workers and by Gelles and co-workers indeed show an increase in a/2<111> population by Cr, but only at higher Cr levels (beyond 6%) [107, 53]. For a lower Cr concentration, only a<100> loops were seen. However, Katoh and co-workers [106] observed predominantly a<100> type loops for Cr level between 3% to 18%, with an exception at 12 %, where a/2<111> loops in less density were also observed. The effect at lower Cr levels was not involved in our study because of limited time and complexity of performing in-situ irradiations. However, in the recent work of Brimbal and co-workers [13] under same irradiation conditions as ours on Fe5%Cr, it was indeed mentioned that a weak proportion of a/2<111> loops indeed existed. Similar conclusion was made after irradiations at RT by Prokhodtseva and co-workers [60] .However, these are contradicted by Jenkins and co-workers [59] who observed only a<100> loops in bcc Fe and Fe8%Cr up to 13 dpa at 500 ºC. But it may be possible that 8%Cr could be close to the concentration value noted under neutron irradiated results mentioned earlier, below which only a<100> loops were seen.

Another important feature that may interfere with the type of loops seen after irradiation could be the purity level of the alloys [113] . It was described by Wakai and co-workers after electron irradiation in a series of low purity and high purity FeCr alloys with Cr level 9%, 18% and 50%. In the low purity alloy, the major impurity content measured in mass ppm were [C] = 100 - 240, [N] = 75 -259, [O] = 20 - 500, [S] = 10 -50; while in high purity alloys it was [C] = 3 - 21, [N] = 3-10, [O] = 51- 63, [S] = 1 -3 (concentration of other elements can be seen in the reference [113]). It was noted that for irradiation up to 1 dpa in the

---

[3] While the simulations studies seem to explain the observed experimental results, we should be cautious because as we have mentioned a few times earlier that modelling FeCr system is complex due to unavailability of reliable potentials.

temperature range between 400 - 500 °C, only a<100> loops were present in low purity alloys, whereas both a<100> and a/2<111> were present in the high purity alloys. Thus, the discrepancies mentioned earlier in the literature results on Cr influence on Burgers vector may well have been influenced by this effect which was not taken into account. This makes our results robust and much important in the context of the study because the materials irradiated were of very high purity (see materials description in chapter 3). Indeed, except for the results by Brimbal and co-workers and Prokhodtseva and co-workers , the other studies were performed in materials with higher impurity content.

6.2.4 Combined Cr and He effect on dislocation loops in FeCr alloys

Fe14%Cr alloy when irradiated with co-implantation of He at 500 °C showed a very different loop microstructure as compared to the single beam case discussed in the previous section. The net He implantation at the damage zone was 3030 appm He/dpa. In this case, no a/2<111> loops were detected, which were seen in the single beam irradiated Fe14%Cr where Cr was considered as the main influence for their presence. All the identified loops were a<100> type. Their average size was 70 nm, which is very close to average size of a<100> loops observed in the single beam case. The total loop number density was also very close to the single beam case (1.1 x 10^{21} m^{-3})[4]. Upon comparing the results with those in bcc Fe irradiated under similar conditions, it was noted that average loop size was smaller and the number density was higher in Fe14%Cr.

This observation is striking because the only difference in this case as compared to the single beam irradiation is the presence of He. Ab-initio calculations of Fu and Willaime [29] indeed show a positive interaction between He and SIAs, but its weak. Thus, an influence of He on the Burgers vector of dislocation loops in FeCr alloys was not anticipated. However, Fu and Willaime indeed pointed out that SIAs may act as traps for interstitial He atoms if they are weakly mobile since their migration energy is ~0.3 eV. Brimbal and co-workers [13] studied loops in high purity Fe5%Cr after same irradiation conditions as ours. They had observed no significant impact of He on the loop microstructure. Though, a non-negligible decrease in loop number density as compared to the case when He was not present was indeed seen. Seto and co-workers [165] showed similar observation after electron irradiations on Fe8%Cr without and with He co-implantation.

A few experimental results on He influence on the dislocation loops in pure bcc Fe and FeCr alloys does exist (see Chapter 2 “Bibliography”, section 2.6). For instance, after in-situ self-ion irradiations at RT up to 0.45 dpa, Prokhodtseva and co-workers [60] had observed 96% a<100> type loops in Fe when He was not present and almost only a/2<111> type loops when He was co-implanted. Based on this result, they claimed that He stabilizes a/2<111> loops in Fe. But this trend is exactly opposite to what we are observing in Fe14%Cr at 500 °C. Furthermore, Prokhodtseva and co-workers also noted three fold increase in loop number density compared to when no He was present. Similar observations were

---

[4] For the single beam case, number density was estimated by measuring thickness using thickness fringes. However, for the dual beam case, such fringes were not observed in the thin foil due to local foil bending close to the edge. In this case, thickness was determined using EELS.

made by Brimbal and co-workers [13] as well in high purity Fe at 500 ºC which they attributed to their observation of much reduced loop mobilities upon He co-implantation. In this case, the average loop size was also larger compared to single beam case.

Considering the available experimental and theoretical results in the literature, at this juncture we do not have a clear justification of this drastically different loop microstructure due to He in Fe14%Cr. The in-situ observations of Brimbal and co-workers on the reduction of loop mobility in Fe by He leading to higher loop number density corresponds well with the ab-initio results mentioned above that indeed show a weak positive interaction between He and SIAs. But if we take this hypothesis and the idea of a trapping effect mentioned by Fu and Willaime earlier, if similar trapping was playing a role in Fe14%Cr, we would have expected higher density of a/2<111> population and not their complete disappearance. One could debate that in a situation, where initial a/2<111> population is claimed to be due to trapping by Cr, maybe additional trapping by He atoms divide the a/2<111> population in a length scale sufficiently small such that they maybe invisible in conventional TEM. Additional experiments under similar irradiation conditions are needed to better understand the phenomenon.

6.2.5 Cr enrichment on habit plane of prismatic dislocation loops.

Fringes were observed on the habit plane of dislocation loops in ion-irradiated Fe-Cr alloys. They were noted for dose as low as 0.33 dpa in Fe14%Cr. In this case, the pattern was not very pronounced. However, at relatively high doses (45 dpa), the fringe pattern was much more developed and clear (the studied material in this case was Fe5%Cr and Fe10% Cr). This observation was unexpected as the stacking fault energy of a bcc Fe lattice is very high. Thus, the dislocation loops produced under irradiation are not expected to be faulted in bcc Fe based alloys. Analytical measurements by STEM/EDS and APT revealed that there was Cr enrichment on the habit plane of the dislocation loops. The distribution of Cr enriched zones was heterogeneous. This proves that the fringes were occurring due to Cr enrichment on the loop habit planes. We speculate that this Cr enrichment induced fringes is “displacement fringe contrast” [139]. Such a loop with enriched zones may be considered like a thin sheet of precipitate, which would displace the matrix planes in opposite directions on either side of it. In Fe-Cr binary alloys, since the atomic radius of Cr atoms is slightly larger than that of Fe, the displacement may not correspond to a perfect lattice translation. When the electron beam encounters such a precipitate, the incident and the diffracted wave would undergo an abrupt phase change, resulting in these fringes. These type of fringes are reported in reference [139] on partially coherent ϑ’ phase in Al-Cu alloy and hexagonal γ’ phase in Al-Ag. In agreement with what is observed in our study, such fringes run parallel to the line of intersection of the planar precipitate disc and the foil surface. In some cases, they were not very straight, indicating that the thickness of the precipitate is not uniform . This fringe pattern does not reveal information about the structure of the precipitated crystallographic phase.

In a relatively old study, Wakai and co-workers [113] have reported Moire´ fringes on prismatic loops in electron irradiated Fe–Cr alloys between 300 - 700 ºC. It was seen that Cr segregation eventually led to a localised formation of the Cr-rich α' phase. The Cr content of this phase is much higher (>80wt.% Cr) than the Cr content reported on the dislocation loops in the present work.

The solubility limit of Cr at 500 ºC in Fe was experimentally obtained by APT experiments in a thermally aged Fe20 at.% Cr alloy. It was found to be 14 at.% [91] . In our case, for Fe5%Cr and Fe10%Cr, we are under the solubility limit. In the Fe14%Cr (i.e. nearly 15at.%), the concentration difference is less (1%). Thus, the thermal driving force for α/α' unmixing would have been very low. This means the heterogeneous distribution of Cr at the habit plane of the dislocation loops is induced by the irradiation. A flux of PD defects towards the dilatational or compressive strain field of a dislocation loop could induce Cr segregation at or close to the loop core by flux coupling between the PD flux and the Cr flux. However, a crystal is “perfect” within the central zones of a loop. Strain fields are limited only to the dilatational and compressive parts. Thus, the existence of Cr-enriched zones in a region where there are no defects is unexpected. When the loop diameter increases with increasing ion fluence, the Cr segregated at or close to the loop core would be in an area of a perfect crystal. From a thermodynamic point of view, re-dissolution of Cr would have been expected. What, then, prevents this re-dissolution?

We could argue that impurity atoms such as carbon (C), as suggested previously from SANS experiments by Heintze and co-workers [166], play a role. It is well known that Cr is carburigen. During the growth process of the loops, as Cr begins to decorate the loop core by RIS, C might subsequently be trapped by the segregated Cr atoms. This could lead to the formation of C-Cr complexes, which may be equilibrium or non-equilibrium phases at the irradiation temperature. As the loop grows further, these complexes would be in the habit plane of the loop, giving rise to fringes visible by conventional TEM. What is difficult to know experimentally is if a small number of C atoms are enough to stop Cr from re-dissolving or if a known stoichiometric composition needs to be reached. Their disappearance upon in-situ annealing implies that the phase was unstable at the annealing temperature. The presence of fringes until the disappearance of the loops confirm that this phase was present as long as the loop was present.

A justification of the mechanism is not straightforward because C still remains a difficult element to detect and quantify by various experimental techniques. In APT experiments, it is known that C atoms diffuse to specific poles during the process of field evaporation. Therefore, it is difficult to obtain information about their localisation in a sample. Carbon also remains difficult to quantify by EDS due to its low atomic number. Furthermore, inside electron microscopes there is always some C in the residual vacuum which would eventually make a contribution to the X-ray emission spectrum. It should be pointed out that the role of C may also be attributed to other impurities such as oxygen or nitrogen [167].

From a technical point of view, it is essential to take this phenomenon into account when studying the mechanical properties of irradiated F-M steels. Atomic-scale modelling by a combination of Monte Carlo and MD techniques by Terentyev and co-workers [168] has shown an increase in the stress needed to move a dislocation past an array of Cr-decorated prismatic a/2<1 1 1> type dislocation loops. This would cause an increase in the yield stress of the material. However, if there are Cr-enriched zones even inside the loops, then these might also make a contribution to the radiation-induced hardening. To quantify their effect, it is hence essential firstly to have a clear identification of these phases, and secondly a thorough insight into their true origin.

Chapter 7

General conclusions

The primary aim of the study was to understand the influence of Cr and He on the microstructural evolution of high purity bcc Fe and model FeCr binary alloys under irradiations at elevated temperatures. For this purpose, self-ion irradiations were performed in single beam mode (ballistic damage by Fe ions) and dual beam mode (damage by Fe ions and co-implantation of He) at 500 ºC at the JANNuS facility in France. Three different doses were studied: high dose (157 dpa, 17 appm He/dpa for the dual beam case), intermediate dose (45 dpa, 58 appm He/dpa for the dual beam case) and low dose (0.33 dpa, 3030 appm He/dpa for the dual beam case). High and intermediate dose irradiations were ex-situ type. Low dose single beam irradiation was in-situ type, where the real time evolution of the dislocation loops was observed. The microstructure after the irradiation was characterized principally by conventional TEM to study the radiation induced cavities and dislocation loops. Complimentary analytical techniques: EDS in STEM mode and APT were also employed mainly to see the enrichment of Cr on the dislocation loops. A part of the work was complimented by cluster dynamics simulations using CRESCENDO code to have theoretical insights into void swelling suppression by injected ions during ion irradiation experiments. A summary of the main results is given in this section.

Pure bcc Fe

◦ *He influence on void swelling*

Cavity microstructure was analysed by TEM in single beam and dual beam high dose irradiated high purity bcc Fe at 500 ºC, to see the effect of He on void swelling. In this case, the dose at the peak was 157 dpa, (17 appm He/dpa for the dual beam case). A comparison of the microstructure in FIB specimens revealed strong swelling reduction by addition of He. It was achieved by strong reduction in cavity sizes and an increase in number density. For example, in an intermediate depth of 300 - 400 nm, swelling was estimated to be 8.5% for irradiation without He as compared to only 1% when He was co-implanted. The average size of cavities was 67 nm for the former and only 6.8 nm for the later, but with almost two orders of magnitude higher number density. This behaviour was observed all along the damage depth, up to the damage peak.

The behaviour was explained using the idea of the ratio of sink strengths of dislocations and cavities. It is seen in our experiments and in many other literature results quoted in Chapter 6, section 6.1.1, that when He is co-implanted, cavity number density is high. These cavities themselves act as sinks, and hence increase the overall cavity sink strength. But cavities are unbiased sinks, which means, no preferential absorption for any kind of defect. If the number density of cavities increase sufficiently in the irradiated material due to He, it is possible that they can become the dominant sinks for the point defects instead of the dislocations (lines or loops). In that case, the relative interstitial flux towards the dislocations would be reduced, reducing the vacancy flux towards the cavities due to enhanced recombination. Cavities would then be unable to grow, thereby, restricting swelling.

This result emphasizes that caution must be addressed while attributing void swelling behaviour of metals to He. It is long believed that He causes swelling. But as we just saw, it is not always the case. Indeed, He enhances cavity nucleation. However, it does not necessarily mean that void swelling would be higher as opposed to the case when no He is added.

- *Injected interstitial effect*

In the analysis of the depth distribution of cavities in high dose irradiated bcc Fe, it was observed that void swelling reduced drastically around the damage peak area (where dpa damage is the highest). For instance, in the single beam case, it reduced to almost one-third its value as compared to the value at the intermediate zones. It was attributed to the injected Fe ions which are implanted close to the damage peak. These injected ions could behave as interstitials which can artificially suppress cavities. The speculation was qualitatively justified by cluster dynamics simulations using CRESCENDO where a drastic reduction in cavity size and density was observed when 100 appm/s injected ions were added. For the real experimental case, the injected ion rate was 1 appm/s. Simulations did not show injected interstitial effect for this case. However, experimentally we did see an important swelling reduction. We believe it is due to the assumptions made during the simulations. For a simplified approach, it was considered that only mono-interstitials and mono-vacancies are produced by Fe ions. But in reality, displacement cascades are produced along with the formation of point defect clusters within the cascades. Furthermore, a simplification on the cluster mobility was also used. It was assumed that only monomers are mobile, which is not the case in real experimental situations. But these results are qualitatively robust. Thus, it can be concluded that injected ions during ion irradiation experiments indeed reduce swelling adjacent to the damage peak area. It is an artefact of ion irradiation experiments, which is expected to increase as the amount of injected ions implanted increase. Thus, for reliable analysis of cavity microstructure in irradiated materials, intermediate depths far from the damage peak (and also far from the surface to avoid surface effects) must be selected.

FeCr alloys

- *Cr effect on void swelling*

Cavity microstructure was thoroughly studied by TEM in dual beam high dose irradiated FeCr alloys and the results were compared to those in bcc Fe. The analysis was performed at an intermediate depth of 300 - 400 nm (corresponding to 128 dpa, 13 appm He/dpa) to avoid surface effects and injected interstitial effects at the damage peak. It was revealed that the addition of small quantities of Cr, as low as 3wt.%, is highly efficient in strongly reducing void swelling. It was achieved by a drastic reduction of cavity sizes (but accompanied by higher number density). For instance, average cavity size in Fe3%Cr was 0.9 nm as opposed to 6.8 nm in bcc Fe.

Furthermore, the variation of void swelling as a function of Cr content is non-monotonic, with a local maxima around 9 - 10wt.%Cr. However, swelling always stays less in all the FeCr alloys (up to 14wt.%Cr) as compared to bcc Fe. These results have clarified the discrepancies in swelling trend in FeCr alloys observed after fast neutron irradiations mentioned in Chapter 2, section 2.5.2.3.

However, the absolute swelling values remained low - less than 0.1% for all the FeCr alloys. We believe it is due to the choice of the irradiation temperature. Literature data suggests that peak swelling temperature for FeCr alloys under ion irradiation lies between 500 - 580 ºC. Due to this reason, 500 ºC was selected in our study. But, it is possible that for our irradiation conditions (particularly for dose rate of 2.6 x 10^{-3}dpa/s), we may not be exactly at the swelling peak. It is also evident from the single beam irradiations where no cavities were observed in any FeCr alloys. This, hence, questions the validity of 500 ºC temperature range as the peak swelling temperature in these materials.

- *Depth distribution of cavities*

The depth distribution of cavities in FeCr alloys revealed opposite trend to that observed in bcc Fe. Larger cavities and relatively higher void swelling was estimated around and beyond the damage peak as opposed to the areas prior to the damage peak. We believe, this is due to the combination of injected interstitial effect and the presence of He. It would be reasonable to say that injected interstitial effect would also exist in all the FeCr alloys and may not be perturbed by different Cr levels of these materials. Hence, it is possible that the cavities observed beyond the peak damage areas are formed only because of He implantation and not by ballistic damage produced by Fe ions. This hypothesis is justified by the observation that the average size of the cavities in these zones was nearly same in both bcc Fe and Fe14%Cr.

Cavity distribution was homogeneous prior to the damage peak. However, at and mostly beyond the damage peak, it was a mixture of homogeneous distribution, accompanied with cavity association with the dislocation loops. This behaviour is due to the different loop microstructure observed in these zones. In the zones after the damage peak, individually resolvable lops were present. Thus, the correlation between cavities and loops was easy to see. While an entangled dislocation network existed prior to the damage peak. If any correlation existed between the cavities and the loops, it can not be seen because individually resolvable loops did not exist.

- *Cr and combined Cr plus He effect on the dislocation loop microstructure*

Single beam low dose irradiated Fe14%Cr alloy was analysed in-situ and after irradiation to 0.33 dpa at 500 ºC. In-situ observation showed no loop mobility, in accordance with many other ion and electron irradiation experiments (see Chapter 2, section 2.5.2.2). Post irradiation characterization by TEM revealed the presence of both a<100> and a/2<111> loops. However, at 500 ºC, only a<100> loops are known to exist in bcc Fe. Based on this, we conclude that the addition of Cr (14wt.% in our case) in bcc Fe stabilises the otherwise glissile a/2<111> loops. This stabilisation can lead to elevated loop number densities in FeCr alloys as opposed to Fe.

When the same irradiation was performed on Fe14%Cr, but with co-implantation of He, no a/2<111> type loops were observed. Only a<100> loops existed. This observation is striking because ab-initio calculations do not predict a strong positive interaction of He with SIAs [29]. Furthermore, these results are in contrast to those obtained by Prokhodtseva and co-workers [60], where more a/2<111> loops were seen in both bcc Fe and FeCr alloys. At present, we do not have a physical explanation of this phenomenon. Further irradiations may be needed to arrive at a conclusion.

- *Cr enrichment on the habit plane of the dislocation loops*

The presence of Cr-enriched zones on the habit plane of the dislocation loops were revealed after irradiation at 500 ºC to low dose (0.33 dpa, 3030 appm He/dpa) and intermediate dose (45 dpa, 58 appm He/dpa) by complementary experimental techniques: conventional TEM, APT and EDS in STEM mode. This is expected to be due to radiation induced segregation (RIS) of Cr close to the core of the loops. As the loop grows under irradiation, the segregated areas are probably prevented from re-dissolution by impurity elements such as C. When imaged by TEM using classical diffraction contrast imaging techniques, these enriched zones produce displacement fringe contrast on the loop plane. A quantitative estimate of this enrichment was deduced by STEM/EDS and APT. The Cr content in these areas was between 23 to 35 at.% by EDS and 22 ± 2 at.% by APT, which is well below the Cr content of the Cr-rich α' phase. The values obtained are coherent between these two techniques. Upon in-situ annealing at 627 ºC, these loops disappeared by shrinkage without leaving any secondary-phase particle. The fringes were present as long as the loops were present.

References

[1] Klueh R, Harries D. High-Chromium Ferritic and Martensitic Steels for Nuclear Applications. ASTM, Bridgeport, 2001.

[2] Séran J. Technical Note - Synthèse des études sur le gonflement des alliages austénitiques développés au CEA pour le gainage du combustible RNR-Na. CEA/DEN/DANS/DMN/NT/13-006/B, 2014.

[3] Garner FA, Toloczko MB, Sencer BH. Journal of Nuclear Materials 2000;276:123 .

[4] Boutard J, Alamo A, Lindau R, Rieth M. Comptes Rendus Physique 2008;9:287 .

[5] Henry J, Mathon MH, Jung P. Journal of Nuclear Materials 2003;318:249 .

[6] Ullmaier H, Trinkaus H 1992;97:451.

[7] Dai Y, Odette G, Yamamoto T, The Effects of Helium in Irradiated Structural Alloys. In: RJM Konings (Ed.), Comprehensive Nuclear Materials Vol.1. Elsevier, 2012.

[8] Packan NH, Farrell K. Journal of Nuclear Materials 1979;85-86, Part 2:677 .

[9] Horton LL, Bentley J, Jesser WA. Journal of Nuclear Materials 1981;104:1085 .

[10] Johnston W, Lauritzen T, Rosolowski J, Turkalo A. ASTM STP,782, 1982, 809.

[11] Tanaka T, Oka K, Ohnuki S, Yamashita S, Suda T, Watanabe S, Wakai E. Journal of Nuclear Materials 2004;329-333, Part A:294 .

[12] Ohnuki S, Takahashi H, Takeyama T. Journal of Nuclear Materials 1981;104:1121 .

[13] Brimbal D. PhD thesis - Evolution microstructurale du fer pur et d'alliages Fe-Cr sous irradiation avec injection simultanée d'hélium : étude expérimentale et modélisation, Universite Paris SUD 11, 2011.

[14] Zinkle SJ, Was GS. Acta Materialia 2013;61:735 .

[15] Gilbert MR, Dudarev SL, Derlet PM, Pettifor DG. Journal of Physics: Condensed Matter 2008; 20:345214.

[16] Grimes S, Haight R, Alvar K, Barschall H, Borchers R. Phys Rev C 1979;19:2127.

[17] Haight RC. International Conference on Nuclear Data for Science and Technology 2007;1077.

[18] Greenwood L, Graczyk D, Kneff D. Journal of Nuclear Materials 1988;155-157, Part 2:1335 .

[19] Baldev R, Ramachandran D, Vijayalakshmi M. Transactions of the Indian Institute of Metals 2009; 62:89 .

[20] Zinkle SJ, Fusion and Spallation Irradiation Conditions. In: International Workshop on Advanced Computational Science : Application to Fusion and Generation-IV Fission Reactors, Washington DC, 2004.

[21] Zinkle SJ, Busby JT. Materials Today 2009;12:12.

[22] Garner FA. Journal of Nuclear Materials 1984;122:459.

[23] Garner FA, Puigh RJ. Journal of Nuclear Materials 1991;179:577.

[24] Herschbach K. Journal of Nuclear Materials 1985;65:239.

[25] Lo KH, Shek CH, Lai JKL. Materials Science Engineering Reports 2009;65:39.

[26] Kohyama A, Hishinuma A, Gelles DS, Klueh R, Dietz W, Ehrlich K. Journal of Nuclear Materials 1996;233:138.

[27] Stoller R, Odette GR, Wirth BD. Journal of Nuclear Materials 1997;251:49.

[28] Malerba L, Terentyev D, Olsson P, Chakarova R, Wallenius J. Journal of Nuclear Materials 2004; 329-333, Part B:1156 .

[29] Fu CC, Willaime F. Comptes Rendus Physique 2008;9:335 .

[30] Zinkle SJ, Radiation-Induced Effects on Microstructure. In: RJM Konings (Ed.), Comprehensive Nuclear Materials Vol.1. Elsevier, 2012.

[31] Was GS. Fundamentals of Radiation Materials Science. Springer-Verlag, 2007.

[32] Little EA, Stow DA. Metal Science 1980;14:89.

[33] Mansur LK. Journal of Nuclear Materials 1978;78:156 .

[34] Packan NH, Farrell K, Stiegler JO. Journal of Nuclear Materials 1978;78:143 .

[35] Little EA, Stow DA. Journal of Nuclear Materials 1979;87:25.

[36] Sawai T, Suzuki M, Maziasz P, Hishinuma A. Journal of Nuclear Materials 1992;187:146 .

[37] Sencer BH, Garner FA. Journal of Nuclear Materials 2000;283-287, Part 1:164 .

[38] Gilbert M, Yao Z, Kirk M, Jenkins M, Dudarev S. Journal of Nuclear Materials 2009;386-388.

[39] Okamoto P, Rehn L. Journal of Nuclear Materials 1979;83:2.

[40] Nastar M, Soisson F, Radiation-induced Segregation. In: RJM Konings (Ed.), Comprehensive Nuclear Materials Vol.1. Elsevier, 2012.

[41] Norgett M, Robinson M, Torrens I. Nuclear Engineering and Design 1975;33:50.

[42] Was G. Using ions as analogues for neutrons - successes and challenges, Workshop on Ion Implantation as a Neutron Irradiation Analogue, Oxford University UK, 2011.

[43] Wirth B, Odette G, Maroudas D, Lucas G. Journal of Nuclear Materials 1997;244:185 .

[44] Terentyev D, Malerba L, Hou M. Phys Rev B 2007;75:104108.

[45] Marinica MC, Willaime F, Mousseau N. Phys Rev B 2011;83:094119.

[46] Willaime F, Fu CC, Marinica MC, Torre JD. Nuclear Instruments and Methods in Physics Research Section B: Beam Interactions with Materials and Atoms 2005;228:92 .

[47] Nguyen-Manh D, Horsfield AP, Dudarev S. Phys Rev B 2006;73:020101.

[48] Schultz H. In: Landolt-Bornstein NS III/25. 1991.

[49] Marian J, Wirth BD, Schäublin R, Odette GR, Perlado JM. Journal of Nuclear Materials 2003; 323:181 .

[50] Marinica MC, Willaime F, Crocombette JP. Phys Rev Lett 2012;108:025501.

[51] Ackland G, Bacon D, Calder A, Harry T. Philosophical Magazine A 1997;75:713.

[52] Ackland G, Mendelev M, Srolovitz D, Han S, Barashev A. Journal of Physics-Condensed Matter 2004;16:S2629.

[53] Porollo SI, Dvoriashin AM, Vorobyev AN, Konobeev YV. Journal of Nuclear Materials 1998; 256:247 .

[54] Horton LL, Bentley J, Farrell K. Journal of Nuclear Materials 1982;108-109:222 .

[55] Matijasevic M, Renterghem WV, Almazouzi A. Acta Materialia 2009;57:1577 .

[56] Hernandez-Mayoral M, Gomez-Briceno D. Journal of Nuclear Materials 2010;399:146 .

[57] Zinkle SJ, Singh BN. Journal of Nuclear Materials 2006;351:269.

[58] Prokhodtseva A, Décamps B, Schäeublin R. Journal of Nuclear Materials 2013;442:S786.

[59] Jenkins ML, Yao Z, Hernandez-Mayoral M, Kirk MA. Journal of Nuclear Materials 2009;389.

[60] Prokhodtseva A, Décamps B, Ramar A, Schäublin R. Acta Materialia 2013;61:6958.

[61] Masters BC. Nature 1963;200:254.

[62] Hernandez-Mayoral M, Yao Z, Jenkins ML, Kirk MA. Philosophical Magazine 2008;88:2881.

[63] Arakawa K, Ono K, Isshiki M, Mimura K, Uchikoshi M, Mori H. Science 2007;318:956.

[64] Arakawa K. High-energy electron irradiation of metals: Effects of high dose rate and properties of single point defects, Workshop on Ion Implantation as a Neutron Irradiation Analogue, Oxford University UK, 2011.

[65] Brimbal D, Décamps B, Henry J, Meslin E, Barbu A. Acta Materialia 2014;64:391 .

[66] Barbu A. Personal Communication.

[67] Ward AE, Fisher SB. Journal of Nuclear Materials 1989;166:227 .

[68] Arakawa K, Mori H, Ono K. Journal of Nuclear Materials 2002;307-311, Part 1:272 .

[69] Hardouin-Duparc A, Moingeon C, Smetniansky-de-Grande N, Barbu A. Journal of Nuclear Materials 2002;302:143 .

[70] Yoshida N, Kiritani M, Fujita F. Journal of the Physical Society of Japan 1975;39:170.

[71] Arakawa K, Hatanaka M, Mori H, Ono K. Journal of Nuclear Materials 2004;329-333, Part B:1194 .

[72] Eyre BL, Bullough R. Philosophical Magazine 1965;12:31.

[73] Marian J, Wirth BD, Perlado JM. Phys Rev Lett 2002;88:255507.

[74] Dudarev SL, Bullough R, Derlet PM. Phys Rev Lett 2008;100:135503.

[75] Masters BC. Philosophical Magazine 1965;11:881.

[76] Xu H, Stoller RE, Osetsky YN, Terentyev D. Phys Rev Lett 2013;110:265503.

[77] Arakawa K, Amino T, Mori H. Acta Materialia 2011;59:141 .

[78] Arakawa K, Hatanaka M, Kuramoto E, Ono K, Mori H. Phys Rev Lett 2006;96:125506.

[79] Björkas C, Nordlund K. Nuclear Instruments and Methods in Physics Research Section B: Beam Interactions with Materials and Atoms 2007;259:853 .

[80] Fu CC, Willaime F. Phys Rev B 2005;72:064117.

[81] Eldrup M, Singh BN, Zinkle SJ, Byun TS, Farrell K. Journal of Nuclear Materials 2002;307-311, Part 2:912 .

[82] Dvoriashin AM, Porollo SI, Konobeev YV, Garner FA. Journal of Nuclear Materials 2000;283-287, Part 1:157 .

[83] Farrell K, Houston JT. Journal of Nuclear Materials 1970;35:352 .

[84] English CA, Eyre BL, Jenkins ML. Nature 1976;263:400.

[85] Kuramoto E, Yoshida N, Tsukuda N, Kitajima K, Packan NH, Lewis MB, Mansur LK. Journal of Nuclear Materials 1981;104:1091 .

[86] Robinson T. Physica status solidi (c) 1983;75:243.

[87] Yao Z, Hernandez-Mayoral M, Jenkins ML, Kirk MA. Philosophical Magazine 2008;88:2851.

[88] Kitajima K, Futagami K, Kuramoto E. Journal of Nuclear Materials 1979;85-86, Part 2:725 .

[89] Bonny G, Terentyev D, Malerba L. Scripta Materialia 2008;59:1193 .

[90] Xiong W, Selleby M, Chen Q, Odqvist J, Du Y. Critical Reviews in Solid State and Materials Sciences 2010;35:125.

[91] Novy S, Pareige P, Pareige C. Journal of Nuclear Materials 2009;384:96 .

[92] Malerba L, Caro A, Wallenius J. Journal of Nuclear Materials 2008;382:112 .

[93] Sahu J, Krupp U, Ghosh R, Christ HJ. Materials Science and Engineering A 2009;508:1 .

[94] Mirebeau I, Hennion M, Parette G. Phys Rev Lett 1984;53:687.

[95] Olsson P, Abrikosov IA, Vitos L, Wallenius J. Journal of Nuclear Materials 2003;321:84 .

[96] Olsson P, Abrikosov IA, Wallenius J. Phys Rev B 2006;73:104416.

[97] Klaver TPC, Drautz R, Finnis MW. Phys Rev B 2006;74:094435.

[98] Terentyev D, Malerba L, Chakarova R, Nordlund K, Olsson P, Rieth M, Wallenius J. Journal of Nuclear Materials 2006;349:119 .

[99] Vörtler K, Björkas C, Terentyev D, Malerba L, Nordlund K. Journal of Nuclear Materials 2008; 382:24 .

[100] Olsson P, Domain C, Wallenius J. Phys Rev B 2007;75:014110.

[101] Möslang A, Albert E, Recknagel E, Weidinger A, Moser P. Hyperfine Interactions 1983;15:409.

[102] Kuramoto E, Nagano S, Nishi K, Makii K, Aono Y, Takenaka M. Mater Sci Forum 1992;105-110.

[103] Kwon J, Toyama T, Kim YM, Kim W, Hong JH. Journal of Nuclear Materials 2009;386-388:165 .

[104] Terentyev D, Olsson P, Klaver TPC, Malerba L. Computational Materials Science 2008;43:1183 .

[105] Terentyev D, Olsson P, Malerba L, Barashev AV. Journal of Nuclear Materials 2007;362:167 .

[106] Katoh Y, Kohyama A, Gelles DS. Journal of Nuclear Materials 1995;225:154.

[107] Gelles DS. Journal of Nuclear Materials 1982;108-109:515 .

[108] Konobeev Y, Dvoriashin AM, Porollo SI, Garner FA. Journal of Nuclear Materials 2006;355:124 .

[109] Xu S, Yao Z, Jenkins ML. Journal of Nuclear Materials 2009;386-388:161 .

[110] Boulanger L, Serruys Y. Journal of Nuclear Materials 2009;386-388:441 .

[111] Yoshida N, Yamaguchi A, Muroga T, Miyamoto Y, Kitajima K. Journal of Nuclear Materials 1988; 155:1232.

[112] Gelles DS, Ohnuki S, Takahashi H, Matsui H, Kohno Y. Journal of Nuclear Materials 1992;191-194, Part B:1336 .

[113] Wakai E, Hishinuma A, Kato Y, Yano H, Takaki S, Abiko K. Le Journal de Physique IV 1995; 5:C7.

[114] Muroga T, Nonaka Y, Yoshida N. Journal of Nuclear Materials 1996;233:1035.

[115] Gelles DS. Journal of Nuclear Materials 1995;225:163 .

[116] Kiritani M. Journal of Nuclear Materials 1988;160:135 .

[117] Kiritani M, Yoshiie T, Kojima S, Satoh Y, Hamada K. Journal of Nuclear Materials 1990;174:327 .

[118] Garner FA, Sekimura N, Grossbeck ML, Ermi AM, Newkirk JW, Watanabe H, Kiritani M. Journal of Nuclear Materials 1993;205:206 .

[119] Brimbal D, Meslin E, Henry J, Décamps B, Barbu A. Acta Materialia 2013;61:4757 .

[120] Trinkaus H, Singh BN. Journal of Nuclear Materials 2003;323:229 .

[121] Caturla MJ, Ortiz CJ, Fu CC. Comptes Rendus Physique 2008;9:401 .

[122] Ventelon L, Wirth BD, Domain C. Journal of Nuclear Materials 2006;351:119 .

[123] Heinisch HL, Gao F, Kurtz RJ, Le EA. Journal of Nuclear Materials 2006;351:141.

[124] Shim JH, Kwon S, Kim W, Wirth B. Journal of Nuclear Materials 2007;367-370, Part A:292.

[125] Yang L, Zu X, Wang Z, Gao F, Wang X, Heinisch HL, Kurtz RJ. Nuclear Instruments and Methods in Physics Research Section B: Beam Interactions with Materials and Atoms 2007;265:541 .

[126] Heinisch HL, Gao F, Kurtz RJ. Journal of Nuclear Materials 2007;367-370, Part A:311.

[127] Packan NH. Journal of Nuclear Materials 1981;104:1029 .

[128] Horton LL, Mansur LK. American Society for Testing and Materials, Philadeldhia, 1985, 344–362.

[129] Sugano R, Morishita K, Iwakiri H, Yoshida N. Journal of Nuclear Materials 2002;307-311, Part 2:941 .

[130] Farrell K, Houston JT. Journal of Nuclear Materials 1970;35:352 .

[131] Brimbal D, Décamps B, Barbu A, Meslin E, Henry J. Journal of Nuclear Materials 2011;418:313 .

[132] Coze Le J. Final report on model alloy preparation ; EFDA - Contract 06 - 1901 TW6 - TTMS 007- PUREFE. ARMINE: Ecole Nationale Supérieure des Mines de Saint Etienne, 2007.

[133] Fraczkeiwicz A. Material Delivery Report BC4000483543/P5B51. Ecole Nationale Supérieure des Mines de Saint Etienne, 2011.

[134] Serruys Y, Ruault MO, Trocellier P, Henry S, Kaitasov O, Trouslard P. Nuclear Instruments & Methods In Physics Research Section B: Beam Interactions with Materials and Atoms 2005; 240:124 .

[135] Ziegler J. Nuclear Instruments & Methods In Physics Research Section B: Beam Interactions with Materials and Atoms 2004;219:1027.

[136] Stoller RE, Toloczko MB, Was GS, Certain AG, Dwaraknath S, Garner FA. Nuclear Instruments & Methods In Physics Research Section B: Beam Interactions with Materials and Atoms 2013; 310:75.

[137] Jenkins ML, Kirk MA. Characterization of radiation damage by transmission electron microscopy. IOP Publishing Ltd., 2001.

[138] Williams D, Carter C. The transmission electron microscope: a textbook for material science. 2nd ed. New York. Springer, 1996.

[139] Hirsch P, Howie A, Nicholson RB, Pashley DW, Whelan MJ. Electron microscopy of thin crystals. 2nd ed. New York. Robert E. Krieger Publishing Co. Inc., 1977.

[140] Egerton R. Electron energy-loss spectroscopy in the electron microscope. 3rd ed. New York. Springer, 2011.

[141] Ould Amer A. Internship Report - Mesure d'épaisseur par perte d'énergie sur un microscope Jéol 2100, équipé d'un détecteur Gif Gatan. Application a la détermination fine de la fraction volumique des aiguilles de β-Nb précipitant sous irradiation dans l'alliage M5. CEA/DEN/DMN/SRMA/LA2M, 2011.

[142] Miller MK. Atom Probe Tomography - Analysis at the atomic scale. Kluwer Academic/Plenum Publishers, New York, 2000.

[143] Vurpillot F. Basics of the APT / Tomographic reconstruction / Artifacts - 3rd School on Atom Probe Tomography, University of Rouen, France, 2011.

[144] Da Costa G, Vurpillot F, Bostel A, Bouet M, Deconihout B. Review of Scientific Instruments 2005;76.

[145] Jourdan T, Bencteux G. User Documentation for CRESCENDO V1.0. NT-SRMP-2011-09, CEA/DEN, 2011.

[146] Jourdan T, Bencteux G, Adjanor G. Journal of Nuclear Materials 2014;444:298.

[147] Ruben G, Cosgriff E, D'Alfonso A, Findlay S, Le Beau J, Allen L. Ultramicroscopy 2012;113:131.

[148] Farrell K, Lewis MB, Packan NH. Scripta Metallurgica 1978;12:1121 .

[149] Farrell K, Packan NH. Journal of Nuclear Materials 1979;85-6:683.

[150] Mansur LK, Lee EH. Journal of Nuclear Materials 1991;179-181, Part 1:105 .

[151] Stoller R. Journal of Nuclear Materials 1990;174:289.

[152] Katoh Y, Kohno Y, Kohyama A. Journal of Nuclear Materials 1993;205:354.

[153] Tanigawa H, Ando M, Katoh Y, Hirose T, Sakasegawa H, Jitsukawa S, Kohyama A, Iwai T. Journal of Nuclear Materials 2001;297:279 .

[154] Garner FA. Poster - Impact of the injected interstitial effect on ion-induced void swelling in austenitic and ferritic-ODS alloys, Workshop on Ion Beam Simulation of High Dose Neutron Irradiation, University of Michigan USA, 2014.

[155] Lee EH, Mansur LK, Yoo MH. Journal of Nuclear Materials 1979;85-86, Part 1:577 .

[156] Plumton D, Wolfer W. Journal of Nuclear Materials 1984;120:245 .

[157] Garner FA. Journal of Nuclear Materials 1983;117:177 .

[158] Brailsford AD, Mansur LK. Journal of Nuclear Materials 1977;71:110 .

[159] Whitley JB, Kulcinski GL, Wilkes P, Smith Jr HV. Journal of Nuclear Materials 1979;79:159 .

[160] Kumar AS, Garner FA. In: FA Garner, JS Perrin (Eds.), Effects of Radiation on Materials: Twelfth International Symposium. ASTM STP 870, 1985.

[161] Ohnuki S, Takahashi H, Takeyama T. Journal of Nuclear Materials 1981;104:1121 .

[162] Gilbon D, Rivera C. Journal of Nuclear Materials 1988;155:1268.

[163] Wanderka N, Camus E, Wollenberger H. In: IM Robertson, GS Was, LW Hobbs, T de la Rubia (Eds.), Microstructure Evolution During Irradiation, Materials Research Society Symposium Proceedings Vol. 439. 1997, 451–456.

[164] Brimbal D, Décamps B, Henry J, Meslin E, Barbu A. Acta Materialia 2014;64:391.

[165] Seto H, Hashimoto N, Kinoshita H, Ohnuki S. Journal of Nuclear Materials 2011;417:1018.

[166] Heintze C, Bergner F, Ulbricht A, Eckerlebe H. Journal of Nuclear Materials 2011;409:106.

[167] Schuler T, Nastar M. Personal Communication.

[168] Terentyev D, Bergner F, Osetsky Y. Acta Materialia 2013;61:1444.

Appendix A

Sample preparation by electrolytic polishing

For performing irradiations, the specimens were in the form of electro-polished thin foils with electron transparent zones and as bulk dimpled discs of 100 μm. To prepare these samples, the starting material is a mirror polished disc of 100 μm thickness and 3 mm diameter. These are then electro-polished in an electrolyte bath of Struers Tenupol-5 jet-thinning device. To obtain thin foils, the electrolyte jet is incident on both specimen surfaces using a pump.

The choice of the electrolyte and the polishing temperature depends on the specimen to be prepared. For FeCr alloys with high Cr level, i.e. between 10 - 14wt.%, the polishing was performed using a single electrolyte at RT. The electrolyte consisted of 70% ethanol, 20% ethylene glycol mono-butyl ether and 10% perchloric acid. The applied voltage was 47 V, which gives a polishing current between 270 - 290 mA. Owing to high polishing current, the polishing time was rather fast (between 2 to 3 minutes). This gave a specimen with thin electron transparent zones usable for irradiation experiments.

For pure Fe and Fe (3, 5)wt.%Cr, the electro-polishing was a two step process. Initially, the polishing was done using 70% ethanol, 20% ethylene glycol mono-butyl ether and 10% perchloric acid at RT using 47 V. This provided specimens with a hole and electron transparent zones on the borders of the hole. It was then polished for 1 second using a combination of 95% ethanol and 5% perchloric acid at -40 ºC using a voltage of 23 V. This step was performed to have a specimen with relatively thick zones so that thickness fringes could be formed when analysed by TEM.

For bulk dimpled discs, only a good quality mirror polished surface is needed for irradiation experiments. This was obtained by polishing from only one side in Tenupol-5. One side of the 3 mm diameter sample was protected using a circular plastic sheet, and the polishing was performed from the unprotected side. In this case, electrolyte with a mixture of 70% ethanol, 20% ethylene glycol mono-butyl ether and 10% perchloric acid was used for 6 seconds. This polishing is responsible for a surface dimple on the specimen, due to which the samples are called dimpled discs.

Appendix B

Initial non-irradiated microstructure

All the materials were examined by TEM before selecting the final specimens for the irradiations. In this appendix, the TEM images showing their initial non-irradiated microstructure are given for reference purpose. The dislocation density was roughly checked and it was well within the order of magnitude of 10^8 cm^{-2} as indicated by the manufacturer. Since the specimens are not irradiated, no radiation damage (cavities, dislocation loops etc.) can be seen in the microstructure. There were no precipitates (like carbides) in the material.

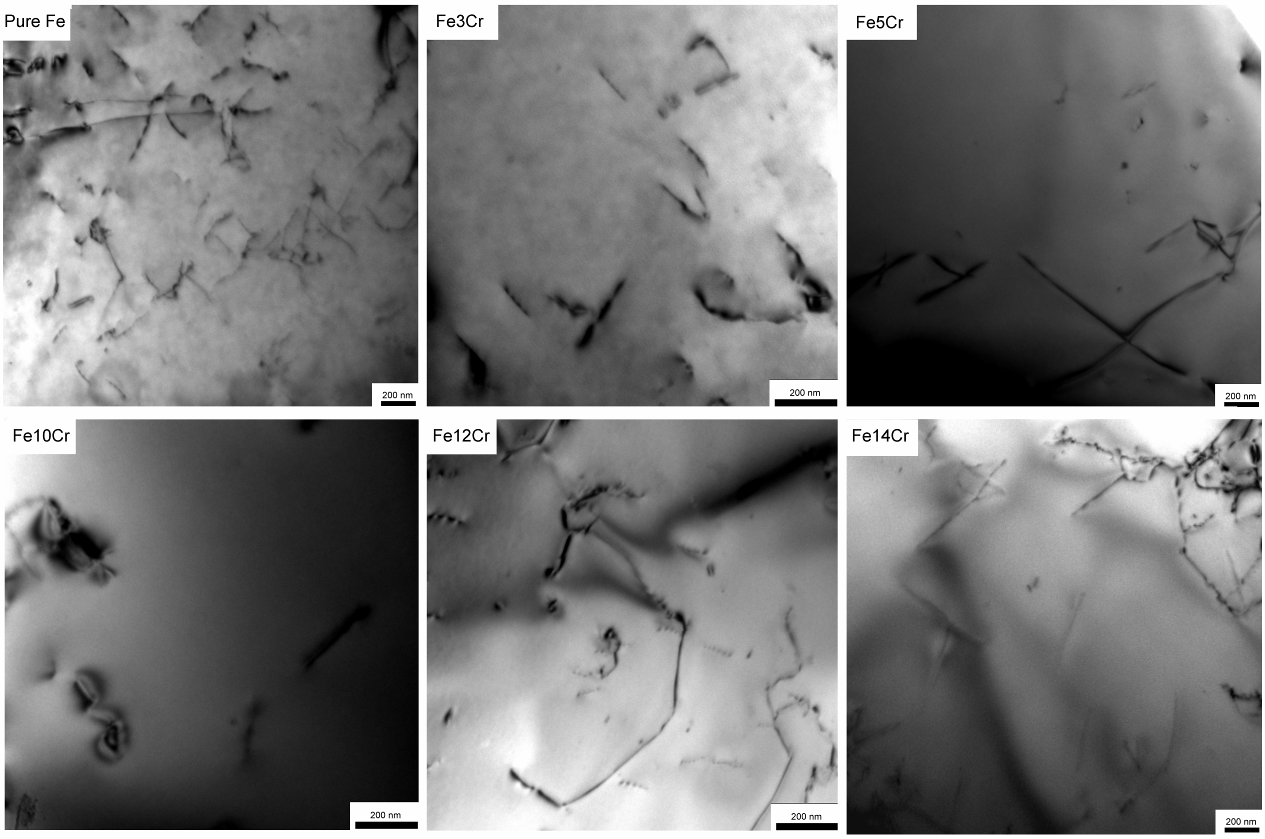

Figure B.1: Unirradiated microstructure of bcc Fe and FeCr alloys showing the initial dislocation density in the materials. BF TEM images of the thin foils prepared by electropolishing.

Appendix C

Specimen holder used for irradiations at JANNuS CEA/Saclay

In this appendix, the design of the specimen holder used for performing high dose irradiations at JANNuS CEA/Saclay is presented (Chapter 3, section 3.3.1). With this specimen holder, nine disc shaped specimens having 3 mm diameter can be irradiated simultaneously. There are six slots for measuring temperature using thermocouples. It is made up of 316 stainless steel. Details of specimen holder used for intermediate dose irradiations can be found in [13].

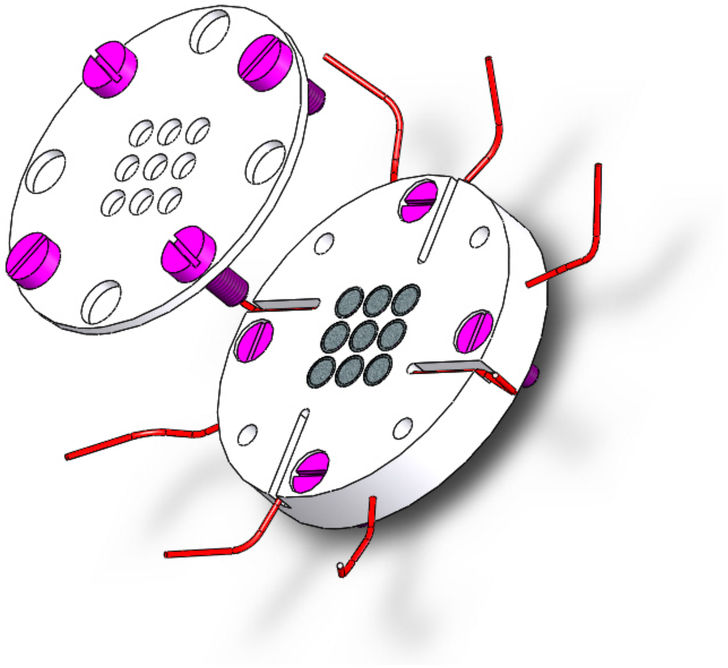

Figure C.1: Design of the specimen holder used for irradiations at JANNuS CEA/Saclay. The slots for thermo-couples are shown by red wires.

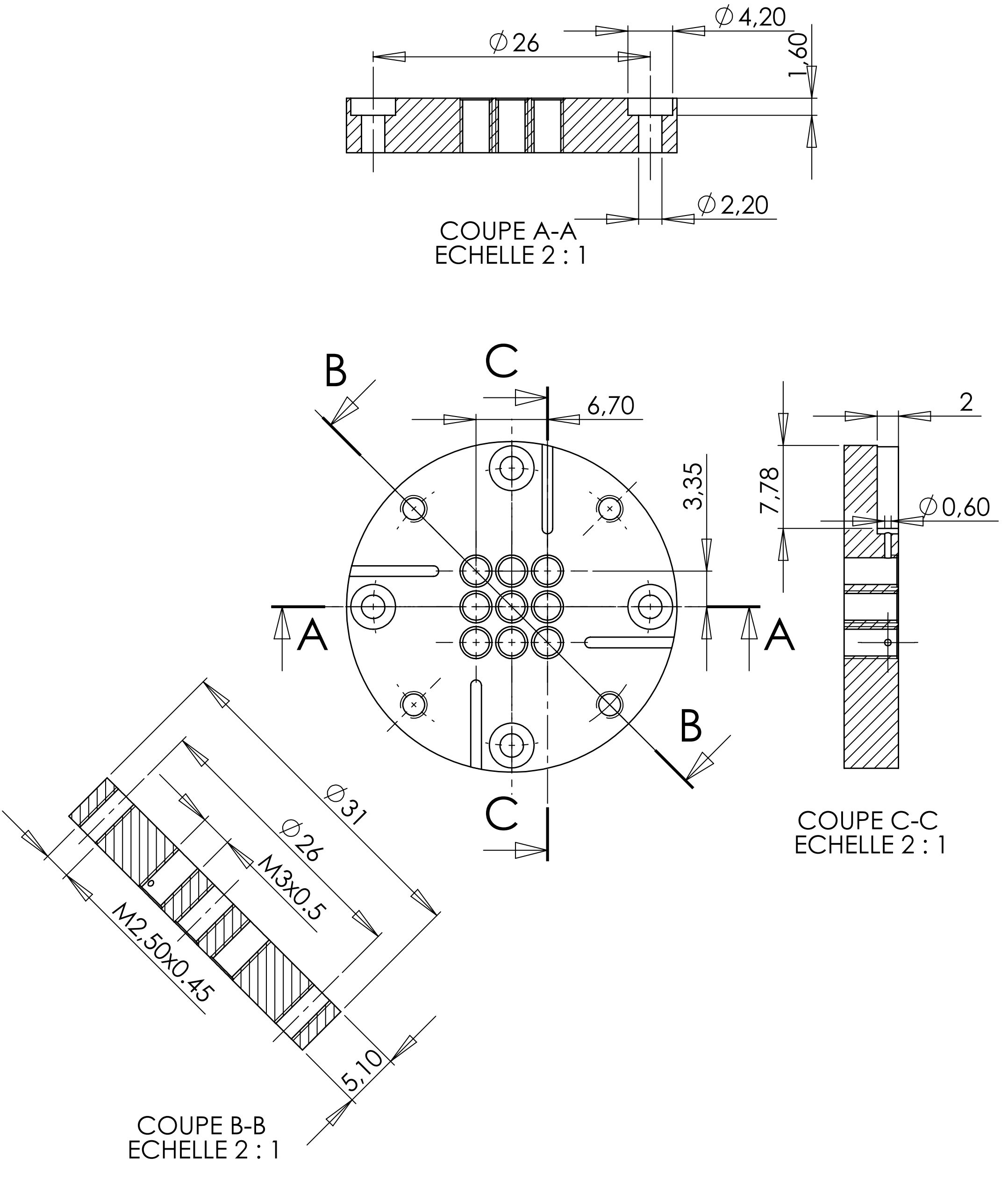

Tolérances générales non spécifiées : +/- 0.1
Ebavurage des pièces.

<u>Dessiné par</u> : **Leseigneur olivier**	**<u>Ech</u> :2:1**	**Embase 9 échantillons**
<u>Date</u> :12/04/11	**CEA - SACLAY - 91191 Gif-sur-Yvette**	
<u>Matière</u> : 316L	**A4**	**Ref. :**

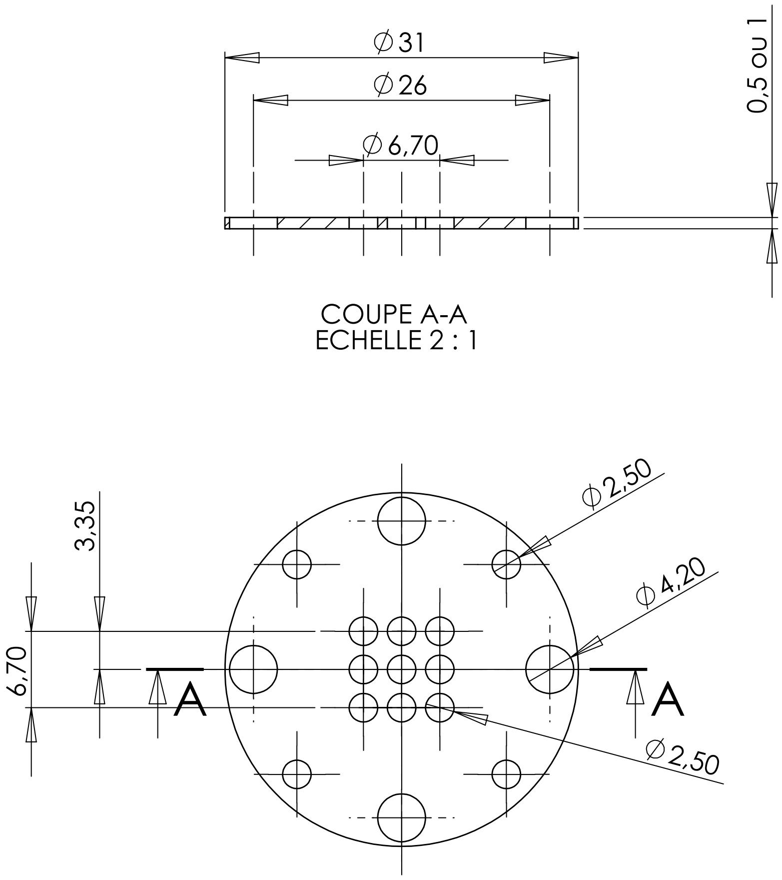

Tolérances générales non spécifiées : +/- 0.1
Ebavurage des pièces.

Dessiné par : **O.Leseigneur**	**Ech : 2:1**	**Embase 9 échantillons**
Date :13/04/11	**CEA - SACLAY - 91191 Gif-sur-Yvette**	
Matière : 316L	**A4**	**Ref. :**

Appendix D

Temperature control during high dose irradiations

During ion irradiations, temperature control of specimens is important. Care should be taken to avoid heating of specimens due to excessive beam power. In our case, the temperature was monitored using one thermo-couple and an infra-red (IR) camera. The thermocouple was considered to show the temperature obtained by heating due to the baking plate. For IR camera, the knowledge of emissivity value of the material at the desired temperature is necessary. This was obtained prior to the irradiation while performing calibration of the camera at a set temperature of 500 ºC on the specimen holder. The value given by the dedicated camera software was 0.17.

It must be noted that beam heating not only depends on the deposited beam power but also on the type of specimen holders used for the experiments. For a conventional specimen holder as ours, where the temperature is maintained by screws behind the specimens, a good thermal contact between the specimens and the screws is a must. When the parameters of specimen holders are satisfied, then a selection of beam current, and hence beam power, is made to avoid temperature rise.

In our case, experimental tests were performed using the specimen holder shown in appendix C to know the heating produced by the beam. It was realised that 1 W.cm^{-2} of beam power gave nearly 40 ºC temperature rise in our set-up. For 2 MeV Fe ions, this corresponded to a beam flux of 3.13 x 10^{12} ions.cm^{-2} (25.3 nA beam current). However, to perform the experiments within the limited allocated time, it was not possible to reduce the beam current to very low values to avoid beam heating. Thus, to obtain a compromise, we used the temperature rise induced by the beam to reach the desired irradiation temperature. During the actual irradiation experiment, the selected beam power was slightly lower than 1 W.cm^{-2}, which produced exactly 30 ºC temperature rise. Hence, 470 ºC was set on the specimen holder using the baking plate and the rest of the heating was given by the beam to reach the required 500 ºC. The temperature was monitored continuously during the irradiation.

An example of temperature monitoring during the experiment using the IR camera is shown in figure D.1. It corresponds to a snapshot of the IR software console. A similar colour of all the specimens is indicating that they have the same temperature. However, two specimens at the bottom show a colour corresponding to temperature even lower than the set temperature of 470 ºC (shown by white arrows in figure D.1) . Physically this is impossible. We believe this is just an artefact which may arise due to non-flat surface. Such an effect is also visible on the specimen holder surface : both on the left and right side of the IR image, we see a dark patch close to the corners around the screws. It was essentially due to slightly non-flat zone in this area and also due to a surface pollution trace which was remaining on the top plate of the specimen holder even after repeated cleaning efforts. This is, hence, just an artefact. Furthermore, around the specimens, a bright ring is present which indicate very high temperature range. This is also an artefact, arising due to a step height between the top specimen holder plate and the depression where the specimens are located (see figure C.1) . Thus, the zone in this area is not flat but at 90º to the IR camera direction.

The time evolution of the specimen temperatures is also shown at the bottom of the figure D.1. It was measured at two spots: one at the central specimen and one on the specimen holder surface. We can see that they are stable around 500 ºC. The depression in this curve for a fixed duration is the time when Faraday cups intercept the beam to measure beam current.

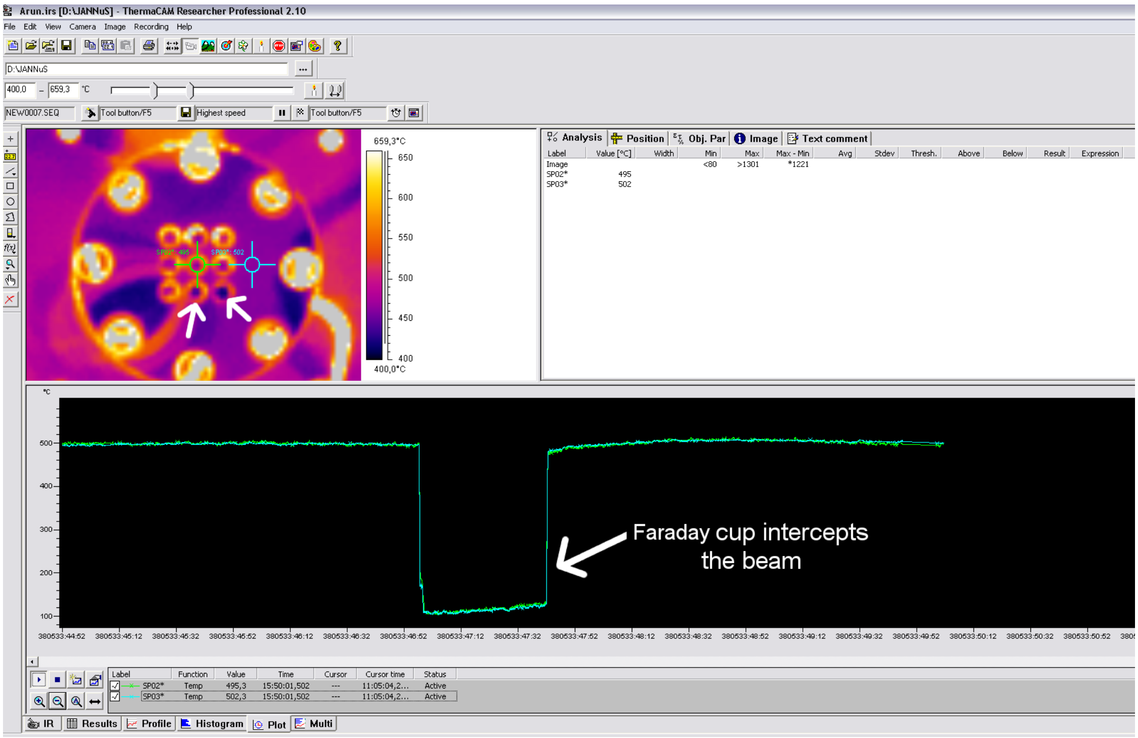
Arun.irs [D:\JANNuS] - ThermaCAM Researcher Professional 2.10

D:\JANNuS

400,0 – 659,3 °C

NEW0007.SEQ Tool button/F5 Highest speed Tool button/F5

Label	Value [°C]	Width	Min	Max	Max - Min	Avg	Stdev	Thresh.	Above	Below	Result	Expression
Image			<80	>1301	*1221							
SP02*	495											
SP03*	502											

Label	Function	Value	Time	Cursor	Cursor time	Status
☑ SP02*	Temp	495,3	15:50:01,502	---	11:05:04,2...	Active
☑ SP03*	Temp	502,3	15:50:01,502	---	11:05:04,2...	Active

Figure D.1: Snapshot of temperature regulation software connected to the IR camera. The thermal image is shown on the left. Line time scans of temperature at two spots is shown by the graph below. The deep well corresponds to the time when Faraday cups drop to measure beam current.

Appendix E

He implanted zone in high dose irradiations

As mentioned in Chapter 3, section 3.3.1, during the dual beam irradiations, an energy degrader consisting of a combination of Al foils was used on He beam. However, an empty window was kept in the degrader system to allow beam current measurements. Due to this, undegraded 2 MeV He ions were also implanted in the specimen. Their implantation depth was much farther, at 3.34 μm below the irradiated surface. The net implantation fluence was one-sixth of the total He fluence (because there are six windows: five are with Al foils and one is empty). Maximum dpa generated by this implantation was ~0.25 dpa. Since, it was not the zone of primary study, a systematic observation was not performed. There were, however, some images taken for pure Fe and Fe(10, 12, 14)%Cr which show the dislocation loops produced by damage due to He and cavities (presumably bubbles) associated with the loops, formed due to He implantation. They are shown in the next pages. Since this zone is farther away from the edge of the FIB thin foil, the thickness is presumably large. Hence, some images are slightly darker (especially for Fe10%Cr and Fe14%Cr). These observations were not performed for Fe(3, 5)%Cr samples.

- ○ Pure Fe

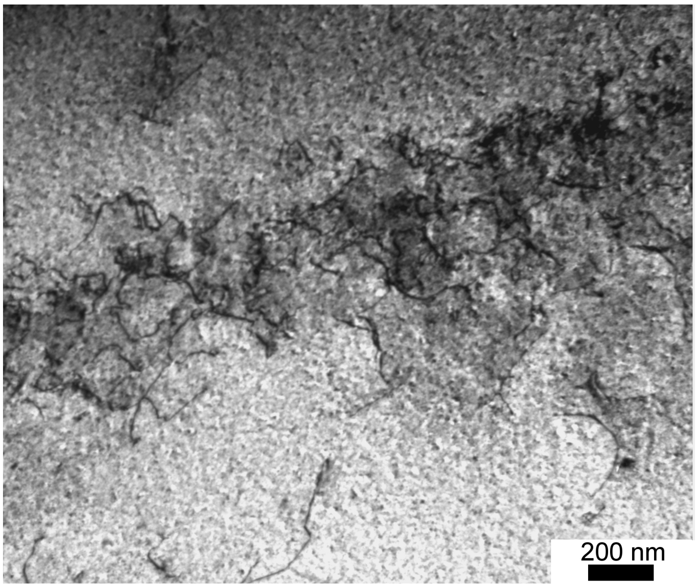

Figure E.1: Dislocation network in Fe at the He implantation zone at 3.34 μm depth. (BF, s > 0)

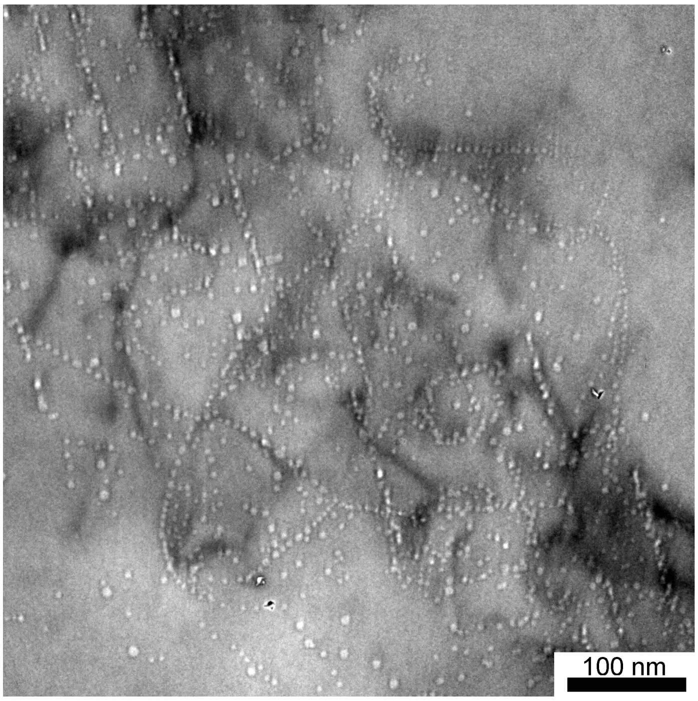

Figure E.2: Cavities in Fe at the He implantation zone at 3.34 μm depth. They are aligned along the dislocation lines within the network. (BF, under-focus = -1136 nm)

- ○ Fe12%Cr

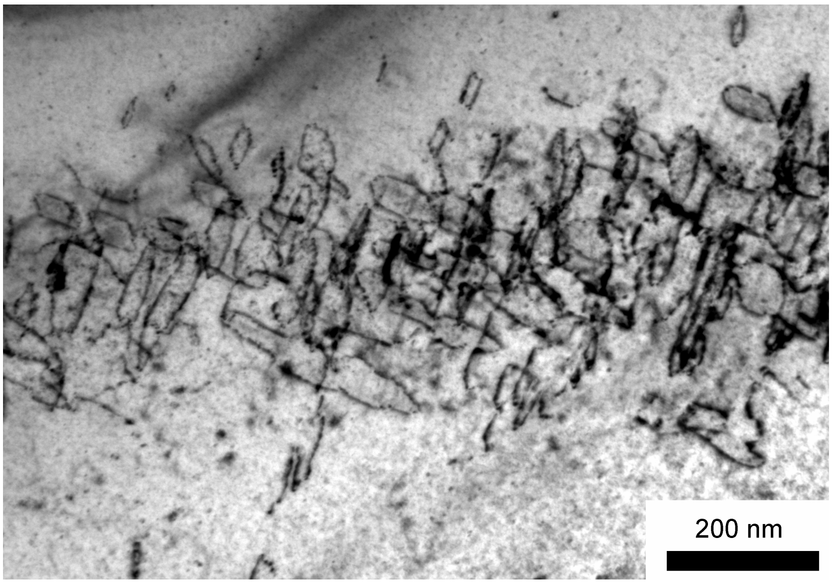

Figure E.3: Dislocation loop network at the He implanted zone in Fe12%Cr. (BF, $s_g > 0$, g = <110>, zone axis = (011)).

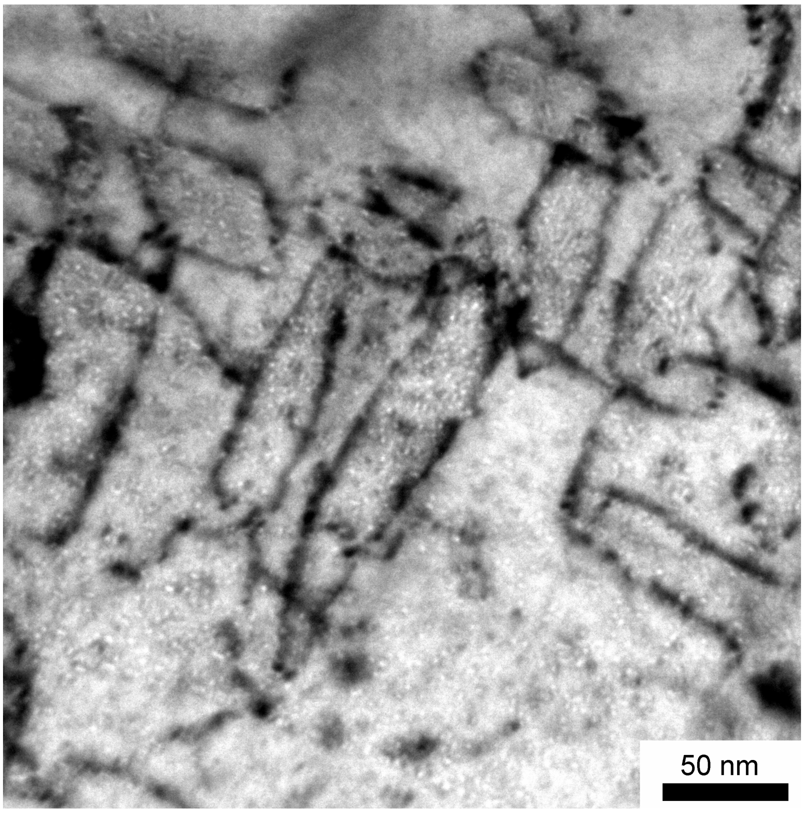

Figure E.4: Cavities inside the loops at the He implanted zone in Fe12%Cr. (BF, $s_g > 0$, zone axis = (011), under-focus = -1136 nm)

- ○ Fe10%Cr

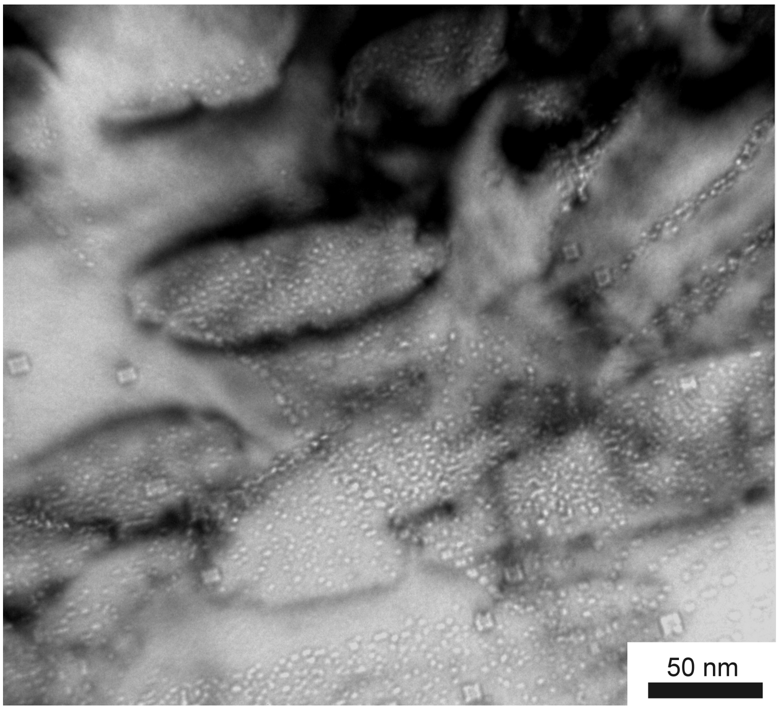

Figure E.5: Cavities inside the loops at the He implanted zone in Fe10%Cr. (BF, $s_g > 0$, zone axis = (011) under-focus = -1136 nm)

- ○ Fe14%Cr

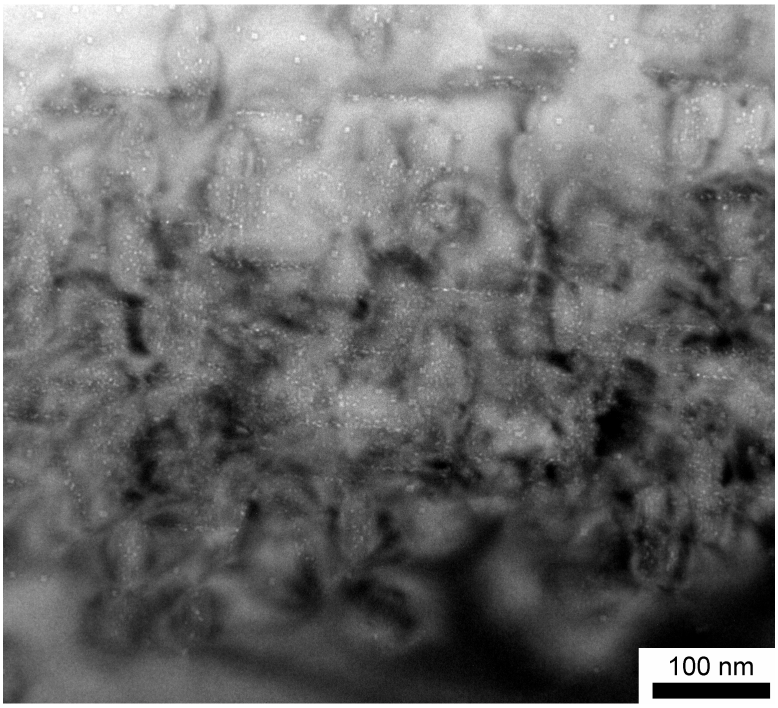

Figure E.6: Cavities associated with loops at the He implanted zone in Fe14%Cr. (BF, under-focus = -1136 nm)

Appendix F

CRESCENDO calculations - simplified cascade approximation

To understand the injected interstitial effect observed in high dose irradiated bcc Fe, another set of simulations using CRESCENDO were performed. These correspond to a projectile energy of 1 MeV. In this case, it was assumed that the damage production is homogeneous along the specimen depth up to 1000 nm. Then, at a given depth (700 nm), excesss interstitials were artificially added to observe a qualitative effect. Five cases were considered : 0, 1, 10, 50 and 100 appm/s injected ion implantation rate. As an example, the depth variation of the damage rate and injected ion implantation rate is given in figure F.1 for the case of 100 appm/s. The maximum damage reached was 3.4 dpa. All the other approximations were the same as in section 6.1.3 i.e. no displacement cascades, only monomers are formed and they are mobile (larger clusters are immobile).

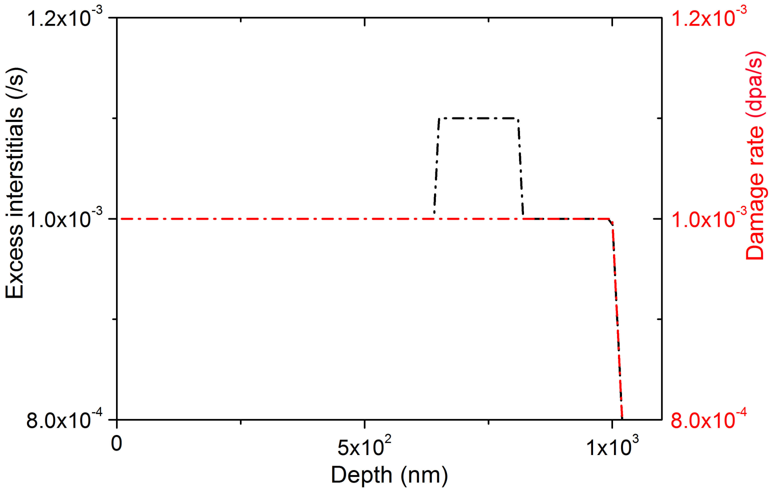

Figure F.1: The depth variation of damage rate and injected ion rate for the case of 100 appm/s ion injection. It was assumed that the damage is homogeneous along the specimen depth.

The results of the vacancy cluster distribution obtained from the simulations for depths 221 nm (far from the injected ion region) and 700 nm (at the injected ion region) are shown in figures F.2 and F.3

respectively. We can see that there is no difference between the different curves at 221 nm depth, which is far from the region of the injected ions. However, at 700 nm depth, the size and concentration decrease with increase in the amount of the injected ions. The effect begins to be prominent from 10 appm/s.

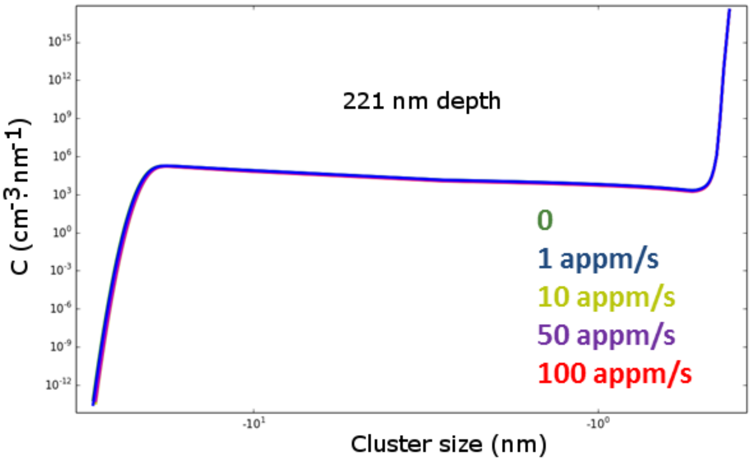

Figure F.2: Vacancy cluster distribution as a function of cluster size at 221 nm depth, far from the zone where injected ions are added. Five cases were considered: 0, 1, 10, 50 and 100 appm/s injected ions - all the curves are superimposed. By convention, vacancies are taken with a negative sign in CRESCENDO. Thus, for real sizes, we must ignore the negative sign.

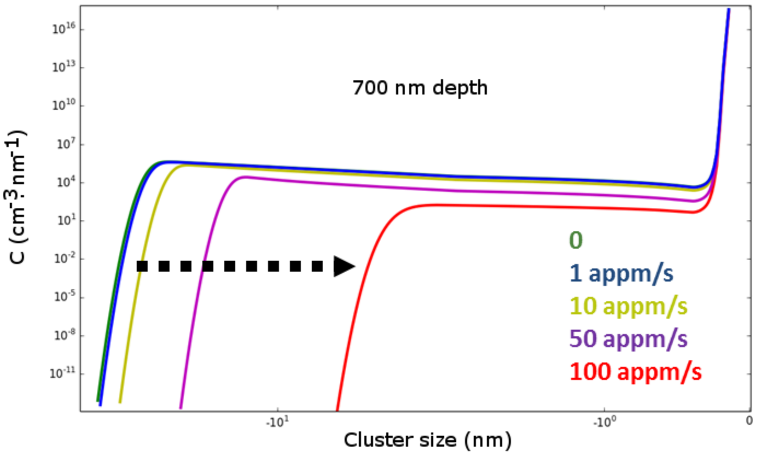

Figure F.3: Vacancy cluster distribution as a function of cluster size at 700 nm depth, where the injected ions are added. Five cases were considered: 0, 1, 10, 50 and 100 appm/s injected ions. By convention, vacancies are taken with a negative sign in CRESCENDO. Thus, for real sizes, we must ignore the negative sign.

For complimentary information, the distribution of interstitial clusters is also estimated at these two depths. They are given in figures F.4 and F.5 respectively. At 221 nm, no effect was seen. But at 700 nm, the excess injected ions contribute to the interstitial clusters. The size of the clusters increase progressively with the increase in the quantity of the injected ions.

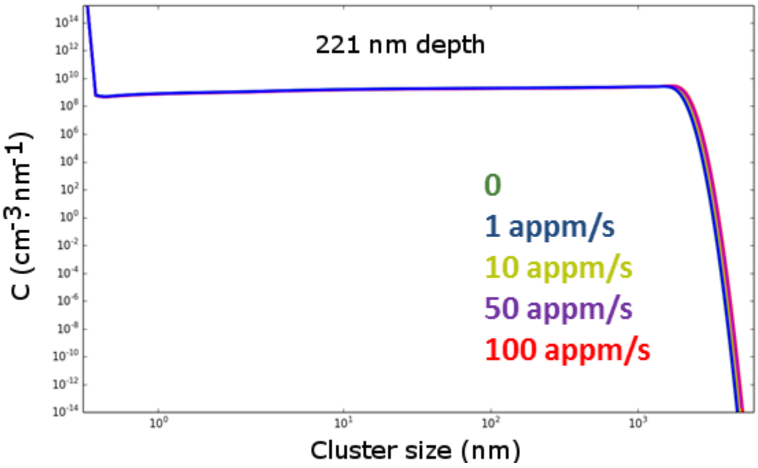

Figure F.4: Interstitial cluster distribution as a function of cluster size at 221 nm depth, far from the zone where injected ions are added. Five cases were considered: 0, 1, 10, 50 and 100 appm/s injected ions.

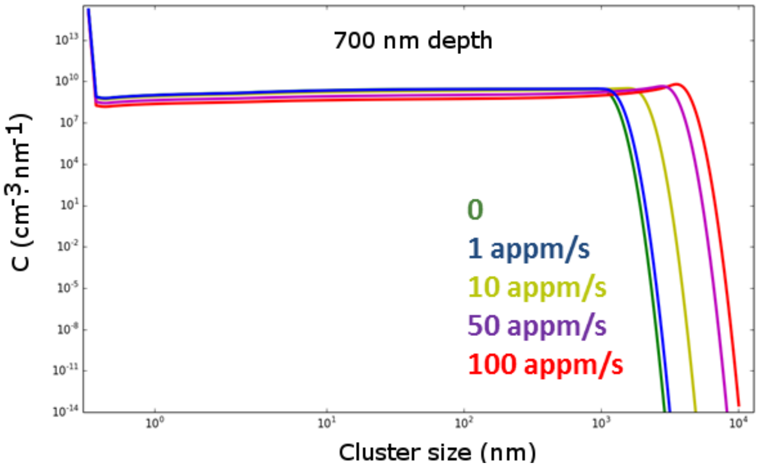

Figure F.5: Interstitial cluster distribution as a function of cluster size at 700 nm depth, where the injected ions are added. Five cases were considered: 0, 1, 10, 50 and 100 appm/s injected ions.